Theoretical and Experimental Study of the Stability of Clamped–Free Coaxial Cylindrical Shells Subjected to Internal and Annular Flows of Viscous Fluid

by

Vinhson Ba Nguyen

Thesis submitted to the Faculty of Graduate Studies and Research
in partial fulfillment of the requirements for the degree of
Doctor of Philosophy

Department of Mechanical Engineering
McGill University
Montréal, Canada

ISBN 0-315-74819-2

Abstract

This thesis presents a theoretical and experimental study of the stability of *cantilevered* coaxial cylindrical shells conveying incompressible, viscous fluid inside the inner shell and/or in the annulus between the two shells. Two analytical models are developed with experimental verification.

In the first model, fluid viscous effects are *partially* taken into consideration. Both shells are generally considered flexible. Shell motions are described by Flügge's shell equations, modified to take into account the *steady* viscous loads—flow pressurization and skin friction—acting on the shells. These equations are solved by means of the extended Galerkin method, in which the shell equations and the free–end boundary conditions can be satisfied simultaneously. The *unsteady* viscous forces are approximated by their inviscid counterparts, the formulation of which is based on linearized potential–flow theory with the assumption that the fluid is inviscid. The solution for these forces is obtained with the Fourier–transform technique; in connection with this technique, different so–called out–flow models are examined, concerning the effect of the downstream flow perturbations on the dynamics of the system.

The second analytical model, on the other hand, *fully* accounts for the viscous effects of the flow. Here, only the inner shell is flexible, while the outer shell is replaced by an identical rigid cylinder. Shell motions are also described by Flügge's modified shell equations, which incorporate the *steady* viscous loads exerted on the shell. These equations are solved numerically with the finite–difference method. The *unsteady* viscous forces are evaluated from flow perturbations which are the solution of the linearized, unsteady Navier–Stokes equations subject to the divergence–free constraint on the flow velocity perturbation. A recently developed, time–marching finite–difference method using "artificial compressibility" is applied to solve the Navier–Stokes equations; for the problem under consideration, this method employs the pressure and velocity perturbations as the dependent flow variables on a staggered grid.

In the experimental part of the thesis, tests involving either annular or inner flow are conducted on cantilevered silicone rubber shells concentrically located within rigid

plexiglas cylinders. Measurements are made of (i) the critical flow velocity of the system for various lengths of the shell and annular widths, and (ii) the dominant frequencies of oscillation of the shell for certain selected cases. Both divergence- and flutter-type instabilities are observed.

Comparisons between analytical results and test measurements show that the agreement between experiment and the two proposed analytical models is generally good, both qualitatively and quantitatively, in terms of the overall (lowest) critical flow velocities and frequencies of oscillation (first model only) of the tested shells.

Finally, future work is suggested with regard to improving the second model and conducting further calculations.

Résumé

Cette thèse présente une étude théorique et expérimentale sur la stabilité de coques cylindriques coaxialles encastrées–libres, dont la coque interne et/ou l'espace annulaire sont soumis à un écoulement de fluide visqueux et incompressible. Deux modèles analytiques ont été développés et vérifiés expérimentalement.

Dans le premier modèle, les effets fluides visqueux sont *partiellement* pris en considération. Les deux coques sont généralement considérées flexibles. Les déplacements des coques sont décrits par les équations de Flügge. Ces dernières sont modifiées pour tenir compte des charges *stationnaires*—la pressurisation dans l'écoulement et la friction en surface—agissant sur les coques. Ces équations sont solutionnées par une méthode de Galerkin modifiée dans laquelle les équations et les conditions limites peuvent être satisfaites simultanément. Les forces visqueuses *instationnaires* ont été approximées par leur contre–parties nonvisqueuses, la formulation desquelles est basée sur la théorie linéaire des écoulements potentiels, donc sur l'hypothèse que le fluide est nonvisqueux. Ces forces sont obtenues en utilisant la technique de la transformée de Fourier; en relation avec cette technique, différents modèles dits "out–flow models" sont examinés, qui tiennent compte des effets des perturbations en aval de l'écoulement sur la dynamique du système.

D'autre part, le second modèle analytique considère *entièrement* les effets visqueux dans l'écoulement. Dans ce cas paticulier, seule la coque interne est considérée flexible, tandis que la coque externe est supposée rigide. Les déplacements de la coque sont aussi décrits par les équations de Flügge modifiées afin d'incorporer les forces visqueuses *stationnaires* agissant sur la coque. Ces équations ont été résolues numériquement avec la méthode des différences finies (FDM). Les forces visqueuses *instationnaires* sont évaluées à partir des perturbations dans l'écoulement. Ces perturbations constituent une solution des équations linéarisées de Navier–Stokes sujettes à une condition de divergence nulle des champs de vitesse. Une méthode récemment développée d'intégration temporelle par différences finies employant une "compressibilité artificielle", fut appliquée pour solutionner les équations de Navier–Stokes; pour le problème considéré, cette méthode

utilise les perturbations de pression et de la vitesse comme variables dépendantes de l'écoulement, sur un maillage décalé.

Dans la partie expérimentale de la thèse, des essais impliquant des écoulements soit annulaires soit internes, ont été effectués sur des coques en silicone-caoutchouc, localisées concentriquement à l'intérieur de cylindres de "plexiglas" rigides. Des mesures ont été effectuées sur (i) la vitesse critique du système pour diverses longueurs de la coque et largeurs de l'anneau, et (ii) les fréquences dominantes de l'oscillation de la coque, pour certains cas spécifiques. Des instabilités de type de divergence ainsi que de type de flottement ont été observées.

Les comparaisons entre les résultats analytiques et les mesures reflètent un accord généralement bon, aussi bien qualitativement que quantitativement, que ce soit en termes de la vitesse critique principale ou des fréquences d'oscillation (premier mode seulement) des coques mises à l'essai.

Finalement, des travaux connexes futurs sont suggérés dans le but d'améliorer le deuxième modèle et pour pouvoir procéder à d'autres calculs.

Contributions to New Knowledge

The original contributions of the thesis, to new knowledge in the field of flow–induced vibrations, are as follows.

- The development of a new analytical model, based on potential–flow theory and the extended Galerkin method, for predicting the dynamics and instabilities of *cantilevered* coaxial cylindrical shells, conveying incompressible viscous flow within the inner shell and/or in the annular region. The dynamical behaviour of the cantilevered shell system is found to be very much different from that of the clamped–clamped or pinned–pinned shell system.

- The development of another new analytical model to examine the *unsteady* viscous effects of the annular flow on the cylindrical shell concentrically located in a coaxial rigid cylinder. For the first time, (i) unsteady viscous forces exerted on the shell are *properly* formulated and evaluated, and (ii) the existing time–marching finite-difference method with "artificial compressibility" is applied to solve a fluid–shell coupling problem.

- Extensive experimental measurements—critical flow velocities and frequencies of oscillation—on cantilevered shells subjected to annular flow and internal flow. These are obtained to support the theories presented herein and can be used to assess future theoretical work on the same subject.

Acknowledgements

The author wishes to express his deep gratitude to his supervisors, Prof. M. P. Païdoussis and Prof. A. K. Misra, for their continuous encouragement, invaluable suggestions, and patient guidance throughout this research.

The author is indebted to Dr. Nick Chepurniy for providing extensive free computing time, on behalf of CRAY Research (Canada) Inc., on the CRAY X–MP 2/8 computer located in Dorval (Canada) and for his enthusiastic technical support, without either one of which the completion of the numerical work presented Chapter 5 would have been impossible. Special tribute is paid to Michael Head of the McGill Computing Centre for his expertise on computer communication networks, making possible to have access to the CRAY computer from a personal computer at McGill University. Many thanks are owed to Steve Markhauser for his superb technical assistance on numerous aspects of the experimental work presented in Chapter 4.

The author is thankful to François Bélanger for many critical discussions on the numerical aspects of Chapter 5. The author would also like to make special mention of three of his colleagues, namely Dr. Ll. R. Curling, Dr. J. O. Gagnon, and Njuki W. Mureithi, for willingly giving their technical help or handy advice whenever a problem came up.

The financial support received as scholarships from the Natural Sciences and Engineering Research Council of Canada (NSERC) and from the author's supervisors through NSERC and Le Fonds pour la Formation de Chercheurs et l'Aide à la Recherche (FCAR) is gratefully acknowledged.

Finally, the author is very grateful to his parents for their constant moral support in the course of this work.

Table of Contents

Abstract ii

Résumé iv

Contributions to New Knowledge vi

Acknowledgements vi

Table of Contents vii

List of Tables xiv

List of Figures xvii

Nomenclature xxii

1 Introduction 1

1.1 Literature Review 1

1.1.1 General Remarks 1

1.1.2 Axial Flow inside Tubular Structures 2

1.1.3 Axial Flow outside Cylindrical Structures 4

1.1.4 Annular Flow in Coaxial Cylindrical Structures 6

1.2 Aims and Overview of the Thesis 11

2 An Analytical Model: Detailed Development 13

2.1 Introduction 13

2.2 Formulation of the Analytical Model 14

2.2.1 System Definitions and Assumptions 14

2.2.2 Governing Equations of Motion 14

2.2.3 Perturbation Pressures 16

2.3 Method of Solution 19

2.3.1 Introduction 19

2.3.2 Solution for the Perturbation Pressures 20

2.3.2.1 Annular Flow 20

2.3.2.2 Internal Flow 23

2.3.2.3 Nondimensionalization and Generalized Forces 23

2.3.3 Steady Viscosity–Related Stress Resultants 27

2.3.4 Solution to the Governing Equations of Motion 33

2.3.5 Summary 40

2.4 Preliminary Calculations 41

2.4.1 Introduction 41

2.4.2 Natural Frequencies of a Cylinder in the Absence of Flow 42

2.4.3 Convergence Study 42

2.4.3.1 Integration Stepsize 43

2.4.3.2 Domain of Integration 43

2.4.3.3 Number of Admissible Functions 44

2.4.4 Out–Flow Models 44

2.4.4.1 Effect of Having No Model 45

2.4.4.2 Selection of ℓ 45

2.4.4.3 Selection of Most Suitable Model 46

2.4.5 Summary 47

2.5 Theoretical Results 48

2.5.1 Introduction 48

2.5.2 Internal Flow Alone 49

2.5.2.1 General Dynamics of the System 49

2.5.2.2 Effect of Annular Gap 50

2.5.2.3 Effect of Length of the Shell 51

2.5.3 Annular Flow Alone 52
2.5.3.1 General Dynamics of the System 52
2.5.3.2 Effect of Dissipation 53
2.5.3.3 Effect of Steady Viscous Forces on Stability 55
2.5.3.4 Effect of L/a 57
2.5.3.5 Effect of Annular Gap 57
2.5.4 Internal and Annular Flows Together 58
2.5.5 Summary 59
2.6 Conclusion 60

3 Flexible Shell in a Coaxial Conduit: Effect of System Parameters 61
3.1 Introduction 61
3.2 Solution Procedure 62
3.2.1 Formulation of the Problem 62
3.2.2 Unsteady Radial Forces 63
3.2.3 Steady Viscosity–Related Stress Resultants 64
3.2.4 Extended Galerkin Method 65
3.3 Theoretical Results 66
3.3.1 Introduction 66
3.3.2 Stability of the System of a Clamped–Clamped Shell 67
3.3.2.1 Effect of Shell Length 67
3.3.2.2 Effect of Shell Thickness 68
3.3.2.3 Effect of Annular Gap 69
3.3.2.4 System with Counter–Current Flows 69
3.3.3 Stability of the System of a Cantilevered Shell 70
3.3.3.1 System with Co–Current Flows 70
3.3.3.2 Effects of Shell Thickness, Length, and Annular Width 71
3.3.4 Summary 72
3.4 Conclusion 72

4 **Experimental Verification** 73

4.1 Introduction . . . 73

4.2 Description of the Apparatus and Procedure . . . 73

4.2.1 Apparatus . . . 73

4.2.2 Measuring Instruments . . . 75

4.2.3 Testing Procedure . . . 76

4.3 Experimental Results—Annular Flow . . . 77

4.3.1 Observations . . . 77

4.3.2 Frequencies of Oscillation . . . 78

4.3.3 Effects of L/a and g/a . . . 80

4.4 Experimental Results—Internal Flow . . . 81

4.4.1 Observations . . . 81

4.4.2 Frequencies of Oscillation . . . 82

4.4.3 Effect of L/a . . . 82

4.5 Conclusion . . . 83

5 **Viscous Theory** 84

5.1 Introduction . . . 84

5.2 Formulation of the Analytical Model . . . 85

5.2.1 System Definition and Assumptions . . . 85

5.2.2 Governing Equations of Motion . . . 86

5.2.3 Unsteady Viscous Forces . . . 87

5.2.4 Summary . . . 92

5.3 Method of Solution . . . 92

5.3.1 Introduction . . . 92

5.3.2 Solution to the Governing Equations of Motion . . . 93

5.3.3 Solution to the Linearized Navier–Stokes Equations . . . 102

5.3.3.1 Numerical Formulation . . . 102

5.3.3.2 Initial and Boundary Conditions . . . 106

5.3.3.3 Evaluation of the r, x, and θ Sweeps . . . 108

5.3.4 Determination of the Unsteady Viscous Forces 116
5.3.5 Remarks on the Moving Boundary 117
5.3.6 Summary 119
5.4 Numerical Results 119
5.4.1 Numerical Procedure 119
5.4.2 Numerical Results 120
5.5 Conclusion 124

6 Conclusion **126**
6.1 Contributions of the Thesis 126
6.2 Suggestions for Future Work 129

Bibliography **131**

Tables **137**

Figures **150**

A Expression for $H_{km}(\bar{\alpha})$ **195**

B Out–Flow Models: Description **197**
B.1 In the Fourier Transform Method 197
B.1.1 Introduction 197
B.1.2 Model 0: No Model 198
B.1.3 Model 1: Straight Decay Model 198
B.1.4 Model 2: Curved Decay Model 199
B.1.5 Model 3: Refined Curved Model 200
B.1.6 Remarks 201
B.2 In the Finite–Difference Method 202

C Definition of [M], [C] and [K] **204**

D Integrals Involving Beam Eigenfunctions **207**

E Velocity Profiles and Turbulent Viscosity in Annuli **212**

E.1 Velocity Profiles in annuli 212

E.2 Turbulent Viscosity in Annuli 213

F Finite–Difference Expressions for Derivatives **215**

F.1 In a Uniform Grid 215

F.2 In a Non–Uniform Grid 216

F.2.1 Near a Flexible Wall 216

F.2.2 Near a Rigid Wall 217

F.2.3 At the Flexible Wall 218

G Evaluation of S_r, S_θ, S_x, S_∇ **220**

H Evaluation of Derivatives in a Non–Uniform Staggered Grid **225**

H.1 Generation of a Staggered Grid 225

H.2 Flow Variables in the Staggered Grid 226

H.3 Evaluation of Derivatives in a Stretched Grid 226

H.3.1 General Remarks 226

H.3.2 Grid Points far from Physical Boundaries 227

H.3.2.1 Location of $(\mathcal{V}_r)_{i,j}$ 227

H.3.2.2 Location of $(\mathcal{V}_\theta)_{i,j}$ 228

H.3.2.3 Location of $(\mathcal{V}_x)_{i,j}$ 229

H.3.2.4 Location of $(\mathcal{P})_{i,j}$ 229

H.3.2.5 Applicability of the Approximations 229

H.3.3 Grid Points near the Flexible Physical Boundary 230

H.3.3.1 Location of $(\mathcal{V}_\theta)_{i,2}$ 230

H.3.3.2 Location of $(\mathcal{V}_x)_{i,2}$ 231

H.3.4 Grid Points near the Rigid Physical Boundary 231

H.3.4.1 Location of $(\mathcal{V}_\theta)_{i,M-1}$ 231

H.3.4.2 Location of $(\mathcal{V}_x)_{i,M-1}$ 232

I Computer Listing **233**

List of Tables

2.1 Comparison between natural frequencies of a cantilevered shell, as measured by Gill (1972) and as calculated by Sharma's (1974) sextic approximation and by this theory with different numbers of admissible functions M, for different circumferential and axial mode numbers, n and m, respectively. 137

2.2 Comparison between critical flow velocities $\bar{U}_{ic}$ of a cantilevered shell, as calculated by Païdoussis and Denise (1972) and by the present theory with different integration stepsizes $\Delta\bar{\alpha}$, for different circumferential mode numbers n and three different flow models; the axial mode number m shown in each case is associated with instability. 138

2.3 Comparison between critical flow velocities $\bar{U}_{ic}$ of a cantilevered shell, as calculated by Païdoussis and Denise (1972) and by the present theory with different integration domains $(-z, z)$, for different circumferential mode numbers n and three different flow models; the axial mode number m shown in each case is associated with instability. 139

2.4 Comparison between critical flow velocities $\bar{U}_{ic}$ of a cantilevered shell, as calculated by Païdoussis and Denise (1972) and by the present theory with different number of admissible functions M, for different circumferential mode numbers n and three different flow models; the axial mode number m shown in each case is associated with instability. 140

2.5 The effect of the out–flow model used in the calculations on $\bar{U}_{ic}$; the calculations were conducted for $n = 2$, with $\Delta\bar{\alpha} = 4.0$, $(-z, z) = (-200, 200)$, $M = 4$, $\ell = 3$. 141

2.6 The effect of length ℓ on the critical flow velocity, $\bar{U}_{ic}$, for different circumferential mode numbers n and three different flow models; here, $\Delta\bar{\alpha} = 4.0$, $(-z, z) = (-200, 200)$, $M = 4$. An asterisk signifies that $\bar{U}_{ic} < 0.1$. 142
2.7 The effect of varying the length–to–radius ratio of a cantilevered shell on the critical flow velocity, $\bar{U}_{ic}$, for different circumferential mode numbers n and three different flow models; the axial mode number m shown in each case is associated with instability. The calculations were conducted with $\Delta\bar{\alpha}$, $(-z, z) = (-200, 200)$, $M = 4$ and $\ell = 3.0$. 143
2.8 The critical flow velocities, $\bar{U}_{ic}$, with n = 1–8 for the 1/10–gap system subjected to internal flow according to the inviscid and viscous (i.e., including steady viscous effects) versions of the theory, with the axial mode number m involved in each case. Cases in which stability is first lost by divergence, for a particular n, are marked by †. 144
2.9 The critical flow velocities, $\bar{U}_{ic}$, associated with n = 1–9 for the 1/10– and 1/100–gap systems subjected to internal flow according to inviscid theory, with the axial mode number m involved in each case. Cases in which stability is first lost by divergence, for a particular n, are marked by †. 145
2.10 The effect of varying the length–to–radius ratio on the overall critical flow velocity, $\bar{U}^*_{ic}$, for the 1/10–gap system subjected to internal flow, according to the inviscid and viscous (i.e., including steady viscous effects) versions of the theory; the circumferential mode number n associated with $\bar{U}^*_{ic}$ is shown in each case. 146
2.11 Critical annular flow velocities, $\bar{U}_{oc}$, with different n for the 1/10–gap system, according to the inviscid and viscous versions of the theory; "S" stands for single–mode flutter, "C" for coupled–mode flutter, and "D" for divergence. The identification of the mode number m at instability for some of the results with dissipation ($\mu_i \neq 0$) was not clear–cut; hence, no value of m is given. 147

2.12 The effect of steady viscous forces and structural damping on stability with $n = 1$, showing that they can be either stabilizing or destabilizing, depending on the gap size. 148

4.1 The effect of annular fluid on the critical internal flow velocity, $\bar{U}^*_{ic}$, for different lengths of a cantilevered silicone rubber shell. The fluid is air. 149

List of Figures

2.1 Schematic of the system under consideration. 150

2.2 Comparison of the *in vacuo* natural frequencies calculated by this theory with Gill's (1972) measurements and Sharma's (1974) sextic-approximation calculations; the shell parameters are given in Section 2.4.2. (a) $n = 2$; (b) $n = 3$; (c) $n = 4$. 151

2.3 The so-called "out-flow" models considered in this theory for the decay of perturbations beyond the free end of the shells; Model 0 effectively corresponds to no model at all. $\xi \equiv x/L = 1$ corresponds to the free end of the shell; $\xi = \ell (\equiv L'/L)$ is the point where perturbations are assumed to vanish. 154

2.4 Comparison of the dimensionless critical flow velocities, $\bar{U}_{ic}$, calculated by the present theory with Païdoussis and Denise's (1972) theoretical and experimental values, for a cantilevered elastomer shell conveying air flow; the system parameters are given in Section 2.4.3. 155

2.5 Typical Argand diagram involving the real, $\mathrm{Re}(\bar{\Omega}_i)$, and imaginary, $\mathrm{Im}(\bar{\Omega}_i)$, parts of the dimensionless eigenfrequencies of the so-called 1/10-gap system, consisting of a cantilevered steel shell surrounded by quiescent annular fluid (water) while conveying internal water flow, as the dimensionless flow velocity $\bar{U}_i$ is varied; the system parameters are given in Section 2.5.1. These calculations were carried out for $n = 2$, $m = 1, 2, 3$; - - - - , inviscid theory; ——— , with steady viscous terms taken into account. 156

2.6 The dimensionless critical flow velocity $\bar{U}_{ic}$ of a cantilevered steel shell, surrounded by quiescent annular fluid (water) while conveying internal water flow, as a function of n for two different annular gaps; the system parameters are given in Section 2.5.1. These calculations were done with the inviscid theory; ——, flutter boundary; - - - -, divergence boundary (for the modes in which stability is first lost by divergence). Note: "$1/k$–gap" system means one where (annular gap) / (inner–shell radius) = $1/k$. 157

2.7 The effect of L/a on the overall (lowest) critical dimensionless flow velocity, $\bar{U}^*_{ic}$, for the 1/10–gap system conveying internal water flow and quiescent annular fluid (water); the circumferential mode number, n, associated with first loss of stability is shown in the figure. ○, inviscid flow; △, with steady viscous effects taken into account. 158

2.8 Typical Argand diagram for the dimensionless eigenfrequencies $\bar{\Omega}_i$ of the 1/10–gap system conveying annular water flow and quiescent internal fluid (water), as the dimensionless flow velocity $\bar{U}_o$ is varied; the system parameters are given in Section 2.5.1. These calculations were carried out for $n = 2$, $m = 1, 2, 3$; - - - -, inviscid theory; ——, with steady viscous effects taken into account. 159

2.9 The effect of structural damping (variable μ_i) on stability of the 1/10–gap system with annular water flow according to the viscous version of the theory, showing the emergence of a minimum $\bar{U}_{oc}$ for flutter, at $n = 5$ when $\mu_i \neq 0$; - - - -, divergence boundary; ——, flutter boundary. . . . 160

2.10 The effect of L/a on the overall (lowest) critical dimensionless flow velocity, $\bar{U}^*_{oc}$, for the 1/10–gap system conveying annular water flow and quiescent internal fluid (water); the circumferential mode number, n, associated with first loss of stability is shown for each value of L/a for which calculations were conducted. - - - -, divergence boundary; ——, flutter boundary. The viscous results were obtained with $\mu_i = 5 \times 10^{-3}$. 161

2.11 The effect of annular gap size on the critical annular flow velocity $\bar{U}_{oc}$ according to the inviscid theory as n is varied. In cases where divergence precedes flutter, the divergence boundaries (- - - -) are also shown. . . 162
2.12 Stability map with $n = 3$ for the 1/10–gap system simultaneously subjected to internal and annular flows according to the inviscid theory. . . 163
3.1 Schematic of the system under consideration. 164
3.2 The overall (lowest) critical dimensionless annular flow velocity, $\bar{U}^{*}_{oc}$, in the $\frac{1}{10}$–gap system as a function of the dimensionless length of the shell L/a, with the circumferential mode, n, associated with first loss of stability indicated in the figure; ○, inviscid flow; △, with steady viscous effects taken into account. The shell is clamped at both ends and the inner fluid is stagnant. 165
3.3 The overall critical dimensionless annular flow velocity, $\bar{U}^{*}_{oc}$, in the $\frac{1}{10}$–gap system as a function of the dimensionless wall–thickness of the shell h_i/a, with the circumferential mode, n, associated with first loss of stability indicated in the figure; ○, inviscid flow; △, with steady viscous effects taken into account. The shell is clamped at both ends and the inner fluid is stagnant. 166
3.4 The overall critical dimensionless annular flow velocity, $\bar{U}^{*}_{oc}$, as a function of the dimensionless annular gap $(b-a)/a$, with the circumferential mode, n, associated with first loss of stability marked in the figure; ○, inviscid flow; △, with steady viscous effects taken into account. The shell is clamped at both ends and the inner fluid is stagnant. 167
3.5 The critical dimensionless annular flow velocity, $\bar{U}_{oc}$, in the $\frac{1}{10}$–gap system as a function of the circumferential mode, n; —— , flows in the same direction; - - - - , flows in opposite directions. The shell is clamped at both ends and the inner flow velocity is constant ($\bar{U}_i = 0.01$). 168

3.6 The critical dimensionless annular flow velocity, $\bar{U}_{oc}$, in the $\frac{1}{10}$–gap system as a function of the circumferential mode, n, for two different inner flow velocities; ○, $\bar{U}_i = 0$; △, $\bar{U}_i = \bar{U}_o$; - - - - , divergence boundary; —— , flutter boundary. The divergence boundaries for the two values of $\bar{U}_i$ are generally coincident. The shell is cantilevered. 169

3.7 The overall critical dimensionless annular flow velocity, $\bar{U}^*_{oc}$, in the $\frac{1}{10}$–gap system as a function of h_i/a for two different shell lengths, with the circumferential mode, n, associated with first loss of stability marked in the figure; ○, $L/a = 5$; △, $L/a = 10$; - - - - , divergence boundary; —— , flutter boundary. The shell is cantilevered and the inner fluid is stagnant. 170

3.8 The overall critical dimensionless annular flow velocity, $\bar{U}^*_{oc}$, as a function of h_i/a for two different annular widths ($L/a = 10$), with the circumferential mode, n, associated with first loss of stability marked in the figure; ○, $(b-a)/a = 1/5$; △, $(b-a)/a = 1/10$; - - - - , divergence boundary; —— , flutter boundary. The shell is cantilevered and the inner fluid is stagnant. 171

4.1 Schematic of the test apparatus involving *annular* flow. 172

4.2 Schematic of the test apparatus involving *internal* flow. 173

4.3 Photographs of a silicone rubber shell inside a plexiglas cylinder with two mounted fotonic sensors: (a) side view, (b) top view. 174

4.4 Photograph of the entire experimental setup. 175

4.5 Photograph of the free–end cross section of the shell fluttering with $n = 2$. 176

4.6 A typical cross spectral density (CSD): (a) amplitude of the shell motion(s) versus the frequency(ies) of oscillation, and (b) phase difference of the shell motions at the locations of the two fotonic sensors. 177

4.7 Predicted and measured frequencies of the shell at various annular flow velocities: (a) $n = 1$, (b) $n = 2$. The system has $g/a = 1/10$, $L/a = 8$. . . 178

4.8 Predicted and measured frequencies of the shell at various annular flow velocities: (a) $n = 1$, (b) $n = 2$, and (c) $n = 3$. The system has $g/a = 1/4$, $L/a = 8$. 179

4.9 Cross section of the shell vibrating in (a) $n = 1$, (b) $n = 2$, (c) $n = 3$, and (d) $n = 4$. 181
4.10 Overall critical annular flow velocity, U^*_{oc}, as a function of length–to–radius ratio of the shell, L/a, for (a) $g/a = 1/10$, (b) $g/a = 1/4$, and (c) $g/a = 1/2$. 182
4.11 Predicted and measured frequencies of the shell at various internal flow velocities: (a) $n = 1$, (b) $n = 2$, and (c) $n = 3$. The system has $g/a = 1.5$, $L/a = 8$. 184
4.12 Overall critical internal flow velocity, U^*_{ic}, as a function of length–to–radius ratio of the shell, L/a, for $g/a = 1.5$. 186
5.1 Schematic of the system under consideration. 187
5.2 Schematic of the arrangement of (i) flow variables in the present staggered mesh and (ii) nodes on the flexible shell. $\blacktriangledown$: $\mathcal{V}_r$; $\triangledown$: $\mathcal{V}_x$; $\bigcirc$: $\mathcal{P}$, $\mathcal{V}_\theta$; $\bullet$: nodes on the shell. 188
5.3 Radial displacement of the shell at $\xi = 1$ as a function of time, initially excited in $m = 2$ (axial mode) and $n = 2$ (circumferential mode). The shell oscillates *in vacuo* and in the absence of internal dissipation. (a) : $\Delta t = T_o/24$; (b) : $\Delta t = T_o/48$. 189
5.4 Radial displacement of the shell at $\xi = 1$ as a function of time in the 1/10–gap system, initially excited in $m = 2$ (axial mode) and $n = 2$ (circumferential mode). (a) : $\bar{U} = 0.35$; (b) : $\bar{U} = 0.40$; (c) : $\bar{U} = 0.45$. 190
5.5 Radial displacement of the shell at $\xi = 1$ as a function of time in the 1/2–gap system, initially excited in $m = 1$ (axial mode) and $n = 2$ (circumferential mode). (a) : $\bar{U} = 0.90$; (b) : $\bar{U} = 0.95$; (c) : $\bar{U} = 1.00$. 192
5.6 The effect of annular gap width on the overall critical flow velocity, $\bar{U}^*_c$. Theory 1 : inviscid theory with steady viscous effects included (Chapter 2); Theory 2 : theory of Chapter 5. 194

Nomenclature

a	inner–shell radius
$A_m, \ldots, F_m$	constants [see Equations (2.31) and (2.32)]
b	outer–shell radius
d_i	$2a$, mean diameter of the inner shell
d_h	$2(b-a)$, hydraulic diameter
E	Young's modulus of the shell material (Chapter 5)
E_i, E_o	Young's moduli of the inner–shell and outer–shell materials
f_i, f_o	friction factors of the inner and outer flows [see Equation (2.83)]
g	$b-a$
h	wall–thickness of the shell (Chapter 5)
h_i, h_o	wall–thicknesses of the inner and outer shells
I_n, K_n	modified Bessel functions of order n
k	(i) axial wave number [see Equation (2.105)] (ii) $h^2/12a^2$ [see Equations (5.1)–(5.3)] (iii) pseudo–time level (k appears as a superscript only)
k_i	$h_i^2/12a^2$
k_o	$h_o^2/12b^2$
ℓ	L'/L
l	(i) circumferential wave number [see Equation (2.105)] (ii) Prandtl's mixing length (Appendix E)
L	length of the flexible portion of the shell
L'	total length in which flow perturbations are non–zero
m	axial wave number
M	(i) number of admissible functions taken [see Equation (2.122)] (ii) number of v_θ grid points aligned vertically (see Figure 5.2)

M_x	bending moment
$M_{x\theta}$	twisting moment
n	(i) circumferential wave number (ii) physical–time level (n appears as a superscript only)
N	number of nodes within the flexible portion of the shell
N_x	axial (normal) force per unit length
$N_{x\theta}$	shearing force per unit length
N_{xI},$N_{\theta I}$,$N_{x\theta I}$	axial, hoop, and shear stress resultants [see Equation (2.97)]
p	shell–motion–induced perturbation of P_t/ρ [see Equation (5.20)]
$\bar{p}$	θ–independent amplitude of p [see Equation (5.79)]
$\hat{p}^{n+1}$	$\bar{p}^{n+1} - \bar{p}^n$
$\hat{p}$	transient value of $\hat{p}^{n+1}$ in pseudo–time
p_e	perturbation pressure surrounding the outer shell
p_i,p_o	perturbation pressures in the inner and annular flows [see Equation (2.30)]
P	instantaneous pressure in the perturbed flow field [see Equation (2.27)]
$P_i(x,r)$	time–averaged pressure of the inner fluid [see Equation (2.77)]
$P_o(x,r)$	time–averaged pressure of the annular fluid [see Equation (2.79)]
P_s	stagnation pressure [see Equation (2.27)]
$\bar{P}$	(i) mean, undisturbed pressure in the flow [see Equation (2.29)] (ii) steady part of P_t/ρ [see Equation (5.20)]
$\bar{P}_{rIi}$	steady radial differential pressure on the inner shell [see Equation (2.86)]
$\bar{P}_{rIo}$	steady radial differential pressure on the outer shell [see Equation (2.89)]
$\bar{P}_{xIi}$	traction load on the inner shell [see Equation (2.88)]
$\bar{P}_{xIo}$	traction load on the outer shell [see Equation (2.92)]
q_1,q_2,q_3	steady viscous forces acting on the shell (Chapter 5)
q_{1i},q_{2i},q_{3i}	steady viscous forces acting on the inner shell [see Equation (2.99)]

q_{1o},q_{2o},q_{3o}	steady viscous forces acting on the outer shell [see Equation (2.99)]
q_i,q_o	unsteady inviscid forces acting on the inner and outer shells [see Equation (2.60)]
q_x,q_θ,q_r	unsteady viscous forces acting on the shell in the x–, θ–, r–direction [see Equations (5.27)–(5.29)]
$\bar{q}_i,\bar{q}_o$	reference forces per unit area [see Equation (2.54)]
Q_x	transverse shearing force per unit length
r	radial coordinate
r_m	radius at which the mean velocity is maximum in the turbulent flow [see Equation (2.82)]
R	inner radius of a pipe
$\mathrm{Re}_i,\mathrm{Re}_o$	Reynolds numbers of the inner and annular flows
$R_m(x)$	functional form of an out–flow model
t	physical time
u,v,w	axial, circumferential, and radial displacements of the shell (Chapter 5)
$\bar{u},\bar{v},\bar{w}$	θ–independent amplitudes of u,v,w [see Equation (5.30)]
$\hat{u},\hat{v},\hat{w}$	$\bar{u}/L,\bar{v}/L,\bar{w}/L$
u_i,v_i,w_i	axial, circumferential, and radial displacements of the inner shell
u_o,v_o,w_o	axial, circumferential, and radial displacements of the outer shell
$U(r)$	steady part of V_x [see Equation (5.20)]
U_i,U_o	mean, undisturbed velocities of the inner and annular inviscid flows
$U_{\tau i}$	stress velocity on the interior surface of the inner shell [see Equation (2.78)]
$U_{\tau oi}$	stress velocity on the exterior surface of the inner shell [see Equation (2.80)]
$U_{\tau oo}$	stress velocity on the interior surface of the outer shell [see Equation (2.81)]
$\mathcal{U}_i,\mathcal{U}_o$	reference flow velocities [see Equation (2.54)]
$\mathbf{v}$	(v_x,v_θ,v_r), shell–motion–induced perturbation of $\mathbf{V}$ [see Equation (5.20)]
$\hat{\mathbf{v}}^{n+1}$	$\bar{\mathbf{v}}^{n+1} - \bar{\mathbf{v}}^{n}$

$\hat{\mathbf{v}}$	transient value of $\hat{\mathbf{v}}^{n+1}$ in pseudo–time
$\bar{v}_x, \bar{v}_\theta, \bar{v}_x, \bar{p}$	θ–independent amplitudes of v_x, v_θ, v_r, p [see Equation (5.79)]
$\tilde{v}_x, \tilde{v}_\theta, \tilde{v}_x, \tilde{p}$	intermediate values of $\breve{v}_x, \breve{v}_\theta, \breve{v}_x, \breve{p}$ [see Equation (5.95)]
$\breve{v}_x, \breve{v}_\theta, \breve{v}_x, \breve{p}$	intermediate values of $\bar{v}_x, \bar{v}_\theta, \bar{v}_x, \bar{p}$ [see Equation (5.96)]
V_x,V_θ,V_r	components of the mean–flow velocity vector $\mathbf{V}$
V_x',V_θ',V_r'	fluctuation velocity components of the turbulent flow
$\mathcal{V}$,$\mathcal{P}$	$\hat{v}, \hat{p}$ or $\bar{v}, \bar{p}$
x	axial coordinate
y	coordinate measured from the wall

Greek letters

α	(i) Fourier–transform variable (Chapter 2) (ii) Δt (Chapter 5)
β	artificial compressibility
γ	$\rho_s a^2(1-\nu^2)/E$ [see Equations (5.1)–(5.3)]
γ_i	$\rho_{si} a^2(1-\nu_i^2)/E_i$
γ_o	$\rho_{so} b^2(1-\nu_o^2)/E_o$
ε	r/L
ε_i	a/L
ε_o	b/L
η	r/L
θ	polar coordinate
μ_i,μ_o	structural damping factors of the inner–shell and outer–shell materials
ν	Poisson's ratio of the shell material (Chapter 5)
ν_i, ν_o	(i) Poisson's ratios of the inner–shell and outer–shell materials (ii) kinematic viscosities of the inner and annular fluids
ν_m	molecular kinematic viscosity of the fluid
$\nu(r)$	$\nu_m + \nu_t(r)$
$\nu_t(r)$	turbulence (eddy) viscosity of the annular flow (Chapter 5)

ξ	x/L
ρ_i, ρ_o	densities of the fluids inside the inner shell and in the annulus
ρ_s	density of the shell material (Chapter 5)
ρ_{si}, ρ_{so}	densities of the inner–shell and outer–shell materials
τ	pseudo–time
τ_{wi}	fluid frictional force per unit area on the interior surface of the inner shell [see Equation (2.78)]
τ_{woi}	fluid frictional force per unit area on the exterior surface of the inner shell [see Equation (2.80)]
τ_{woo}	fluid frictional force per unit area on the interior surface of the outer shell [see Equation (2.81)]
ϕ_i, ϕ_o	velocity potential perturbations of the inner and annular flows
Φ_m	beam eigenfunctions
χ	viscous damping coefficient of the shell material (Chapter 5)
χ_i, χ_o	viscous damping coefficients of the inner–shell and outer–shell materials
Ψ	velocity potential
Ω	angular frequency of oscillation

Chapter 1

Introduction

1.1 Literature Review

1.1.1 General Remarks

Research into the dynamics of cylindrical structures containing, or immersed in, flowing fluid has been pursued quite intensively over the past thirty years or so. Although the first serious study of the dynamics of flexible pipes conveying fluid was undertaken by Bourrières (1939), interest in the subject did not really come about until the occurrence of oscillations of the Trans–Arabian aboveground oil pipelines (Ashley and Haviland 1950). Since then, fluid–structure interactions have been found to be responsible for failures of many crucial components in such diversified engineering applications as nuclear reactors, heat exchangers, jet pumps, aircraft jet engines, and so on.

In general, cylindrical structures may be excited by either *axial* flow or *cross* flow, the former of which could be further divided into three different classes, depending on how the flowing fluid comes in contact with the structure(s) involved: (i) axial flow inside tubular structures, (ii) axial flow outside cylindrical structures, and (iii) axial flow in annular regions between coaxial cylinders.

This literature review is meant to be selective, not exhaustive; only key references will be mentioned to show various stages of research development on *axial flow*—the type of flow to be considered in this thesis. For interested readers, a rather recent, very comprehensive survey on all kinds of flow–induced instabilities given by Païdoussis

(1987) should be consulted.

1.1.2 Axial Flow inside Tubular Structures

This is the oldest, most fundamental type of problem, dating back to the early 1950's when Ashley and Haviland (1950), Feodos'ev (1951), Housner (1952), and Niordson (1953) investigated the stability of pipes containing flowing fluid. Using different means of analysis, involving beam theory, they all came to the same conclusion that, at sufficiently high flow velocities, pinned–pinned pipes may buckle like columns subjected to compressive axial loading. This phenomenon is commonly referred to as divergence, which is another term for buckling instability.

It is known that pipes conveying fluid with both ends supported belong to the family of gyroscopic conservative systems. With linear beam theory, Païdoussis and Issid (1974) studied in a general way the dynamics of both members of this family, namely pinned–pinned and clamped–clamped pipes; they found that conservative systems are not only subject to divergence but also to coupled–mode flutter (a form of oscillatory instability). Later, Païdoussis (1975) showed that, in the case of thin–walled pipes, thin–shell theory predicts the same dynamical behaviour of the system and that the critical flow velocity obtained by beam theory converges to that given by shell theory as the length of the pipe increases. Predictions for divergence of pipes with ends supported have been well verified by series of experiments conducted by Naguleswaran and Williams (1968), Liu and Mote (1974), and more recently Jendrzejczyk and Chen (1985). Nevertheless, post–divergence oscillatory instability has never been observed experimentally, therefore confirming a theoretical prediction made by Holmes (1978) through nonlinear analysis that coupled–mode flutter cannot occur.

Benjamin (1961a,b) examined the dynamics of a cantilevered system of articulated pipes (consisting of a finite number of rigid pipes connected by flexible joints) containing flowing fluid; the system is non–conservative. As the number of rigid pipes approaches infinity, he predicted analytically the existence of oscillatory instability (of the single–mode flutter type) of cantilevered pipes conveying fluid and the possibility of divergence if gravity is operative and if the fluid is sufficiently heavy. Only the former prediction was later confirmed by Gregory and Païdoussis' (1966a,b) theoretical and experimental work. Païdoussis (1970) subsequently found that vertical, continuously flexible pipes are never subject to divergence. Thus, the dynamics of articulated and continuously flexible pipes conveying fluid is not strictly analogous in the sense that articulated systems may exhibit radically different dynamical behaviour from the continuous systems they are supposed to represent—see Païdoussis and Deksnis (1970).

Païdoussis and Denise (1970,1971,1972) demonstrated for the first time, both theoretically and experimentally, that thin–walled pipes (or cylindrical shells) conveying incompressible fluid flow are subject to both shell– and beam–mode instabilities at sufficiently high flow velocities: shells with both ends clamped lose stability by divergence, while cantilevered ones do so by flutter. In those studies, the motions of the pipe were described by Flügge's thin–shell equations and the fluid forces were obtained by potential flow theory; reasonably good agreement was obtained between analytical results and experiments.

Similar predictions were also reported for the case of simply–supported shells by Weaver and Unny (1973) with the aid of the Flügge–Kempner shell equation and of the Fourier integral theory. The problem was later re–examined by Shayo and Ellen (1974), who derived asymptotic expressions for the generalized pressures, thus avoiding considerable numerical computation required in previous methods of solution, and showed the relationship between travelling wave and standing wave instabilities for shells of large length–to–radius ratios. The problem was further studied by Pham and Misra (1981) with special attention given to the effect of a superimposed linearly varying or constant axial loading on the shell.

Shayo and Ellen (1978) investigated the importance of the fluid behaviour beyond the free end of the shell on the dynamics of cantilevered shells conveying fluid, an aspect not considered in earlier analyses due to the utilization of different methods of solution (e.g. Païdoussis and Denise 1972), by introducing the so–called "downstream flow models" to describe fluid behaviour in that region, in conjunction with the Fourier–transform technique.

The research on axial flow inside cylindrical structures, having established the fundamental behaviour of the system, "ran out of steam", so to speak, by 1980 for lack of practical interest in the problem: unless the cylindrical shell were very flexible (e.g. made of elastomer), the flow velocities required to give rise to these instabilities were too high to be of practical concern. Nevertheless, interest was resuscitated by applications in the area of biomechanics, notably in the study of the collapse and flutter of pulmonary passages due to high aspiration rates (Grotberg and Davis 1980, Webster *et al.* 1985).

1.1.3 Axial Flow outside Cylindrical Structures

The dynamics and the stability behaviour of cylinders subjected to external axial flow are generally quite similar to those of pipes conveying fluid.

The early theoretical work on unconfined axial flow by Païdoussis (1966a) showed that cylinders first lose stability by divergence and then at higher flow velocities by coupled–mode flutter if the cylinders are supported at both ends, or by single–mode flutter if the cylinders are cantilevered. What is particularly interesting about this type of flow is that the post–divergence behaviour, whether it be coupled–mode flutter for cylinders with both ends supported or single–mode flutter for cantilevered cylinders, does materialize in experiments (Païdoussis 1966b). For cylinders supported at both ends, the oscillatory instabilities were shown to be caused by lateral frictional forces resulting from lateral motion of the cylinder.

Research on the stability of cylindrical shells exposed to external subsonic or supersonic axial flows were also undertaken in a number of studies, including that by Dowell (1966); these studies were mainly concerned with flutter of the shell(s) at very high compressible flows. One important study, on the same subject, that must be mentioned here is by Dowell and Widnall (1966), who applied the Laplace transform technique in the evaluation of the aerodynamic generalized forces on the shell. The use of a transform method to treat such a problem was considered to be a novelty; other researchers pursued this idea, but, as Dowell and Widnall (1966) recommended, they employed a more realistic transform method—the *Fourier* transform method—in their work, so as to avoid certain difficulties experienced with the *Laplace* transform method.

In subsequent investigations, Païdoussis (1973,1979) found that if the flow along the cylinder is confined either by a conduit or by adjacent structures (e.g. a cluster of uniform cylinders in a rigid channel), then there is an increase in the hydrodynamic virtual mass of the fluid, which effectively lowers the critical flow velocities associated with instabilities; nevertheless, the fundamental nature of the stability behaviour remains unchanged. With the Fourier transform technique and Galerkin's method, Païdoussis and Ostoja–Starzewski (1981) studied the effect of fluid compressibility on the stability of a system consisting of a pinned–pinned, flexible cylinder in a generally bounded, axial flow. It was shown that the effect of compressibility on the dynamics of the system is rather weak for slender cylinders, but becomes more significant for nonslender ones.

For the first time, Chen (1975) presented a general method to study the effect of fluid coupling on the dynamics of a group of parallel, closely spaced, flexible cylinders in a dense, axially flowing fluid. Because of this coupling, which reflects the fact that any motion of a cylinder will excite all other surrounding cylinders, the instabilities of the system occur at much lower flow velocities than for either a single flexible cylinder or a flexible cylinder surrounded by rigid ones. Predicted natural frequencies for various arrangements of cylinders were found to be in good agreement with experimental data (Chen and Jendrzejczyk 1978).

In a much more thorough theoretical investigation of the fluid coupling, Païdoussis and Suss (1977) dealt with a cluster of parallel, flexible cylinders in a cylindrical channel in the presence of axial fluid flow. Both inviscid and viscous hydrodynamic coupling in motions of the cylinders was treated; in addition, the confinement of the fluid was taken into account completely, which is due to the small spacing among cylinders, as well as between the channel wall and the adjacent cylinders. It was found that the theoretical model and experiment agree qualitatively in most essential features of the dynamical behaviour of the system, while quantitative agreement is remarkably good in terms of the first critical buckling velocities (Païdoussis 1979, Païdoussis, Curling and Gagnon 1982).

Hannoyer and Païdoussis (1978) examined the dynamics and stability of uniform tubular beams simultaneously subjected to internal and external flows under different end–support conditions. In the case of clamped–clamped beams, the effect of the two flows on stability was shown to be additive; if either flow is just below the corresponding critical value for instability, an increase in the other flow precipitates instability. This stability characteristic does not always hold true for cantilevered beams; if the system is just below the threshold of instability due to either flow, instability may be eliminated if the other flow is increased.

Further theoretical and experimental work by Hannoyer and Païdoussis (1979a,b) was focussed on the effect of either internal or external nonuniformity of cantilevered axisymmetric beams on their stability in the presence of internal and external flows. The effect of the boundary layer of the external flow was approximately taken into account in the theoretical model. Beams within a conical internal conduit were found to be much less stable than similar cylindrical ones subjected to the same flow discharge. In the case of external flow, the opposite effect was observed; fully conical cantilevered beams do not become unstable; for truncated conical cantilevers, instabilities are possible at substantially higher flow velocities if the tip of the free end is streamlined sufficiently.

1.1.4 Annular Flow in Coaxial Cylindrical Structures

Annular–flow–induced instabilities are sometimes referred to as leakage–flow–induced instabilities, which were found to occur often in such engineering components as fuel stringers in coolant channels (UK Advanced Gas Cooled Reactors) and certain types of pistons and valves, where the annular flow passage is quite narrow. An excellent review on leakage–flow–instabilities was given by Mulcahy (1983).

Early studies on the stability of flexible cylinders in axisymmetrically confined flow were carried out by Chen (1974), Païdoussis and Pettigrew (1979), and Païdoussis and Ostoja–Starzewski (1981). The mathematical models developed therein are in principle applicable to any degree of confinement and, although different from one to another due to the nature of the problems being solved, they all lead to the same conclusion: flow confinement destabilizes the system.

However, problems involving cylinders in highly confined axial flow were not given full attention until Hobson (1982) considered a rigid cylindrical body, hinged at one point and coaxially positioned in a flow–carrying duct, generally of nonuniform cross–sectional area. The mathematical model showed that the main ingredient for instability via a negative–damping mechanism is the enhanced coupling between fluid and structure caused by the narrowness of the annular gap; in other words, the extreme confinement of the narrow annular passage produces a substantial increase in the negative fluid damping, which easily overcomes the positive structural damping, leading to oscillatory instabilities. The model was also capable of explaining, in an approximate manner, the stability effect of an upstream constriction or of the gradual enlargement of the flow passage.

Mateescu and Païdoussis (1985) re–formulated the problem and presented a more rigorous, analytical inviscid model. It was shown that there exists a critical location of the hinge: if the hinge is situated upstream of that location, then the system remains stable at all flow velocities; on the other hand, oscillatory instability is possible if the hinge is moved farther downstream past that location. In addition, the critical location of the hinge is substantially influenced by axial variations of the annular gap. Some improvement to the model was later made to account for the unsteady viscous effects which were found to have a stabilizing influence on the system (Mateescu and Païdoussis 1987). The theory developed in these studies was eventually validated by experiments at a very fundamental level: the unsteady pressures for various positions of the hinge, frequencies of oscillation and flow velocities, were measured and then compared with the corresponding analytical ones. Good agreement was obtained, except near the body extremities (Mateescu, Païdoussis and Bélanger 1988). Recently, the theory has been further extended to deal with turbulent annular flow (Mateescu, Païdoussis and Bélanger 1991b).

A geometry of practical concern, where flow–induced problems are not unusual, is that of coaxial cylindrical shells, with still or flowing fluid in the annulus and sometimes in the inner shell also (Païdoussis 1980,1987). A few typical examples are shrouds, flow–directing baffles and thermal shields in gas– or water–cooled nuclear reactors, or thermal shields in aircraft jet engines. In general, the primary interests in research on this type of configurations have been (i) the dynamics of the system, which are greatly affected by the virtual mass of the annular fluid and the hydrodynamic coupling between the shells, if the fluid is stationary, and (ii) the stability of the system if the fluid is flowing.

The case of coaxial shells with annular (and sometimes internal) still fluid will be considered first. Chen and Rosenberg (1975) studied the dynamics of two concentrically located circular cylindrical shells containing and separated by quiescent fluids. The shells are simply–supported at both ends. With the use of Flügge's shell equations and potential–flow theory, a closed–form solution was obtained for the natural frequencies of the shell system containing incompressible fluid. It was found that the lowest frequency of the coupled system is associated with one of the out–of–phase modes, and is lower than the frequencies of the individual shells. Au–Yang (1976) considered a similar problem, consisting of two coaxial cylinders of different lengths immersed in a restricted inviscid fluid medium. The analytical model, well–verified by experiment, demonstrated that the cylinders have their coupled axial mode numbers directly proportional to their lengths; for the uncoupled modes, each cylinder vibrates as if the other were rigid.

As the finite–element method becomes more and more popular in solving dynamical problems involving structures with complicated physical boundary conditions, quite a few researchers have turned to this numerical method, often for a quick solution, when a mathematical model is neither available nor feasible. Brown and Lieb (1980) used FESAP (a finite–element package) to examine the dynamical behaviour of narrow–gap, fluid–coupled, coaxial flexible cylinders as variations are made to such parameters as cylinder wall thickness, gap width, and boundary conditions. Similarly, Chung *et al.* (1981) with NASTRAN and SAP4 evaluated the vibration characteristics of a fixed–free flexible cylindrical shell, concentrically positioned in a rigid cylinder, with the annulus filled with fluid. In these studies, numerical results for natural frequencies and mode shapes of the flexible cylinders were found to be generally in fair agreement with the measured experimental values. It should be noted that, in any finite–element analysis, the accuracy of the solution could easily be improved (e.g. by increasing the number of modelling elements), but the computing cost would normally render the analysis prohibitively expensive.

Yeh and Chen (1977) were the first to examine the effect of fluid viscosity on the dynamics of coaxial cylindrical shells separated by fluid. The analysis involved the use of Flügge's shell equations and Navier–Stokes equations for viscous fluid, with a travelling-wave–type solution taken for the shells and the fluid. The main finding of this study was that the effect of the fluid viscosity on the system natural frequencies is negligibly small in most practical systems. However, the modal damping ratio is noticeably increased for some cases when the fluid viscosity is included, especially for the lower frequencies. For a coupled shell system, the viscous effects are mostly pronounced for the out–of–phase modes, but are negligible for the in–phase modes. The effect of fluid viscosity on natural frequencies, as a function of annular gap and shell thickness, was also touched upon by Brown and Lieb (1980).

In all the above–mentioned studies of the dynamics of coaxial cylindrical shells, the fluid was taken to be *stationary*. Krajcinovic (1974) appears to be the first one to formulate the problem with the annular fluid being either still or *flowing*. The shells were treated as being infinitely long, and "piston theory" was employed to determine the unsteady local pressures on the surfaces of the shells. However, only results for the lowest natural frequencies of the system at zero flow velocity were given. A more general analysis came later when Weppelink (1979) investigated the free vibrations of a flexible cylindrical shell (clamped–clamped or cantilevered) in a concentric rigid cylinder, where incompressible fluid is flowing inside the inner shell and/or in the annulus. The fluid dynamic forces were calculated from potential flow theory, and the shell motions were described by the Morley–Koiter shell equations.

Païdoussis, Chan and Misra (1984) conducted the first comprehensive study on the stability of systems where the shells are coaxial and generally flexible while the fluid flowing inside the inner shell and/or in the annulus is inviscid and generally compressible. The fluid motions were governed by potential flow theory and the shell motions by Flügge's shell equations. It was found that, for the clamped–clamped shells considered, stability was lost by divergence at sufficiently high flows of either the internal or annular fluid, followed by coupled–mode flutter. The main effects of fluid viscosity were later taken into account by Païdoussis, Misra and Chan (1985), specifically those associated with the steady, time–independent viscous loads on the shell due to loss of pressure along the shell (i.e. axially variable pressurization and surface traction effects). These viscous effects were found to be very important on the stability of the system.

El Chebair, Misra and Païdoussis (1990) attempted to account for the unsteady, time–dependent viscous forces in an approximate way by adapting the work originally developed for quiescent fluids by Yeh and Chen (1977) to flowing fluids. This attempt was only partially successful, having run into difficulties when the no–slip boundary condition was rigorously applied at the shell surface in the method of solution. Although the Navier–Stokes equations were used for the calculation of the unsteady viscous forces exerted on the shells, they were in fact never solved. In any event, for shells with both ends supported, unsteady viscous forces were found to have only a slight influence on the dynamics of the system. At the same time, the first experimental study of annular–flow–induced instabilities of clamped–clamped coaxial shells was undertaken (El Chebair, Païdoussis and Misra 1989), which verified the dynamical behaviour of the system, qualitatively very well indeed, but quantitatively only within the usual margin of uncertainty associated with the effect of shell imperfections.

Finally, the earlier experimental study by Ziada, Bühlmann and Bolleter (1988) should be mentioned, involving slightly conical cantilevered shells subjected to both internal and annular flows. Their principal objective was to determine the excitation mechanism which had created difficulties in the heat–shielding shroud of a jet engine; these difficulties were shown to be flow–induced. It was found that, for shells of such geometry, the annular flow destabilized the system while the internal flow stabilized it; on the basis of that research, the design was modified and the problem solved. Clearly, had a theory been available for the dynamics of cantilevered coaxial conical shells subjected to internal and annular flows, then it could have been applied directly to solve such a problem. This illustration served as an added impetus for the present research work; its main aim, however, is much more fundamental: to study the stability of cantilevered coaxial cylindrical shells conveying incompressible viscous fluid.

1.2 Aims and Overview of the Thesis

The primary objective of this thesis is to develop and experimentally validate two different analytical models for predicting instabilities of cantilevered coaxial cylindrical shells subjected to flowing incompressible viscous fluid in the annular region between the two shells and/or within the inner shell.

Both analytical models take into consideration the main effects of fluid viscosity, namely, the steady (time–independent) viscous loads on the shells. These models differ in the way the unsteady fluid forces are calculated: in the first model, potential flow theory is used to formulate those forces, the solution of which is then obtained by means of the Fourier transform technique; in the second model, such forces are obtained by solving the Navier–Stokes equations with the finite–difference method.

This thesis consists of six self–contained chapters. Chapter 1 has given a brief review of previous studies closely related to the research work of the thesis. It has also stated the goals undertaken by the thesis, and now presents the outline of the thesis.

In Chapter 2, the development of the first analytical model for predicting instabilities of cantilevered coaxial cylindrical shells conveying internal and/or annular flows is given in detail. Presented are (a) the formulation of the problem with Flügge's modified shell equations and potential flow theory, (b) the solution of the fluid–dynamic forces acting on the shells by means of the Fourier–transform generalized–force approach, (c) the solution of the governing equations of motion with the *extended* Galerkin method, (d) the validation of the present analytical model by solving a number of test problems and comparing the results generated with previously obtained experimental and analytical ones, and (e) a new set of results on some typical steel–water systems considered earlier by Païdoussis *et al.* (1984,1985).

Chapter 3 is an extension of Chapter 2 as far as analytical results are concerned. This chapter begins with the theory developed in Chapter 2, but simplified for the case in which the outer shell is rigid while the inner one remains flexible. Both systems of clamped–clamped and cantilevered shells are considered. For the case of a clamped–clamped shell, the effects of (a) shell length, (b) shell–wall thickness, (c) annular width, and (d) counter–flows, on the stability of the system are investigated. The same system parameters, except (d), are also studied for the case of a cantilevered shell.

Chapter 4 is focussed on experimentation. Presented here are (a) a description of the apparatus, (b) the procedure of conducting experiments involving a cantilevered shell concentrically positioned in a rigid cylinder and subjected to either internal or annular flow, and (c) a comparison between the experimental results and the corresponding analytical ones obtained with the theory presented in Chapter 2.

In Chapter 5, the second analytical model is developed. An unsteady viscous theory is developed to evaluate the effect of unsteady viscous loads on the stability of cantilevered coaxial cylindrical shells conveying annular flow. Presented in detail are (a) the formulation of unsteady viscous forces from the Navier–Stokes equations, (b) the discretization of the Navier–Stokes equations and Flügge's shell equations, (c) the time integration of these two sets of equations by the finite–difference method with a fully implicit scheme, and (d) a comparison of results obtained with this new theory with those obtained with the theory in Chapter 2 and with experimental data presented in Chapter 4.

Finally, Chapter 6 wraps up the thesis with a summary of the important findings of the thesis, conclusions regarding the contributions of the thesis, and recommendations for future work.

Chapter 2

An Analytical Model: Detailed Development

2.1 Introduction

The main goal of this chapter is to develop an analytical model to study the stability of cantilevered coaxial cylindrical shells conveying internal and/or annular incompressible flowing fluid. In this model, the original system is replaced by a system with pre-stressed flexible shells subjected to inviscid flow. The key assumption here is that the forces pre-stressing the shells are the same as those resulting from flow pressurization and traction effects on the shell surfaces in the original system. The unsteady fluid forces will be formulated with potential-flow theory, thus not accounting for unsteady viscous effects. For narrow annuli, these effects may become important, and hence a full viscous theory (Chapter 5) should be used.

The following theory is presented for the general system in which both shells are flexible. Certain important aspects of the theory will be verified by solving a number of classical problems, and the results compared with previous experimental and analytical ones. For practical and economical reasons, the theory will then be used to study a simpler case with the outer shell replaced by a rigid cylinder whereas the inner one remains flexible. This simplified system, nevertheless, still retains all dynamical characteristics of the general one.

2.2 Formulation of the Analytical Model

2.2.1 System Definitions and Assumptions

Figure 2.1 shows the system under consideration. It consists of two coaxial cylindrical shells of length L. At the upstream end, $x = 0$, the shells are assumed to be connected (clamped) to semi–infinite rigid cylinders of the same radii and wall thicknesses as the two shells. At the downstream end, $x = L$, which is unsupported, the fluid is generally discharged freely into the surrounding medium, unless one of the two shells is rigid, in which case the same arrangement as for the upstream end may be considered to apply to that cylindrical conduit.

The inner and outer shells have mean radii a and b, and wall thicknesses h_i and h_o, respectively, such that h_i/a, $h_o/b \ll 1$. The shells are assumed to be elastic and isotropic with Young's moduli E_i and E_o, densities ρ_{si} and ρ_{so}, and Poisson's ratios ν_i and ν_o, in all cases subscripts i and o being associated with the inner and outer shells, respectively. Incompressible fluid is generally flowing both inside the inner shell and in the annulus, with densities ρ_i and ρ_o, and flow velocities U_i and U_o, respectively.

Shell motions are assumed to be sufficiently small, so that linear shell theory may be employed. As already mentioned, these perturbations will be formulated using potential–flow theory. Nevertheless, the flows are considered to be viscous, in the steady sense, and hence pressurization, necessary to overcome pressure drops, and traction effects on the shells are indeed taken into consideration. Finally, flow perturbations are assumed to vanish upstream and far downstream of the flexible shells.

2.2.2 Governing Equations of Motion

In its most general form, the present theory considers both cylinders involved to be flexible thin shells. Shell motions are described by Flügge's (1960) shell equations, as modified by Païdoussis, Misra and Chan (1985) to take into account the stress resultants due to steady viscous effects.

With inner–shell and outer–shell quantities characterized by subscripts i and o, respectively, the equations of motion for the two shells are given by

$$
\begin{aligned}
L_{1i}(u_i, v_i, w_i) \;=\;& u_i'' + \frac{1}{2}(1-\nu_i)u_i^{\bullet\bullet} + \frac{1}{2}(1+\nu_i)v_i'^{\bullet} + \nu_i w_i' + k_i\left\{\frac{1}{2}(1-\nu_i)u_i^{\bullet\bullet} - w_i'''\right. \\
&\left. + \frac{1}{2}(1-\nu_i)w_i'^{\bullet\bullet}\right\} + \left[q_{1i}u_i'' + q_{2i}(v_i^{\bullet} + w_i) + q_{3i}(u_i^{\bullet\bullet} - w_i')\right] - \gamma_i\left\{\frac{\partial^2 u_i}{\partial t^2}\right\} = 0, \qquad (2.1)
\end{aligned}
$$

$$
\begin{aligned}
L_{2i}(u_i, v_i, w_i) \;=\;& \frac{1}{2}(1+\nu_i)u_i'^{\bullet} + v_i^{\bullet\bullet} + \frac{1}{2}(1-\nu_i)v_i'' + w_i^{\bullet} + k_i\left\{\frac{3}{2}(1-\nu_i)v_i''\right. \\
&\left. - \frac{1}{2}(3-\nu_i)w_i''^{\bullet}\right\} + \left[q_{1i}v_i'' + q_{3i}(v_i^{\bullet\bullet} + w_i^{\bullet})\right] - \gamma_i\left\{\frac{\partial^2 v_i}{\partial t^2}\right\} = 0, \qquad (2.2)
\end{aligned}
$$

$$
\begin{aligned}
L_{3i}(u_i, v_i, w_i) \;=\;& \nu_i u_i' + v_i^{\bullet} + w_i + k_i\left\{\frac{1}{2}(1-\nu_i)u_i'^{\bullet\bullet} - u_i''' - \frac{1}{2}(3-\nu_i)v_i''^{\bullet} + \nabla_i^4 w_i\right. \\
&\left. + 2w_i^{\bullet\bullet} + w_i\right\} - \left[q_{1i}w_i'' + q_{3i}(u_i' - v_i^{\bullet} + w_i^{\bullet\bullet})\right] + \gamma_i\left\{\frac{\partial^2 w_i}{\partial t^2} - \frac{q_i}{\rho_{si}h_i}\right\} = 0, \qquad (2.3)
\end{aligned}
$$

$$
\begin{aligned}
L_{1o}(u_o, v_o, w_o) \;=\;& u_o'' + \frac{1}{2}(1-\nu_o)u_o^{\bullet\bullet} + \frac{1}{2}(1+\nu_o)v_o'^{\bullet} + \nu_o w_o' + k_o\left\{\frac{1}{2}(1-\nu_o)u_o^{\bullet\bullet} - w_o'''\right. \\
&\left. + \frac{1}{2}(1-\nu_o)w_o'^{\bullet\bullet}\right\} + \left[q_{1o}u_o'' + q_{2o}(v_o^{\bullet} + w_o) + q_{3o}(u_o^{\bullet\bullet} - w_o')\right] - \gamma_o\left\{\frac{\partial^2 u_o}{\partial t^2}\right\} = 0, \qquad (2.4)
\end{aligned}
$$

$$
\begin{aligned}
L_{2o}(u_o, v_o, w_o) \;=\;& \frac{1}{2}(1+\nu_o)u_o'^{\bullet} + v_o^{\bullet\bullet} + \frac{1}{2}(1-\nu_o)v_o'' + w_o^{\bullet} + k_o\left\{\frac{3}{2}(1-\nu_o)v_o''\right. \\
&\left. - \frac{1}{2}(3-\nu_o)w_o''^{\bullet}\right\} + \left[q_{1o}v_o'' + q_{3o}(v_o^{\bullet\bullet} + w_o^{\bullet})\right] - \gamma_o\left\{\frac{\partial^2 v_o}{\partial t^2}\right\} = 0, \qquad (2.5)
\end{aligned}
$$

$$
\begin{aligned}
L_{3o}(u_o, v_o, w_o) \;=\;& \nu_o u_o' + v_o^{\bullet} + w_o + k_o\left\{\frac{1}{2}(1-\nu_o)u_o'^{\bullet\bullet} - u_o''' - \frac{1}{2}(3-\nu_o)v_o''^{\bullet} + \nabla_o^4 w_o\right. \\
&\left. + 2w_o^{\bullet\bullet} + w_o\right\} - \left[q_{1o}w_o'' + q_{3o}(u_o' - v_o^{\bullet} + w_o^{\bullet\bullet})\right] + \gamma_o\left\{\frac{\partial^2 w_o}{\partial t^2} - \frac{q_o}{\rho_{so}h_o}\right\} = 0, \qquad (2.6)
\end{aligned}
$$

where

$$
(\;)^{\bullet} = \frac{\partial(\;)}{\partial\theta}, \quad (\;)' = a\frac{\partial(\;)}{\partial x}, \quad (\;)' = b\frac{\partial(\;)}{\partial x}, \quad k_i = \frac{1}{12}\left(\frac{h_i}{a}\right)^2, \quad k_o = \frac{1}{12}\left(\frac{h_o}{b}\right)^2,
$$

$$
\gamma_i = \frac{\rho_{si}a^2(1-\nu_i^2)}{E_i}, \quad \gamma_o = \frac{\rho_{so}b^2(1-\nu_o^2)}{E_o}, \quad \nabla_i^2 = a^2\frac{\partial^2}{\partial x^2} + \frac{\partial^2}{\partial\theta^2}, \quad \nabla_o^2 = b^2\frac{\partial^2}{\partial x^2} + \frac{\partial^2}{\partial\theta^2};
$$

$u(x,\theta,t)$, $v(x,\theta,t)$ and $w(x,\theta,t)$ are the axial, circumferential and radial displacements of the middle surface of the undeformed shell; q_1, q_2 and q_3 denote the nondimensional forces associated with steady viscous effects (Section 2.3.3); $q_i = (p_i - p_o)\big|_{r=a}$ and

$q_o = (p_o - p_e)\big|_{r=a}$, with p_i, p_o and p_e being the perturbation pressures in the inner fluid, the annular fluid and the fluid surrounding the outer shell, respectively. Thus, q_i and q_o represent the unsteady radial forces acting on the shells per unit area (Section 2.3.2.3).

Shell motions must satisfy the following boundary conditions (Flügge 1960): (i) at the clamped end, u, v, w and $\partial w/\partial x$ are all equal to zero; (ii) at the free end, the normal force N_x, the bending moment M_x, and Kirchhoff's effective shearing stress resultants $Q_x - (\partial M_{x\theta}/\partial\theta)/a$ and $N_{x\theta} - M_{x\theta}/a$ must all vanish. Thus, in terms of shell displacements, these boundary conditions are equivalent to

(i) at $x = 0$,

$$u_i = v_i = w_i = 0, \qquad \frac{\partial w_i}{\partial x} = 0; \tag{2.7}$$

$$u_o = v_o = w_o = 0, \qquad \frac{\partial w_o}{\partial x} = 0; \tag{2.8}$$

(ii) at $x = L$,

$$R_{1i}(u_i, v_i, w_i) = u_i' + \nu_i \dot{v}_i + \nu_i w_i - k_i w_i'' = 0, \tag{2.9}$$

$$R_{2i}(u_i, v_i, w_i) = \dot{u}_i + v_i' + 3k_i(v_i' - \dot{w}_i') = 0, \tag{2.10}$$

$$R_{3i}(u_i, v_i, w_i) = w_i'' + \nu_i \ddot{w}_i - \nu_i \dot{v}_i - u_i' = 0, \tag{2.11}$$

$$R_{4i}(u_i, v_i, w_i) = -w_i''' - (2-\nu_i)\ddot{w}_i' + \left(\frac{3-\nu_i}{2}\right)\ddot{v}_i' - \left(\frac{1-\nu_i}{2}\right)\ddot{u}_i + u_i'' = 0; \tag{2.12}$$

$$R_{1o}(u_o, v_o, w_o) = u_o' + \nu_o \dot{v}_o + \nu_o w_o - k_o w_o'' = 0, \tag{2.13}$$

$$R_{2o}(u_o, v_o, w_o) = \dot{u}_o + v_o' + 3k_o(v_o' - \dot{w}_o') = 0, \tag{2.14}$$

$$R_{3o}(u_o, v_o, w_o) = w_o'' + \nu_o \ddot{w}_o - \nu_o \dot{v}_o - u_o' = 0, \tag{2.15}$$

$$R_{4o}(u_o, v_o, w_o) = -w_o''' - (2-\nu_o)\ddot{w}_o' + \left(\frac{3-\nu_o}{2}\right)\dot{v}_o' - \left(\frac{1-\nu_o}{2}\right)\ddot{u}_o + u_o'' = 0. \tag{2.16}$$

2.2.3 Perturbation Pressures

As mentioned in the last section, the unsteady fluid forces (q_i and q_o) in the governing equations of motion are simply the differences between the perturbation pressures on the two sides of the shells. Thus, the determination of these forces reduces to that of the perturbation pressures. Since the analysis here applies equally to the internal and annular flows, the subscripts i and o will be suppressed until required for clarity.

The perturbation pressures will be formulated by means of potential flow theory[1]. Thus, for this purpose, the flow is considered to be inviscid and irrotational, and also isentropic. Hence, the velocity $\mathbf{V}$ may be expressed in terms of a velocity potential $\Psi(x,\theta,r,t)$, such that

$$\mathbf{V} = \nabla\Psi. \tag{2.17}$$

Moreover, Ψ is considered to consist of a steady component due to the mean, undisturbed flow velocity U in the x–direction and an unsteady component ϕ associated with perturbations due to shell motions; in other words,

$$\Psi = Ux + \phi. \tag{2.18}$$

Hence, from Equation (2.17), the velocity components of the perturbed flow field may be expressed as

$$V_x = U + \frac{\partial\phi}{\partial x}, \quad V_\theta = \frac{1}{r}\frac{\partial\phi}{\partial\theta}, \quad V_r = \frac{\partial\phi}{\partial r}. \tag{2.19}$$

With the substitution of Equation (2.18) into (2.17) and thence into the continuity equation for an incompressible flow, $\nabla\cdot\mathbf{V} = 0$, ϕ is found to be governed by the Laplace equation,

$$\frac{\partial^2\phi}{\partial r^2} + \frac{1}{r}\frac{\partial\phi}{\partial r} + \frac{1}{r^2}\frac{\partial^2\phi}{\partial\theta^2} + \frac{\partial^2\phi}{\partial x^2} = 0, \tag{2.20}$$

which is subject to the impermeability boundary conditions on the shell surface(s), ss, requiring that

$$V_r = \left.\frac{\partial\phi}{\partial r}\right|_{\mathrm{SS}} = \frac{\partial w}{\partial t} + U\frac{\partial w}{\partial x}. \tag{2.21}$$

Thus, for the annular flow, Equations (2.20) and (2.21) take the form

$$\frac{\partial^2\phi_o}{\partial r^2} + \frac{1}{r}\frac{\partial\phi_o}{\partial r} + \frac{1}{r^2}\frac{\partial^2\phi_o}{\partial\theta^2} + \frac{\partial^2\phi_o}{\partial x^2} = 0; \tag{2.22}$$

$$\left.\frac{\partial\phi_o}{\partial r}\right|_{r=a} = \begin{cases} \dfrac{\partial w_i}{\partial t} + U_o\dfrac{\partial w_i}{\partial x} & \text{for} \quad 0 \le x \le L, \\ 0 & \text{for} \quad x < 0 \text{ and } x \gg L; \end{cases} \tag{2.23}$$

$$\left.\frac{\partial\phi_o}{\partial r}\right|_{r=b} = \begin{cases} \dfrac{\partial w_o}{\partial t} + U_o\dfrac{\partial w_o}{\partial x} & \text{for} \quad 0 \le x \le L, \\ 0 & \text{for} \quad x < 0 \text{ and } x \gg L; \end{cases} \tag{2.24}$$

a similar set of equations also applies to the internal flow,

$$\frac{\partial^2\phi_i}{\partial r^2} + \frac{1}{r}\frac{\partial\phi_i}{\partial r} + \frac{1}{r^2}\frac{\partial^2\phi_i}{\partial\theta^2} + \frac{\partial^2\phi_i}{\partial x^2} = 0; \tag{2.25}$$

[1] This is clearly an approximation. Nevertheless, as mentioned in the foregoing, certain aspects of the viscous nature of the fluid flow *are* taken into account (Section 2.3.3).

$$\left.\frac{\partial \phi_i}{\partial r}\right|_{r=a} = \begin{cases} \frac{\partial w_i}{\partial t} + U_i \frac{\partial w_i}{\partial x} & \text{for} \quad 0 \le x \le L, \\ 0 & \text{for} \quad x < 0 \text{ and } x \gg L. \end{cases} \tag{2.26}$$

Here, a note should be given, concerning the boundary conditions (2.23), (2.24) and (2.26). Since ϕ_i and ϕ_o are both shell–motion induced and the shells are clamped–free, it is natural to assume that $\phi_i = \phi_o = 0$ for $x < 0$; i.e., flows entering the system are undisturbed. On the other hand, as the downstream end of the shells is free to move, it is *unrealistic* to assume that $\phi_i = \phi_o = 0$ for $x = L + \Delta L$, where $\Delta L \to 0$. However, ϕ_i and ϕ_o should vanish when ΔL is sufficiently large.

The perturbed pressure may then be determined from Bernoulli's equation for unsteady flow,

$$\frac{\partial \Psi}{\partial t} + \frac{1}{2}V^2 + \frac{P}{\rho} = \frac{P_s}{\rho}, \tag{2.27}$$

where $V^2 = V_x^2 + V_\theta^2 + V_r^2$, P_s is the stagnation pressure, and P is the pressure in the perturbed flow field. Expressing the pressure in terms of its mean, undisturbed value $\bar{P}$ and its perturbation counterpart p, such that $P = \bar{P} + p$, and substituting (2.18) and (2.19) into Equation (2.27) gives

$$\left\{\frac{1}{2}U^2 + \frac{\bar{P}}{\rho} - \frac{P_s}{\rho}\right\} + \left\{\frac{\partial \phi}{\partial t} + U\frac{\partial \phi}{\partial x} + \frac{p}{\rho}\right\} + \frac{1}{2}\left\{\left(\frac{\partial \phi}{\partial r}\right)^2 + \left(\frac{1}{r}\frac{\partial \phi}{\partial \theta}\right)^2 + \left(\frac{\partial \phi}{\partial x}\right)^2\right\} = 0. \tag{2.28}$$

In this equation, the first term is time–independent while the second one is time–dependent. Equation (2.28) therefore implies that its first two terms must individually vanish, yielding

$$\bar{P} = P_s - \frac{1}{2}\rho U^2, \tag{2.29}$$

$$p = -\rho\left\{\frac{\partial \phi}{\partial t} + U\frac{\partial \phi}{\partial x}\right\}, \tag{2.30}$$

for which it has been assumed that all second–order perturbations, grouped in the third term of Equation (2.28), are negligibly small—by considering motions of the shell to be small. It is seen that p is readily given by (2.30) once ϕ has been determined from Equations (2.22)–(2.24) for the annular flow, or from Equations (2.25)–(2.26) for the internal flow.

2.3 Method of Solution

2.3.1 Introduction

Section 2.2 has presented two different sets of equations, which are integral parts of the theory and must be solved sequentially.

The first set of equations, known as the Laplace equations, need to be solved in order to determine the unsteady fluid–dynamic forces exerted on the shells. The method of solution for these equations is the Fourier–Transform Generalized–Force technique (Section 2.3.2), also employed by Païdoussis *et al.* (1984,1985). Such forces, once calculated, are substituted into Flügge's modified shell equations, which are then solved with the extended form of Galerkin's method (Section 2.3.4). With regard to the second set of equations, all steady viscosity–related forces on the shells have been evaluated and given by Païdoussis, Misra and Chan (1985); since the same procedure will be followed herein, only the final results will be presented without details of the derivation (Section 2.3.3).

For the purposes of satisfying Equations (2.1)–(2.6), the solutions of the shell displacements are expressed in the following functional forms:

$$\left\{\begin{array}{c} u_i \\ v_i \\ w_i \end{array}\right\} = \sum_{n=1}^{\infty}\sum_{m=1}^{\infty}\left\{\begin{array}{c} A_m \cos n\theta \,(a\partial/\partial x) \\ B_m \sin n\theta \\ C_m \cos n\theta \end{array}\right\}\Phi_m(x)\, e^{i\Omega t}, \tag{2.31}$$

$$\left\{\begin{array}{c} u_o \\ v_o \\ w_o \end{array}\right\} = \sum_{n=1}^{\infty}\sum_{m=1}^{\infty}\left\{\begin{array}{c} D_m \cos n\theta \,(b\partial/\partial x) \\ E_m \sin n\theta \\ F_m \cos n\theta \end{array}\right\}\Phi_m(x)\, e^{i\Omega t}, \tag{2.32}$$

where m and n are the axial and circumferential wave numbers, respectively; $A_m, \ldots, F_m$ are constants to be determined; $\Phi_m(x)$ are appropriate admissible functions for the x–variations of shell displacements, here taken to be the eigenfunctions of a cantilevered beam (Bishop and Johnson 1960), and Ω is the angular frequency of oscillation. As expected, the $\Phi_m(x)$ do not satisfy the free–end boundary conditions (2.9)–(2.16); for this reason, the extended form of the Galerkin method is required to ensure that Equations

(2.1)–(2.16) are all satisfied equally. More discussion on this aspect will be given later (Section 2.3.4).

The solutions to the perturbation velocity potentials and pressures are taken to be of the form

$$\left\{ \begin{array}{c} \phi_i \\ p_i \end{array} \right\} = \sum_{n=1}^{\infty} \left\{ \begin{array}{c} \bar{\phi}_i(x,r) \\ \bar{p}_i(x,r) \end{array} \right\} \cos n\theta \, e^{i\Omega t}, \quad \left\{ \begin{array}{c} \phi_o \\ p_o \end{array} \right\} = \sum_{n=1}^{\infty} \left\{ \begin{array}{c} \bar{\phi}_o(x,r) \\ \bar{p}_o(x,r) \end{array} \right\} \cos n\theta \, e^{i\Omega t}. \tag{2.33}$$

The determination of $\bar{\phi}_i$, $\bar{\phi}_o$, $\bar{p}_i$ and $\bar{p}_o$ is the subject of the analysis of the next section.

2.3.2 Solution for the Perturbation Pressures

2.3.2.1 Annular Flow

Substituting ϕ_o from Equations (2.33) into (2.22) and taking the Fourier transform of the resulting equation gives

$$\sum_{n=1}^{\infty} \left\{ \frac{\partial^2 \bar{\phi}_o^*}{\partial r^2} + \frac{1}{r}\frac{\partial \bar{\phi}_o^*}{\partial r} - \left(\alpha^2 + \frac{n^2}{r^2} \right) \bar{\phi}_o^* \right\} \cos n\theta = 0, \tag{2.34}$$

where $\bar{\phi}_o^*$ denotes the Fourier transform of $\bar{\phi}_o$ defined by

$$\bar{\phi}_o^*(\alpha, r) = \int_{-\infty}^{\infty} \bar{\phi}_o(x,r)\, e^{i\alpha x}\, dx, \tag{2.35}$$

and $e^{i\Omega t} \neq 0$ (in fact, $|e^{i\Omega t}| = 1$) has been taken into consideration.

It is noted that the right–hand side of Equation (2.34) is zero whereas the left–hand side is an infinite series of $\cos n\theta$. Since $\cos n\theta \neq 0$ in general, the coefficient of $\cos n\theta$ for any given n must equal zero, or

$$\frac{\partial^2 \bar{\phi}_o^*}{\partial r^2} + \frac{1}{r}\frac{\partial \bar{\phi}_o^*}{\partial r} - \left(\alpha^2 + \frac{n^2}{r^2} \right) \bar{\phi}_o^* = 0. \tag{2.36}$$

Equation (2.36) is known as Bessel's modified equation, admitting solutions of the general form

$$\bar{\phi}_o^*(\alpha, r) = C_{1o} I_n(\alpha r) + C_{2o} K_n(\alpha r), \tag{2.37}$$

where $I_n(\alpha r)$ and $K_n(\alpha r)$ are the nth–order modified Bessel functions of the first and second kinds, respectively, and C_{1o} and C_{2o} are constants of integration to be determined from the boundary conditions at the shell surfaces, namely Equations (2.23) and (2.24).

The procedure to evaluate C_{1_o} and C_{2_o} is as follows. Equations (2.31)–(2.33) are appropriately substituted into Equations (2.23) and (2.24), then the Fourier transforms of the resultant equations are taken, and finally $\bar{\phi}_o^*$ is replaced by its functional form on the right–hand side of (2.37). Thus, the boundary conditions (2.23) and (2.24) are effectively equivalent to

$$\sum_{n=1}^{\infty}\left\{\left[\alpha I_n'(\alpha a)\right]C_{1_o}+\left[\alpha K_n'(\alpha a)\right]C_{2_o}\right\}\cos n\theta \;=\; \sum_{n=1}^{\infty}\left\{i\left(\Omega-U_o\alpha\right)\sum_{m=1}^{\infty}C_m\left[\Phi_m^*(\alpha)+R_m^*(\alpha)\right]\right\}\cos n\theta, \tag{2.38}$$

$$\sum_{n=1}^{\infty}\left\{\left[\alpha I_n'(\alpha b)\right]C_{1_o}+\left[\alpha K_n'(\alpha b)\right]C_{2_o}\right\}\cos n\theta \;=\; \sum_{n=1}^{\infty}\left\{i\left(\Omega-U_o\alpha\right)\sum_{m=1}^{\infty}F_m\left[\Phi_m^*(\alpha)+R_m^*(\alpha)\right]\right\}\cos n\theta. \tag{2.39}$$

Before C_{1_o} and C_{2_o} are obtained from Equations (2.38) and (2.39), it is important to discuss the reasons for introducing into these equations the new function $R_m^*(\alpha)$, which is the Fourier transform of $R_m(x)$.

As previously touched upon, the method of solution being employed is the Fourier transform method (see, for example, Bracewell 1974), implicit in which is the specification of $\bar{\phi}(x,r)$, $\partial\bar{\phi}/\partial x$, and $\bar{p}(x,r)$ at $\pm\infty$, whereas the variations of these quantities are dependent on x through the beam–eigenfunction expansions, which are specified only within the interval $[0,L]$. Furthermore, on physical grounds, although it may reasonably be argued that perturbations in flow and pressure are nearly zero for $x<0$ (and hence at $x=-\infty$), the same would be quite unreasonable if applied for $x>L$; perturbations should die out in a finite length beyond the free end of the shells and do so as smoothly as in reality. Hence, the need arises, both mathematically and physically, of specifying how $\bar{\phi}$ and $\bar{p}$ decay beyond $x=L$—since decay they must, on physical grounds, by dissipation and diffusion. The functional form of the decay of the perturbations is in fact given by $R_m(x)$, $L<x\leq L'$, which may be visualized as an "extension" of the beam eigenfunctions $\Phi_m(x)$, $0\leq x\leq L$. Thus, effectively, it is assumed that flow perturbations vanish for $x\geq L'$, where $L'>L$.

The functional form of $R_m(x)$ constitutes what has been referred to as an "out–

flow" model; such models were first proposed by Shayo and Ellen (1978) and later elaborated further by Païdoussis, Luu and Laithier (1986). The procedure of how the optimum L' is selected is discussed in Section 2.4.4.2 while the description of such models and the corresponding functional forms of $R_m(x)$ may be found in Appendix B.

Equating the coefficients of $\cos n\theta$ on the two sides of (2.38) and of (2.39) leads to

$$\left[\alpha I_n'(\alpha a)\right] C_{1o} + \left[\alpha K_n'(\alpha a)\right] C_{2o} = i\,(\Omega - U_o\alpha) \sum_{m=1}^{\infty} C_m \left[\Phi_m^*(\alpha) + R_m^*(\alpha)\right], \tag{2.40}$$

$$\left[\alpha I_n'(\alpha b)\right] C_{1o} + \left[\alpha K_n'(\alpha b)\right] C_{2o} = i\,(\Omega - U_o\alpha) \sum_{m=1}^{\infty} F_m \left[\Phi_m^*(\alpha) + R_m^*(\alpha)\right], \tag{2.41}$$

from which C_{1o} and C_{2o} are found to be

$$C_{1o} = \frac{i(\Omega - U_o\alpha)}{\alpha} \sum_{m=1}^{\infty} \left\{ \frac{-K_n'(\alpha b) C_m + K_n'(\alpha a) F_m}{I_n'(\alpha b) K_n'(\alpha a) - I_n'(\alpha a) K_n'(\alpha b)} \right\} \left[\Phi_m^*(\alpha) + R_m^*(\alpha)\right], \tag{2.42}$$

$$C_{2o} = \frac{i(\Omega - U_o\alpha)}{\alpha} \sum_{m=1}^{\infty} \left\{ \frac{I_n'(\alpha b) C_m - I_n'(\alpha a) F_m}{I_n'(\alpha b) K_n'(\alpha a) - I_n'(\alpha a) K_n'(\alpha b)} \right\} \left[\Phi_m^*(\alpha) + R_m^*(\alpha)\right]. \tag{2.43}$$

As a result of (2.42) and (2.43), Equation (2.37) may be rewritten as

$$\bar{\phi}_o^*(\alpha, r) = \frac{i(\Omega - U_o\alpha)}{\alpha} \sum_{m=1}^{\infty} \left\{ \left[W_{1n}(\alpha, r) C_m + W_{2n}(\alpha, r) F_m\right] \left[\Phi_m^*(\alpha) + R_m^*(\alpha)\right] \right\}, \tag{2.44}$$

where

$$W_{1n}(\alpha, r) = \frac{I_n'(\alpha b) K_n(\alpha r) - I_n(\alpha r) K_n'(\alpha b)}{I_n'(\alpha b) K_n'(\alpha a) - I_n'(\alpha a) K_n'(\alpha b)}, \tag{2.45}$$

$$W_{2n}(\alpha, r) = \frac{I_n(\alpha r) K_n'(\alpha a) - I_n'(\alpha a) K_n(\alpha r)}{I_n'(\alpha b) K_n'(\alpha a) - I_n'(\alpha a) K_n'(\alpha b)}; \tag{2.46}$$

in these expressions C_m and F_m have been defined in Equations (2.31) and (2.32), respectively; primes denote differentiation with respect to the argument of Bessel's modified functions. To obtain $\bar{p}_o^*$, Equations (2.33) are substituted into (2.30), and then the Fourier transform of the resultant equation is taken with $\phi_o^*(\alpha, r)$ replaced by its value in (2.44) and, finally, the coefficients of $\cos n\theta$ on the two sides of the equation are equated, giving

$$\bar{p}_o^*(\alpha, r) = \frac{\rho_o(\Omega - U_o\alpha)^2}{\alpha} \sum_{m=1}^{\infty} \left\{ \left[W_{1n}(\alpha, r) C_m + W_{2n}(\alpha, r) F_m\right] \left[\Phi_m^*(\alpha) + R_m^*(\alpha)\right] \right\}. \tag{2.47}$$

2.3.2.2 Internal Flow

With the same procedure as was carried out for the annular flow, $\bar{\phi}_i^*(\alpha, r)$ of the internal flow is also found to be governed by a modified Bessel equation, similar to Equation (2.36),

$$\frac{\partial^2 \bar{\phi}_i^*}{\partial r^2} + \frac{1}{r}\frac{\partial \bar{\phi}_i^*}{\partial r} - \left(\alpha^2 + \frac{n^2}{r^2}\right)\bar{\phi}_i^* = 0, \tag{2.48}$$

which admits solutions of the form

$$\bar{\phi}_i^*(\alpha, r) = C_{1i} I_n(\alpha r) + C_{2i} K_n(\alpha r). \tag{2.49}$$

Here, it should be recalled that $\lim_{x\to 0} K_n(x) = \infty$. Hence, for $\bar{\phi}_i^*$ to be finite as r approaches 0, C_{2i} must be set to zero ($C_{2i} = 0$). Meanwhile, C_{1i} is determined from the boundary condition (2.26). Substituting (2.31) and (2.33) into (2.26), taking the Fourier transform of the resulting equation and making use of (2.49), and finally equating the coefficients of $\cos n\theta$ on the two sides of the equation yields

$$\left[\alpha I_n'(\alpha a)\right] C_{1i} = i(\Omega - U_i\alpha)\sum_{m=1}^{\infty} C_m \left[\Phi_m^*(\alpha) + R_m^*(\alpha)\right], \tag{2.50}$$

or equivalently,

$$C_{1i} = \frac{i(\Omega - U_i\alpha)}{\alpha}\sum_{m=1}^{\infty}\frac{C_m}{I_n'(\alpha a)}\left[\Phi_m^*(\alpha) + R_m^*(\alpha)\right]. \tag{2.51}$$

With C_{1i} given by (2.51) and $C_{2i} = 0$, Equation (2.49) becomes

$$\bar{\phi}_i^*(\alpha, r) = \frac{i(\Omega - U_i\alpha)}{\alpha}\sum_{m=1}^{\infty}\frac{I_n(\alpha r)}{I_n'(\alpha a)} C_m \left[\Phi_m^*(\alpha) + R_m^*(\alpha)\right]; \tag{2.52}$$

thus, $\bar{p}_i^*(\alpha, r)$ can now be obtained from (2.30). Proceeding in the same manner as was done for $\bar{p}_o^*(\alpha, r)$ results in

$$\bar{p}_i^*(\alpha, r) = \frac{\rho_i(\Omega - U_i\alpha)^2}{\alpha}\sum_{m=1}^{\infty}\frac{I_n(\alpha r)}{I_n'(\alpha a)} C_m \left[\Phi_m^*(\alpha) + R_m^*(\alpha)\right]. \tag{2.53}$$

2.3.2.3 Nondimensionalization and Generalized Forces

As it is more convenient to deal with dimensionless quantities, Equations (2.1)–(2.6) will be nondimensionalized prior to being solved. For this purpose, the following reference velocities and forces per unit area are defined:

$$\mathcal{U}_i = \left[\frac{E_i}{\rho_{si}(1 - \nu_i^2)}\right]^{1/2}, \qquad \mathcal{U}_o = \left[\frac{E_o}{\rho_{so}(1 - \nu_o^2)}\right]^{1/2},$$

$$\bar{q}_i = \frac{\rho_{si} h_i L}{\gamma_i} = \frac{E_i h_i L}{a^2(1-\nu_i^2)}, \qquad \bar{q}_o = \frac{\rho_{so} h_o L}{\gamma_o} = \frac{E_o h_o L}{b^2(1-\nu_o^2)}, \tag{2.54}$$

from which the following dimensionless parameters are introduced:

$$\bar{U}_i = \frac{U_i}{\mathcal{U}_i}, \quad \bar{U}_o = \frac{U_o}{\mathcal{U}_o}, \quad \bar{\Omega}_i = \frac{\Omega a}{\mathcal{U}_i}, \quad \bar{\Omega}_o = \frac{\Omega b}{\mathcal{U}_o}, \quad \Omega_r = \frac{\bar{\Omega}_i}{\bar{\Omega}_o} = \frac{a\mathcal{U}_o}{b\mathcal{U}_i},$$

$$\varepsilon = \frac{r}{L}, \quad \varepsilon_i = \frac{a}{L}, \quad \varepsilon_o = \frac{b}{L}, \quad \bar{\alpha} = \alpha L, \quad \xi = \frac{x}{L}, \quad \ell = \frac{L'}{L}, \tag{2.55}$$

$$\bar{A}_m = \frac{A_m}{L}, \quad \bar{B}_m = \frac{B_m}{L}, \quad \bar{C}_m = \frac{C_m}{L}, \quad \bar{D}_m = \frac{D_m}{L}, \quad \bar{E}_m = \frac{E_m}{L}, \quad \bar{F}_m = \frac{F_m}{L}.$$

Thus, in terms of (2.54) and (2.55), the perturbation pressures evaluated in (2.47) and (2.53) may be written as

$$\bar{p}_i^*(\bar{\alpha},\varepsilon) = \frac{\rho_i \mathcal{U}_i^2}{\bar{\alpha}} \left\{ \frac{\bar{\Omega}_i}{\varepsilon_i} - \bar{U}_i \bar{\alpha} \right\}^2 \sum_{m=1}^{\infty} \frac{I_n(\bar{\alpha}\varepsilon)}{I_n'(\bar{\alpha}\varepsilon_i)} \bar{C}_m \left\{ \Phi_m^*(\bar{\alpha}) + R_m^*(\bar{\alpha}) \right\}, \tag{2.56}$$

$$\bar{p}_o^*(\bar{\alpha},\varepsilon) = \frac{\rho_o \mathcal{U}_o^2}{\bar{\alpha}} \left\{ \frac{\bar{\Omega}_i}{\varepsilon_o \Omega_r} - \bar{U}_o \bar{\alpha} \right\}^2 \sum_{m=1}^{\infty} \left\{ W_{1n}(\bar{\alpha},\varepsilon)\bar{C}_m + W_{2n}(\bar{\alpha},\varepsilon)\bar{F}_m \right\} \times \left\{ \Phi_m^*(\bar{\alpha}) + R_m^*(\bar{\alpha}) \right\}, \tag{2.57}$$

where

$$W_{1n}(\bar{\alpha},\varepsilon) = \frac{I_n'(\bar{\alpha}\varepsilon_o)K_n(\bar{\alpha}\varepsilon) - I_n(\bar{\alpha}\varepsilon)K_n'(\bar{\alpha}\varepsilon_o)}{I_n'(\bar{\alpha}\varepsilon_o)K_n'(\bar{\alpha}\varepsilon_i) - I_n'(\bar{\alpha}\varepsilon_i)K_n'(\bar{\alpha}\varepsilon_o)}, \tag{2.58}$$

$$W_{2n}(\bar{\alpha},\varepsilon) = \frac{I_n(\bar{\alpha}\varepsilon)K_n'(\bar{\alpha}\varepsilon_i) - I_n'(\bar{\alpha}\varepsilon_i)K_n(\bar{\alpha}\varepsilon)}{I_n'(\bar{\alpha}\varepsilon_o)K_n'(\bar{\alpha}\varepsilon_i) - I_n'(\bar{\alpha}\varepsilon_i)K_n'(\bar{\alpha}\varepsilon_o)}. \tag{2.59}$$

Finally, the terms q_i and q_o in Equations (2.3) and (2.6), respectively, are given by

$$q_i = (p_i - p_o)\Big|_{r=a}, \qquad q_o = (p_o - p_e)\Big|_{r=b} = p_o\Big|_{r=b}, \tag{2.60}$$

where the quiescent fluid surrounding the outer shell has been assumed to have a negligibly small inertial effect on the dynamics of the system (e.g., if the fluid is air), or $p_e = 0$; p_i and p_o are obtainable from (2.56) and (2.57), respectively, after inverse Fourier transformation and utilization of (2.33). The following analysis will be devoted to the evaluation of the generalized forces associated with perturbation pressures in the flows.

For the inner shell, if q_i is taken to have the form

$$q_i(\xi,\theta,t) = \sum_{n=1}^{\infty} \sum_{m=1}^{\infty} Q_{mn}(\xi) \cos n\theta \, e^{i\Omega t}, \tag{2.61}$$

then substituting (2.33) and (2.61) into the first of (2.60), taking its Fourier transform and utilizing (2.56) and (2.57), then taking the inverse transform and equating the coefficients of $\cos n\theta$ on the two sides of the resulting equation will give

$$\begin{aligned} Q_{mn}(\xi) &= \frac{\rho_i \mathcal{U}_i^2 \bar{C}_m}{2\pi} \int_{-\infty}^{\infty} \frac{1}{\bar{\alpha}} \left\{ \frac{\bar{\Omega}_i}{\varepsilon_i} - \bar{U}_i \bar{\alpha} \right\}^2 \left\{ \frac{I_n(\bar{\alpha}\varepsilon_i)}{I_n'(\bar{\alpha}\varepsilon_i)} \right\} \{\Phi_m^*(\bar{\alpha}) + R_m^*(\bar{\alpha})\} e^{-i\bar{\alpha}\xi} \,\mathrm{d}\bar{\alpha} \\ &- \frac{\rho_o \mathcal{U}_o^2}{2\pi} \int_{-\infty}^{\infty} \frac{1}{\bar{\alpha}} \left\{ \frac{\bar{\Omega}_i}{\varepsilon_o \Omega_r} - \bar{U}_o \bar{\alpha} \right\}^2 \left\{ W_{1n}(\bar{\alpha}, \varepsilon_i) \bar{C}_m + W_{2n}(\bar{\alpha}, \varepsilon_i) \bar{F}_m \right\} \\ &\qquad \times \{\Phi_m^*(\bar{\alpha}) + R_m^*(\bar{\alpha})\} e^{-i\bar{\alpha}\xi} \,\mathrm{d}\bar{\alpha}. \end{aligned} \tag{2.62}$$

In the process of solving the equations of motion by the extended Galerkin method (Section 2.3.4), all the terms are made to have the same common factor L. It is noted that the resulting term $\gamma_i q_i/(\rho_{si} h_i L)$ from Equation (2.3) is simply $q_i/\bar{q}_i$, with $\bar{q}_i$ having been defined in (2.54). Thus, for later convenience, $Q_{mn}(\xi)$ needs to be nondimensionalized with respect to $\bar{q}_i$. In the present method of solution, $Q_{mn}(\xi)$ is eventually multiplied by $\Phi_k(\xi)$ and integrated over the domain $[0,1]$ of ξ. Hence, the dimensionless generalized force may be written as

$$\bar{Q}_{kmn} = \frac{1}{\bar{q}_i} \int_0^1 \Phi_k(\xi)\, Q_{mn}(\xi) \,\mathrm{d}\xi. \tag{2.63}$$

The substitution of (2.62) into (2.63) leads to

$$\begin{aligned} \bar{Q}_{kmn} &= \frac{\rho_i \mathcal{U}_i^2 \bar{C}_m}{2\pi \bar{q}_i} \int_{-\infty}^{\infty} \frac{1}{\bar{\alpha}} \left\{ \frac{\bar{\Omega}_i}{\varepsilon_i} - \bar{U}_i \bar{\alpha} \right\}^2 \left\{ \frac{I_n(\bar{\alpha}\varepsilon_i)}{I_n'(\bar{\alpha}\varepsilon_i)} \right\} \{H_{km}(\bar{\alpha}) + N_{km}(\bar{\alpha})\} \,\mathrm{d}\bar{\alpha} \\ &- \frac{\rho_o \mathcal{U}_o^2}{2\pi \bar{q}_i} \int_{-\infty}^{\infty} \frac{1}{\bar{\alpha}} \left\{ \frac{\bar{\Omega}_i}{\varepsilon_o \Omega_r} - \bar{U}_o \bar{\alpha} \right\}^2 \left\{ W_{1n}(\bar{\alpha}, \varepsilon_i) \bar{C}_m + W_{2n}(\bar{\alpha}, \varepsilon_i) \bar{F}_m \right\} \\ &\qquad \times \{H_{km}(\bar{\alpha}) + N_{km}(\bar{\alpha})\} \,\mathrm{d}\bar{\alpha}, \end{aligned} \tag{2.64}$$

where $H_{km}(\bar{\alpha})$ and $N_{km}(\bar{\alpha})$ are defined as

$$H_{km}(\bar{\alpha}) = \left\{ \int_0^1 \Phi_k(\xi)\, e^{-i\bar{\alpha}\xi} \,\mathrm{d}\xi \right\} \left\{ \int_0^1 \Phi_m(\xi)\, e^{i\bar{\alpha}\xi} \,\mathrm{d}\xi \right\}, \tag{2.65}$$

$$N_{km}(\bar{\alpha}) = \left\{ \int_0^1 \Phi_k(\xi)\, e^{-i\bar{\alpha}\xi} \,\mathrm{d}\xi \right\} \left\{ \int_1^\ell R_m(\xi)\, e^{i\bar{\alpha}\xi} \,\mathrm{d}\xi \right\}, \tag{2.66}$$

both of which can be determined analytically. The evaluation of $H_{km}(\bar{\alpha})$ and $N_{km}(\bar{\alpha})$ is presented in Appendices A and B, respectively. $\bar{Q}_{kmn}$ may also be expressed explicitly as a quadratic function of $\bar{\Omega}_i$,

$$\bar{Q}_{kmn} = \left\{ q_{kmn}^{(1)} \bar{C}_m + r_{kmn}^{(1)} \bar{F}_m \right\} \bar{\Omega}_i^2 + 2 \left\{ q_{kmn}^{(2)} \bar{C}_m + r_{kmn}^{(2)} \bar{F}_m \right\} \bar{\Omega}_i + \left\{ q_{kmn}^{(3)} \bar{C}_m + r_{kmn}^{(3)} \bar{F}_m \right\}, \tag{2.67}$$

where

$$q_{kmn}^{(j)} = (-1)^{j+1}\frac{\rho_i \mathcal{U}_i^2}{2\pi\bar{q}_i}\left\{\frac{\bar{U}_i^{j-1}}{\varepsilon_i^{3-j}}\right\}\int_{-\infty}^{\infty}\bar{\alpha}^{j-2}\left\{\frac{I_n(\bar{\alpha}\varepsilon_i)}{I_n'(\bar{\alpha}\varepsilon_i)}\right\}\{H_{km}(\bar{\alpha})+N_{km}(\bar{\alpha})\}\,\mathrm{d}\bar{\alpha}$$
$$+\ (-1)^{j}\frac{\rho_o \mathcal{U}_o^2}{2\pi\bar{q}_i}\left\{\frac{\bar{U}_o^{j-1}}{(\varepsilon_o\Omega_r)^{3-j}}\right\}\int_{-\infty}^{\infty}\bar{\alpha}^{j-2}W_{1n}(\bar{\alpha}\varepsilon_i)\{H_{km}(\bar{\alpha})+N_{km}(\bar{\alpha})\}\,\mathrm{d}\bar{\alpha},$$

$$r_{kmn}^{(j)} = (-1)^{j}\frac{\rho_o \mathcal{U}_o^2}{2\pi\bar{q}_i}\left\{\frac{\bar{U}_o^{j-1}}{(\varepsilon_o\Omega_r)^{3-j}}\right\}\int_{-\infty}^{\infty}\bar{\alpha}^{j-2}W_{2n}(\bar{\alpha}\varepsilon_i)\{H_{km}(\bar{\alpha})+N_{km}(\bar{\alpha})\}\,\mathrm{d}\bar{\alpha},$$

with the value of j being 1, 2 or 3.

Similarly, for the outer shell, q_o may be written as

$$q_o(\xi,\theta,t) = \sum_{n=1}^{\infty}\sum_{m=1}^{\infty} S_{mn}(\xi)\cos n\theta\, e^{i\Omega t}; \tag{2.68}$$

using the same procedure as was carried out for the generalized force on the inner shell results in

$$\bar{S}_{kmn} = \left\{s_{kmn}^{(1)}\bar{C}_m + t_{kmn}^{(1)}\bar{F}_m\right\}\bar{\Omega}_i^2 + 2\left\{s_{kmn}^{(2)}\bar{C}_m + t_{kmn}^{(2)}\bar{F}_m\right\}\bar{\Omega}_i + \left\{s_{kmn}^{(3)}\bar{C}_m + t_{kmn}^{(3)}\bar{F}_m\right\}, \tag{2.69}$$

where

$$s_{kmn}^{(j)} = (-1)^{j+1}\frac{\rho_o \mathcal{U}_o^2}{2\pi\bar{q}_o}\left\{\frac{\bar{U}_o^{j-1}}{(\varepsilon_o\Omega_r)^{3-j}}\right\}\int_{-\infty}^{\infty}\bar{\alpha}^{j-2}W_{1n}(\bar{\alpha}\varepsilon_o)\{H_{km}(\bar{\alpha})+N_{km}(\bar{\alpha})\}\,\mathrm{d}\bar{\alpha},$$

$$t_{kmn}^{(j)} = (-1)^{j+1}\frac{\rho_o \mathcal{U}_o^2}{2\pi\bar{q}_o}\left\{\frac{\bar{U}_o^{j-1}}{(\varepsilon_o\Omega_r)^{3-j}}\right\}\int_{-\infty}^{\infty}\bar{\alpha}^{j-2}W_{2n}(\bar{\alpha}\varepsilon_o)\{H_{km}(\bar{\alpha})+N_{km}(\bar{\alpha})\}\,\mathrm{d}\bar{\alpha}.$$

To recap, what has been done in the foregoing analysis is the derivation of the unsteady fluid–dynamic forces exerted on two coaxial cylindrical flexible shells due to the internal and annular flows. For the system with a flexible shell concentrically inside a rigid cylinder, the force on the outer cylinder [Equation (2.69)] is of no practical interest while the one on the inner shell, Equation (2.67), reduces to

$$\bar{Q}_{kmn} = \left\{q_{kmn}^{(1)}\bar{C}_m\right\}\bar{\Omega}_i^2 + \left\{2q_{kmn}^{(2)}\bar{C}_m\right\}\bar{\Omega}_i + \left\{q_{kmn}^{(3)}\bar{C}_m\right\}, \tag{2.70}$$

where the $q_{kmn}^{(j)}$ are the same as those defined for Equation (2.67).

For the reason to be discussed next, attention is now focussed on $W_{1n}(\bar{\alpha},\varepsilon_i)$, which appeared in the second integrand of $q_{kmn}^{(j)}$ and can be obtained directly from (2.58),

$$W_{1n}(\bar{\alpha},\varepsilon_i) = \frac{I_n'(\bar{\alpha}\varepsilon_o)K_n(\bar{\alpha}\varepsilon_i) - I_n(\bar{\alpha}\varepsilon_i)K_n'(\bar{\alpha}\varepsilon_o)}{I_n'(\bar{\alpha}\varepsilon_o)K_n'(\bar{\alpha}\varepsilon_i) - I_n'(\bar{\alpha}\varepsilon_i)K_n'(\bar{\alpha}\varepsilon_o)}. \tag{2.71}$$

It is seen that as the radius of the outer cylinder becomes very large, $\varepsilon_o \to \infty$, the inner shell becomes simultaneously subjected to internal and *external* axial flows, a configuration similar to that analyzed by Hannoyer and Païdoussis (1978) with beam theory. The present theory is sufficiently general to handle such a problem; all that needs to be done here is to evaluate $\lim_{\varepsilon_o \to \infty} W_{1n}(\bar{\alpha}, \varepsilon_i)$, because $W_{1n}(\bar{\alpha}, \varepsilon_i)$, given by (2.71), has the form ∞/∞ as ε_o approaches ∞. From the limiting values of the modified Bessel functions,

$$\lim_{x \to \infty} I_n(x) = \infty, \qquad \lim_{x \to \infty} K_n(x) = 0,$$

and from their recurrence relationships,

$$\begin{aligned} I_n'(x) &= \frac{n}{x} I_n(x) + I_{n+1}(x), \\ K_n'(x) &= \frac{n}{x} K_n(x) - K_{n+1}(x), \end{aligned}$$

it may be seen that

$$\lim_{x \to \infty} I_n'(x) = \infty, \qquad \lim_{x \to \infty} K_n'(x) = 0. \tag{2.72}$$

As a result of (2.72), the limiting value of (2.71) is found to be

$$\lim_{\varepsilon_o \to \infty} W_{1n}(\bar{\alpha}, \varepsilon_i) = \lim_{\varepsilon_o \to \infty} \frac{I_n'(\bar{\alpha}\varepsilon_o) K_n(\bar{\alpha}\varepsilon_i)}{I_n'(\bar{\alpha}\varepsilon_o) K_n'(\bar{\alpha}\varepsilon_i)} = \frac{K_n(\bar{\alpha}\varepsilon_i)}{K_n'(\bar{\alpha}\varepsilon_i)}. \tag{2.73}$$

With Equation (2.73), the present theory becomes particularly useful in solving problems involving cantilevered cylindrical shells (thin-walled cylinder) containing inner flowing fluid and surrounded by stationary or axially moving, externally unconfined fluid (Section 2.4).

2.3.3 Steady Viscosity–Related Stress Resultants

As explained earlier, the viscous nature of the fluid results in both steady and unsteady viscosity–related loads being exerted on the shells, the latter of which will be the subject of investigation of Chapter 5. The steady loads have already been derived (Païdoussis, Misra and Chan 1985) from the time–mean Navier–Stokes equations for the case of clamped–clamped shells. The same procedure will be followed herein to calculate such loads acting on the clamped–free shells. Since details of the derivation have been given by Païdoussis *et al.* (1985), they will not be repeated here; however, the final results with all the assumptions involved will be presented.

The steady loads are evaluated under the assumption of a fully-developed turbulent, incompressible flow. The fluid pressure and the surface frictional force inside a circular cylinder and in the annulus between two coaxial cylinders are derived by further assuming that the cylinders are rigid.

Figure 2.1 is referred to once more in this section. The flow velocity components in the cylindrical coordinates x, θ and r are $V_x + V_x'$, V_θ' and V_r', respectively; V_x is the mean velocity in the axial direction while V_x', V_θ' and V_r' are the fluctuating velocity components of the turbulent flow. (Here, $V_\theta = V_r = 0$.) For a flow velocity V_x and static pressure P, the time-mean Navier-Stokes equations may be written as (Laufer 1953):

$$\frac{1}{\rho}\frac{\partial P}{\partial x} = -\frac{1}{r}\frac{\mathrm{d}}{\mathrm{d}r}\left\{r\overline{V_x'V_r'}\right\} + \frac{\nu}{r}\frac{\mathrm{d}}{\mathrm{d}r}\left\{r\frac{\mathrm{d}V_x}{\mathrm{d}r}\right\}, \tag{2.74}$$

$$\frac{1}{\rho}\frac{\partial P}{\partial r} = -\frac{1}{r}\frac{\mathrm{d}}{\mathrm{d}r}\left\{r\overline{(V_r')^2}\right\} + \frac{\overline{(V_\theta')^2}}{r}, \tag{2.75}$$

$$0 = \frac{\mathrm{d}}{\mathrm{d}r}\left\{\overline{V_r'V_\theta'}\right\} + 2\frac{\overline{V_r'V_\theta'}}{r}, \tag{2.76}$$

where $\overline{(\;)}$ denotes the time mean of ( ); ρ and ν are the density and the kinematic viscosity of the fluid, respectively; these equations apply to both internal and annular flows.

After lengthy mathematical manipulations, the solutions of the above equations for the internal and annular fluid regions are obtained. The results of interest are given below.

- For the internal flow,

$$P_i(x,r) = -2\left(\frac{\rho_i}{a}\right)U_{\tau i}^2 x - \rho_i\overline{(V_{ri}')^2} + \rho_i\int_a^r \frac{\overline{(V_{\theta i}')^2} - \overline{(V_{ri}')^2}}{r}\,\mathrm{d}r + P_i(0,a), \tag{2.77}$$

with $U_{\tau i}$, the so-called stress velocity, being given by

$$U_{\tau i} = \left\{-\nu_i\frac{\mathrm{d}V_{xi}}{\mathrm{d}r}\bigg|_{r=a}\right\}^{1/2} = \left\{\frac{\tau_{wi}}{\rho_i}\right\}^{1/2} = \left\{\frac{1}{8}f_i U_i^2\right\}^{1/2}, \tag{2.78}$$

where U_i is the mean axial velocity of the internal fluid, τ_{wi} is the fluid frictional force per unit area on the interior surface of the inner shell, $P_i(x,r)$ is the time-averaged pressure of the internal fluid, and $P_i(0,a)$ is the internal-fluid pressure at the position $x = 0$, $r = a$.

- For the annular flow,

$$P_o(x,r) = -\left\{\frac{2b}{b^2 - r_m^2}\right\}\rho_o U_{\tau oo}^2 x - \rho_o\overline{(V_{ro}')^2} + \rho_o\int_a^r \frac{\overline{(V_{\theta o}')^2} - \overline{(V_{ro}')^2}}{r}\,\mathrm{d}r + P_o(0,a), \quad (2.79)$$

with $U_{\tau oi}$ and $U_{\tau oo}$ being the stress velocities on the outer surface of the inner shell and the inner surface of the outer shell, respectively,

$$U_{\tau oi} = \left\{-\nu_o\frac{\mathrm{d}V_{xo}}{\mathrm{d}r}\bigg|_{r=a}\right\}^{1/2} = \left\{\frac{\tau_{woi}}{\rho_o}\right\}^{1/2} = \left\{\frac{1}{8}\frac{r_m^2 - a^2}{a(b-a)}f_{oi}U_o^2\right\}^{1/2}, \quad (2.80)$$

$$U_{\tau oo} = \left\{-\nu_o\frac{\mathrm{d}V_{xo}}{\mathrm{d}r}\bigg|_{r=b}\right\}^{1/2} = \left\{\frac{\tau_{woo}}{\rho_o}\right\}^{1/2} = \left\{\frac{1}{8}\frac{b^2 - r_m^2}{b(b-a)}f_{oo}U_o^2\right\}^{1/2}; \quad (2.81)$$

here U_o is the mean axial velocity of the annular fluid, τ_{woi} and τ_{woo} are the fluid frictional forces per unit area on the exterior surface of the inner shell and on the interior surface of the outer shell, respectively, $P_o(x,r)$ is the annular time-averaged pressure, $P_o(0,a)$ is the annular–fluid pressure at the position $x = 0$ and $r = a$, and r_m is the radius at which the mean velocity V_{xo} is maximum.

In Equations (2.79)–(2.81), r_m cannot be evaluated analytically; it is herein determined from a multi–linear representation of Brighton and Jones' (1964) experimental measurements. Nevertheless, these measurements showed that if $a/b \geq 0.8$ then r_m can be approximated by its counterpart in the case of laminar flow; in other words,

$$r_m = \left\{\frac{b^2 - a^2}{2\ln(b/a)}\right\}^{1/2}. \quad (2.82)$$

The friction factor f, appearing in Equations (2.78), (2.80) and (2.81), is a function of the Reynolds number Re, and of the relative roughness of the cylinder k/d, where k is the average height of surface protrusions and d is the diameter of the cylinder. The friction factor may be found graphically from a Moody diagram, which is a plot of f versus Re for different values of k/d. Alternatively, it may be determined from a number of empirical formulas. A common practice is to use the Colebrook equation (Murdock 1976),

$$\frac{1}{\sqrt{f}} = -2\log_{10}\left\{\frac{k/d}{3.7} + \frac{2.51}{\mathrm{Re}\sqrt{f}}\right\}. \quad (2.83)$$

To avoid solving the above implicit Colebrook equation, Moody himself derived the following approximation, which matches Equation (2.83) within ±5% for $k/d \leq 0.015$

and $\mathrm{Re} \le 10^7$:

$$f_a = 0.0055\left\{1+\left[20000\left(\frac{k}{d}\right)+\frac{10^6}{\mathrm{Re}}\right]^{1/3}\right\}. \tag{2.84}$$

The accuracy of f_a can be significantly improved if f_a is substituted back into Equation (2.83), namely

$$\frac{1}{\sqrt{f}} = -2\log_{10}\left\{\frac{k/d}{3.7}+\frac{2.51}{\mathrm{Re}\sqrt{f_a}}\right\}; \tag{2.85}$$

the value of f so obtained is then within $\pm 0.7\%$ for $k/d \le 0.05$ and $\mathrm{Re} \le 10^8$ from that of Equation (2.83).

Equations (2.84) and (2.85) are valid for both internal and annular flows. For internal flow, d_i is the diameter of the inner cylinder, $2a$, and $\mathrm{Re}_i = U_i d_i/\nu_i = 2aU_i/\nu_i$. For annular flow, d_o is equal to the equivalent hydraulic diameter $d_h = 2(b-a)$, and $\mathrm{Re}_o = U_o d_o/\nu_o = 2(b-a)U_o/\nu_o$.

With the fluid pressures determined, the basic loads on the shells can now be evaluated. The steady radial differential pressure on the inner shell is given by $\bar{P}_{rIi} = P_i(x,a) - P_o(x,a)$ which, in terms of (2.77) and (2.79), may be written as

$$\bar{P}_{rIi} = \left\{\frac{2b}{b^2-r_m^2}\rho_o U_{\tau oo}^2 - \frac{2\rho_i}{a}U_{\tau i}^2\right\}x + P_i(0,a) - P_o(0,a), \tag{2.86}$$

where I stands for *initial* or steady–state, and use has been made of the condition that at the surfaces of the inner shell,

$$\left.\overline{(V_{ri}')^2}\right|_{r=a} = \left.\overline{(V_{ro}')^2}\right|_{r=a} = 0.$$

$P_i(0,a)$ and $P_o(0,a)$ may be determined from Equations (2.77) and (2.79), respectively, if the static pressures of the two flows at either end of the shell are known. Since the shell is cantilevered, the exit pressures of the two flows are essentially the same; as a result,

$$\Delta P_i \;=\; P_i(0,a) - P_o(0,a) \;=\; \frac{2\rho_i}{a}U_{\tau i}^2 L - \frac{2b}{b^2-r_m^2}\rho_o U_{\tau oo}^2 L. \tag{2.87}$$

The corresponding surface traction in the axial direction on the inner shell is $\bar{P}_{xIi} = \tau_{wi} + \tau_{woi}$, or in terms of the corresponding stress velocities defined in Equations (2.78) and (2.80),

$$\bar{P}_{xIi} = \rho_i U_{\tau i}^2 + \rho_o U_{\tau oi}^2. \tag{2.88}$$

Similarly, with the presumption that the outer shell is surrounded by quiescent fluid at pressure P_e, the steady radial differential pressure on the outer shell is found from $\bar{P}_{rIo} = P_o(x,b) - P_e$, or

$$\bar{P}_{rIo} = -\left\{\frac{2b}{b^2 - r_m^2}\rho_o U_{\tau oo}^2\right\} x + \rho_o \int_a^b \frac{\overline{(V'_{\theta o})^2} - \overline{(V'_{ro})^2}}{r}\,\mathrm{d}r + P_o(0,a) - P_e, \tag{2.89}$$

where the fact that $\overline{(V'_{ro})^2}|_{r=b} = 0$ has been utilized, and

$$\Delta P_o \;=\; P_o(0,a) - P_e \;=\; \frac{2b}{b^2 - r_m^2}\rho_o U_{\tau oo}^2 L. \tag{2.90}$$

The quantities in the integral correspond to the mean-squared tangential and radial flow velocities in the annular flow; the value of this integral is quoted from Païdoussis *et al.* (1985),

$$S \;=\; \int_a^b \frac{\overline{(V'_{\theta o})^2} - \overline{(V'_{ro})^2}}{r}\,\mathrm{d}r \;=\; \left\{0.7864 - \frac{0.56\,r_m}{b - r_m} + \left[\frac{0.56\,r_m^2}{(b - r_m)^2} - \frac{0.5064\,r_m}{b - r_m}\right]\ln\left(\frac{b}{r_m}\right)\right\} U_{\tau oo}^2$$
$$- \left\{0.7864 + \frac{0.56\,r_m}{r_m - a} - \left[\frac{0.56\,r_m^2}{(r_m - a)^2} + \frac{0.5064\,r_m}{r_m - a}\right]\ln\left(\frac{r_m}{a}\right)\right\} U_{\tau oi}^2, \tag{2.91}$$

and has been found to be numerically rather insignificant, as compared to the other terms on the right-hand side of Equation (2.89). Finally, the corresponding traction load on the outer shell is given by

$$\bar{P}_{xIo} \;=\; \tau_{woo} \;=\; \rho_o U_{\tau oo}^2. \tag{2.92}$$

It is noted that, for both internal and annular flows, Equations (2.88) and (2.92) as well as (2.86) and (2.89) may be expressed in the functional forms

$$\bar{P}_{xI} = B, \qquad \bar{P}_{rI} = -(Cx + D), \tag{2.93}$$

where

$$\begin{aligned} B_i &= \rho_i U_{\tau i}^2 + \rho_o U_{\tau oi}^2, & B_o &= \rho_o U_{\tau oo}^2 \\ C_i &= \frac{2\rho_i}{a} U_{\tau i}^2 - \frac{2b}{b^2 - r_m^2}\rho_o U_{\tau oo}^2 & C_o &= \frac{2b}{b^2 - r_m^2}\rho_o U_{\tau oo}^2 \\ D_i &= -\Delta P_i & D_o &= -(\rho_o S + \Delta P_o) \end{aligned} \tag{2.94}$$

with ΔP_i, ΔP_o and S being defined in (2.87), (2.90) and (2.91), respectively.

Now that the pressures and shear stresses acting on the shells have been fully determined, they will be transformed into the terms q_{1i} to q_{3i} in Equations (2.1)–(2.3) and q_{1o} to q_{3o} in Equations (2.4)–(2.6). By balancing forces on an infinitesimal shell element in the $x-$, $\theta-$ and $r-$direction, the stress resultants may be determined and are found to be

$$N_{\theta I} = \bar{P}_{rI}\bar{r}, \qquad \frac{\partial N_{x\theta I}}{\partial x} = -\frac{1}{\bar{r}}\frac{\partial N_{\theta I}}{\partial \theta}, \qquad \frac{\partial N_{xI}}{\partial x} = -\bar{P}_{xI} - \frac{1}{\bar{r}}\frac{\partial N_{x\theta I}}{\partial \theta}, \tag{2.95}$$

where $N_{\theta I}$ and N_{xI} are the hoop and axial stress resultants, respectively, while $N_{x\theta I}$ is the shear stress resultant; $\bar{r}$ is equal to a for the inner shell and b for the outer one. In (2.95), the first equation shows that $N_{\theta I}$ is independent of θ, or $\partial N_{\theta I}/\partial\theta = 0$; hence, the second equation becomes $N_{x\theta I} = f_1(\theta)$, and the third simplifies to $\partial N_{xI}/\partial x = -\bar{P}_{xI} - \frac{1}{\bar{r}}f_1'(\theta)$ or $N_{xI} = -Bx + f_2(\theta)$. However, since the shells are axisymmetric, $N_{x\theta I}$ and N_{xI} must be functionally independent of θ; in other words,

$$N_{x\theta I} = C_1, \qquad N_{xI} = -Bx + C_2, \tag{2.96}$$

where C_1 and C_2 may be determined from the end boundary conditions. At $x = 0$, $N_{x\theta I} = 0$ or $C_1 = 0$; at $x = L$, $N_{xI} = 0$ or $C_2 = BL$. Thus, with the substitution of these values into (2.96) and $\bar{P}_{rI}$ from (2.93) into (2.95), the following relationships are obtained:

$$N_{xI} = -B(x - L), \quad N_{\theta I} = -\bar{r}(Cx + D), \quad N_{x\theta I} = 0. \tag{2.97}$$

Finally, the terms q_1 to q_3 may be calculated from the following relationships (Païdoussis, Misra and Chan 1985):

$$q_1 = \left\{\frac{1-\nu^2}{Eh}\right\} N_{xI}, \quad q_2 = \left\{\frac{\bar{r}(1-\nu^2)}{Eh}\right\} \bar{P}_{xI}, \quad q_3 = \left\{\frac{1-\nu^2}{Eh}\right\} N_{\theta I}, \tag{2.98}$$

where subscripts i or o may be added as necessary, with $\bar{r} = a$ or b, respectively. It is noted that q_1, q_2 and q_3 as given by (2.98) are dimensionless and may be expressed in the following functional forms:

$$q_1 = \hat{A}_1\xi + \hat{B}_1, \qquad q_2 = \hat{B}_2, \qquad q_3 = \hat{A}_3\xi + \hat{B}_3, \tag{2.99}$$

where ξ is a nondimensionalized length variable defined in (2.55), and

$$\hat{A}_1 = -\left\{\frac{1-\nu^2}{Eh}\right\} BL, \quad \hat{A}_3 = -\left\{\frac{1-\nu^2}{Eh}\right\} CL\bar{r},$$

$$\hat{B}_1 = \left\{\frac{1-\nu^2}{Eh}\right\} BL, \quad \hat{B}_2 = \left\{\frac{1-\nu^2}{Eh}\right\} B\bar{r}, \quad \hat{B}_3 = \left\{\frac{1-\nu^2}{Eh}\right\} D\bar{r}, \tag{2.100}$$

are all dimensionless constants, resulting from the substitution of (2.93) and (2.97) into (2.98).

Thus, Equations (2.99), together with (2.87), (2.90), (2.91) and (2.94), fully specify these dimensionless steady–viscous forces acting on the shells.

2.3.4 Solution to the Governing Equations of Motion

With the unsteady generalized fluid forces and steady viscous loads acting on the shells completely determined, the solution for the governing equations of motion (2.1)–(2.6) subject to the free–end boundary conditions (2.9)–(2.16) can now be carried out using the extended form of Galerkin's method (see, for example, Anderson 1972) which, for the present system, is expressed by the following variational statement

$$\delta E = \delta E_i + \delta E_o = 0, \tag{2.101}$$

with

$$\begin{aligned} \delta E_i &= \int_0^{2\pi} \left\{ \frac{\mathcal{D}_i}{\varepsilon_i} \int_0^1 \left[L_{1i}\delta u_i + L_{2i}\delta v_i - L_{3i}\delta w_i \right] \mathrm{d}\xi \right. \\ &- \left. \mathcal{D}_i \left[R_{1i}\delta u_i + \left(\frac{1-\nu_i}{2}\right) R_{2i}\delta v_i + k_i(R_{3i}\delta w_i' + R_{4i}\delta w_i) \right]_{\xi=1} \right\} \mathrm{d}\theta, \end{aligned} \tag{2.102}$$

$$\begin{aligned} \delta E_o &= \int_0^{2\pi} \left\{ \frac{\mathcal{D}_o}{\varepsilon_o} \int_0^1 \left[L_{1o}\delta u_o + L_{2o}\delta v_o - L_{3o}\delta w_o \right] \mathrm{d}\xi \right. \\ &- \left. \mathcal{D}_o \left[R_{1o}\delta u_o + \left(\frac{1-\nu_o}{2}\right) R_{2o}\delta v_o + k_o(R_{3o}\delta w_o' + R_{4o}\delta w_o) \right]_{\xi=1} \right\} \mathrm{d}\theta, \end{aligned} \tag{2.103}$$

where $\mathcal{D}_i = E_i h_i/(1-\nu_i^2)$ and $\mathcal{D}_o = E_o h_o/(1-\nu_o^2)$; $w_i' = \varepsilon_i \partial w_i/\partial\xi$ and $w_o' = \varepsilon_o \partial w_o/\partial\xi$; L's were defined in (2.1)–(2.6) and R's in (2.9)–(2.16), and subscripts i and o are associated with the inner and outer shells, respectively. The minus sign associated with the term $L_{3i}\delta w_i$ in (2.102) is necessary as L_{3i} represents the negative of the load per unit surface (unit length and unit radian). As a matter of fact, in the original expression of L_{3i} that Flügge derived, most of the terms were preceded by minus signs; for convenience in writing, Flügge himself switched the sign of the expression. The same explanation can be given to $-L_{3o}\delta w_o$ in (2.103).

Since δE_i and δE_o are generally independent, the implication of Equation (2.101) is that both δE_i and δE_o must individually vanish, or

$$\delta E_i = 0, \qquad \delta E_o = 0, \tag{2.104}$$

and hence these two equations must be solved simultaneously. Each of the variational statements (2.104) may be derived from an extended form of the principle of virtial work (Altman and De Oliveira 1988) or from Hamilton's principle. It should be mentioned here that the clamped–end boundary conditions (2.7) and (2.8) are automatically satisfied by the admissible functions chosen for u, v and w [Equations (2.31) and (2.32)].

As the procedure to solve the first equation of (2.104) is *exactly* identical to that of the second one, only the former will be presented in full, whereas the final results from the second equation will be given in Appendix C.

The variations in u_i, v_i and w_i are simply derived from (2.31). Expressed in terms of dimensionless parameters as were defined in (2.55), these variations may be written as follows

$$\begin{Bmatrix} \delta u_i \\ \delta v_i \\ \delta w_i \end{Bmatrix} = L \sum_{l=1}^{\infty} \sum_{k=1}^{\infty} \begin{Bmatrix} \delta \bar{A}_k \cos l\theta \, (\varepsilon_i \partial/\partial \xi) \\ \delta \bar{B}_k \sin l\theta \\ \delta \bar{C}_k \cos l\theta \end{Bmatrix} \Phi_k(\xi)\, e^{i\Omega t}. \tag{2.105}$$

In the above expressions, for the purpose of evaluating (2.102), different indices have been used for the two summations—k and l denote the axial and circumferential wave numbers, respectively.

Each of the terms in (2.102) will now be considered individually. Substituting (2.31) into (2.9)–(2.12), multiplying the resulting R's by the appropriate variations in (2.105), and then evaluating such products at $\xi = 1$ gives

$$R_{1i}\delta u_i\Big|_{\xi=1} = \sum_{l=1}^{\infty}\sum_{n=1}^{\infty} \cos l\theta \cos n\theta f_{1R}(n), \tag{2.106}$$

$$R_{2i}\delta v_i\Big|_{\xi=1} = \sum_{l=1}^{\infty}\sum_{n=1}^{\infty} \sin l\theta \sin n\theta f_{2R}(n), \tag{2.107}$$

$$R_{3i}\delta w_i\Big|_{\xi=1} = \sum_{l=1}^{\infty}\sum_{n=1}^{\infty} \cos l\theta \cos n\theta f_{3R}(n), \tag{2.108}$$

$$R_{4i}\delta w_i'\Big|_{\xi=1} = \sum_{l=1}^{\infty}\sum_{n=1}^{\infty}\cos l\theta\cos n\theta f_{4R}(n), \tag{2.109}$$

where

$$f_{1R}(n) = L^2 e^{2i\Omega t}\sum_{k=1}^{\infty}\sum_{m=1}^{\infty}\delta\bar{A}_k\Big\{\Big[\nu_i n\varepsilon_i\Phi_k'(1)\Phi_m(1)\Big]\bar{B}_m + \Big[\nu_i\varepsilon_i\Phi_k'(1)\Phi_m(1)\Big]\bar{C}_m\Big\}, \tag{2.110}$$

$$\begin{aligned} f_{2R}(n) &= L^2 e^{2i\Omega t}\sum_{k=1}^{\infty}\sum_{m=1}^{\infty}\delta\bar{B}_k\Big\{-\Big[n\varepsilon_i\Phi_k(1)\Phi_m'(1)\Big]\bar{A}_m + \Big[(1+3k_i)\varepsilon_i\Phi_k(1)\Phi_m'(1)\Big]\bar{B}_m \\ &\quad + \Big[3nk_i\varepsilon_i\Phi_k(1)\Phi_m'(1)\Big]\bar{C}_m\Big\}, \end{aligned} \tag{2.111}$$

$$\begin{aligned} f_{3R}(n) &= L^2 e^{2i\Omega t}\sum_{k=1}^{\infty}\sum_{m=1}^{\infty}\delta\bar{C}_k\left\{\left[\frac{n^2}{2}(1-\nu_i)\varepsilon_i\Phi_k(1)\Phi_m'(1)\right]\bar{A}_m\right. \\ &\quad \left. + \left[\frac{n}{2}(3-\nu_i)\varepsilon_i\Phi_k(1)\Phi_m'(1)\right]\bar{B}_m + \Big[n^2(2-\nu_i)\varepsilon_i\Phi_k(1)\Phi_m'(1)\Big]\bar{C}_m\right\}, \end{aligned} \tag{2.112}$$

$$f_{4R}(n) = L^2 e^{2i\Omega t}\sum_{k=1}^{\infty}\sum_{m=1}^{\infty}\delta\bar{C}_k\Big\{-\Big[\nu_i n\varepsilon_i\Phi_k'(1)\Phi_m(1)\Big]\bar{B}_m - \Big[n^2\nu_i\varepsilon_i\Phi_k'(1)\Phi_m(1)\Big]\bar{C}_m\Big\}, \tag{2.113}$$

and the fact that, for a cantilevered beam,

$$\Phi_m''(1) = 0, \qquad \Phi_m'''(1) = 0,$$

has been taken into consideration in the evaluation of (2.106)–(2.109).

Similarly, substituting (2.31) and (2.61) into Equations (2.1)–(2.3) and multiplying the resulting L's by the appropriate variations in (2.105) yields the following products

$$L_{1i}\delta u_i = \sum_{l=1}^{\infty}\sum_{n=1}^{\infty}\cos l\theta\cos n\theta f_{1L}(n), \tag{2.114}$$

$$L_{2i}\delta v_i = \sum_{l=1}^{\infty}\sum_{n=1}^{\infty}\sin l\theta\sin n\theta f_{2L}(n), \tag{2.115}$$

$$L_{3i}\delta w_i = \sum_{l=1}^{\infty}\sum_{n=1}^{\infty}\cos l\theta\cos n\theta f_{3L}(n), \tag{2.116}$$

where

$$\begin{aligned} f_{1L}(n) &= L^2 e^{2i\Omega t}\sum_{k=1}^{\infty}\sum_{m=1}^{\infty}\delta\bar{A}_k\left\{\left[\left(\bar{\Omega}_i^2 - \frac{n^2}{2}(1+k_i)(1-\nu_i) - q_{3i}n^2\right)\varepsilon_i^2\Phi_k'(\xi)\Phi_m'(\xi)\right.\right. \\ &\quad \left. + (1+q_{1i})\varepsilon_i^4\Phi_k'(\xi)\Phi_m'''(\xi)\right]\bar{A}_m + \left[\frac{n}{2}(1+\nu_i)\varepsilon_i^2\Phi_k'(\xi)\Phi_m'(\xi) + q_{2i}n\varepsilon_i\Phi_k'(\xi)\Phi_m(\xi)\right]\bar{B}_m \end{aligned}$$

$$+\left[\left(\nu_i - \frac{n^2k_i}{2}(1-\nu_i) - q_{3i}\right)\varepsilon_i^2\Phi_k'(\xi)\Phi_m'(\xi) - k_i\varepsilon_i^4\Phi_k'(\xi)\Phi_m'''(\xi)\right.$$

$$\left. + q_{2i}\varepsilon_i\Phi_k'(\xi)\Phi_m(\xi)\right]\bar{C}_m\Bigg\}, \tag{2.117}$$

$$\begin{aligned} f_{2L}(n) &= L^2e^{2i\Omega t}\sum_{k=1}^{\infty}\sum_{m=1}^{\infty}\delta\bar{B}_k\Bigg\{-\left[\frac{n}{2}(1+\nu_i)\varepsilon_i^2\Phi_k(\xi)\Phi_m''(\xi)\right]\bar{A}_m \\ &+\left[\left(\bar{\Omega}_i^2 - n^2(1+q_{3i})\right)\Phi_k(\xi)\Phi_m(\xi) + \left(\frac{1}{2}(1+3k_i)(1-\nu_i) + q_{1i}\right)\varepsilon_i^2\Phi_k(\xi)\Phi_m''(\xi)\right]\bar{B}_m \\ &+\left[\frac{nk_i}{2}(3-\nu_i)\varepsilon_i^2\Phi_k(\xi)\Phi_m''(\xi) - n(1+q_{3i})\Phi_k(\xi)\Phi_m(\xi)\right]\bar{C}_m\Bigg\}, \end{aligned} \tag{2.118}$$

$$\begin{aligned} f_{3L}(n) &= L^2e^{2i\Omega t}\sum_{k=1}^{\infty}\sum_{m=1}^{\infty}\delta\bar{C}_k\Bigg\{\Bigg[\left(\nu_i - \frac{n^2k_i}{2}(1-\nu_i) - q_{3i}\right)\varepsilon_i^2\Phi_k(\xi)\Phi_m''(\xi) \\ &- k_i\varepsilon_i^4\lambda_m^4\Phi_k(\xi)\Phi_m(\xi)\Bigg]\bar{A}_m + \left[n(1+q_{3i})\Phi_k(\xi)\Phi_m(\xi) - \frac{nk_i}{2}(3-\nu_i)\varepsilon_i^2\Phi_k(\xi)\Phi_m''(\xi)\right]\bar{B}_m \\ &+\Bigg[\left(1 + k_i\varepsilon_i^4\lambda_m^4 + k_i(n^2-1)^2 + n^2q_{3i} - \bar{\Omega}_i^2\right)\Phi_k(\xi)\Phi_m(\xi) - (2k_in^2 + q_{1i})\varepsilon_i^2\Phi_k(\xi)\Phi_m''(\xi) \\ &- \frac{1}{\bar{q}_i}\Phi_k(\xi)Q_{mn}(\xi)\Bigg]\bar{C}_m\Bigg\}, \end{aligned} \tag{2.119}$$

where λ_m are the roots of the transcendental equation $\cosh\lambda_m\cos\lambda_m + 1 = 0$; further details on λ_m may be found in Appendix A.

Before further analysis is made, it is useful to recall the orthogonality property of the sine and cosine functions; for any two integers l and n,

$$\int_0^{2\pi}\cos l\theta\cos n\theta\,\mathrm{d}\theta = \int_0^{2\pi}\sin l\theta\sin n\theta\,\mathrm{d}\theta = \begin{cases} 0 & \text{if } l \neq n, \\ \pi & \text{if } l = n, \end{cases}$$

which lead to

$$\int_0^{2\pi}\left\{\sum_{l=1}^{\infty}\sum_{n=1}^{\infty}\cos l\theta\cos n\theta f_c(n)\right\}\mathrm{d}\theta = \sum_{l=1}^{\infty}\sum_{n=1}^{\infty}\left\{\int_0^{2\pi}\cos l\theta\cos n\theta\,\mathrm{d}\theta\right\}f_c(n) = \sum_{n=1}^{\infty}\pi f_c(n), \tag{2.120}$$

$$\int_0^{2\pi}\left\{\sum_{l=1}^{\infty}\sum_{n=1}^{\infty}\sin l\theta\sin n\theta f_s(n)\right\}\mathrm{d}\theta = \sum_{l=1}^{\infty}\sum_{n=1}^{\infty}\left\{\int_0^{2\pi}\sin l\theta\sin n\theta\,\mathrm{d}\theta\right\}f_s(n) = \sum_{n=1}^{\infty}\pi f_s(n), \tag{2.121}$$

where $f_c(n)$ and $f_s(n)$ are some particular functions of n. In effect, Equations (2.120) and (2.121) show how the terms $\cos l\theta\cos n\theta$ and $\sin l\theta\sin n\theta$ in Equations (2.106)–(2.109) and (2.114)–(2.116) are *decoupled* once the extended Galerkin method is applied via Equation (2.101).

Now, if all the terms q_{1i}, q_{2i} and q_{3i} in Equations (2.117)–(2.119) are replaced by their functional forms in (2.99), then substituting (2.106)–(2.109) and (2.114)–(2.116) into (2.102) and performing (i) the integration over the domain $[0, 2\pi]$ of θ with (2.120) and (2.121) taken into account and (ii) the integration over the domain $[0, 1]$ of ξ will lead to

$$\pi L^2 e^{2i\Omega t}\left(\frac{D_i}{\varepsilon_i}\right)\sum_{n=1}^{\infty}\sum_{k=1}^{M}\left\{W_{1kn}\,\delta\bar{A}_k + W_{2kn}\,\delta\bar{B}_k + W_{3kn}\,\delta\bar{C}_k\right\} = 0,$$

and because $\pi L^2 e^{2i\Omega t}(D_i/\varepsilon_i) \neq 0$ for all t,

$$\sum_{n=1}^{\infty}\sum_{k=1}^{M}\left\{W_{1kn}\,\delta\bar{A}_k + W_{2kn}\,\delta\bar{B}_k + W_{3kn}\,\delta\bar{C}_k\right\} = 0. \tag{2.122}$$

In Equation (2.122), M is the number of admissible functions taken for the analysis, thus replacing the upper limits of the summations of the axial wave numbers in (2.31) and (2.105), i.e. $1 \le k \le M$ and $1 \le m \le M$; the coefficients W_{1kn}, W_{2kn}, W_{3kn} are functions of $\bar{A}_m$, $\bar{B}_m$, $\bar{C}_m$ being associated with the inner shell,

$$\begin{aligned}
W_{1kn} = \sum_{m=1}^{M}\Bigg\{&\Bigg[\left(\bar{\Omega}_i^2 - \frac{n^2}{2}\Big[(1+k_i)(1-\nu_i) + 2\hat{B}_{3i}\Big]\right)\varepsilon_i^2\int_0^1 \Phi_k'(\xi)\,\Phi_m'(\xi)\,\mathrm{d}\xi \\
&- n^2\varepsilon_i^2\hat{A}_{3i}\int_0^1 \xi\,\Phi_k'(\xi)\,\Phi_m'(\xi)\,\mathrm{d}\xi + \left(1+\hat{B}_{1i}\right)\varepsilon_i^4\int_0^1 \Phi_k'(\xi)\,\Phi_m'''(\xi)\,\mathrm{d}\xi \\
&+ \varepsilon_i^4\hat{A}_{1i}\int_0^1 \xi\,\Phi_k'(\xi)\,\Phi_m'''(\xi)\,\mathrm{d}\xi\Bigg]\bar{A}_m + \Bigg[\frac{n}{2}(1+\nu_i)\varepsilon_i^2\int_0^1 \Phi_k'(\xi)\,\Phi_m'(\xi)\,\mathrm{d}\xi \\
&+ n\varepsilon_i\hat{B}_{2i}\int_0^1 \Phi_k'(\xi)\,\Phi_m(\xi)\mathrm{d}\xi - \nu_i n\varepsilon_i^2\Phi_k'(1)\Phi_m(1)\Bigg]\bar{B}_m \\
&+ \Bigg[\left(\nu_i - \frac{n^2k_i}{2}(1-\nu_i) - \hat{B}_{3i}\right)\varepsilon_i^2\int_0^1 \Phi_k'(\xi)\,\Phi_m'(\xi)\,\mathrm{d}\xi - \varepsilon_i^2\hat{A}_{3i}\int_0^1 \xi\,\Phi_k'(\xi)\,\Phi_m'(\xi)\,\mathrm{d}\xi \\
&- k_i\varepsilon_i^4\int_0^1 \Phi_k'(\xi)\,\Phi_m'''(\xi)\,\mathrm{d}\xi + \varepsilon_i\hat{B}_{2i}\int_0^1 \Phi_k'(\xi)\,\Phi_m(\xi)\,\mathrm{d}\xi - \nu_i\varepsilon_i^2\Phi_k'(1)\Phi_m(1)\Bigg]\bar{C}_m\Bigg\},
\end{aligned} \tag{2.123}$$

$$\begin{aligned}
W_{2kn} = \sum_{m=1}^{M}\Bigg\{&\Bigg[-\frac{n}{2}(1+\nu_i)\varepsilon_i^2\int_0^1 \Phi_k(\xi)\,\Phi_m''(\xi)\,\mathrm{d}\xi + \frac{n\varepsilon_i^2}{2}(1-\nu_i)\Phi_k(1)\Phi_m'(1)\Bigg]\bar{A}_m \\
&+ \Bigg[[\bar{\Omega}_i^2 - n^2(1+\hat{B}_{3i})]\int_0^1 \Phi_k(\xi)\,\Phi_m(\xi)\,\mathrm{d}\xi - n^2\hat{A}_{3i}\int_0^1 \xi\,\Phi_k(\xi)\,\Phi_m(\xi)\,\mathrm{d}\xi \\
&+ \left(\frac{1}{2}(1+3k_i)(1-\nu_i) + \hat{B}_{1i}\right)\varepsilon_i^2\int_0^1 \Phi_k(\xi)\,\Phi_m''(\xi)\,\mathrm{d}(\xi) + \varepsilon_i^2\hat{A}_{1i}\int_0^1 \xi\,\Phi_k(\xi)\,\Phi_m''(\xi)\,\mathrm{d}\xi \\
&- \frac{\varepsilon_i^2}{2}(1-\nu_i)(1+3k_i)\Phi_k(1)\Phi_m'(1)\Bigg]\bar{B}_m + \Bigg[\frac{nk_i}{2}(3-\nu_i)\varepsilon_i^2\int_0^1 \Phi_k(\xi)\,\Phi_m''(\xi)\,\mathrm{d}\xi
\end{aligned}$$

$$- n\left(1+\hat{B}_{3i}\right)\int_0^1 \Phi_k(\xi)\,\Phi_m(\xi)\,\mathrm{d}\xi - n\hat{A}_{3i}\int_0^1 \xi\,\Phi_k(\xi)\,\Phi_m(\xi)\,\mathrm{d}\xi$$

$$\left. - \frac{3}{2} n k_i \varepsilon_i^2 (1-\nu_i)\Phi_k(1)\Phi_m'(1)\right]\bar{C}_m\Bigg\}, \tag{2.124}$$

$$\begin{aligned} W_{3kn} &= \sum_{m=1}^{M}\Bigg\{\Bigg[\left(\frac{n^2 k_i}{2}(1-\nu_i) - \nu_i + \hat{B}_{3i}\right)\varepsilon_i^2\int_0^1 \Phi_k(\xi)\,\Phi_m''(\xi)\,\mathrm{d}\xi + \varepsilon_i^2\hat{A}_{3i}\int_0^1 \xi\,\Phi_k(\xi)\,\Phi_m''(\xi)\,\mathrm{d}\xi \\ &\quad + k_i\varepsilon_i^4\lambda_m^4\int_0^1 \Phi_k(\xi)\,\Phi_m(\xi)\,\mathrm{d}\xi - \frac{n^2\varepsilon_i^2 k_i}{2}(1-\nu_i)\Phi_k(1)\Phi_m'(1)\Bigg]\bar{A}_m \\ &\quad + \Bigg[\frac{n k_i}{2}(3-\nu_i)\varepsilon_i^2\int_0^1 \Phi_k(\xi)\,\Phi_m''(\xi)\,\mathrm{d}\xi - n\left(1+\hat{B}_{3i}\right)\int_0^1 \Phi_k(\xi)\,\Phi_m(\xi)\,\mathrm{d}\xi \\ &\quad - n\hat{A}_{3i}\int_0^1 \xi\,\Phi_k(\xi)\,\Phi_m(\xi)\,\mathrm{d}\xi + n k_i\nu_i\varepsilon_i^2\Phi_k'(1)\Phi_m(1) - \frac{n k_i\varepsilon_i^2}{2}(3-\nu_i)\Phi_k(1)\Phi_m'(1)\Bigg]\bar{B}_m \\ &\quad + \Bigg[\left(\bar{\Omega}_i^2 - [1 + k_i\varepsilon_i^4\lambda_m^4 + k_i(n^2-1)^2 + n^2\hat{B}_{3i}]\right)\int_0^1 \Phi_k(\xi)\,\Phi_m(\xi)\,\mathrm{d}\xi \\ &\quad - n^2\hat{A}_{3i}\int_0^1 \xi\,\Phi_k(\xi)\,\Phi_m(\xi)\,\mathrm{d}\xi + \left(2k_i n^2 + \hat{B}_{1i}\right)\varepsilon_i^2\int_0^1 \Phi_k(\xi)\,\Phi_m''(\xi)\,\mathrm{d}\xi \\ &\quad + \varepsilon_i^2\hat{A}_{1i}\int_0^1 \xi\,\Phi_k(\xi)\,\Phi_m''(\xi)\,\mathrm{d}\xi + \frac{1}{\bar{q}_i}\int_0^1 \Phi_k(\xi)\,Q_{mn}(\xi)\,\mathrm{d}\xi + k_i\nu_i n^2\varepsilon_i^2\Phi_k'(1)\Phi_m(1) \\ &\quad - k_i n^2\varepsilon_i^2(2-\nu_i)\Phi_k(1)\Phi_m'(1)\Bigg]\bar{C}_m\Bigg\}, \end{aligned} \tag{2.125}$$

where $\hat{A}_{1i}, \ldots, \hat{B}_{3i}$ were defined in Equations (2.100).

Because $\delta\bar{A}_k$, $\delta\bar{B}_k$ and $\delta\bar{C}_k$ are totally arbitrary, Equation (2.122) is equivalent to

$$\sum_{n=1}^{\infty} W_{1kn} = 0, \qquad \sum_{n=1}^{\infty} W_{2kn} = 0, \qquad \sum_{n=1}^{\infty} W_{1kn} = 0. \tag{2.126}$$

As may be seen from Equations (2.123)–(2.125), each term of any of the above three series is a function of n and is independent of other terms in the same series. Equations (2.126) thus imply that individual W_{1kn}, W_{2kn} and W_{3kn} must be equal to zero, namely

$$\begin{aligned} W_{1kn} &= \sum_{m=1}^{M}\left\{J_{kmn}^{1,1}\,\bar{A}_m + J_{kmn}^{1,2}\,\bar{B}_m + J_{kmn}^{1,3}\,\bar{C}_m + J_{kmn}^{1,4}\,\bar{D}_m + J_{kmn}^{1,5}\,\bar{E}_m + J_{kmn}^{1,6}\,\bar{F}_m\right\} = 0, \\ &\;\vdots \\ W_{3kn} &= \sum_{m=1}^{M}\left\{J_{kmn}^{3,1}\,\bar{A}_m + J_{kmn}^{3,2}\,\bar{B}_m + J_{kmn}^{3,3}\,\bar{C}_m + J_{kmn}^{3,4}\,\bar{D}_m + J_{kmn}^{3,5}\,\bar{E}_m + J_{kmn}^{3,6}\,\bar{F}_m\right\} = 0. \end{aligned} \tag{2.127}$$

Similarly, with the foregoing analysis carried out for the second equation of (2.104), the following equations will be obtained

$$W_{4kn} = \sum_{m=1}^{M} \left\{ J_{kmn}^{4,1} \bar{A}_m + J_{kmn}^{4,2} \bar{B}_m + J_{kmn}^{4,3} \bar{C}_m + J_{kmn}^{4,4} \bar{D}_m + J_{kmn}^{4,5} \bar{E}_m + J_{kmn}^{4,6} \bar{F}_m \right\} = 0,$$

$$\vdots \tag{2.128}$$

$$W_{6kn} = \sum_{m=1}^{M} \left\{ J_{kmn}^{6,1} \bar{A}_m + J_{kmn}^{6,2} \bar{B}_m + J_{kmn}^{6,3} \bar{C}_m + J_{kmn}^{6,4} \bar{D}_m + J_{kmn}^{6,5} \bar{E}_m + J_{kmn}^{6,6} \bar{F}_m \right\} = 0,$$

Thus, Equation (2.101) is in effect equivalent to a set of $6M$ equations, Equations (2.127)–(2.128) inclusive, in which $\bar{A}_m$, $\bar{B}_m$, ..., $\bar{F}_m$ are the unknowns to be solved for.

Equations (2.127) and (2.128) may be grouped together and put in the matrix form

$$\Big([\mathrm{M}]\bar{\Omega}_i^2 + [\mathrm{C}]\bar{\Omega}_i + [\mathrm{K}]\Big)\{\mathrm{X}\} = \{0\}. \tag{2.129}$$

It should be emphasized here that [M], [C] and [K] in Equation (2.129) are not the traditional mass, damping and stiffness matrices but are proportional to them. [M], [C] and [K] are the coefficient matrices of $\bar{\Omega}_i^2$, $\bar{\Omega}_i^1$ and $\bar{\Omega}_i^0$, respectively. The elements of [M], [C], [K] and {X} are given in Appendix C.

So far, energy dissipated internally in the material of the shells has been neglected. If dissipation is considered to be a hysteretic effect (structural damping), it may be taken into account by replacing Young's modulus E by $E\Big(1 + \frac{\mu}{\Omega}\frac{\partial}{\partial t}\Big)$ in Equations (2.1)–(2.6), where μ is called the structural damping factor. Alternatively, dissipation may be considered to be a viscoelastic effect (viscoelastic damping), in which case E is replaced by $E\Big(1 + \chi\frac{\partial}{\partial t}\Big)$, where χ is the viscoelastic damping coefficient. In general, E is replaced by $E\Big\{1 + \Big(\frac{\mu}{\Omega} + \chi\Big)\frac{\partial}{\partial t}\Big\}$ with the understanding that either μ or χ will be zero for a given system. As a reminder of the notation used in Equations (2.1)–(2.6), $E\Big\{1 + \Big(\frac{\mu}{\Omega} + \chi\Big)\frac{\partial}{\partial t}\Big\}$ is to be written with the subscript i for Equations (2.1)–(2.3), namely $E_i\Big\{1 + \Big(\frac{\mu_i}{\Omega} + \chi_i\Big)\frac{\partial}{\partial t}\Big\}$, and with the subscript o for Equations (2.4)–(2.6), namely $E_o\Big\{1 + \Big(\frac{\mu_o}{\Omega} + \chi_o\Big)\frac{\partial}{\partial t}\Big\}$.

To give a simple illustration of changes Equation (2.129) may be subject to when internal damping is included, it is assumed that both inner and outer shells are made of the same material and hence neither subscript i nor o is required for μ and χ (and other material properties). Equation (2.129) then becomes

$$\Big([\mathrm{M}]\bar{\Omega}_i^2 + [\mathrm{C}]\bar{\Omega}_i + [1 + i(\mu + \chi\Omega)][\mathrm{K}]\Big)\{\mathrm{X}\} = \{0\}. \tag{2.130}$$

Since

$$i\chi\Omega = i\left(\frac{\chi\mathcal{U}_i}{L}\right)\left(\frac{L}{a}\right)\left(\frac{\Omega a}{\mathcal{U}_i}\right) = \left(\frac{i}{\varepsilon_i}\frac{\chi\mathcal{U}_i}{L}\right)\bar{\Omega}_i,$$

Equation (2.130) may be rearranged and rewritten as

$$\left([\mathrm{M}']\bar{\Omega}_i^2 + [\mathrm{C}']\bar{\Omega}_i + [\mathrm{K}']\right)\{\mathrm{X}\} = \{0\}, \tag{2.131}$$

where

$$[\mathrm{M}'] = [\mathrm{M}], \quad [\mathrm{C}'] = [\mathrm{C}] + \left(\frac{i}{\varepsilon_i}\frac{\chi\mathcal{U}_i}{L}\right)[\mathrm{K}], \quad [\mathrm{K}'] = (1+\mu i)[\mathrm{K}]. \tag{2.132}$$

If a new vector $\{\mathrm{Y}\}$ is introduced and defined as

$$\{\mathrm{Y}\} = \left\{ \begin{array}{c} \{\mathrm{X}\} \\ \bar{\Omega}_i\{\mathrm{X}\} \end{array} \right\}, \tag{2.133}$$

Equation (2.129) [or Equation (2.131) if internal dissipation is to be accounted for] can be simplified to

$$\left([\mathrm{P}] + \bar{\Omega}_i[\mathrm{Q}]\right)\{\mathrm{Y}\} = \{0\}, \tag{2.134}$$

where

$$[\mathrm{P}] = \begin{bmatrix} [0] & [\mathrm{I}] \\ [\mathrm{K}] & [\mathrm{C}] \end{bmatrix}, \qquad [\mathrm{Q}] = \begin{bmatrix} [-\mathrm{I}] & [0] \\ [0] & [\mathrm{M}] \end{bmatrix},$$

with [I] being the identity matrix of the same size as [M], [C] and [K]. Equation (2.134) represents a standard eigenvalue problem and can readily be solved by any available computer subroutines such as those of IMSL (International Mathematical and Scientific Libraries), giving the eigenfrequencies of the system.

2.3.5 Summary

Section 2.3 has presented in detail (i) the evaluation of the unsteady generalized fluid forces acting on the shells by means of the Fourier transform technique and (ii) the procedure of solving the governing equations of motion using the extended Galerkin method. It has also given all final, important results for the steady viscous forces appearing in the governing equations of motion.

2.4 Preliminary Calculations

2.4.1 Introduction

Before the theory presented earlier in this chapter was actually applied to the system under consideration (Section 2.5), a series of preliminary calculations were conducted to examine different aspects of the theory.

Firstly, natural frequencies of a cylindrical shell *in vacuo* were calculated (Section 2.4.2). The aim of these calculations was to assess how well the extended Galerkin method works through Equation (2.101) in solving the equations of motion [(2.1)–(2.6)] subject to the free–end boundary conditions [(2.9)–(2.14)], and hence to validate certain segments of the computer program developed for Section 2.5.

Secondly, as the solution for the unsteady fluid forces is obtained by the Fourier transform method, numerical integration is required and was performed in the present analysis using a composite formula based on the two–point Gaussian quadrature. For computational economy, it is thus necessary to determine the optimum values of such important parameters involved as the integration stepsize $\Delta\bar{\alpha}$, the domain of integration $(-z, z)$, and the number of admissible functions M taken for the analysis. The selection of these values was based on the calculations of the critical flow velocity of a cantilevered cylinder conveying fluid (Section 2.4.3).

Finally, different out–flow models, the concept of which has been introduced earlier in the Fourier transform method, were examined (Section 2.4.4) with regard to (i) their essence in the theory, (ii) the most suitable distance beyond the free end of the shells for flow perturbations to die out, and (iii) the best of the models considered for specifying the downstream flow perturbation behaviour.

It should be noted that the results to be presented below were obtained without steady viscous effects (Section 2.3.4) included. There were two reasons for doing so: (i) all the above–mentioned aspects are part of the inviscid theory only, and (ii) the present results could be compared with previous theoretical ones which did not involve any viscous effects.

2.4.2 Natural Frequencies of a Cylinder in the Absence of Flow

Natural frequencies of a cantilevered cylindrical shell were calculated, in the absence of fluid flow ($\bar{U}_i = \bar{U}_o = 0$) and for the following parameters:

$$E_i = 2.1 \times 10^{11}\,\mathrm{N/m^2},\ \nu_i = 0.28,\ \rho_{si} = 7.8 \times 10^3\,\mathrm{kg/m^3},\ L = 0.502\,\mathrm{m},$$

$$a = 0.0635\,\mathrm{m},\ h_i = 0.0016\,\mathrm{m},\ \mu_i \text{ and } \chi_i \text{ are zero.}$$

These parameters are the same as those in Gill's (1972) experiments and in Sharma's (1974) theoretical calculations, to which the present results are compared, in Figure 2.2 and Table 2.1.

In Figure 2.2, the results obtained with six admissible functions ($M = 6$) are compared with Gill's measurements and with Sharma's sextic approximation. It is seen that the agreement is quite good and, in fact, the present results are closer to the experimental values than Sharma's. The agreement improves further, if only slightly, when the calculations are carried out with a larger M, since the natural frequencies then become smaller, especially as the axial wave number, m, increases—thus, bringing the present results closer to the measured natural frequencies.

In general, the theoretical results are closest to the experimental ones for higher n, the circumferential wave number, and lower m, and *vice versa.* Since the effect of M on the natural frequencies is not overwhelming, especially for low m (= 1,2), quite a number of the calculations that follow have been conducted with $M = 6$, or even 4, to reduce the computing time required.

2.4.3 Convergence Study

The optimum values of the parameters involved in numerical integration were judged on the convergence rate of the solution. In this study, the critical dimensionless flow velocity of the cantilevered cylindrical shell conveying fluid in Païdoussis and Denise's (1972) problem was calculated. The same physical properties and geometrical data of the shell were used:

$$E_i = 89.57 \times 10^4\,\mathrm{N/m^2},\ \nu_i = 0.5,\ \rho_{si} = 0.85 \times 10^3\,\mathrm{kg/m^3},\ a = 7.85 \times 10^{-3}\,\mathrm{m},\ \ell = 3.0,$$

$L/a = 12.9,\ h_i = 0.178 \times 10^{-3}\,\mathrm{m},\ \rho_{\mathrm{air}} = 1.1564\,\mathrm{kg/m^3}\ [(a/h_i)(\rho_{\mathrm{air}}/\rho_{si}) = 0.06]$.

For comparative purposes, the present results will be tabulated together with those obtained by Païdoussis and Denise (1972) using a different theory; in the tables to be presented, the latter results are shown merely as a reference, not as a means to measure how accurate the present results are, or how fast the solution under consideration converges.

2.4.3.1 Integration Stepsize

When the integration stepsize was being examined, the following parameters were held fixed:

$$(-z, z) = (-200, 200), \qquad M = 4.$$

The results obtained for three different flow models[2] are presented in Table 2.2. As may be seen, there is a large difference between $\Delta\bar{\alpha} = 4.0$ and $\Delta\bar{\alpha} = 2.0$ in terms of the critical (dimensionless) flow velocity, $\bar{U}_{ic}$. For $n = 1$, for instance, the relative discrepancies are 2.26% with Model 1, 11.76% with Model 2, and 9.39% with Model 3. It is obvious that $\Delta\bar{\alpha} = 4.0$ is too large. On the other hand, there is very little difference between $\Delta\bar{\alpha} = 2.0$ and $\Delta\bar{\alpha} = 1.0$, especially with Models 1 and 3 in which the predictions for $\bar{U}_{ic}$ are identical up to the fourth significant digit for $n = 1$ and up to the sixth one for $n = 2$ and $n = 3$. The foregoing comparison has shown that $\Delta\bar{\alpha} = 2.0$ is perfectly adequate for the present numerical integration procedure.

2.4.3.2 Domain of Integration

When the domain of integration was varied, the following parameters were held fixed:

$$\Delta\bar{\alpha} = 4, \qquad M = 4.$$

Table 2.3 shows how the domain of integration chosen affects the critical flow velocity $\bar{U}_{ic}$. With Models 1 and 3, the relative difference between two successive values of $\bar{U}_{ic}$ reduces almost by one half as the domain of integration is increased by 100,

---

[2] Further discussions on these models are given in Section 2.4.4.

starting from $(-150, 150)$. With Model 2, the convergence of $\bar{U}_{ic}$ is not obvious because the relative difference remains almost unchanged for the four domains considered. In all cases, however, discrepancies are found to be very small. Thus, a domain of integration as small as $(-150, 150)$ may be considered to be sufficient as far as the lowest three circumferential wave numbers are concerned. Nevertheless, $(-200, 200)$ will be adopted for all subsequent calculations.

2.4.3.3 Number of Admissible Functions

In this case, the following values were taken for the other two parameters:

$$\Delta\bar{\alpha} = 2.0, \qquad (-z, z) = (-200, 200).$$

The effect of the number of admissible functions M on $\bar{U}_{ic}$ is shown in Table 2.4, where M is incremented by 2 from 4 to 10. For $n = 1$, the relative differences in $\bar{U}_{ic}$ corresponding to any two successive chosen values of M are (0.58%, 0.25%, 0.13%) with Model 1, (1.02%, 0.41%, 0.21%) with Model 2, and (0.93%, 0.37%, 0.19%) with Model 3. The same trend is also observed for $n = 2$. Here, it is important to mention that, for $n = 1$ and 2, the critical flow velocities are associated with $m = 2$. For $n = 3$, instability occurs in $m = 3$ with Model 1 for all four values of M considered; with Models 2 and 3, instability also occurs in $m = 3$ but only for $M = 4$ and 6, and then in $m = 2$ for $M = 8$ and 10. As a result, $\bar{U}_{ic}$ converges monotonically with Model 1 [(0.25%, 0.08%, 0.03%)], but *not* with Model 2 [(0.31%, 0.21%, 0.30%)] or Model 3 [(0.83%, 0.19%, 0.28%)] due the change in the critical axial mode m (from 3 to 2). Nevertheless, insofar as the lowest critical flow velocity is concerned, which is associated with $n = 2$, it may be seen that $M = 6$ is sufficiently large to be used in future calculations (Section 2.5).

2.4.4 Out–Flow Models

In what follows, four different flow models are evaluated (as a note, the words "out–flow" and "flow" are used interchangeably throughout the thesis): Models 0 to 3. For interested readers, the physical and mathematical descriptions of these models are given in Appendix B, and may also be found in Païdoussis, Luu and Laithier (1986). The same test problem as was considered in Section 2.4.3 is utilized here to examine various aspects of the flow models. In addition, the following parameters were taken for the calculations of $\bar{U}_{ic}$:

$$(-z, z) = (-200, 200), \qquad \Delta\bar{\alpha} = 4.0, \qquad M = 4.$$

2.4.4.1 Effect of Having No Model

Having no model in the theory is basically the same as applying Model 0. Indeed, Model 0 was the first one used to calculate the critical flow velocity, $\bar{U}_{ic}$. Table 2.5 shows the values of $\bar{U}_{ic}$ obtained with Models 0 to 3. It is seen that the results with no model are abnormal, in the sense that the dynamical behaviour predicted for a cantilevered shell is the same as that of a shell with both ends supported: the shell loses stability first by divergence, and then by coupled-mode flutter. In fact, Model 0 is physically unrealistic and hence so are the results. This will be discussed below.

Clearly, it is mathematically *essential* to model the flow perturbation behaviour beyond $\xi = 1$ and not to impose any artificial discontinuities in that behaviour. In other words, the inclusion of an out-flow model in the present theory is a necessity, *not* a refinement as may have thought (Shayo and Ellen 1978). Moreover, such a flow model may also be necessary for shells with the downstream end pinned because, as shown in Appendix B, the functional form of a flow model is generally a function of *both* the lateral displacement and the slope of the shell at its downstream end; in this case, the pinned end has no displacement, but it has a non-zero slope. It is further noted that the values of $\bar{U}_{ic}$ according to Models 2 and 3, which have the least amount of discontinuity, are rather close and reasonable.

2.4.4.2 Selection of ℓ

Calculations have been performed with different values of ℓ, and the esults are given in Table 2.6. It should be reiterated that flow perturbations completely die out at $\xi = \ell$. Ideally, the solution should converge as ℓ approaches ∞. However, as seen from Table 2.6, there is generally no convergence in the solution obtained with any of the three models (1–3), although Appendix B shows that, as ℓ approaches ∞, the solution *does* converge with Model 1, but *not* with Models 2 and 3.

The convergence problem associated with Models 2 and 3 was identified as being related to the expression for $N_{km}(\bar{\alpha})$ in Equation (2.64). Although $N_{km}(\bar{\alpha})$ is finite for any value of ℓ, nevertheless in the limit, $\lim_{\ell\to\infty} N_{km}(\bar{\alpha})$ ceases to exist (Appendix B); hence, in the numerical calculations, when ℓ becomes very large, the overall problem becomes ill–behaved (a similar example pertains to $\ell\cos\ell$; for any large ℓ, $\ell\cos\ell$ is finite, but $\lim_{\ell\to\infty}\ell\cos\ell$ does not exist). For Model 1, the zigzag pattern of $\bar{U}_{ic}$, corresponding to the values of ℓ considered in Table 2.6, may well be due to the fluctuations of the harmonic term $e^{i\bar{\alpha}\ell}$ in Equation (B.5).

Another observation of Table 2.6 is that, for $\ell = 3$, the results obtained with Models 1–3 are of the same order of magnitude; on the other hand, for $\ell \ll 3$ or $\ell \gg 3$, the results (particularly, the ones denoted by $*$) obtained with one of the models could be very different from (i) those obtained with other models, and (ii) those obtained with the same model but for $\ell = 3$. Attempts have been made to account for this observation, but no satisfactory explanation is found; the intriguing nature of $\ell = 3$ remains to be studied in future work. Such a phenomenon was also reported, though not elaborated upon, in Païdoussis, Luu and Laithier (1986), where $\ell = 2.8$ was adopted. Since $\ell = 3$ is the largest value obtained without any numerical problem in the solution, it will be adopted for all subsequent calculations.

2.4.4.3 Selection of Most Suitable Model

Presented in Table 2.7 are numerical results for $\bar{U}_{ic}$ as a function of n and L/a with Models 1 to 3. Qualitatively, the variations according to the three models are similar. Quantitatively, it may be observed that the results with Models 2 and 3 are very close, stemming from the fact that these two models only differ for large ξ, far away from the free end of the shell (Figure 2.3). Thus, for the same case, the relative difference in $\bar{U}_{ic}$ obtained with Models 2 and 3 is about 0.6%, while the values of $\bar{U}_{ic}$ obtained with Model 1, on the one hand, and Model 2 or 3, on the other, differ by about 10%.

The results of this table make either Model 2 or 3 more acceptable than Model

1; the choice of Model 3 as the most suitable, to be utilized in subsequent calculations, was made on physical grounds as being most realistic for prescribing the smoothest decay, characterized by the second and fourth boundary conditions of (B.20), of flow perturbations.

Some further physical observations may be made from the results of Table 2.7. It is seen that for $10 \leq L/a \leq 20$ the critical circumferential mode is $n = 2$, while for $L/a = 5$ it is $n = 3$. Moreover, for a given n, the axial mode associated with instability, namely the one that undergoes a Hopf bifurcation is not always $m = 2$; higher m may be involved, especially as L/a is increased (e.g., for $L/a \geq 15$, $n = 3$).

Finally, the results obtained with Model 3 with $M = 6$ are compared with Païdoussis and Denise's (1972) theoretical and experimental results in Figure 2.4. As may be seen, the results for $\bar{U}_{ic}$ by the two theories are almost identical for $n = 1$, but larger differences are evident for $n = 2$ and 3. Here, it should be remarked that in the method of solution utilized by Païdoussis and Denise, the question of specifying fluid flow behaviour beyond $\xi = 1$ did not arise; hence, the differences in Figure 2.4 are likely due to the two different methods of solution. Significantly, however, the present theoretical results are closer to the experimental ones for small L/a, as is reasonable, because the effect of the fluid beyond the free end of the shell, not taken into account by the earlier theory, becomes more significant for short shells.

2.4.5 Summary

Section 2.4 has presented the results of preliminary calculations conducted to verify some important aspects of the present theory.

- As a means to check the extended Galerkin method, natural frequencies of a cantilevered shell in the absence of fluid flow were calculated and found to be in excellent agreement with available experimental and analytical results.

- Concerning the numerical integration procedure employed in the Fourier transform method, the optimum values of the integration stepsize $\Delta\bar{\alpha}$, the integration domain $(-z, z)$, and the number of admissible functions M were desired. The selection of these values was based on the critical flow velocity $\bar{U}_{ic}$ of a cantilevered shell conveying fluid flow. Such optimum values were found to be

$$\Delta\bar{\alpha} = 2.0, \quad (-z, z) = (-200, 200), \quad M = 6.$$

- Different out–flow models were examined and compared. It was found that (i) the presence of a flow model in the theory is a necessity, (ii) the optimum value of ℓ at which ($\xi = \ell$) flow perturbations vanish is about 3.0, and (iii) Model 3 appears to be the best in prescribing the downstream flow perturbation behaviour.

2.5 Theoretical Results

2.5.1 Introduction

Although the theory given in Sections 2.2 and 2.3 was developed for the general case of two coaxial *flexible* shells, nevertheless for the calculations to be performed here, the outer one is replaced by a rigid conduit. This is done partly to achieve some computational economy, but also because most physical problems of interest are like that; another reason is that, at least for shells with both ends supported, the dynamical behaviour of such systems is qualitatively the same whether one or both shells are flexible (Païdoussis *et al.* 1984,1985), the main effect of an outer flexible conduit being to diminish the critical flow velocities.

The calculations were conducted for shells with the same geometries and properties as those in the earlier studies of clamped–clamped shells (Païdoussis *et al.* 1984,1985), namely:

$$E_i = 2.0 \times 10^{11}\,\mathrm{N/m^2};\ \nu_i = 0.3,\ \rho_{si} = 7.8 \times 10^3\,\mathrm{kg/m^3},\ \rho_i = \rho_o = 10^3\,\mathrm{kg/m^3};$$

$$b = 100\,\mathrm{mm},\ a = (10/11)b \text{ for the so-called 1/10-gap system,}$$

$$a = (100/101)b \text{ for the 1/100-gap system, } L = 1.00\,\mathrm{m},\ h_i = 0.5\,\mathrm{mm};$$

$$\text{thus, } \mathcal{U}_i = 5308\,\mathrm{m/s} \text{ and } \rho_i a/(\rho_{si} h_i) = 23.30.$$

Although the present results are specific to this system, they have nevertheless been found to be qualitatively valid, in terms of the general dynamical behaviour of the system, over considerable ranges of dimensionless parameters relating shell and fluid properties and geometric factors.

It is known (Evensen 1974, Evensen and Olson 1968) that shells are subject to important softening–type nonlinearities. Since the theory is linear, the results generated are expected to be physically correct only for sufficiently small-amplitude perturbations; thus, the intricate behaviour of the system beyond the first loss of stability as predicted by the present theory may not be reliable. However, the results are still of academic interest and are therefore presented.

Three different cases of flows will be considered and discussed in the following order: (i) internal flow alone, $\bar{U}_o = 0$ (Section 2.5.2), (ii) annular flow alone, $\bar{U}_i = 0$ (Section 2.5.3), and (iii) both internal and annular flows together (Section 2.5.4).

2.5.2 Internal Flow Alone

2.5.2.1 General Dynamics of the System

Typical results are shown in Figure 2.5, involving internal flow only, while the annular fluid is quiescent ($\bar{U}_o = 0$). Calculations were carried out using inviscid theory, with or without steady viscous effects taken into account.

Figure 2.5 is in the form of an Argand diagram, in which the real and imaginary parts of the eigenfrequencies of the system $\bar{\Omega}_i$, for $n = 2$ and $m = 1, 2, 3$, are plotted against each other, with the flow velocity $\bar{U}_i$ as the parameter. Clearly, if $\mathrm{Im}(\bar{\Omega}_i) \leq 0$ the system is unstable, the stability having been lost when $\mathrm{Im}(\bar{\Omega}_i) = 0$ by flutter, if $\mathrm{Re}(\bar{\Omega}_i) \neq 0$ and by divergence if $\mathrm{Re}(\bar{\Omega}_i) = 0$. In Figure 2.5, it is seen that single–mode flutter occurs in the second axial mode, $m = 2$, at $\bar{U}_{ic} = 0.0311$ with no steady viscous effects, and at a slightly higher flow, $\bar{U}_{ic} = 0.0326$, when such effects are included.

More extensive results in which n was varied are shown in Table 2.8. It is seen that all modes are slightly stabilized by the inclusion of steady viscous terms, even (albeit very slightly) the $n = 1$ mode, which corresponds to beam–like motions of the shell; it is recalled that, according to beam theory applicable to thicker cylinders conveying fluid, the net effect of viscous forces is exactly zero (Païdoussis 1987). It is also seen in Table 2.8 that stability according to inviscid theory is lost in the fourth circumferential mode, $n = 4$, whilst in the third circumferential mode, $n = 3$, with the steady viscous forces taken into account; thus, the critical flow velocities depicted by Figure 2.5 for $n = 2$ are not the overall (lowest) critical ones. From Table 2.8, the overall stabilizing effect due to the viscous terms is calculated to be 15% on $\bar{U}_{ic}$.

The physical explanation for this stabilizing influence of viscous effects is the same as for clamped–clamped shells (Païdoussis, Misra and Chan 1985): the steady loads due to viscosity induce a tensile hoop stress and a tensile axial load, the latter of which is largest at $\xi = 0$ and vanishes at $\xi = 1$. Both the hoop stress and the axial tension effectively render the shell stiffer, thus raising $\bar{U}_{ic}$. However, this effect is not very pronounced, since for this shell $L/a = 11$ only; calculations for larger L/a will be presented in Section 2.5.2.3.

A final point of interest in the results of Table 2.8 is associated with the fact that the $n = 6$–8 modes lose stability by divergence according to inviscid theory, followed at slightly higher flow by restabilization and then by single–mode flutter at $\bar{U}_i = 0.03115$ for $n = 6$, and by coupled–mode flutter[3] at $\bar{U}_{ic} = 0.03895$ for $n = 7$ and at $\bar{U}_{ic} = 0.05185$ for $n = 8$.

2.5.2.2 Effect of Annular Gap

The effect of narrowing the annular gap on stability of the system was investigated by means of inviscid theory only. Although the annulus is filled with quiescent fluid, this fluid nevertheless does participate in the dynamics of the system inertially; examination of the generalized fluid forces [Equation (2.64)] on the inner shell shows that setting $\bar{U}_o = 0$ does not totally eliminate the forces associated with the annular fluid. The results for the critical flow velocity, $\bar{U}_{ic}$, corresponding to $n = 1$–9 are shown numerically

[3] In this analysis, no differentiation is made in the notation "coupled–mode flutter" between (i) cases where the two modes involved are of the same mode number (m) but one is from the right–hand plane of Ω_i (Figure 2.5) and the other from the left–hand side plane (not shown), and (ii) cases where different modes m are involved.

in Table 2.9 and graphically in Figure 2.6.

It is seen that there is a very substantial reduction in $\bar{U}_{ic}$ in every mode n as the annular gap size is diminished; a tenfold diminution in the annular gap leads to a maximum of 44% reduction in $\bar{U}_{ic}$ in the $n = 3$ mode. The physical reason for this destabilizing effect of the stagnant annular fluid is associated with the correspondingly large increase in virtual or added mass. Thus, although the stiffness of the system is not affected by the annular gap size, the increase in added mass may be thought as an *effective* reduction in stiffness, hence causing a reduction in all $\bar{U}_{ic}$, as well as in the *overall* critical flow velocity $\bar{U}_{ic}$, namely $\bar{U}_{ic}^*$. This effect is weakest for $n = 1$, as seen in Figure 2.6.

Finally, it should be pointed out that similarly to Table 2.8, some of the results in Table 2.9 correspond to loss of stability by divergence, namely those associated with n = 6–9 for the 1/10–gap system and n = 8,9 for the 1/100–gap system. In each case, flutter of the coupled–mode variety follows at higher $\bar{U}_i$; for instance, for $n = 7$ in the 1/10–gap system, divergence occurs at $\bar{U}_i = 0.03427$ and coupled–mode flutter at $\bar{U}_i = 0.03895$, in the $m = 1$ mode(s) in both cases.

2.5.2.3 Effect of Length of the Shell

The results for the overall critical flow velocity $\bar{U}_{ic}^*$ and the associated circumferential wave number n are presented in Table 2.10 and Figure 2.7 for different length–to–radius ratios of the shell, L/a; the radius a was fixed at $(10/11) \times 100\,\mathrm{mm}$ as listed in Section 2.5.1.

According to inviscid–flow theory, $\bar{U}_{ic}^*$ is diminished monotonically with increasing L/a. Furthermore, as previously found (Païdoussis and Denise 1972), the value of n associated with loss of stability becomes larger as L/a is reduced. The situation is slightly more complicated when steady viscous effects are taken into account. Firstly, as L/a is increased sufficiently, there is a stabilizing effect, with $\bar{U}_{ic}^*$ becoming slightly larger ($\bar{U}_{ic}^* = 0.02717$ for $L/a = 25$, and 0.02841 for $L/a = 30$); the physical reason for this phenomenon is that the stabilizing effect of the steady viscous forces of the internal flow, which increases with L/a due to the higher pressurization and traction effects, overcomes the destabilizing effect of increased L/a due to the inviscid forces. Here, it should be recalled that the dimensionless $\bar{U}_i$ does not involve length; thus, variations of $\bar{U}_{ic}^*$ with L/a correspond to similar variations of the critical *dimensional* flow velocities, U_{ic}^*. Secondly, the progression to higher n as L/a is decreased is not as smooth as in the case of purely inviscid flow.

Perhaps, the most important point that emerges from Table 2.10 is that the relative difference in $\bar{U}_{ic}^*$ between inviscid and viscous versions of the theory increases with L/a: for $L/a = 5$, this difference is 10% (based on the inviscid result) whereas it becomes 52% for $L/a = 30$. It is quite obvious that steady viscous effects are hardly negligible for long shells.

2.5.3 Annular Flow Alone

2.5.3.1 General Dynamics of the System

In the present case, the flow is purely annular while the fluid filling the inside of the inner shell is stagnant. Results were again obtained with both inviscid and viscous versions of the theory, so that steady viscous effects of the annular flow could be assessed.

Shown in Figure 2.8 is a typical Argand diagram for $n = 2$ of the 1/10–gap system, where "$1/k$–gap system" means that the ratio of (annular gap)$/a = 1/k$. It is seen that, according to inviscid–flow theory, the system loses stability in its second axial mode by single–mode flutter (Hopf bifurcation) at $\bar{U}_o \simeq 34 \times 10^{-3}$. The first mode is not plotted beyond $\bar{U}_o = 7 \times 10^{-3}$, but suffice to say that it remains stable. Thus, the behaviour of the system as predicted by inviscid theory is similar to the case with internal flow.

However, unlike for internal flow, steady viscous effects due to the annular flow on the stability of the system are profound. Figure 2.8 shows that the system now loses stability by divergence at a flow velocity approximately ten times smaller ($\bar{U}_{oc} \simeq 3.4 \times 10^{-3}$, $m = 1$), followed by coupled–mode flutter at a considerably higher flow velocity ($\bar{U}_{oc} \simeq 15 \times 10^{-3}$) (involving the two branches of the same mode, $m = 1$, from the left– and right–hand sides of the complex $\bar{\Omega}_i$–plane).

The results of Figure 2.8 are for $n = 2$. The values of $\bar{U}_{oc}$ for different n are shown in Table 2.11, in which the results on the far right ($\mu_i \neq 0$) of the table should be ignored for the moment. It is observed that, for $n \geq 2$, $\bar{U}_{oc}$ according to the viscous theory is one order of magnitude less than that obtained via the inviscid theory. On the other hand, for $n = 1$, $\bar{U}_{oc}$ are sensibly the same (still, the system is slightly destabilized). Both theories nevertheless predict a *local* minimum of $\bar{U}_{oc}$ at $n = 3$. With steady viscous effects taken into account, $\bar{U}_{oc}$ becomes smaller and smaller with increasing n ($n \geq 5$), at least up to $n = 8$.

Mathematically, such a steady drop in $\bar{U}_{oc}$ may be identified with the destabilizing effect of the viscous force q_{3i}, which is the dominant pressurization term [Equation (2.98)]. It is seen from Equations (2.2) and (2.3) that q_{3i} is associated with the first and second derivatives of v_i and w_i with respect to θ, thus leading to terms proportional to n and n^2; hence, the destabilizing effect of the steady viscous forces increases with n without limit. However, this result is physically unreasonable since it implies that with sufficiently large n the system is unstable for $\bar{U}_{oc} > \epsilon$, $\epsilon \to 0$. The resolution of this question is discussed in the immediately following section.

2.5.3.2 Effect of Dissipation

The key to this paradox lies in the fact that all dissipative terms, both structural and fluid unsteady viscous dissipation, have *not* been accounted for in the results presented so far. Both mechanisms are expected to give rise to increased damping as n is increased.

Because the treatment of unsteady viscous forces is beyond the scope of the present theory, it was decided to take into account all dissipative terms as if they were of the structural (hysteretic) type[4]. Accordingly, calculations have been conducted, where Young's modulus E_i in Equations (2.1)–(2.3) [in the present calculations, only the inner shell is flexible] was replaced by $E_i\left(1+\frac{\mu_i}{\Omega}\frac{\partial}{\partial t}\right)$, presuming shell motions to be oscillatory and lightly damped (Bishop and Johnson 1960); thus, this model is suitable for the prediction of the effect of dissipation at the onset of flutter, where overall damping is evanescent. On the other hand, for divergence, which is of course non-oscillatory and hence independent of damping, the results obtained for $\mu_i = 0$ should be adequate.

[4]Viscoelastic, rather than structural, damping could have been used instead.

Calculations were conducted with $\mu_i = 5 \times 10^{-3}$, 5×10^{-2} and 5×10^{-1}, where the first value would be of the right order of magnitude for steel shells if only structural damping is considered; the higher values of μ_i were considered to see what the effect of increased damping due to fluid unsteady viscous effects might be, at least qualitatively. The results for $\mu_i = 5 \times 10^{-3}$ are shown in the rightmost columns of Table 2.11, while those for $\mu_i = 5 \times 10^{-2}$ and 5×10^{-1} are plotted in Figure 2.9; the values of $\bar{U}_{oc}$ for $\mu_i = 5 \times 10^{-3}$ and 5×10^{-2} differ by less than 4% for $n \geq 2$ and less than 1% for $n \geq 5$, being larger for the larger μ_i. Interestingly, for $n = 1$ dissipation destabilizes the system, as is known to be possible for nonconservative systems (Païdoussis 1987).

With the exception of $n = 1$, it is seen from Figure 2.9 that flutter is more prevalent than when dissipative terms were neglected. Furthermore, in terms of overall stability of the system, there exists a divergence instability for low values of n, and flutter is associated with a higher but finite values of n; in these results, $n = 5$ for $\mu_i = 5 \times 10^{-3}$ and 5×10^{-2}, and $n = 4$ for $\mu_i = 5 \times 10^{-1}$.

Thus, inclusion of dissipation corrects the physically strange findings obtained without it when steady viscous effects are taken into account. It should be remarked here that, although the results calculated with $\mu_i = 5 \times 10^{-1}$ are all associated with flutter (Figure 2.9), the dissipative model for such high values is unreliable for $\bar{\Omega}_i \simeq 0$ and hence cannot predict divergence; divergence should be presumed to occur nonetheless, as obtained with $\mu_i = 0$, 5×10^{-3}, and 5×10^{-2} (at sensibly the same value of $\bar{U}_{oc}$).

In summary, the predicted dynamical behaviour with steady viscous forces taken into account is that, except for $n = 1$, the system loses stability by divergence first, followed by coupled–mode flutter at higher $\bar{U}_o$, similarly to predictions by the inviscid theory, but with the following important differences: (i) critical velocities are much smaller, (ii) the flow velocity gap between divergence and flutter is much greater, and (iii) flutter in the case of viscous theory is of the coupled–mode variety as opposed to the single–mode type.

2.5.3.3 Effect of Steady Viscous Forces on Stability

Here it should be noted that the destabilizing effect of some of the steady viscous forces on the inner shell, specifically q_{3i} as seen in Equations (2.1)–(2.3), depends not only on the circumferential wave number n as was mentioned in the foregoing discussion, but also on the gap size of the system. Thus, the trend of the magnitudes of the critical flow velocities for various n encountered in the 1/10–gap system may not necessarily be the same for systems with much wider gaps.

The influence of the annular gap size on stability of the system via the steady viscous forces may be qualitatively predicted by examining the expressions of q_{1i}, q_{2i} and q_{3i}. With the stress velocities replaced by their expressions in (2.78), (2.80) and (2.81), the constants B_i, C_i and D_i given earlier by (2.94) may be rewritten as

$$\begin{aligned} B_i &= \frac{\rho_i f_i}{8} U_i^2 + \frac{\rho_o f_{oi}}{8} \frac{r_m^2 - a^2}{a(b-a)} U_o^2, \\ C_i &= \frac{\rho_i f_i}{4a} U_i^2 - \frac{\rho_o f_{oo}}{4(b-a)} U_o^2, \\ D_i &= \frac{\rho_o f_{oo} L}{4(b-a)} U_o^2 - \frac{\rho_i f_i L}{4a} U_i^2. \end{aligned} \tag{2.135}$$

Substituting (2.93) and (2.97) into (2.98) and then making use of (2.135) leads to

$$q_{1i} = -\left(\frac{1-\nu_i^2}{E_i h_i}\right)\left\{\frac{\rho_i f_i}{8} U_i^2 + \frac{\rho_o f_{oi}}{8} \frac{r_m^2 - a^2}{a(b-a)} U_o^2\right\}(x - L), \tag{2.136}$$

$$q_{2i} = a\left(\frac{1-\nu_i^2}{E_i h_i}\right)\left\{\frac{\rho_i f_i}{8} U_i^2 + \frac{\rho_o f_{oi}}{8} \frac{r_m^2 - a^2}{a(b-a)} U_o^2\right\}, \tag{2.137}$$

$$q_{3i} = a\left(\frac{1-\nu_i^2}{E_i h_i}\right)\left\{\frac{\rho_o f_{oo}}{4(b-a)} U_o^2 - \frac{\rho_i f_i}{4a} U_i^2\right\}(x - L). \tag{2.138}$$

In the absence of the internal flow ($\bar{U}_i = 0$), it is seen from Equations (2.136)–(2.138) that

$$q_{1i} \sim \left\{\frac{r_m^2 - a^2}{a(b-a)}\right\} \bar{U}_o^2, \qquad q_{2i} \sim \left\{\frac{r_m^2 - a^2}{a(b-a)}\right\} \bar{U}_o^2, \qquad q_{3i} \sim \left\{\frac{L}{b-a}\right\} \bar{U}_o^2; \tag{2.139}$$

consequently, the associated forces as q_{1i}, q_{2i} and q_{3i} enter Equations (2.1)–(2.3) have the form

$$F_{1i}(q_{1i}) \sim \left\{\frac{r_m^2 - a^2}{a(b-a)}\right\} \bar{U}_o^2 f(n), \tag{2.140}$$

$$F_{2i}(q_{2i}) \sim \left\{\frac{r_m^2 - a^2}{a(b-a)}\right\} \bar{U}_o^2 f(n), \tag{2.141}$$

$$F_{3i}(q_{3i}) \sim \left\{\frac{L}{b-a}\right\} \bar{U}_o^2 g(n, n^2), \tag{2.142}$$

where $f(n)$, $g(n, n^2)$ denote functions of n and of n as well as n^2, respectively.

It has been pointed out (Païdoussis, Misra and Chan 1985) that q_{1i} and q_{2i} are associated with surface traction, causing axial tension in the shell, and hence can be identified as stabilizing steady viscous forces. On the other hand, q_{3i} represents the compressive loads, acting radially inward, tending to buckle the shell; therefore, they are identified as destabilizing forces. The expressions in (2.139) show that all q_{1i}, q_{2i} and q_{3i} are dependent on the gap size, $(b-a)$. However, the factor $\{(r_m^2 - a^2)/a(b-a)\} \simeq 1$ for any gap size; thus, as far as stability is concerned, q_{1i} and q_{2i} depend on $(b-a)$ only implicitly, through $\bar{U}_o^2$, since it has been found that $\bar{U}_{oc}$ becomes larger as $(b-a)$ is increased (Section 2.5.3.4). On the other hand, insofar as q_{3i} is concerned, this effect is moderated by division by $(b-a)$, as seen in the second equation of (2.139). The overall result is that for *low values of* n [where the effect of $g(n, n^2)$ does not become important], the destabilizing effect of $F_{3i}(q_{3i})$ is overwhelmingly strong for narrow-gap systems; however, it may be overtaken by the stabilizing effect of $F_{1i}(q_{1i})$ and $F_{2i}(q_{2i})$ relatively stronger in wider-gap systems[5].

Some results with $n = 1$ are shown in Table 2.12 for the 1/10- and 1/2-gap systems. As may be seen for the 1/10-gap system, the steady viscous forces have a destabilizing effect on the critical flow velocity which drops by 0.2% with $\mu_i = 0$ and by 2.4% with $\mu_i = 5 \times 10^{-3}$. On the contrary, the steady viscous forces tend to stabilize the 1/2-gap system, raising the critical flow velocity by 1.7% with $\mu_i = 0$ and by 1.5% with $\mu_i = 5 \times 10^{-3}$. In both systems, structural damping (included in the calculations) has a destabilizing effect only. The fact that the steady viscous forces can possibly stabilize

[5] This, by the way, applies equally to the stability of shells with other boundary conditions than those considered here.

a system subjected to the annular flow is an important finding of this study and has never been reported heretofore.

As a further remark to the foregoing discussion, if overall stability is lost in a sufficiently high circumferential mode, or if L and n are sufficiently large, the effect of $F_{3i}(q_{3i})$ will be dominant [as seen from Equation (2.142)] and viscous forces will *destabilize* the system; for the cases presented in Table 2.11, the destabilizing nature of steady viscous forces prevail for all $n \geq 1$.

2.5.3.4 Effect of L/a

The effect of varying L/a on stability, according to both inviscid and viscous (with $\mu_i = 5 \times 10^{-3}$) theories is shown in Figure 2.10; for the viscous theory, both the divergence and flutter boundaries are shown. As expected, the values of $\bar{U}^*_{oc}$ become progressively smaller as L/a is increased, which is reasonable on physical grounds.

The results by inviscid theory in all cases are associated with loss of stability by flutter, except those for $L/a = 20$ and 30, which are associated with divergence; nevertheless, flutter in these two cases follows at slightly higher flow (3% and 10% higher, respectively). The viscous results, on the other hand, indicate that the initial loss of stability in all cases is by divergence, followed by flutter, with an appreciable flow velocity gap between the two. In both sets of results, the circumferential mode number associated with loss of stability becomes progressively smaller as L/a becomes larger, an exception being the case of $L/a = 10$ in the inviscid results.

2.5.3.5 Effect of Annular Gap

The critical flow velocities $\bar{U}_{oc}$ predicted by inviscid theory for different n and gap sizes are shown in Figure 2.11. It is seen that, for any given n, the value of $\bar{U}_{oc}$ keeps diminishing as the gap becomes narrower. In addition, for all gap sizes of this particular system, the overall critical flow velocity $\bar{U}^*_{oc}$ is associated with $n = 6$ (and $m = 1$). For the wider gaps (1/5, 1/10), stability is lost by single-mode flutter in the n = 1–5 modes; however, for $n \geq 6$, loss of stability is by divergence, followed by restabilization and then by coupled-mode flutter in the same mode ($m = 1$) at slightly higher flows. Similarly, for the narrower gaps (1/20, 1/100), instability is found to be single-mode flutter for $n = 1$–6, or divergence followed by coupled-mode flutter for $n \geq 7$ ($m = 1$).

It is worthwhile to mention that the axial mode number m associated with each $\bar{U}_{oc}$ (though, not shown in Figure 2.11) does not generally vary systematically as n is varied, except that for $n \geq 6$ it is always $m = 1$; for example, in the 1/10-gap system, for $n = 1$–5, the axial wave number associated with $\bar{U}_{oc}$ is, respectively, $m = 4, 3, 3, 4, 3$ as seen in Table 2.11 ($\mu_i = 0$).

2.5.4 Internal and Annular Flows Together

It has been shown that each flow by itself, whether internal or annular, is capable of leading to instability of the system; nevertheless, if one of the two flows is present and the system is stable, the addition of the second flow does not necessarily bring it closer to instability, as may be seen in Figure 2.12, specifically for $n = 3$. Conversely, the addition of the second flow may render a system stable that would be unstable if one of the two flows were present alone. For instance, in a system subjected to a constant internal flow, $\bar{U}_i = 0.010$, the system becomes unstable (in this particular circumferential mode) if the annular flow is sufficiently high, namely $\bar{U}_{oc} = 0.032$. However, if $\bar{U}_i$ had been zero, the instability due to the annular flow would have occurred earlier, at $\bar{U}_{oc} = 0.025$. Hence, in this particular example, the effect of having $\bar{U}_i \neq 0$ has been stabilizing rather than destabilizing. A different effect is obtained for $\bar{U}_i = 0.030$ and $\bar{U}_o = 0$, at which point the system is unstable by virtue of internal flow alone; however, if $\bar{U}_o$ is incremented, the system is first restabilized, and then at higher $\bar{U}_o$ flutter ensues once again.

The reason for this intricate behaviour of the system in the presence of both flows together may be found in the Argand diagrams of Figures 2.5 and 2.8. It is seen that, as each of the flows is increased, the flow-induced damping, $\text{Im}(\bar{\Omega}_i) > 0$, also increases, subsequently reaching a maximum and then becoming smaller again with local non-monotonic variations, before turning negative. Thus, in general terms, there is a middle range of one flow that causes maximum stabilization when the other flow is being varied. Some of these observations are qualitatively similar to those by Hannoyer and Païdoussis (1978) for cantilevered tubular beams simultaneously subjected to internal and external axial flows, although the dynamical behaviour of the latter system was not as intricate as that of Figure 2.12 here, notably the fact that there are ranges of one flow for which stability can only be achieved provided that the other flow is neither too low nor too high.

Thus, the effect on stability of the two flows simultaneously present is not as simple as in the case of shells clamped at both ends, where the two flows acted purely additively. The difference lies in the latter system being inherently conservative, whereas the cantilevered system is inherently nonconservative (Païdoussis 1987).

The foregoing calculations were for inviscid flow. Similar results are expected to be obtained when viscous effects are taken into account, the only difference being that the system is much more sensitive to changes in the annular flow, since the transition from stability to instability occurs in a range of $\bar{U}_o$ one order of magnitude smaller than had been the case for inviscid flow. Nevertheless, the equivalent of Figure 2.12 with the viscous flow model has not been generated because of the elaborate procedure involved and the large amount of computing time required.

2.5.5 Summary

Section 2.5 has presented the results for the dynamical behaviour of the system of cantilevered coaxial cylindrical shells, with the outer "shell" being rigid while the inner one remains flexible. The system was subjected to internal flow and/or annular flow. Investigated were the effects of varying annular gap, of varying length of the shell, and of steady viscous loads on stability of the system.

It was found that, whether the system is conveying internal flow or annular flow, reducing the annular gap diminishes the critical flow velocities in all circumferential modes, n; longer shells are generally associated with smaller critical flow velocities. In the case of internal flow, steady viscous effects are stabilizing in all circumferential modes, n. Such effects become destabilizing in the case of annular flow, but only for narrow gaps; for wider gaps, however, they could be stabilizing if n is sufficiently low. As far as overall critical flow velocities are concerned, internal dissipation plays an important role in rectifying the strange finding that the critical velocity keeps on decreasing with increasing n as steady viscous effects are taken into account. When both flows are simultaneously present, the effect of one flow on the system could be stabilizing or destabilizing, depending on the current value of the other flow.

2.6 Conclusion

In Chapter 2, an analytical model was introduced to predict the dynamical behaviour of the system of cantilevered coaxial cylindrical shells subjected to internal and/or annular flow. In this model, potential–flow theory was used to formulate the unsteady fluid–dynamic forces acting on the shells, the solution of which was subsequently obtained by the Fourier transform method. Shell motions were described by Flügge's equations, modified by Païdoussis, Misra and Chan (1985) to take into account steady viscous loads that give rise to pressurization and traction effects on the shells. Due to the complexity of the boundary conditions at the free end of the shells, the equations were solved by the extended Galerkin method. Before the theory was actually applied to give theoretical results for the system under consideration, some important aspects of the theory were verified as a number of classical problems were solved and the results generated were then compared with previously obtained experimental and analytical ones.

Chapter 3

Flexible Shell in a Coaxial Conduit: Effect of System Parameters

3.1 Introduction

The aim of this chapter is to complete some important items that had not been treated in previous studies concerning the system of clamped–clamped or cantilevered coaxial cylindrical shells within the scope of the theory developed in Chapter 2. A brief review of the previous, related work is considered, which will be particularly useful in understanding what will be covered in this Chapter.

For the system of *clamped–clamped shells*, although the effect of some system parameters on the critical flow velocity associated with a specific circumferential mode of the shells has been investigated in the past by Païdoussis *et al.* (1984,1985) and El Chebair *et al.* (1989,1990), the influence of these parameters on the overall (i.e. lowest) critical flow velocity, which is in fact the most important from a practical viewpoint, has never heretofore been reported. Furthermore, it is also of interest to study the stability of the system when subjected to counter–current flows, since so far only the case of co–current flows has been undertaken.

For the system of *cantilevered shells*, results in Chapter 2 (also Païdoussis, Nguyen and Misra 1991) showed that steady viscous forces strongly destabilize the system, and the overall critical flow velocity is greatly dependent on the amount of internal damping present in the shell material, assumed to be purely hysteretic. However, only limited calculations into the effect of system parameters have been conducted; for instance, investigations into how such an important parameter as the annular width affects the stability of the system have up until now been carried out by means of inviscid theory only.

This chapter is concerned with the system of a flexible clamped–clamped or cantilevered cylindrical shell in a *rigid* coaxial conduit conveying internal and/or annular incompressible, viscous flow. Attention is first given to the influence of such system parameters as wall–thickness and length of the shell, and annular width on the overall critical flow velocity. Steady viscous effects are then examined when the system is subjected to counter–current, as opposed to co–current, flows in the case of a clamped–clamped shell and to co–current flows in the case of a cantilevered shell.

Since the theory introduced in Chapter 2 is used in the present analysis, many of the final results will be quoted or inferred from those of the previous chapter, thus avoiding the repetition of the derivations. In addition, new results will be presented, particularly those pertaining to the case of counter–current flows. It is also felt necessary to reformulate the problem and reiterate the solution procedure. Finally, the notation employed in this chapter is the same as that of Chapter 2; thus, no confusion is expected to arise.

3.2 Solution Procedure

3.2.1 Formulation of the Problem

Figure 3.1 shows the system of coaxial cylinders under consideration; it is almost identical to that considered in Chapter 2, except that, here, the outer cylinder is rigid. A portion of the inner cylinder is flexible and thin enough to be considered as a shell; at its upstream end, $x = 0$, the shell is assumed to be connected (clamped) to a semi-infinite rigid cylinder of the same inner or outer radii as the shell, for internal or annular flow, respectively; at the downstream end, $x = L$, the shell is either clamped onto another semi–infinite rigid cylinder (clamped–clamped shell) or unsupported (cantilevered shell).

Shell motions are described by Flügge's modified equations, Equations (2.1)–(2.3), which take into account the stress resultants due to steady viscous effects. These equations are subject to the end boundary conditions of the shell: (i) if the shell is clamped–clamped, the equations of motion must satisfy the boundary conditions (2.7) at both $x = 0$ *and* $x = L$; (ii) if the shell is clamped–free (cantilevered), the equations of motion must satisfy the boundary conditions (2.7) at $x = 0$ and (2.9)–(2.12) at $x = L$.

The perturbation pressures, giving rise to the unsteady radial forces acting on the shell, are formulated by means of potential–flow theory, i.e. via Bernoulli's equation for unsteady flow. The perturbation pressure p_i associated with the internal flow is determined by

$$p_i = -\rho_i \left\{ \frac{\partial \phi_i}{\partial t} + U_i \frac{\partial \phi_i}{\partial x} \right\}, \tag{3.1}$$

where the perturbation velocity potential ϕ_i is governed by the Laplace equation (2.25) subject to the impermeability boundary conditions (2.26).

Similarly, p_o associated with the annular flow is given by

$$p_o = -\rho_o \left\{ \frac{\partial \phi_o}{\partial t} + \lambda U_o \frac{\partial \phi_o}{\partial x} \right\}, \tag{3.2}$$

where ϕ_o is determined from the equation set (2.22)–(2.24), in which U_o is to be replaced by λU_o; $\lambda = 1$ if the annular fluid flows in the positive x–direction, and $\lambda = -1$ if the annular fluid flows in the negative x–direction. It is important to point out that, in the case of counter–current flows, it makes no difference whatsoever as to which of the two fluids flows in the negative x–direction if both ends of the shell are clamped. As far as the cantilevered shell system is concerned, $\lambda = 1$ is taken always for the sake of physical realism; i.e., both internal and annular flows are co–current.

3.2.2 Unsteady Radial Forces

The functional forms (2.31) and (2.33) are taken for the shell displacements and for the perturbation pressures and velocity potentials. Once Equations (2.22) and (2.25) are solved by means of the Fourier transform method, the perturbation pressures, p_i and

p_o, are determined from Equations (3.1) and (3.2), respectively. The unsteady radial force exerted on the shell is then given by $q_i = (p_i - p_o)\big|_{r=a}$.

Using the functional form (2.61) for q_i and defining the dimensionless generalized force $\bar{Q}_{kmn}$ according to (2.63) leads to the following expression, for the case of a clamped–clamped shell,

$$\begin{aligned} \bar{Q}_{kmn} &= \frac{U_i^2 \bar{C}_m}{2\pi \bar{q}_i} \int_{-\infty}^{\infty} \frac{1}{\bar{\alpha}} \left\{ \rho_i Z_{1n}(\bar{\alpha}, \varepsilon_i) \left(\frac{\bar{\Omega}}{\varepsilon_i} - \bar{U}_i \bar{\alpha} \right)^2 \right. \\ &- \left. \rho_o Z_{2n}(\bar{\alpha}, \varepsilon_i) \left(\frac{\bar{\Omega}}{\varepsilon_i} - \lambda \bar{U}_o \bar{\alpha} \right)^2 \right\} H_{km}(\bar{\alpha}) \, \mathrm{d}\bar{\alpha}, \end{aligned} \tag{3.3}$$

which may be inferred from Equation (2.64) by eliminating the terms associated with $\bar{F}_m$ (for the outer shell); in essence, $\bar{U}_o$ is replaced by $\lambda \bar{U}_o$, and $N_{km}(\bar{\alpha})$ is eliminated since no out–flow model is required for a clamped–clamped shell. Similarly, for the case of a cantilevered shell,

$$\begin{aligned} \bar{Q}_{kmn} &= \frac{U_i^2 \bar{C}_m}{2\pi \bar{q}_i} \int_{-\infty}^{\infty} \frac{1}{\bar{\alpha}} \left\{ \rho_i Z_{1n}(\bar{\alpha}, \varepsilon_i) \left(\frac{\bar{\Omega}}{\varepsilon_i} - \bar{U}_i \bar{\alpha} \right)^2 \right. \\ &- \left. \rho_o Z_{2n}(\bar{\alpha}, \varepsilon_i) \left(\frac{\bar{\Omega}}{\varepsilon_i} - \bar{U}_o \bar{\alpha} \right)^2 \right\} \{ H_{km}(\bar{\alpha}) + N_{km}(\bar{\alpha}) \} \, \mathrm{d}\bar{\alpha}. \end{aligned} \tag{3.4}$$

In Equations (3.3)–(3.4), $Z_{1n}(\bar{\alpha}, \varepsilon_i)$ and $Z_{2n}(\bar{\alpha}, \varepsilon_i)$ are defined as

$$Z_{1n}(\bar{\alpha}, \varepsilon) = \frac{I_n(\bar{\alpha}\varepsilon)}{I_n'(\bar{\alpha}\varepsilon_i)}, \qquad Z_{2n}(\bar{\alpha}, \varepsilon) = \frac{I_n'(\bar{\alpha}\varepsilon_o) K_n(\bar{\alpha}\varepsilon) - I_n(\bar{\alpha}\varepsilon) K_n'(\bar{\alpha}\varepsilon_o)}{I_n'(\bar{\alpha}\varepsilon_o) K_n'(\bar{\alpha}\varepsilon_i) - I_n'(\bar{\alpha}\varepsilon_i) K_n'(\bar{\alpha}\varepsilon_o)};$$

$H_{km}(\bar{\alpha})$ and $N_{km}(\bar{\alpha})$ were defined in (2.65) and (2.66), respectively; other dimensional and nondimensional parameters were defined in (2.55).

3.2.3 Steady Viscosity–Related Stress Resultants

The viscous nature of the fluid results in both steady (time–independent) and unsteady (time–dependent) viscosity–related loads being exerted on the shell, the latter of which is the subject of investigation of Chapter 5. The steady viscous loads have already been evaluated from the time–mean Navier–Stokes equations (Laufer 1953) for both systems of clamped–clamped shells (Païdoussis, Misra and Chan 1985) and clamped–free shells as in Chapter 2 (also Païdoussis, Nguyen and Misra 1991).

In the case of co-current flows, the steady radial and axial viscous loads on the shell are found to be [Equations (2.86) and (2.88)]

$$\bar{P}_{rIi} = \left\{\frac{2b}{b^2 - r_m^2}\rho_o U_{roo}^2 - \frac{2\rho_i}{a}U_{ri}^2\right\} x + P_i(0,a) - P_o(0,a), \tag{3.5}$$

$$\bar{P}_{xIi} = \rho_i U_{ri}^2 + \rho_o U_{roi}^2. \tag{3.6}$$

In the case of counter-current flows, which is herein considered for the system of a clamped-clamped shell only, the same procedure as in Chapter 2 is used to determine the steady viscous loads, giving

$$\bar{P}_{rIi} = -\left\{\frac{2\rho_i}{a}U_{ri}^2 + \frac{2b}{b^2 - r_m^2}\rho_o U_{roo}^2\right\} x + \left(\frac{2b}{b^2 - r_m^2}\right)\rho_o U_{roo}^2 L + P_i(0,a) - P_o(L,a), \tag{3.7}$$

$$P_{xIi} = \rho_i U_{ri}^2 - \rho_o U_{roi}^2, \tag{3.8}$$

where $P_o(L,a)$ is the entrance pressure of the annular flow. The minus sign in Equation (3.8) stems from the fact that the annular flow shears the shell in the negative x-direction.

The determination of the differential pressures $\Delta P = P_i(0,a) - P_o(0,a)$ in Equation (3.5) and $\Delta P = P_i(0,a) - P_o(L,a)$ in Equation (3.7) requires that the static pressures of both flows at either end of the shell be known. In the case of a cantilevered shell, where the inner and annular fluids flow co-currently and merge into each other at the free end of the shell, the exit pressures of the two flows are essentially the same. In the case of a clamped-clamped shell, where the two flows can be either co-current or counter-current and are separated throughout, it is assumed that the exit pressures of the flows are also equal. This assumption by no means changes the nature of the system; the only advantage resulting thereby is that the radial differential pressure $\bar{P}_{rIi}$ depends only on the pressure drops of the two flows along the shell. For both types of flows, the foregoing reasoning effectively leads to

$$\Delta P = \frac{2\rho_i}{a}U_{ri}^2 L - \frac{2b}{b^2 - r_m^2}\rho_o U_{roo}^2 L. \tag{3.9}$$

3.2.4 Extended Galerkin Method

In the case of a cantilevered shell, the *extended* Galerkin method is required to solve the governing equations of motion subject to the free-end boundary conditions, since functional forms of the shell displacements satisfying simultaneously these two sets of equations are not known to exist. For the present system, with only the inner shell being flexible, the method is expressed by the first equation of (2.104). In the absence of the free-end boundary conditions, as is the case of a clamped-clamped shell, the extended Galerkin method gives the same results as does the usual form of Galerkin's method (Païdoussis *et al.* 1984,1985). Interested readers should consult Section 2.3.4.

3.3 Theoretical Results

3.3.1 Introduction

Section 3.3 presents the results concerning the effect of varying length L, shell wall thickness h_i, and annular gap $(b-a)$ on the stability of both clamped-clamped and cantilevered shell systems. In most cases to be considered, the internal fluid is stagnant ($\bar{U}_i = 0$). The analysis also covers the stability of a clamped-clamped shell subjected to counter-current flows and that of a cantilevered shell conveying co-current flows.

Calculations were conducted with the series in Equation (2.31) truncated at $m = 3$ for the case of a clamped-clamped shell (as was the case in Païdoussis, Chan and Misra 1984) and $m = 6$ for the case of a cantilevered shell (as was the case in Chapter 2). For convenience, the material properties (steel shells and water as the working fluid) and the geometric dimensions of the cylinders are the same as had been taken in previous studies (Païdoussis *et al.* 1984,1985). In addition, the shells were considered to be subject to internal dissipation which could be approximated by a hysteretic model as was used in Chapter 2. However, here, an equivalent viscoelastic model[1] will be utilized instead, whereby E_i, appearing through γ_i in Equations (2.1)–(2.3), is replaced by $E_i\left(1+\chi_i\frac{\partial}{\partial t}\right)$ with χ_i determined from μ_i for each Ω. Thus, calculations were performed with the following set of parameters:

$$E_i = 2.0\times10^{11}\,\mathrm{N/m^2},\ \ \nu_i = 0.3,\ \ \rho_{si} = 7.8\times10^3\,\mathrm{kg/m^3},\ \ \mu_i = 5\times10^{-3},\ \ \chi_i = \frac{\mu_i}{\Omega},$$

[1]It is worthwhile to point out that this model has the advantage, over the hysteretic one, that it does not increase the stiffness of the system and does not destroy the self-adjoint character of the problem.

$$a = \frac{1}{11}\,\mathrm{m}, \quad b = \frac{1}{10}\,\mathrm{m}, \quad h_i = 0.5 \times 10^{-3}\,\mathrm{m}, \quad L = 1.0\,\mathrm{m}, \quad \rho_i = \rho_o = 10^3\,\mathrm{kg/m^3};$$

in studying the effect of system parameters, a was held fixed, while b, h_i or L could be varied.

The system of a clamped–clamped shell will be considered first, followed by the system of a cantilevered shell. However, before any results are presented, one important remark, similar to that already given in Section 2.5.1, should be made here. Since the theory is linear, the results generated are expected to be physically correct only for sufficiently small–amplitude perturbations; hence, the intricate behaviour of the system beyond the first loss of stability as predicted by the present theory may not be reliable.

3.3.2 Stability of the System of a Clamped–Clamped Shell

3.3.2.1 Effect of Shell Length

Shown in Figure 3.2 are the results for $\bar{U}^*_{oc}$ as a function of the ratio L/a in a $\frac{1}{10}$–gap system [i.e., $(b-a)/a = 1/10$]. It should be reiterated here that $\bar{U}^*_{oc}$ denotes the overall (lowest) critical flow velocity, whereas $\bar{U}_{oc}$ refers to the critical flow velocity associated with some particular n. Two variants of the theory have been used to calculate $\bar{U}^*_{oc}$; in the inviscid variant, the fluid is assumed to be purely inviscid while, in the viscous variant, steady viscous effects of the flow(s) are taken into account.

The values of $\bar{U}^*_{oc}$ predicted by the viscous variant of the theory is of the order of three to six times smaller than that by the inviscid counterpart as L/a is varied from 5 to 20. This destabilizing effect of the steady viscous forces with increasing L/a is not surprising since, as was already pointed out in Chapter 2 (Section 2.5.3.3), the destabilizing effect of the crushing compressive load q_3 appearing in Equations (2.1)–(2.3) is in fact proportional to L; thus, these results quantify the influence of L/a on stability.

In general, as L/a is increased, $\bar{U}^*_{oc}$ decreases and so does the circumferential mode associated with $\bar{U}^*_{oc}$. Consequently, if L is large enough, the shell will eventually lose its stability by divergence in the $n = 1$ (beam) mode. This observation is similar to that made earlier by Païdoussis and Denise (1972) for the system of an unconfined clamped–clamped shell conveying internal flow.

3.3.2.2 Effect of Shell Thickness

The variation of $\bar{U}^*_{oc}$ with shell thickness, expressed nondimensionally as h_i/a, is plotted in Figure 3.3. Again, the steady viscous forces have a destabilizing effect on the system. As may be seen from the figure, $\bar{U}^*_{oc}$ increases with h_i/a, whereas the circumferential mode n associated with $\bar{U}^*_{oc}$ decreases. The effect of h_i/a on $\bar{U}^*_{oc}$ and n may be understood by considering the strain energies resulting from circumferential bending and stretching of the shell.

For shells with both ends supported, if the strain energies are plotted against the circumferential wave number n, it will be observed that the bending energy $\mathcal{E}_b$ increases with n while the stretching energy $\mathcal{E}_s$ varies in the reverse manner, resulting in a curve for the total strain energy $\mathcal{E}_t$ (i.e. $\mathcal{E}_t = \mathcal{E}_b + \mathcal{E}_s$) of quasi–parabolic form (Arnold and Warburton 1949). The approximate value of n at which $\mathcal{E}_t$ is minimum may be determined when $\mathcal{E}_b = \mathcal{E}_t$. Considering an element of the shell, so small as to be approximated as a plate of thickness h_i, it has been shown (Timoshenko and Woinowsky–Krieger 1959) that for such a plate $\mathcal{E}_b$ is proportional to h_i^3 while $\mathcal{E}_s$ is proportional to h_i. The *notional* relationships between $\mathcal{E}_b$, $\mathcal{E}_s$ and h_i are thus

$$\mathcal{E}_b = C_b n h_i^3, \qquad \mathcal{E}_s = \frac{C_s}{n} h_i,$$

where C_b and C_s are some proportionality constants. Hence, equating $\mathcal{E}_b = \mathcal{E}_t$ leads to

$$n^2 = \frac{C_s}{C_b h_i^2},$$

which implies that, as far as $(\mathcal{E}_t)_{\min}$ is concerned, n decreases with increasing h_i.

On the other hand, the energy $\mathcal{E}_f$ required to overcome $\mathcal{E}_t$, and hence to collapse the shell, comes from the centrifugal fluid–dynamic force, which is known to be proportional to U^2 according to inviscid theory. Implicitly, $\mathcal{E}_f$ is also proportional to U^2,

$$\mathcal{E}_f = U^2 f(n),$$

where $f(n)$ is some function of the circumferential wave number n. It is apparent that the system loses stability when

$$\mathcal{E}_t - \mathcal{E}_f = \mathcal{E}_t - U^2 f(n) = 0,$$

which implies that $\bar{U}^*_{oc}$ will become higher if there is an increase in $(\mathcal{E}_t)_{\min}$ due to increasing h_i.

3.3.2.3 Effect of Annular Gap

Figure 3.4 shows how $\bar{U}^*_{oc}$ varies with the annular gap, expressed in the dimensionless form $(b-a)/a$. As might be expected, for both cases of inviscid and viscous flows, the system becomes unstable at lower flow velocities as the annular gap gets narrower. This phenomenon has been well explained in the previous studies.

Firstly, the reduction in the annular gap results in a corresponding increase in the virtual or added mass of the annular fluid; the increase in the added mass is associated with higher fluid dynamic forces and hence causes an effective reduction in the stiffness of the shell and a diminution of $\bar{U}^*_{oc}$. Secondly, in the case of a viscous fluid, a higher upstream pressure is required to push the fluid through a narrower annular gap, thus resulting in a larger pressure drop along the shell and a stronger destabilizing effect due to pressurization. Once again, however, these effects are here quantified explicitly, and the effect on the *overall* stability is given. Another observation from Figure 3.4 is that, for the range of gap sizes considered, the circumferential mode n associated with $\bar{U}^*_{oc}$ remains unchanged, at least for the parameters being studied.

It should be reiterated here that the results presented in Figures 3.2–3.4 were obtained for a system with annular flow and a stagnant inner fluid ($\bar{U}_i = 0$).

3.3.2.4 System with Counter–Current Flows

Figure 3.5 compares the results for $\bar{U}_{oc}$ as a function of n, obtained with the viscous variant of the theory for two types of flows: co- and counter–current flows. In both cases, the internal flow velocity was constant and taken to be $\bar{U}_i = 0.010$. It may be seen from this figure that the system subjected to counter–current flows loses stability at slightly lower flow velocities than when subjected to co–current flows. The difference between the two types of flows in terms of $\bar{U}_{oc}$ ranges from virtually 0% (with respect to $\bar{U}_{oc}$ for co–current flows) at $n = 1$ to a maximum of 11.6% at $n = 5$. As far as the overall critical flow velocity $\bar{U}^*_{oc}$ is concerned, which happens to be associated with $n = 4$, the difference is 8.3%.

The above results are specific to the value of L/a and of other geometrical parameters chosen for the calculations, and also to the assumption made earlier that the exit pressures of the two flows are equal. Under *these conditions*, it was found that, in the case of co–current flows, the static pressure of the annular flow is higher than that of the inner flow; consequently, the entire shell is subjected to a radially–inward compressive load, decreasing linearly from some certain value at $x = 0$ to zero at $x = L$. In the case of counter–current flows, about two–thirds of the shell from the downstream end ($x = L$) are under circumferential compression, and the last one–third is under circumferential tension because the entrance pressure of the inner flow is higher than the exit pressure of the annular flow. The maximum value of the compressive load in the latter case is about 1.5 times that in the former case; this may explain the reductions in $\bar{U}_{oc}$ for the range of n considered, despite the fact that a small portion of the shell is under tension.

3.3.3 Stability of the System of a Cantilevered Shell

3.3.3.1 System with Co–Current Flows

Figure 3.6 presents the results obtained for $\bar{U}_{oc}$ as a function of n for two cases of flows, $\bar{U}_i = 0$ and $\bar{U}_i = \bar{U}_o$, for which only the viscous variant of the theory was used. In all circumferential modes considered, except $n = 1$, flutter of coupled-mode type (solid curves) is preceded by divergence (broken curves, essentially coincident) at a much lower flow velocity.

As far as the first loss of stability (divergence) is concerned, the system becomes unstable at a slightly higher flow velocity when $\bar{U}_i = \bar{U}_o$ ($\bar{U}^*_{oc} = 0.00331$, $n = 4$) than when $\bar{U}_i = 0$ ($\bar{U}^*_{oc} = 0.00321$, $n = 4$), although in the scale of the figure the two broken curves are essentially coincident. The stabilizing effect as a result of $\bar{U}_i = \bar{U}_o$ may be attributed to the fact that the steady viscous forces due to the internal flow increase the axial tension in the shell and reduce the compressive hoop stress in the shell wall caused by the annular flow, thus resulting in an increase in the stiffness of the shell, thereby stabilizing the system. Furthermore, the inviscid results obtained in Section 2.5.4 [or by Païdoussis, Nguyen and Misra (1991)] also showed a similar effect when $\bar{U}_i = \bar{U}_o$. There is no doubt that the presence of internal flow in the present case would give rise to an increase in $\bar{U}^*_{oc}$, albeit small. It may be expected that a stronger stabilizing effect would have resulted if $\bar{U}_i$ had been taken to be larger, say $\bar{U}_i > \bar{U}_o$ (provided, of course, $\bar{U}_i$ remained smaller than the critical value for instability by the internal flow alone).

Another observation from Figure 3.6 that should be touched upon here is that the internal flow has a post–divergence destabilizing effect on the system. Nevertheless, as has been mentioned earlier, any predictions beyond first loss of stability by the present linear theory are questionable, in the sense that they may not occur in reality; hence, physical explanations for such post–divergence behaviour of the system may not be too meaningful and are not attempted. Still, the results in Figure 3.6 nevertheless *are* of academic interest and are therefore presented (here and in subsequent figures of Chapter 3).

3.3.3.2 Effects of Shell Thickness, Length, and Annular Width

Figure 3.7 shows the results for $\bar{U}^*_{oc}$ as a function of the shell thickness h_i/a for two different lengths of the shell, $L/a = 5$ and $L/a = 10$. Although the type of instability is flutter preceded by divergence, the stability of the system is affected by the parameters pretty much in the same way as in the case of clamped–clamped shells considered earlier. In other words, $\bar{U}^*_{oc}$ increases and the circumferential mode n associated with $\bar{U}^*_{oc}$ decreases with increasing h_i/a; furthermore, for a given thickness of the shell, both $\bar{U}^*_{oc}$ and its associated n decrease as L/a goes up.

Figure 3.8 is similar to Figure 3.7 in the sense that it shows the variation of $\bar{U}^*_{oc}$ with h_i/a, but now for two different annular widths. Again, similarly to what was observed for the system of a clamped–clamped shell, the smaller the annular width, the lower the overall critical flow velocity $\bar{U}^*_{oc}$; in addition, the circumferential mode n

associated with $\bar{U}_{oc}^*$ remains almost unchanged as the annular width is varied. It may be worth reiterating once more that the results presented in Figures 3.7 and 3.8 (unlike some in Figure 3.6) were obtained for the system with annular flow and a stagnant inner fluid.

3.3.4 Summary

Section 3.3 has presented the results concerning the effect of length and wall–thickness of the shell and annular width on the stability of both clamped–clamped and cantilevered shell systems. Further investigation was made on the steady viscous effects when the clamped–clamped shell system is subjected to co– and counter–current flows, or when the cantilevered shell system is subjected to co–current flows.

It was found that the overall critical flow velocity is diminished when (i) the length of the shell is increased, or (ii) the annular gap or the shell wall thickness is reduced. Due to steady viscous forces, (i) the system of a clamped–clamped shell when conveying counter–current flows loses stability earlier than when conveying co–current flows, and (ii) the system of a cantilevered shell subjected to co–current flows becomes stabilized more with larger $\bar{U}_i$.

3.4 Conclusion

In Chapter 3, the theory in Chapter 2 was used to investigate some important aspects concerning the stability of a flexible cylindrical shell within a rigid coaxial conduit. Some new results of the unsteady fluid forces and of the steady viscous loads on the shell were also presented for the case of counter–current flows. This chapter covered the effect of wall–thickness and length of the shell, and of annular width on the stability of the clamped–clamped or cantilevered shell system. Finally, steady viscous effects were studied when the clamped–clamped shell system was subjected to counter–current flows and when the cantilevered shell system was subjected to co–current flows.

Chapter 4

Experimental Verification

4.1 Introduction

There is little doubt that experimental verification is desirable in the development of any new analytical model. The goal of the present experimental work was to validate—to the fullest possible extent—(i) the theory presented in Chapter 2, and (ii) a new theory to be developed in Chapter 5, for the study of instabilities of cantilevered coaxial cylindrical shells subjected to internal and/or annular incompressible viscous flow.

In the tests conducted, measurements were made of the critical flow velocity of a cantilevered cylindrical flexible shell, confined within a concentric rigid cylinder and subjected to *either* internal flow *or* annular flow. In certain selected cases, frequencies of oscillation of the shell were also recorded for various flow velocities.

This chapter is devoted to (i) describing the apparatus used in the tests, (ii) explaining the testing procedure, and (iii) comparing experimental results with their analytical counterparts obtained with the theory in Chapter 2.

4.2 Description of the Apparatus and Procedure

4.2.1 Apparatus

Figure 4.1 shows a schematic vertical cross section of the experimental setup for the tests involving *annular flow.* In the upper half of the setup (above the horizontal surface marked "table"), a cylindrical shell made of silicone rubber is positioned coaxially within a bigger cylinder made of transparent plexiglas; the free end of the shell is at least 19 mm (3/4 inches) lower than that of the outer cylinder. The lower half consists mainly of an axisymmetric hollow body with contracting sections near its top and bottom. Mounted inside this body are a honeycomb and three screens, the role of all of which is to break up large turbulent eddies and enhance mixing (hence uniformity) of the air flow that comes in from a reservoir, pressurized and maintained by an air compressor(s). The air flow, leaving the hollow body and entering the annular region, is further rendered uniform and straight by a long solid cylinder with an ogival, streamlined lower end. The annular region is ultimately bounded by the rubber shell and the plexiglas cylinder; plexiglas cylinders of different inner radii give different widths of the annular gap. For convenience, the same notation as was used in Chapter 2 (or Figure 2.1) is adopted here. Shells and cylinders associated with annular flow had the following dimensions:

$$h_i = 1.37\,\text{mm},\quad a = 24.84\,\text{mm},\quad b = 28.02\,\text{mm (1/10–gap)},$$
$$b = 32.63\,\text{mm (1/4–gap)},\quad b = 38.1\,\text{mm (1/2–gap)},$$

where the g/a–gap refers to the experimental setup with $g/a = [b - (a + h_i/2)]/a$. The value of g/a in the term "g/a–gap" is based on the *designed* width of the gap. However, the actual values of g/a, which are determined from the test measurements and will be used in all theoretical calculations, may be somewhat different: 0.100 for the 1/10–gap, 0.286 for the 1/4–gap, and 0.506 for the 1/2–gap.

Figure 4.2 is the setup for the tests involving *internal flow*. It is very similar to the setup for annular flow, the only difference being that an adaptor of gradually decreasing inner radius is used to guide smoothly the air flow from the hollow body into the shell. In the case of internal flow, only one annular gap (filled with quiescent fluid) was considered with the following dimensions:

$$h_i = 1.37\,\text{mm},\quad a = 24.79\,\text{mm},\quad b = 63.35\,\text{mm (3/2–gap)}.$$

The above–mentioned rubber shells were cast in a special mould. Liquid Silastic E–RTV silicone rubber was first mixed with a catalyst, called "curing agent", and then injected into the mould. Such a mixture remained workable for 2 hours and reached full physical strength in about 72 hours. The material properties of the rubber were determined from measurements of the first-mode frequency of oscillation and logarithmic decrements for a vertically hanging cantilever (solid rubber tube cast from the same batch of silicone rubber as the shells) at various lengths (Païdoussis and des Trois Maisons 1969). For the particular batch of silicone rubber used in the present study, it was found that

$$E_i = 2.8246 \times 10^5\,\mathrm{N/m^2},\ \rho_{si} = 1158.8\,\mathrm{kg/m^3},\ \nu_i = 0.47,\ \mu_i = 0.01948.$$

Here, it is recalled that E_i is Young's modulus; ρ_{si} is the density; ν_i is Poison's ratio, and μ_i is the hysteretic damping coefficient.

4.2.2 Measuring Instruments

The flow velocity in the annulus or within the shell was determined from the flow rate measured by a rotameter (tapered–tube–and–float type) for low flows, or by an orifice plate for high flows. Both devices were located upstream of the apparatus. With the rotameter, the readings taken were *air temperature*, *outlet pressure* of the rotameter, and *percentage* of the calibrated flow rate under prescribed conditions; the flow rate was then calculated according to the manufacturer's instructions. With the orifice, the readings of *air temperature*, *inlet pressure* and *differential head* (pressure drop) across the orifice were recorded; the ASME–recommended procedure (for instance, Bean 1971) was then employed to calculate the flow rate. Orifice plates having holes of various sizes were available to accommodate a wide range of flow rates.

To detect small–amplitude vibrations of the shell induced by the flow, two fibre–optic sensors (MTI KD–100 "Fotonic" sensors) were mounted 90° azimuthally apart and 25 mm (1 inch) above the clamped end of the shell. The side and top views of such a setup are shown in the photographs of Figure 4.3. The signals produced by these sensors were fed into and processed by a dual–channel Hewlett–Packard 5420A Digital Signal Analyzer, which appears as three separate decks in the left half of the photograph labelled Figure 4.4. The two U–tubes (grey and red) near the centre of this photograph are manometers of different sensitivities, giving different ranges of differential heads across the orifice. Cross Spectral Densities (CSDs), generated by the analyzer, revealed the dominant frequencies of the shell excited by the flow. The corresponding phase plots, showing the phase differences of the shell displacements monitored by the two sensors, helped (to a certain extent) identify the modes associated with such frequencies. The onset of instability of the shell was assessed visually.

4.2.3 Testing Procedure

Tests, involving either annular or internal flow, were all conducted with great care and with the same preparatory steps. The testing procedure to be sequentially described below applies to annular flow. Variations, if any, for experiments with internal flow will be pointed out later.

1. First of all, the critical flow velocity was obtained for the rubber shell with length–to–radius ratio L/a ($5 \leq L/a \leq 8$). The experiment was repeated at least 6 (and at most 16) times, so that as many values of the critical flow velocity were taken, and hence the average value and the uncertainty involved could be calculated.

2. The fibre–optic sensors were then set up and calibrated in such a way that the vibration signals given by these sensors were in the linear range.

3. The flow velocity was incremented up to (but *not* including) the critical limit obtained in Step 1, to avoid damage to the fibre–optic sensors. For each new flow velocity, a CSD was obtained after averaging 30 time records to eliminate noise. Step 3 was repeated at least once.

4. Steps 1–3 were carried out for $g/a = 1/10$ and $g/a = 1/4$ by using the appropriate plexiglas cylinders. For $g/a = 1/2$, only Step 1 was conducted while Steps 2 and 3 were skipped due to the difficulty in maintaining steady flow; it should be noted that tests with $g/a = 1/2$ involved very high flows, and the pressure(s) of the air reservoir was not high enough to keep such high flows steady or quasi–steady for a long period of time.

5. Steps 1–4 were repeated as the length of the shell was gradually reduced from $L/a = 8$ to $L/a = 6$ in steps of approximately 0.5. Step 1 continued to be repeated as L/a was further reduced from 6 to 5.

6. To ensure the repetition of the above–recorded results, Steps 1–5 were repeated with another nominally identical shell.

For experiments with internal flow, the same procedure was followed, except that Step 4 was skipped since only one annular gap was considered ($g/a = 1.5$); nevertheless, the effect of quiescent annular fluid on the critical flow velocity was also investigated.

4.3 Experimental Results—Annular Flow

4.3.1 Observations

In general, instabilities are associated with very large displacements of the the shell(s). Both types of instabilities—divergence and flutter—were encountered in certain tests involving annular flow, but flutter occurred in all the tests conducted. With $g/a = 1/10$, divergence and flutter were both observed, but only for $L/a = 8$ which was the length of any newly moulded shell. At such a length, when the flow velocity was sufficiently high, the free–end cross section of the shell became oval and remained stationary, signalling divergence in the second circumferential mode ($n = 2$). As the flow velocity was further increased, the oval cross section started oscillating with its major and minor axes exchanging their places; this is flutter with $n = 2$, and a photograph of the cross section in motion is shown in Figure 4.5. In one test run with the first nominal shell, divergence was observed at the flow velocity of 24.08 m/s, and flutter at 25.35 m/s. For $L/a \leq 7.5$ (the shell was shortened by $\Delta(L/a) = 0.5$ each time), divergence was hardly noticeable before the shell fluttered.

With $g/a = 1/4$ and $1/2$, only flutter was observed but it was short–lived. When the flow velocity was large enough, the cross section of the shell became oval and then oscillated for about 3 cycles; subsequently, the cross section became flattened by the flow—the inner surface of the shell near the free end touched the opposite side (i.e., the shell became closed at the top). After that, the shell started flapping violently against the inner wall of the plexiglas c linder.

It is worthwhile to reiterate here that instabilities discussed so far were associated with $n = 2$. Flutter with $n = 3$ also took place; however, it was observed only once when the first nominal shell was tested with $g/a = 1/10$ and $L/a = 5.5$.

4.3.2 Frequencies of Oscillation

Figure 4.6 shows a typical cross spectral density (CSD) and its corresponding phase plot, for which $g/a = 1/4$, $L/a = 8$, and $U_o = 33.0\,\mathrm{m/s}$. The dominant frequencies, given by the abscissae of the peaks of the three "mountains" in the CSD, and their associated phase angles are (13.3 Hz,−136.6°), (21.1 Hz,−177.9°), and (49.6 Hz,−178.1°). Such peaks are identified by the centres of the three broken circles as seen in Figure 4.6(a); their relative heights indicate that the second peak, which corresponds to 21.1 Hz, represents the *most* dominant frequency. For the reasons to be discussed in the coming footnote, (33.0 m/s,13.3 Hz) is plotted in Figure 4.8(a), while (33.0 m/s,21.1 Hz) and (33.0 m/s,49.6 Hz) are plotted in Figure 4.8(b).

The analytical results (by the theory in Chapter 2) and the measured dominant frequencies[1] (from the CSDs) are presented in Figures 4.7 and 4.8 for $g/a = 1/10$ and

[1] The way these measurements were plotted in Figures 4.7 and 4.8 was based on a number of important observations, which will be discussed below using the case of $g/a = 1/4$ as an example.

Firstly, preliminary calculations presented earlier in Chapter 2 (Section 2.4.2) showed that predicted frequencies of a cantilevered shell *in vacuo* were very close to test measurements by Gill (1972). Moreover, theoretical results as well as experimental data obtained herein showed that frequencies of the shell (subjected to annular flow) in all modes varied very slowly with flow velocity. From these two observations, it can be inferred that a data point (11.5 m/s,10.9 Hz) with a phase angle of approximately 180°, for instance, should be put in Figure 4.8(a) ($n = 1$) rather than Figure 4.8(b) ($n = 2$), in which the lowest frequency ($m = 1$) corresponding to $U_o = 12\,\mathrm{m/s}$ is of the order of 16 Hz. For data points with their frequencies ranging from about 20 Hz to 26 Hz, there was no difficulty in deciding that such points should be plotted in Figure 4.8(b) since (i) they are closest to the frequency curve associated with $n = 2$ and $m = 2$, and (ii) they are too far away from any other curve associated with either $n \neq 2$ or $m \neq 2$.

Secondly, due to the fact that the two fotonic sensors were positioned 90° azimuthally apart, the phase angle corresponding to a frequency excited in $n = 1$ or $n = 3$ could vary from 0° to 180° (after time-record averaging), depending on where the sensors happened to be relative to the oscillating cross section of the shell (Figure 4.9); for $n = 2$, the phase angle is always 180°, at least in principle. As can be seen from Figure 4.8, not only are the ($n = 2, m = 3$) and ($n = 3, m = 3$) frequency curves nearly coincident, they are also equally close to the data points having their frequencies between 47 Hz and 52 Hz. Thus, such points may be put in either Figure 4.8(b) or Figure 4.8(c). All the points (11.5 Hz to 52 Hz) plotted in Figure 4.8(b) are associated with phase angles of the order of 180°; of course, some of them,

$g/a = 1/4$, respectively. In both cases, $L/a = 8$ and the experimental results were obtained for flow velocities ranging from the smallest *measurable* value up to (but *not* including) the critical one. As seen from the figures, the agreement between theory and experiment is generally good—even excellent for $n = 2$.

In the case of $g/a = 1/10$, *only* the second circumferential mode ($n = 2$) was excited; as an illustration, Figure 4.7(a) gives the analytical results for $n = 1$ without experimental counterparts. For $n = 2$, the measured frequencies decrease slightly with flow velocity and are seen to be associated with the lowest three axial modes ($m = 1$–3). With $g/a = 1/4$, all three lowest circumferential modes ($n = 1$–3) were excited, with $n = 2$ being the main one, since the dominant frequencies in this mode appeared in all the CSDs recorded. Here, too, the frequencies of $n = 2$, and of $n = 3$, vary the same way as those in the case of $g/a = 1/10$ ($n = 2$). What is different here is the slight increase in the measured frequency of $n = 1$, followed by a relatively quick drop when the flow velocity is near the critical value (41.4 m/s).

In general, reductions in the frequencies associated with $n = 2$ can be attributed to the flow pressurization that tends to compress the shell, thereby reducing the *effective* stiffness of the system. On the other hand, increases in the $n = 1$ frequencies are likely due to the axial tension in the shell resulting from the shearing forces exerted by the annular flow on the (outer) shell surface.

A close look at all the CSDs of $g/a = 1/4$ (not shown here) indicates that the frequencies of $n = 1$ were most dominant for $U_o \leq 22.3$ m/s; they then subsided, while those of $n = 2$ became stronger as U_o was increased further; the latter were found to be most dominant when $U_o \geq 25.5$ m/s. Consequently, the dominant mode, as the

particularly those between 47 Hz and 52 Hz, could have been in Figure 4.8(c), while the ones presently appearing in this figure have their phase angles much less than 180°. On the other hand, although the point (33.0 m/s, 13.3 Hz) and those in its neighbourhood are closer to the ($n = 2, m = 1$) curve than the ($n = 1, m = 1$) curve, they are plotted in Figure 4.8(a), instead of Figure 4.8(b), because their phase angles are of the order of 130°.

As a final note, for $g/a = 1/4$ and $L/a \leq 8$, the lowest predicted frequencies associated with $n \geq 4$ for any subcritical flow velocity were greater than 80 Hz, and no frequencies of such a magnitude or greater were found in any of the CSDs recorded. These findings imply that frequencies in $n \geq 4$ were *never* excited to a sufficiently sizable amplitude by the flow for the above-mentioned values of g/a and L/a; consequently, this casts some doubt on the experimental results—frequencies and critical flow velocities associated with $n = 4$—reported previously by El Chebair *et al.* (1989) for a similar clamped-free shell.

flow velocity approaches the critical value, is also the one in which the shell becomes unstable. A *similar* pattern was also found in the CSDs of $g/a = 1/10$, where the dominant frequencies were associated $m = 1$ at low flows and with $m = 2$ at higher flows (these frequencies were associated with the same $n = 2$ mode).

4.3.3 Effects of L/a and g/a

The results for the *overall* critical flow velocity U^*_{oc} as a function of L/a are shown in Figure 4.10(a) for $g/a = 1/10$, in Figure 4.10(b) for $g/a = 1/4$, and in Figure 4.10(c) for $g/a = 1/2$. In these figures, pairs of small black circles plotted for certain values of L/a represent measurements obtained from two nominally identical shells.

Qualitatively, theory and experiment agree very well in terms of (i) the critical circumferential mode n associated with U^*_{oc} (here, $n = 2$) and (ii) variations of U^*_{oc} with L/a and g/a; U^*_{oc} generally becomes larger as L/a is reduced or g/a is increased. Quantitatively, the degree of agreement varies not only with L/a, but also with g/a:

- In Figure 4.10(a), for which $g/a = 1/10$, there is very good agreement between theory and experiment for $L/a \geq 6.5$; the discrepancy (based on the larger test value) at $L/a = 6.5$ is calculated to be 11.7%. For $L/a < 6.5$, measurements for U^*_{oc} start to level off, hence widening the gap between theory and experiment. This could be attributed to imperfections of the apparatus used; specifically, the shell and the cylinder were not perfectly concentric. Thus, for a narrow annular passage as in the present case, even a small non–alignment of the two axes could result in relatively considerable non–uniformity of the annular region.

- In Figure 4.10(b), for which $g/a = 1/4$, good agreement is also found between theory and experiment. As seen from the figure, the velocity gap between the solid curve and the data points plotted is rather uniform; nevertheless, in terms of percentage, the difference calculated varies from 25.4% at $L/a = 8$ to 12.1% at $L/a = 5$.

- Of the three, Figure 4.10(c) with $g/a = 1/2$ shows the best agreement between theory and experiment; the discrepancy is of the order of 4% for $L/a \leq 7$. It becomes larger for $L/a > 7$; however, unlike the case of $g/a = 1/10$, the wider velocity gap between the results for such a range of L/a seems to be due to some peculiarity (to be explained next) in the theoretical results.

It is seen from Figure 4.10 that each of the solid curves plotted exhibits a "bump", which seems to grow more pronounced with g/a; it signals a switch from the divergence– to flutter–type instability as L/a is further reduced. The type of instability predicted by different parts of the curves is indicated either by a "D" for divergence, or by an "F" for (single-mode) flutter, as shown in the figure. In general, theoretical predictions for U^*_{oc} are all higher than their experimental counterparts. In addition to the above-stated reasons, discrepancies between theory and experiment may also be due to the fact that unsteady viscous effects have been ignored by the theory in Chapter 2; they are treated in Chapter 5, and then further comparison will be presented.

4.4 Experimental Results—Internal Flow

4.4.1 Observations

There were certain similarities and differences between clamped–free systems subjected to annular flow and those subjected to internal flow regarding their dynamical behaviour. In the case of internal flow, the only type of instability observed was flutter, which was always associated with $n = 2$. Flutter was found to be quite violent and remained so even if the flow was slightly reduced. It might be of interest to mention that the first shell tested for instability was torn apart because of the intensity of the flutter and high stresses in the shell. Once flutter had occurred, the free–end cross section of the shell became oval to such an extent that one side of the inner wall of the shell touched the opposite one; the cross section *appeared* to have the shape of two bows with their main axes of symmetry being perpendicular to each other.

Although only one annular gap was considered in the case of internal flow, the effect of the quiescent annular fluid (air) on the stability of the shell could easily be examined quantitatively by removing the plexiglas cylinder, thus making $g/a \to \infty$.

Table 4.1 shows experimental results of the critical flow velocity U_{ic}^{*} *with* and *without* the plexiglas cylinder installed; these results were obtained from tests on one shell. For three different lengths of the shell tested, there were hardly any changes in U_{ic}^{*} as g/a was increased from 1.5 to ∞. Indeed, this observation was expected; it may be accounted for by two main factors. Firstly, the air density is relatively low, and hence the corresponding inertial effect is also small. Secondly, the inertial effect of the annular fluid changes dramatically with g/a *only* when g/a is very small; it then levels off when g/a is sufficiently large; however, the violence and amplitude of the flutter precluded using very small g/a (e.g., $g/a = 1/10$).

4.4.2 Frequencies of Oscillation

Figure 4.11 shows the analytical and experimental results for the frequencies of the shell ($L/a = 8$) at various flow velocities. The CSDs and their corresponding phase plots indicate that the dominant frequencies excited are mostly associated with $n = 2$. In general, the *measured* frequencies slightly increase with flow velocity; this is mainly due to the flow pressurization that tends to expand the shell radially, hence rendering it stiffer. On the other hand, there are slight reductions in the *predicted* frequencies associated with all $m \neq 1$ (except the lowest two frequencies of $n = 3$), at least for the values of n considered. In spite of this opposite trend, theory and experiment are still in fairly good agreement; for a typical case of $n = 2$ and $m = 2$, the discrepancy between theory and experiment varies from about 8% at $U_i = 29\,\mathrm{m/s}$ to 24% at $U_i = 64\,\mathrm{m/s}$.

4.4.3 Effect of L/a

The effect of L/a on the stability of the system is presented in Figure 4.12, where U_{ic}^{*} is plotted against L/a. Both theory and experiment agree that (i) U_{ic}^{*} increases as L/a is reduced, and (ii) the only type of instability incurred by the shell is flutter, which is associated with $n = 2$ for the range of L/a considered. Quantitatively, the agreement is considered to be fairly good, and its extent appears to be a function of L/a. It becomes better as L/a is increased; predictions for U_{ic}^{*} differ from the test results by an amount varying from 27.0% (based on the smaller test value) at $L/a = 5$ to 3.5% at $L/a = 7.9$. It is also noted that the theoretical results obtained herein are *lower* than their corresponding experimental counterparts; this is opposite to the case of annular flow.

4.5 Conclusion

Chapter 4 covered the experimental work conducted to complement and validate (to the extent possible) the analytical model given in Chapter 2 for the study of the stability of cantilevered coaxial shells subjected to internal and/or annular viscous flow. For the analytical model developed in Chapter 5, further comparison between theory and experiment will be made in Section 5.4.2. Presented in this chapter were (i) the detailed description of the apparatus employed in the tests and of the testing procedure, and (ii) test measurements as well as analytical results for frequencies and critical flow velocities of shells under various flow and geometric conditions. The following main findings were obtained:

- In the case of annular flow, dominant frequencies of the shell, appearing in the CSDs (Cross Spectral Densities), slightly decreased ($n \neq 1$) with increasing flow velocity and agreed very well with analytical results. As far as the overall (lowest) critical flow velocities U_{oc}^* are concerned, theoretical predictions were somewhat higher than experimental results; nevertheless, theory and experiment were generally in good agreement, although the extent of the agreement varied with annular gap width and length of the shell.

- In the case of internal flow, dominant frequencies of the shell slightly increased with flow velocity and verified the analytical results best at low flow velocities. Furthermore, predictions for U_{ic}^* were lower than, but in fairly good agreement with the test measurements.

Chapter 5

Viscous Theory

5.1 Introduction

As was mentioned in previous chapters, the viscous nature of the fluid flows gives rise to both steady and unsteady viscosity–related forces acting on the shells. While the steady viscous forces were evaluated in Chapter 2 for the system of clamped–free coaxial cylindrical shells and by Païdoussis *et al.* (1985) for the system of clamped–clamped shells, the unsteady viscous forces have heretofore been substituted by their inviscid counterparts formulated by potential flow theory, as no theoretically sound model has ever been proposed for the determination of these forces. Thus, the unsteady viscous effect, if any, on the stability of the system still remains to be investigated.

The first attempt to evaluate the unsteady viscous forces exerted on coaxial cylindrical shells conveying fluid was made by El Chebair *et al.* (1990). Nevertheless, the problem did not seem to be properly formulated in the sense that such forces should have been determined from the solution of the momentum (Navier–Stokes) equations; in fact, a full solution of these equations was never achieved in that study. It is well–known that any viscous flow field is governed by the Navier–Stokes equations, which must be solved in order to obtain information about the flow field.

This chapter is devoted to the development of a new analytical model to study the unsteady viscous effect on the stability of the system under consideration. The chapter consists mainly of four parts: (i) formulation of the problem, (ii) procedure to solve the equations governing the shell motions, (iii) procedure to solve the Navier–Stokes equations and determine the unsteady viscous forces therefrom, and (iv) comparison of the results given by the new model with those obtained by the theory in Chapter 2 and experimental data presented in Chapter 4. Because of the enormous amount of computing time required in the solution process, the analysis is carried out only for the system involving a cantilevered flexible cylindrical shell concentrically located inside a rigid cylinder, with incompressible fluid flowing in the annular region and with stagnant fluid within the flexible shell; even so, because calculations had to be done outside McGill University (and thanks to generously donated but limited computing time by CRAY Research Inc.), calculations could only be performed for a limited number of cases.

5.2 Formulation of the Analytical Model

5.2.1 System Definition and Assumptions

Shown in Figure 5.1 is a system of coaxial cylinders. The outer cylinder is rigid and is assumed to be infinitely long. A portion, of length L, of the inner cylinder is flexible and thin enough to be considered as a shell; at its upstream end, $x = 0$, the shell is assumed to be connected (clamped) to a semi–infinite rigid cylinder of the same outer radius as the shell; at the downstream end, $x = L$, the shell is unsupported (cantilevered shell).

The basic notation is reiterated here for the reader's convenience. The inner shell has mean radius a, and the outer cylinder has inner radius b. The shell has thickness h such that $h/a \ll 1$, and is assumed to be elastic and isotropic with Young's modulus E, density ρ_s, and Poisson's ratio ν. In general, incompressible fluid of density ρ is flowing in the annulus with mean flow velocity U. Shell motions are considered to be small enough so that a linear shell theory may be utilized and the shell–motion–induced perturbations to the flow may be derived from linearized theory. These perturbations, which lead to unsteady viscous forces acting on the shell, will be determined by solving the linearized Navier–Stokes equations, considering the entire flow field to be viscous. The steady viscous loads resulting from pressure drops and traction effects on the shell have already been given in Chapter 2, and they can readily be incorporated into the governing equations of motion. Finally, flow perturbations are assumed to vanish upstream and far downstream of the flexible shell.

5.2.2 Governing Equations of Motion

Like the theory presented in Chapter 2, shell motions are herein described by Flügge's (1960) linear shell equations, Equations (2.1)–(2.3) [the subscript i in these equations will be omitted herein since it is no longer necessary], as modified by Païdoussis, Misra and Chan (1985) to take into account the stress resultants due to steady viscous effects.

As internal dissipation in the shell is modelled by viscoelastic damping, Young's modulus E, present in γ [defined for Equations (2.1)–(2.3)] and in q_1, q_2 and q_3 [Equations (2.98)], needs to be replaced by $E\left(1+\chi\frac{\partial}{\partial t}\right)$, where χ is the viscoelastic damping coefficient. Hence, Equations (2.1)–(2.3) take on the new form

$$\left(1+\chi\frac{\partial}{\partial t}\right)\left\{u''+\frac{1}{2}(1-\nu)u^{\bullet\bullet}+\frac{1}{2}(1+\nu)v'^{\bullet}+\nu w'+k\left[\frac{1}{2}(1-\nu)u^{\bullet\bullet}-w'''+\frac{1}{2}(1-\nu)w'^{\bullet\bullet}\right]\right\}$$
$$+\left[q_1u''+q_2(v^{\bullet}+w)+q_3(u^{\bullet\bullet}-w')\right]-\gamma\left(\frac{\partial^2 u}{\partial t^2}-\frac{q_x}{\rho_s h}\right)=0, \tag{5.1}$$

$$\left(1+\chi\frac{\partial}{\partial t}\right)\left\{\frac{1}{2}(1+\nu)u'^{\bullet}+v^{\bullet\bullet}+\frac{1}{2}(1-\nu)v''+w^{\bullet}+k\left[\frac{3}{2}(1-\nu)v''-\frac{1}{2}(3-\nu)w''^{\bullet}\right]\right\}$$
$$+\left[q_1v''+q_3(v^{\bullet\bullet}+w^{\bullet})\right]-\gamma\left(\frac{\partial^2 v}{\partial t^2}-\frac{q_\theta}{\rho_s h}\right)=0, \tag{5.2}$$

$$\left(1+\chi\frac{\partial}{\partial t}\right)\left\{\nu_i u'+v^{\bullet}+w+k\left[\frac{1}{2}(1-\nu_i)u'^{\bullet\bullet}-u'''-\frac{1}{2}(3-\nu)v''^{\bullet}+\nabla^4 w+2w^{\bullet\bullet}+w\right]\right\}$$
$$-\left[q_1w''+q_3(u'-v^{\bullet}+w^{\bullet\bullet})\right]+\gamma\left(\frac{\partial^2 w}{\partial t^2}-\frac{q_r}{\rho_s h}\right)=0, \tag{5.3}$$

where

$$(\ )'=a\frac{\partial(\ )}{\partial x},\quad (\ )^{\bullet}=\frac{\partial(\ )}{\partial\theta},\quad k=\frac{1}{12}\left(\frac{h}{a}\right)^2,\quad \gamma=\frac{\rho_s a^2(1-\nu^2)}{E},\quad \nabla^2=a^2\frac{\partial^2}{\partial x^2}+\frac{\partial^2}{\partial\theta^2};$$

$u(x,\theta,t)$, $v(x,\theta,t)$ and $w(x,\theta,t)$ are the axial, circumferential and radial displacements of the middle surface of the undeformed shell; q_1, q_2 and q_3 denote the nondimensional forces associated with steady viscous effects (Section 2.3.3); q_x, q_θ and q_r represent the unsteady viscous forces acting on the shell in the axial, circumferential and radial directions, respectively (Section 5.2.3).

Shell motions must satisfy the following boundary conditions (Flügge 1960), as already described in Section 2.2.2,

(i) at $x = 0$,

$$u = v = w = 0, \qquad \frac{\partial w}{\partial x} = 0; \tag{5.4}$$

(ii) at $x = L$,

$$u' + \nu v^{\bullet} + \nu w - k w'' = 0, \tag{5.5}$$

$$u^{\bullet} + v' + 3k(v' - w'^{\bullet}) = 0, \tag{5.6}$$

$$w'' + \nu w^{\bullet\bullet} - \nu v^{\bullet} - u' = 0, \tag{5.7}$$

$$-w''' - (2-\nu)w'^{\bullet\bullet} + \left(\frac{3-\nu}{2}\right)v'^{\bullet} - \left(\frac{1-\nu}{2}\right)u^{\bullet\bullet} + u'' = 0. \tag{5.8}$$

Section 5.3.2 will present details of how Equations (5.1)–(5.3) subject to boundary conditions (5.4)–(5.8) may be solved.

5.2.3 Unsteady Viscous Forces

Unsteady viscous forces on the shell are due to shell–motion–induced perturbations in the viscous flow field. These perturbations are assumed to be small and thus may be considered to be the solution of the linearized, time–dependent Navier–Stokes equations. This section will be focussed on the derivation of the appropriate form of the Navier–Stokes equations, from which linearization may be carried out.

The flow in the annulus is assumed to be either fully–developed laminar or fully–developed turbulent; in addition, the fluid is assumed to be incompressible and also isentropic. It is worthwhile to reiterate here that the fluid within the inner flexible shell is quiescent. If the flow is turbulent, the flow field will be described by the following continuity and momentum equations

$$\frac{\partial V_i}{\partial x_i} = 0, \tag{5.9}$$

$$\frac{\partial V_i}{\partial t} + V_j \frac{\partial V_i}{\partial x_j} = \frac{1}{\rho}\frac{\partial P}{\partial x_i} + \frac{\partial}{\partial x_j}\left(\nu_m \frac{\partial V_i}{\partial x_j} - \overline{V_i' V_j'}\right), \tag{5.10}$$

where i and j may be 1, 2 or 3; V_i is the ith component of the mean–flow velocity in Cartesian coordinates; V_i' is the ith component of the turbulent fluctuating velocity;

P is the mean–flow static pressure, and ν_m is the molecular kinematic viscosity of the fluid, which is a fluid property and is constant. It should be noted that Equation (5.10) still holds good if the flow is laminar, since in that case $\overline{V_i'V_j'} = 0$.

To evaluate the terms $\overline{V_i'V_j'}$ in Equation (5.10), a turbulence model will be required. Boussinesq's (1877) eddy viscosity concept assumes that, in analogy to the viscous stresses in laminar flows, the turbulent stresses are proportional to the mean–velocity gradients:

$$-\overline{V_i'V_j'} \; = \; \nu_t\left(\frac{\partial V_i}{\partial x_j} + \frac{\partial V_j}{\partial x_i}\right) - \frac{2}{3}K\delta_{ij}, \tag{5.11}$$

where ν_t is the eddy (or turbulent) kinematic viscosity which, in contrast to the molecular kinematic viscosity ν_m, is not a fluid property but depends strongly on the state of turbulence; ν_t may vary significantly from one point to another and also from flow to flow; K is the kinetic energy of the fluctuating motion, given by

$$K \; = \; \frac{1}{2}\left[\,\overline{(V_1')^2} + \overline{(V_2')^2} + \overline{(V_3')^2}\,\right], \tag{5.12}$$

and δ_{ij} is the Kronecker delta, having the following values

$$\delta_{ij} \; = \; \begin{cases} 1 & \text{if } i = j, \\ 0 & \text{if } i \neq j. \end{cases}$$

The distribution of ν_t is determined by the particular turbulence model employed in the analysis. In this theory, the so–called mixing–length model suggested by Prandtl (1925) will be used. This is the simplest possible model for dealing with the turbulent (or Reynolds) stresses. In view of the computational difficulties that will become evident in due course, its use is justifiable. Details of the evaluation of ν_t using this turbulence model are presented in Appendix E.

With the substitution of (5.11) into Equation (5.10), the following equation is obtained

$$\frac{\partial V_i}{\partial t} + V_j\frac{\partial V_i}{\partial x_j} \; = \; -\frac{1}{\rho}\frac{\partial P}{\partial x_i} + \frac{\partial}{\partial x_j}\left\{\nu_m\frac{\partial V_i}{\partial x_j} + \nu_t\left(\frac{\partial V_i}{\partial x_j} + \frac{\partial V_j}{\partial x_i}\right) - \frac{2}{3}K\delta_{ij}\right\},$$

or

$$\frac{\partial V_i}{\partial t} + V_j\frac{\partial V_i}{\partial x_j} \; = \; -\frac{1}{\rho}\frac{\partial P_t}{\partial x_i} + (\nu_m + \nu_t)\frac{\partial^2 V_i}{\partial^2 x_j} + \frac{\partial \nu_t}{\partial x_j}\left(\frac{\partial V_i}{\partial x_j} + \frac{\partial V_j}{\partial x_i}\right), \tag{5.13}$$

where $P_t = P + (2/3)\rho K$ represents the total pressure in the flow, and the fact that

$$\nu_t\frac{\partial}{\partial x_j}\left(\frac{\partial V_j}{\partial x_i}\right) \; = \; \nu_t\frac{\partial}{\partial x_i}\left(\frac{\partial V_j}{\partial x_j}\right) \; = \; 0 \tag{5.14}$$

by virtue of Equation (5.9) has been taken into account.

Equation (5.13) may also be rewritten in vector form as

$$\frac{\partial \mathbf{V}}{\partial t} + (\mathbf{V}\cdot\nabla)\mathbf{V} = -\frac{1}{\rho}\nabla P_t + (\nu_m + \nu_t)\nabla^2\mathbf{V} + (\nabla\nu_t\cdot\nabla)\mathbf{V} + (\nabla\mathbf{V})\cdot\nabla\nu_t$$

or

$$\underbrace{\frac{\partial \mathbf{V}}{\partial t} + (\mathbf{V}\cdot\nabla)\mathbf{V} = -\frac{1}{\rho}\nabla P_t + \nu\nabla^2\mathbf{V}}_{\text{(a)}} + \underbrace{(\nabla\nu\cdot\nabla)\mathbf{V} + (\nabla\mathbf{V})\cdot\nabla\nu}_{\text{(b)}}, \tag{5.15}$$

where $\nabla\mathbf{V}$ is called a dyad (see the following development or, for example, Wills 1931); $\nu = \nu_m + \nu_t$, and hence $\nabla\nu = \nabla\nu_t$ since ν_m is a constant, as mentioned earlier. It is further noted that, in most turbulent flow regions, ν_t is much larger than ν_m and thus the latter may be neglected if desired.

Because the flow is axisymmetric, it is convenient to express Equation (5.15) in cylindrical coordinates. Part (a) of Equation (5.15) can easily be found in most text books of Fluid Mechanics [for example, Schlichting (1968)], while Part (b) will be evaluated below. In cylindrical coordinates,

$$\begin{aligned}
\nabla &= \mathbf{e}_r\left(\frac{\partial}{\partial r}\right) + \mathbf{e}_\theta\left(\frac{1}{r}\frac{\partial}{\partial\theta}\right) + \mathbf{e}_x\left(\frac{\partial}{\partial x}\right), \\
\mathbf{V} &= \mathbf{e}_r V_r + \mathbf{e}_\theta V_\theta + \mathbf{e}_x V_x, \\
\nu &= \nu_m + \nu_t(r) = \nu(r),
\end{aligned}$$

where $\nu = \nu(r)$ results from the axisymmetric nature of the flow and from the assumption made earlier that the flow is fully–developed; the distribution of $\nu(r)$ in the annulus is given in Appendix E. Since

$$\begin{aligned}
(\nabla\nu\cdot\nabla)\mathbf{V} &= \left\{\left(\mathbf{e}_r\frac{\mathrm{d}\nu}{\mathrm{d}r}\right)\cdot\left[\mathbf{e}_r\left(\frac{\partial}{\partial r}\right) + \mathbf{e}_\theta\left(\frac{1}{r}\frac{\partial}{\partial\theta}\right) + \mathbf{e}_x\left(\frac{\partial}{\partial x}\right)\right]\right\}(\mathbf{e}_r V_r + \mathbf{e}_\theta V_\theta + \mathbf{e}_x V_x) \\
&= \mathbf{e}_r\left(\frac{\partial V_r}{\partial r}\frac{\mathrm{d}\nu}{\mathrm{d}r}\right) + \mathbf{e}_\theta\left(\frac{\partial V_\theta}{\partial r}\frac{\mathrm{d}\nu}{\mathrm{d}r}\right) + \mathbf{e}_x\left(\frac{\partial V_x}{\partial r}\frac{\mathrm{d}\nu}{\mathrm{d}r}\right),
\end{aligned}$$

and

$$\begin{aligned}
(\nabla\mathbf{V})\cdot\nabla\nu &= \begin{bmatrix}
 & \left(\frac{\partial V_r}{\partial r}\right)\mathbf{e}_r\mathbf{e}_r & + & \left(\frac{\partial V_\theta}{\partial r}\right)\mathbf{e}_r\mathbf{e}_\theta & + & \left(\frac{\partial V_x}{\partial r}\right)\mathbf{e}_r\mathbf{e}_x \\
+ & \left(\frac{1}{r}\frac{\partial V_r}{\partial\theta}\right)\mathbf{e}_\theta\mathbf{e}_r & + & \left(\frac{1}{r}\frac{\partial V_\theta}{\partial\theta}\right)\mathbf{e}_\theta\mathbf{e}_\theta & + & \left(\frac{1}{r}\frac{\partial V_x}{\partial\theta}\right)\mathbf{e}_\theta\mathbf{e}_x \\
+ & \left(\frac{\partial V_r}{\partial x}\right)\mathbf{e}_x\mathbf{e}_r & + & \left(\frac{\partial V_\theta}{\partial x}\right)\mathbf{e}_x\mathbf{e}_\theta & + & \left(\frac{\partial V_x}{\partial x}\right)\mathbf{e}_x\mathbf{e}_x
\end{bmatrix}\cdot\left[\mathbf{e}_r\frac{\mathrm{d}\nu}{\mathrm{d}r}\right] \\
&= \mathbf{e}_r\left(\frac{\partial V_r}{\partial r}\frac{\mathrm{d}\nu}{\mathrm{d}r}\right) + \mathbf{e}_\theta\left(\frac{1}{r}\frac{\partial V_r}{\partial\theta}\frac{\mathrm{d}\nu}{\mathrm{d}r}\right) + \mathbf{e}_x\left(\frac{\partial V_r}{\partial x}\frac{\mathrm{d}\nu}{\mathrm{d}r}\right),
\end{aligned}$$

it follows that

$$(\nabla\nu\cdot\nabla)\mathbf{V}+(\nabla\mathbf{V})\cdot\nabla\nu \;=\; \left(\frac{\mathrm{d}\nu}{\mathrm{d}r}\right)\left\{2\left(\frac{\partial V_r}{\partial r}\right)\mathbf{e}_r+\left(\frac{\partial V_\theta}{\partial r}+\frac{1}{r}\frac{\partial V_r}{\partial\theta}\right)\mathbf{e}_\theta+\left(\frac{\partial V_x}{\partial r}+\frac{\partial V_r}{\partial x}\right)\mathbf{e}_x\right\}.$$

Equation (5.15) is in fact equivalent to three independent equations corresponding to the r–, θ– and x–direction, namely

$$\begin{aligned}\left\{\frac{\partial V_r}{\partial t}+V_r\frac{\partial V_r}{\partial r}+\frac{V_\theta}{r}\frac{\partial V_r}{\partial\theta}-\frac{V_\theta^2}{r}+V_x\frac{\partial V_r}{\partial x}\right\} &= 2\frac{\mathrm{d}\nu}{\mathrm{d}r}\frac{\partial V_r}{\partial r}-\frac{1}{\rho}\frac{\partial P_t}{\partial r}\\ &\quad+\nu\left\{\frac{1}{r}\frac{\partial}{\partial r}\left(r\frac{\partial V_r}{\partial r}\right)-\frac{V_r}{r^2}+\frac{1}{r^2}\frac{\partial^2 V_r}{\partial\theta^2}+\frac{\partial^2 V_r}{\partial x^2}-\frac{2}{r^2}\frac{\partial V_\theta}{\partial\theta}\right\},\end{aligned} \tag{5.16}$$

$$\begin{aligned}\left\{\frac{\partial V_\theta}{\partial t}+V_r\frac{\partial V_\theta}{\partial\theta}+\frac{V_\theta}{r}\frac{\partial V_\theta}{\partial\theta}+\frac{V_rV_\theta}{r}+V_x\frac{\partial V_\theta}{\partial x}\right\} &= \frac{\mathrm{d}\nu}{\mathrm{d}r}\left(\frac{\partial V_\theta}{r}+\frac{1}{r}\frac{\partial V_r}{\partial\theta}\right)-\frac{1}{\rho r}\frac{\partial P_t}{\partial\theta}\\ &\quad+\nu\left\{\frac{1}{r}\frac{\partial}{\partial r}\left(r\frac{\partial V_\theta}{\partial r}\right)-\frac{V_\theta}{r^2}+\frac{1}{r^2}\frac{\partial^2 V_\theta}{\partial\theta^2}+\frac{\partial^2 V_\theta}{\partial x^2}+\frac{2}{r^2}\frac{\partial V_r}{\partial\theta}\right\},\end{aligned} \tag{5.17}$$

$$\begin{aligned}\left\{\frac{\partial V_x}{\partial t}+V_r\frac{\partial V_x}{\partial r}+\frac{V_\theta}{r}\frac{\partial V_x}{\partial\theta}+V_x\frac{\partial V_x}{\partial x}\right\} &= \frac{\mathrm{d}\nu}{\mathrm{d}r}\left(\frac{\partial V_x}{\partial r}+\frac{\partial V_r}{\partial x}\right)-\frac{1}{\rho}\frac{\partial P_t}{\partial x}\\ &\quad+\nu\left\{\frac{1}{r}\frac{\partial}{\partial r}\left(r\frac{\partial V_x}{\partial r}\right)+\frac{1}{r^2}\frac{\partial^2 V_x}{\partial\theta^2}+\frac{\partial^2 V_x}{\partial x^2}\right\}.\end{aligned} \tag{5.18}$$

The continuity equation in cylindrical coordinates has the form

$$\frac{1}{r}\frac{\partial}{\partial r}(rV_r)\;+\;\frac{1}{r}\frac{\partial V_\theta}{\partial\theta}\;+\;\frac{\partial V_x}{\partial x}\;=\;0. \tag{5.19}$$

Equations (5.16)–(5.19), describing the mean flow characterized by the velocity $\mathbf{V}$ and the total pressure P_t, provide the basis for the derivation of the equations governing the flow perturbations associated with shell motions. It is important to mention here that, in the flow under consideration, there are two types of disturbances. The first type of disturbances is due to turbulent eddies, whereas the other is induced by shell motions. The combination of these two types of disturbances is often referred to as "unsteady turbulence." The word "mean" that has been used since the beginning of this chapter is intended to be associated with the first type of disturbances only.

Each component of $\mathbf{V}$ as well as P_t may be regarded as consisting of a steady part and a *small* shell–motion–induced perturbation, namely

$$V_r=v_r,\quad V_\theta=v_\theta,\quad V_x=U(r)+v_x,\quad P_t/\rho=\bar{P}+p, \tag{5.20}$$

where $U(r)$ and $\bar{P}$ denote the steady parts of V_x and P_t/ρ, respectively, while the steady parts of V_r and V_θ are zero, since the flow is axisymmetric; v_r, v_θ, v_x, and p are flow perturbations associated with the components of $\mathbf{V}$ and P_t/ρ.

With the substitution of (5.20) into Equations (5.16)–(5.19) and with the assumptions that (i) the steady flow also satisfies the continuity and Navier–Stokes equations and (ii) all quadratic terms in the flow perturbations are negligible with respect to the linear terms, the following equations are obtained

$$\begin{aligned}\left\{\frac{\partial v_r}{\partial t} + U(r)\frac{\partial v_r}{\partial x}\right\} &= 2\frac{\mathrm{d}\nu}{\mathrm{d}r}\left(\frac{\partial v_r}{\partial r}\right) - \frac{\partial p}{\partial r} \\ &+ \nu\left\{\frac{1}{r}\frac{\partial}{\partial r}\left(r\frac{\partial v_r}{\partial r}\right) - \frac{v_r}{r^2} + \frac{1}{r^2}\frac{\partial^2 v_r}{\partial \theta^2} + \frac{\partial^2 v_r}{\partial x^2} - \frac{2}{r^2}\frac{\partial v_\theta}{\partial \theta}\right\}, \end{aligned} \tag{5.21}$$

$$\begin{aligned}\left\{\frac{\partial v_\theta}{\partial t} + U(r)\frac{\partial v_\theta}{\partial x}\right\} &= \frac{\mathrm{d}\nu}{\mathrm{d}r}\left(\frac{\partial v_\theta}{\partial r} + \frac{1}{r}\frac{\partial v_r}{\partial \theta}\right) - \frac{1}{r}\frac{\partial p}{\partial \theta} \\ &+ \nu\left\{\frac{1}{r}\frac{\partial}{\partial r}\left(r\frac{\partial v_\theta}{\partial r}\right) - \frac{v_\theta}{r^2} + \frac{1}{r^2}\frac{\partial^2 v_\theta}{\partial \theta^2} + \frac{\partial^2 v_\theta}{\partial x^2} + \frac{2}{r^2}\frac{\partial v_r}{\partial \theta}\right\}, \end{aligned} \tag{5.22}$$

$$\begin{aligned}\left\{\frac{\partial v_x}{\partial t} + U(r)\frac{\partial v_x}{\partial x} + \frac{\mathrm{d}U}{\mathrm{d}r}v_r\right\} &= \frac{\mathrm{d}\nu}{\mathrm{d}r}\left(\frac{\partial v_x}{\partial r} + \frac{\partial v_r}{\partial x}\right) - \frac{\partial p}{\partial x} \\ &+ \nu\left\{\frac{1}{r}\frac{\partial}{\partial r}\left(r\frac{\partial v_x}{\partial r}\right) + \frac{1}{r^2}\frac{\partial^2 v_x}{\partial \theta^2} + \frac{\partial^2 v_x}{\partial x^2}\right\}, \end{aligned} \tag{5.23}$$

and

$$\frac{1}{r}\frac{\partial}{\partial r}(r v_r) + \frac{1}{r}\frac{\partial v_\theta}{\partial \theta} + \frac{\partial v_x}{\partial x} = 0, \tag{5.24}$$

which are subject to the no–slip condition at the interfaces with the cylinders: at the outer surface of the flexible shell, $r = a + h/2$,

$$v_x = \frac{\partial u}{\partial t}, \qquad v_\theta = \frac{\partial v}{\partial t}, \qquad v_r = \frac{\partial w}{\partial t}, \tag{5.25}$$

where u, v and w are the axial, circumferential and radial displacements of the shell, respectively; at the inner surface of the rigid cylinder, $r = b$,

$$v_x = v_\theta = v_r = 0. \tag{5.26}$$

It is seen that v_r, v_θ, v_x and p are fully specified by Equations (5.21)–(5.24) and, in principle, can be solved for. Once these perturbations are determined, the unsteady viscous forces (or stresses) on the shell are given by (Schlichting 1968):

$$q_x = \sigma_{rx} = \rho\nu\left\{\frac{\partial v_r}{\partial x} + \frac{\partial v_x}{\partial r}\right\}\Bigg|_{ss}, \tag{5.27}$$

$$q_\theta = \sigma_{r\theta} = \rho\nu\left\{r\frac{\partial}{\partial r}\left(\frac{v_\theta}{r}\right) + \frac{1}{r}\frac{\partial v_r}{\partial \theta}\right\}\Bigg|_{ss}, \tag{5.28}$$

$$q_r = \sigma_{rr} = \left\{-(\rho p) + 2\rho\nu\frac{\partial v_r}{\partial r}\right\}\Bigg|_{ss}, \tag{5.29}$$

where ρp is the perturbation pressure, as defined in (5.20); the notation "ss" stands for the condition that the expression(s) be evaluated at the shell surface.

The procedure to solve Equations (5.21)–(5.24) for the flow perturbations and hence to evaluate (5.27)–(5.29) will be given in Section 5.3.3.

5.2.4 Summary

Section 5.2 has formulated the problem involving a cantilevered, flexible cylindrical shell confined inside a coaxial rigid cylinder and subjected to an incompressible viscous fluid flow in the annular region. In the formulation, the shell displacements were described by Flügge's shell equations, and the unsteady viscous forces acting on the shell were calculated from the flow velocity and pressure perturbations governed by the unsteady linearized Navier–Stokes equations.

5.3 Method of Solution

5.3.1 Introduction

The method of solution to be presented covers two different, but interrelated procedures: one for solving Flügge's shell equations (Section 5.3.2) and the other for solving the linearized Navier–Stokes equations (Section 5.3.3).

Since a closed–form solution for the Navier–Stokes equations is not possible due to their complexity, a numerical solution will be obtained instead, with the aid of a special technique developed by Soh and Goodrich (1988) and originally intended to give an unsteady solution for the incompressible Navier–Stokes equations. This technique is based on the popular finite–difference method, and is for the first time applied to solve a fluid–shell coupling problem. (A similar, fluid–cylinder coupling problem has also been considered by Mateescu *et al.* 1991a.) In the solution process, as the output (solution) of one set of equations is the input for the other and *vice versa*, Flügge's shell equations will have to be solved numerically, also by the finite–difference method.

5.3.2 Solution to the Governing Equations of Motion

For the purposes of solving Equations (5.1)–(5.3), the shell displacements u, v, and w are expressed in the following functional forms

$$\left\{\begin{array}{c} u(x,\theta,t) \\ v(x,\theta,t) \\ w(x,\theta,t) \end{array}\right\} = \sum_{n=1}^{\infty} \left\{\begin{array}{c} \bar{u}(x,t)\cos n\theta \\ \bar{v}(x,t)\sin n\theta \\ \bar{w}(x,t)\cos n\theta \end{array}\right\}, \tag{5.30}$$

where n is the circumferential wave number. Similarly, the solutions for q_x, q_θ, and q_r are taken to be

$$\left\{\begin{array}{c} q_x(x,\theta,t) \\ q_\theta(x,\theta,t) \\ q_r(x,\theta,t) \end{array}\right\} = \sum_{n=1}^{\infty} \left\{\begin{array}{c} \bar{q}_x(x,t)\cos n\theta \\ \bar{q}_\theta(x,t)\sin n\theta \\ \bar{q}_r(x,t)\cos n\theta \end{array}\right\}. \tag{5.31}$$

Thus, in terms of (5.30) and (5.31), Equations (5.1)–(5.3) may be rewritten as

$$\begin{aligned} \sum_{n=1}^{\infty} \Bigg[\left(1+\chi\frac{\partial}{\partial t}\right) & \left\{ a^2\frac{\partial^2 \bar{u}}{\partial x^2} - \frac{n^2}{2}(k+1)(1-\nu)\bar{u} + \frac{n}{2}(1+\nu)a\frac{\partial \bar{v}}{\partial x} - ka^3\frac{\partial^3 \bar{w}}{\partial x^3} \right. \\ & \left. + \left(\nu - \frac{kn^2}{2}(1-\nu)\right)a\frac{\partial \bar{w}}{\partial x}\right\} + \left\{ q_1 a^2\frac{\partial^2 \bar{u}}{\partial x^2} + q_2\,(n\bar{v}+\bar{w}) - q_3\left(n^2\bar{u} + a\frac{\partial \bar{w}}{\partial x}\right)\right\} \\ & - \gamma\left\{\frac{\partial^2 \bar{u}}{\partial t^2} - \frac{\bar{q}_x}{\rho_s h}\right\}\Bigg] \cos n\theta = 0, \end{aligned} \tag{5.32}$$

$$\begin{aligned} \sum_{n=1}^{\infty} \Bigg[\left(1+\chi\frac{\partial}{\partial t}\right) & \left\{ -\frac{n}{2}(1+\nu)a\frac{\partial \bar{u}}{\partial x} + \frac{1}{2}(3k+1)(1-\nu)a^2\frac{\partial^2 \bar{v}}{\partial x^2} - n^2\bar{v} + \frac{kn}{2}(3-\nu)a^2\frac{\partial^2 \bar{w}}{\partial x^2} - n\bar{w}\right\} \\ & + \left\{ q_1 a^2\frac{\partial^2 \bar{v}}{\partial x^2} - q_3\left(n^2\bar{v} + n\bar{w}\right)\right\} - \gamma\left\{\frac{\partial^2 \bar{v}}{\partial t^2} - \frac{\bar{q}_\theta}{\rho_s h}\right\}\Bigg] \sin n\theta = 0, \end{aligned} \tag{5.33}$$

$$\begin{aligned} \sum_{n=1}^{\infty} \Bigg[\left(1+\chi\frac{\partial}{\partial t}\right) & \left\{ -ka^3\frac{\partial^3 \bar{u}}{\partial x^3} + \left(\nu - \frac{kn^2}{2}(1-\nu)\right) a\frac{\partial \bar{u}}{\partial x} - \frac{kn}{2}(3-\nu)a^2\frac{\partial^2 \bar{v}}{\partial x^2} + n\bar{v} + ka^4\frac{\partial^4 \bar{w}}{\partial x^4} \right. \\ & \left. - 2kn^2a^2\frac{\partial^2 \bar{w}}{\partial x^2} + \left(1 + k(n^2-1)^2\right)\bar{w}\right\} - \left\{ q_1 a^2\frac{\partial^2 \bar{w}}{\partial x^2} + q_3\left(a\frac{\partial \bar{u}}{\partial x} - n\bar{v} - n^2\bar{w}\right)\right\} \\ & + \gamma\left\{\frac{\partial^2 \bar{w}}{\partial t^2} - \frac{\bar{q}_r}{\rho_s h}\right\}\Bigg] \cos n\theta = 0, \end{aligned} \tag{5.34}$$

which are subject to the following boundary conditions: at the clamped end, $x = 0$,

$$\sum_{n=1}^{\infty} \bar{u}\cos n\theta \;=\; \sum_{n=1}^{\infty} \bar{v}\sin n\theta \;=\; \sum_{n=1}^{\infty} \bar{w}\cos n\theta \;=\; \sum_{n=1}^{\infty} \frac{\partial \bar{w}}{\partial x}\cos n\theta \;=\; 0; \tag{5.35}$$

and at the unsupported end, $x = L$,

$$\sum_{n=1}^{\infty}\left\{a\frac{\partial \bar{u}}{\partial x} + n\nu\bar{v} - ka^2\frac{\partial^2 \bar{w}}{\partial x^2} + \nu\bar{w}\right\}\cos n\theta = 0, \tag{5.36}$$

$$\sum_{n=1}^{\infty}\left\{-n\bar{u} + (1+3k)a\frac{\partial \bar{v}}{\partial x} + 3kna\frac{\partial \bar{w}}{\partial x}\right\}\sin n\theta = 0, \tag{5.37}$$

$$\sum_{n=1}^{\infty}\left\{-a\frac{\partial \bar{u}}{\partial x} - \nu n\bar{v} + a^2\frac{\partial^2 \bar{w}}{\partial x^2} - n^2\nu\bar{w}\right\}\cos n\theta = 0, \tag{5.38}$$

$$\sum_{n=1}^{\infty}\left\{-a^2\frac{\partial^2 \bar{u}}{\partial x^2} - \frac{n^2}{2}(1-\nu)\bar{u} - \frac{n}{2}(3-\nu)a\frac{\partial \bar{v}}{\partial x} + a^3\frac{\partial^3 \bar{w}}{\partial x^3} - (2-\nu)n^2a\frac{\partial \bar{w}}{\partial x}\right\}\cos n\theta = 0. \tag{5.39}$$

It is noted that Equations (5.32)–(5.39) have the unit of length; hence, they will be rendered dimensionless if divided by L, the length of the flexible shell. For the purpose of nondimensionalization, in this section and the subsequent ones, the following dimensionless parameters are defined:

$$\begin{gathered}\xi = \frac{x}{L},\quad \eta = \frac{r}{L},\quad \varepsilon_i = \frac{a}{L},\quad \varepsilon_o = \frac{b}{L},\quad \hat{u} = \frac{\bar{u}}{L},\quad \hat{v} = \frac{\bar{v}}{L},\quad \hat{w} = \frac{\bar{w}}{L},\\ \hat{q}_x = \frac{\gamma\bar{q}_x}{\rho_s hL},\quad \hat{q}_\theta = \frac{\gamma\bar{q}_\theta}{\rho_s hL},\quad \hat{q}_r = \frac{\gamma\bar{q}_r}{\rho_s hL}.\end{gathered} \tag{5.40}$$

Another observation that should be made here is that since $\sin n\theta$ and $\cos n\theta$ are not generally equal to zero and the series in (5.32)–(5.39) are infinite, the coefficients of $\sin n\theta$ and $\cos n\theta$ in these series must vanish. Thus, Equations (5.32)–(5.39) are effectively equivalent to

$$\begin{aligned}&\left[1+\chi\frac{\partial}{\partial t}\right]\left\{\varepsilon_i^2\frac{\partial^2\hat{u}}{\partial\xi^2} - \frac{n^2}{2}(k+1)(1-\nu)\hat{u} + \frac{n}{2}(1+\nu)\varepsilon_i\frac{\partial\hat{v}}{\partial\xi} - k\varepsilon_i^3\frac{\partial^3\hat{w}}{\partial\xi^3} + \left[\nu - \frac{kn^2}{2}(1-\nu)\right]\varepsilon_i\frac{\partial\hat{w}}{\partial\xi}\right\}\\ &\quad + \left\{q_1\varepsilon_i^2\frac{\partial^2\hat{u}}{\partial\xi^2} + q_2(n\hat{v}+\hat{w}) - q_3\left(n^2\hat{u} + \varepsilon_i\frac{\partial\hat{w}}{\partial\xi}\right)\right\} - \left\{\gamma\frac{\partial^2\hat{u}}{\partial t^2} - \hat{q}_x\right\} \;=\; 0,\end{aligned} \tag{5.41}$$

$$\begin{aligned}&\left[1+\chi\frac{\partial}{\partial t}\right]\left\{-\frac{n}{2}(1+\nu)\varepsilon_i\frac{\partial\hat{u}}{\partial\xi} + \frac{1}{2}(3k+1)(1-\nu)\varepsilon_i^2\frac{\partial^2\hat{v}}{\partial\xi^2} - n^2\hat{v} + \frac{kn}{2}(3-\nu)\varepsilon_i^2\frac{\partial^2\hat{w}}{\partial\xi^2} - n\hat{w}\right\}\\ &\quad + \left\{q_1\varepsilon_i^2\frac{\partial^2\hat{v}}{\partial\xi^2} - q_3\left(n^2\hat{v} + n\hat{w}\right)\right\} - \left\{\gamma\frac{\partial^2\hat{v}}{\partial t^2} - \hat{q}_\theta\right\} \;=\; 0,\end{aligned} \tag{5.42}$$

$$\left[1+\chi\frac{\partial}{\partial t}\right]\left\{-k\varepsilon_i^3\frac{\partial^3\hat{u}}{\partial\xi^3} + \left[\nu - \frac{kn^2}{2}(1-\nu)\right]\varepsilon_i\frac{\partial\hat{u}}{\partial\xi} - \frac{kn}{2}(3-\nu)\varepsilon_i^2\frac{\partial^2\hat{v}}{\partial\xi^2} + n\hat{v} + k\varepsilon_i^4\frac{\partial^4\hat{w}}{\partial\xi^4}\right.$$

$$
\begin{aligned}
&- 2kn^2\varepsilon_i^2\frac{\partial^2\hat{w}}{\partial\xi^2} + \Big[1 + k(n^2-1)^2\Big]\hat{w}\Big\} - \Big\{q_1\varepsilon_i^2\frac{\partial^2\hat{w}}{\partial\xi^2} + q_3\Big(\varepsilon_i\frac{\partial\hat{u}}{\partial\xi} - n\hat{v} - n^2\hat{w}\Big)\Big\} \\
&+ \Big\{\gamma\frac{\partial^2\hat{w}}{\partial t^2} - \hat{q}_r\Big\} = 0,
\end{aligned}
\tag{5.43}
$$

subject to the boundary conditions:

- at $\xi = 0$,

$$
\hat{u} = \hat{v} = \hat{w} = \frac{\partial\hat{w}}{\partial\xi} = 0; \tag{5.44}
$$

- at $\xi = 1$,

$$
\varepsilon_i\frac{\partial\hat{u}}{\partial\xi} + n\nu\hat{v} - ka^2\frac{\partial^2\hat{w}}{\partial\xi^2} + \nu\hat{w} = 0, \tag{5.45}
$$

$$
- n\hat{u} + (1+3k)\varepsilon_i\frac{\partial\hat{v}}{\partial\xi} + 3kn\varepsilon_i\frac{\partial\hat{w}}{\partial\xi} = 0, \tag{5.46}
$$

$$
- \varepsilon_i\frac{\partial\hat{u}}{\partial\xi} - \nu n\hat{v} + \varepsilon_i^2\frac{\partial^2\hat{w}}{\partial\xi^2} - n^2\nu\hat{w} = 0, \tag{5.47}
$$

$$
- \varepsilon_i^2\frac{\partial^2\hat{u}}{\partial\xi^2} - \frac{n^2}{2}(1-\nu)\hat{u} - \frac{n}{2}(3-\nu)\varepsilon_i\frac{\partial\hat{v}}{\partial\xi} + \varepsilon_i^3\frac{\partial^3\hat{w}}{\partial\xi^3} - (2-\nu)n^2\varepsilon_i\frac{\partial\hat{w}}{\partial\xi} = 0. \tag{5.48}
$$

It may be seen that the only independent spatial variable in Equations (5.41)–(5.48) is ξ, the nondimensionalized axial variable defined in (5.40). To solve these equations using the finite–difference method requires that the shell be represented by $(N+1)$ nodal points, all evenly spaced in the axial direction; node 0 is at $\xi = 0$, the clamped end of the shell, and node N is at $\xi = 1$, the unsupported end. Each node j is associated with three unknowns u_j, v_j and w_j representing, respectively, the axial, circumferential and radial displacements of the shell at $\xi = \xi_j$, with the subscript j denoting the number of the node under consideration. Equations (5.41)–(5.43) will then be written for all nodes i, such that $1 \le i \le N$, with nodes 1 and N given more attention because these are the locations where the boundary conditions are taken into account.

At node 0, the boundary conditions (5.44) could be rewritten as

$$
\hat{u}_0 = \hat{v}_0 = \hat{w}_0 = 0, \tag{5.49}
$$

and if the first derivative of $\hat{w}$ with respect to ξ is replaced by the $O[(\Delta\xi)^2]$–accurate central difference representation, then

$$\frac{1}{2\Delta\xi}\left(\hat{w}_1 - \hat{w}_{-1}\right) = 0 \qquad \text{or} \qquad \hat{w}_{-1} = \hat{w}_1, \tag{5.50}$$

where node -1 is fictitious and is symmetrical with node 1 about node 0; $\Delta\xi$ being the spacing between any two successive nodes is determined by

$$\Delta\xi = \frac{1}{N} = \xi_{i+1} - \xi_i.$$

At node N, the boundary conditions (5.45)–(5.48) are imposed, thereby increasing the number of equations to $(3N+4)$, whereas there are only $3N$ unknowns associated with N nodal points. To increase the number of unknowns, another fictitious node $(N+1)$ beyond the free end of the shell is introduced, thus increasing the number of unknowns to $(3N+3)$; nevertheless, the number of equations is still one higher than that of unknowns. This difficulty may be resolved by realizing that, for node N (*and for node N alone*), it is possible to combine Equation (5.43) and the boundary condition (5.48) to yield one single equation, hence reducing the total number of equations by one and making it equal to the number of unknowns.

What has just been discussed above involves differentiating Equation (5.48) with respect to ξ and multiplying the resulting equation by $k\varepsilon_i$; after some rearrangements, the following equation is obtained

$$-k\varepsilon_i^3\frac{\partial^3\hat{u}}{\partial\xi^3} - \frac{kn^2}{2}(1-\nu)\varepsilon_i\frac{\partial\hat{u}}{\partial\xi} - \frac{kn}{2}(3-\nu)\varepsilon_i^2\frac{\partial^2\hat{v}}{\partial\xi^2} + k\varepsilon_i^4\frac{\partial^4\hat{w}}{\partial\xi^4} - 2kn^2\varepsilon_i^2\frac{\partial^2\hat{w}}{\partial\xi^2} = -k\nu n^2\varepsilon_i^2\frac{\partial^2\hat{w}}{\partial\xi^2}. \tag{5.51}$$

It is seen that the terms on the left–hand side of (5.51) are *all* present in the first pair of braces in Equation (5.43); substituting the right–hand side of (5.51) for these terms simplifies Equation (5.43) to

$$\left(1+\chi\frac{\partial}{\partial t}\right)\left\{\nu\varepsilon_i\frac{\partial\hat{u}}{\partial\xi} + n\hat{v} - k\nu n^2\varepsilon_i^2\frac{\partial^2\hat{w}}{\partial\xi^2} + \left[1+k(n^2-1)^2\right]\hat{w}\right\}$$
$$-\left\{q_1\varepsilon_i^2\frac{\partial^2\hat{w}}{\partial\xi^2} + q_3\left(\varepsilon_i\frac{\partial\hat{u}}{\partial\xi} - n\hat{v} - n^2\hat{w}\right)\right\} + \left\{\gamma\frac{\partial^2\hat{w}}{\partial t^2} - \hat{q}_r\right\} = 0. \tag{5.52}$$

Thus, discretized about node N are the six equations: (5.41), (5.42), (5.52), and (5.45)–(5.47).

In the present analysis, a *fully implicit* scheme is adopted to carry out numerical time integration; all equations involved are evaluated at the new time level $(n+1)$ where $\hat{u}_j^{n+1}$, $\hat{v}_j^{n+1}$ and $\hat{w}_j^{n+1}$ are nodal unknowns to be solved for. Consequently, all first and second time derivatives are approximated by the $O[(\Delta t)^2]$–accurate backward difference representations, namely

$$\left(\frac{\partial f}{\partial t}\right)^{n+1} = \frac{1}{2\Delta t}\left[3f^{n+1} - 4f^n + f^{n-1}\right] \quad + O[(\Delta t)^2], \tag{5.53}$$

$$\left(\frac{\partial^2 f}{\partial t^2}\right)^{n+1} = \frac{1}{(\Delta t)^2}\left[2f^{n+1} - 5f^n + 4f^{n-1} - f^{n-2}\right] \quad + O[(\Delta t)^2], \tag{5.54}$$

where f denotes a nodal unknown, and Δt is the time step taken for the numerical time integration.

On the other hand, for inner nodes i such that $2 \leq i \leq (N-1)$, all spatial derivatives are approximated by the $O[(\Delta\xi)^2]$–accurate central difference representations:

$$\left(\frac{\partial f}{\partial \xi}\right)_i = \frac{1}{2\Delta\xi}\left[f_{i+1} - f_{i-1}\right] \quad + O[(\Delta\xi)^2], \tag{5.55}$$

$$\left(\frac{\partial^2 f}{\partial \xi^2}\right)_i = \frac{1}{(\Delta\xi)^2}\left[f_{i+1} - 2f_i + f_{i-1}\right] \quad + O[(\Delta\xi)^2], \tag{5.56}$$

$$\left(\frac{\partial^3 f}{\partial \xi^3}\right)_i = \frac{1}{2(\Delta\xi)^3}\left[f_{i+2} - 2f_{i+1} + 2f_{i-1} - f_{i-2}\right] \quad + O[(\Delta\xi)^2], \tag{5.57}$$

$$\left(\frac{\partial^4 f}{\partial \xi^4}\right)_i = \frac{1}{(\Delta\xi)^4}\left[f_{i+2} - 4f_{i+1} + 6f_i - 4f_{i-1} + f_{i-2}\right] \quad + O[(\Delta\xi)^2]. \tag{5.58}$$

For node $i = 1$, the approximations (5.55) and (5.56) can still be applied, because $\hat{u}_0$, $\hat{v}_0$ and $\hat{w}_0$ as required for these approximations are given by the first three of the clamped–end boundary conditions, Equations (5.49). However, the approximations (5.57) and (5.58) further involve $\hat{u}_{-1}$, $\hat{v}_{-1}$ and $\hat{w}_{-1}$, only the last of which is known and prescribed by the fourth clamped–end boundary condition, Equation (5.50). Thus, as far as $\hat{w}$ is concerned, (5.57) and (5.58) do not pose any difficulty. However, for $\hat{u}$ and $\hat{v}$, which happen not to have any fourth derivative, the third derivatives are approximated by the following forward difference representation, which still takes $\hat{u}_0$ and $\hat{v}_0$ into account but does not make use of $\hat{u}_{-1}$ and $\hat{v}_{-1}$,

$$\left(\frac{\partial^3 f}{\partial \xi^3}\right)_i = \frac{1}{2(\Delta\xi)^3}\left[-f_{i+3} + 6f_{i+2} - 12f_{i+1} + 10f_i - 3f_{i-1}\right] \quad + O[(\Delta\xi)^2]. \tag{5.59}$$

Similarly, for node $i = N$, the approximations (5.55) and (5.56) still hold; expression (5.58) is of no concern because none of $\hat{u}$, $\hat{v}$ and $\hat{w}$ has any fourth derivative; but the approximation (5.57) requires $\hat{u}_{N+2}$, $\hat{v}_{N+2}$ and $\hat{w}_{N+2}$, which are new unknowns and cannot be accounted for. This obstacle can be bypassed by using the following backward difference representation for third spatial derivatives

$$\left(\frac{\partial^3 f}{\partial \xi^3}\right)_i = \frac{1}{2(\Delta\xi)^3}\Big[3f_{i+1} - 10f_i + 12f_{i-1} - 6f_{i-2} + f_{i-3}\Big] \quad + O[(\Delta\xi)^2]. \tag{5.60}$$

It should be recalled here that although $\hat{u}_{N+1}$, $\hat{v}_{N+1}$ and $\hat{w}_{N+1}$ are also new unknowns [through expressions (5.55), (5.56) and (5.60)], they are in principle determinable by three additional equations given by the first three free-end boundary conditions [Equations (5.45)–(5.47)]. The derivation of (5.59) and (5.60) is presented in Appendix F.

For the sake of convenience and simplicity in writing the equations of motion for each nodal point in finite difference form, the following group of constants are defined:

$$\begin{aligned}
&\varsigma_1 = \frac{(\Delta t)^2}{\gamma},\ \ \varsigma_2 = \frac{\chi}{2\Delta t},\ \ \varsigma_3 = \varsigma_1\left(1 + 3\varsigma_2\right),\ \ a_1 = \frac{\varsigma_3\varepsilon_i^2}{(\Delta\xi)^2},\ \ a_2 = \frac{\varsigma_3 n^2}{2}(k+1)(1-\nu),\\
&a_3 = \frac{\varsigma_3\varepsilon_i n}{4\Delta\xi}(1+\nu),\ \ a_4 = \frac{\varsigma_3 k\varepsilon_i^3}{2(\Delta\xi)^3},\ \ a_5 = \frac{\varsigma_3\varepsilon_i}{2\Delta\xi}\left[\nu - \frac{kn^2}{2}(1-\nu)\right],\\
&b_1 = a_3,\ \ b_2 = \frac{\varsigma_3\varepsilon_i^2}{2(\Delta\xi)^2}(3k+1)(1-\nu),\ \ b_3 = \varsigma_3 n^2,\ \ b_4 = \frac{\varsigma_3 kn\varepsilon_i^2}{2(\Delta\xi)^2}(3-\nu),\ \ b_5 = \varsigma_3 n,\\
&c_1 = a_4,\ \ c_2 = a_5,\ \ c_3 = b_4,\ \ c_4 = b_5,\ \ c_5 = \frac{\varsigma_3 k\varepsilon_i^4}{(\Delta\xi)^4},\ \ c_6 = \frac{2\varsigma_3 kn^2}{(\Delta\xi)^2},\\
&c_7 = \varsigma_3\left[1 + k(n^2-1)^2\right],\ \ c_8 = \frac{\varsigma_3\nu\varepsilon_i}{2\Delta\xi},\ \ c_9 = \frac{\varsigma_3 k\nu n^2\varepsilon_i^2}{(\Delta\xi)^2},\ \ d_1 = \frac{\varepsilon_i}{2\Delta\xi},\ \ d_2 = n\nu,\\
&d_3 = \frac{k\varepsilon_i^2}{(\Delta\xi)^2},\ \ d_4 = \nu,\ \ d_5 = n,\ \ d_6 = \frac{\varepsilon_i(1+3k)}{2\Delta\xi},\ \ d_7 = \frac{3kn\varepsilon_i}{2\Delta\xi},\ \ d_8 = \frac{\varepsilon_i^2}{(\Delta\xi)^2},\ \ d_9 = n^2\nu,
\end{aligned} \tag{5.61}$$

as well as a group of functions of ξ, implicit via q_1, q_2 or q_3:

$$\begin{aligned}
&\hat{a}_1^j = \frac{\varsigma_1 q_1\varepsilon_i^2}{(\Delta\xi)^2},\ \ \hat{a}_2^j = \varsigma_1 q_3 n^2,\ \ \hat{a}_3^j = \varsigma_1 q_2 n,\ \ \hat{a}_4^j = \frac{\varsigma_1 q_3\varepsilon_i}{2\Delta\xi},\ \ \hat{a}_5^j = \varsigma_1 q_2,\\
&\hat{b}_1^j = \hat{a}_1^j,\ \ \hat{b}_2^j = \hat{a}_2^j,\ \ \hat{b}_3^j = \varsigma_1 q_3 n;\ \ \hat{c}_1^j = \hat{a}_4^j,\ \ \hat{c}_2^j = \hat{b}_3^j,\ \ \hat{c}_3^j = \hat{a}_1^j,\ \ \hat{c}_4^j = \hat{a}_2^j,
\end{aligned} \tag{5.62}$$

where the superscript j is the number of the node for which the function is evaluated.

After all time and spatial derivatives in Equations (5.41)–(5.43), (5.45)–(5.47), and (5.52) are appropriately substituted by the difference approximations given in (5.53)–(5.60), the resulting equations will be rearranged and rewritten in such a form that all nodal unknowns [corresponding to time level $(n+1)$] are on the left–hand side of the equation and all known quantities [associated with time levels n, $(n-1)$, and $(n-2)$] are on the right–hand side.

<u>For node 1</u>,

$$
\begin{aligned}
&(2 + 2a_1 + 2\hat{a}_1^1 + a_2 + \hat{a}_2^1)\hat{u}_1^{n+1} - \hat{a}_3^1\hat{v}_1^{n+1} - (a_4 + \hat{a}_5^1)\hat{w}_1^{n+1} - (a_1 + \hat{a}_1^1)\hat{u}_1^{n+1} - a_3\hat{v}_2^{n+1} \\
&\quad + (\hat{a}_4^1 - 2a_4 - a_5)\hat{w}_2^{n+1} + a_4\hat{w}_3^{n+1} = \varsigma_1\,(\hat{q}_x)_1^{n+1} + \mathcal{F}(\hat{u}_1) + \varsigma_2\,\{(2a_1 + a_2)\mathcal{L}(\hat{u}_1) \\
&\quad - a_4\mathcal{L}(\hat{w}_1) - a_1\mathcal{L}(\hat{u}_1) - a_3\mathcal{L}(\hat{v}_2) - (2a_4 + a_5)\mathcal{L}(\hat{w}_2) + a_4\mathcal{L}(\hat{w}_3)\}\,,
\end{aligned}
\tag{5.63}
$$

$$
\begin{aligned}
&(2 + 2\hat{b}_1^1 + 2b_2 + \hat{b}_2^1 + b_3)\hat{v}_1^{n+1} + (\hat{b}_3^1 + 2b_4 + b_5)\hat{w}_1^{n+1} + b_1\hat{u}_2^{n+1} - (\hat{b}_1^1 + b_2)\hat{v}_2^{n+1} - b_4\hat{w}_2^{n+1} \\
&\quad = \varsigma_1\,(\hat{q}_\theta)_1^{n+1} + \mathcal{F}(\hat{v}_1) + \varsigma_2\,\{(2b_2 + b_3)\mathcal{L}(\hat{v}_1) + (2b_4 + b_5)\mathcal{L}(\hat{w}_1) + b_1\mathcal{L}(\hat{u}_2) \\
&\quad - b_2\mathcal{L}(\hat{v}_2) - b_4\mathcal{L}(\hat{w}_2)\}\,,
\end{aligned}
\tag{5.64}
$$

$$
\begin{aligned}
&-10c_1\hat{u}_1^{n+1} + (\hat{c}_2^1 + 2c_3 + c_4)\hat{v}_1^{n+1} + (2 + 2\hat{c}_3^1 + \hat{c}_4^1 + 7c_5 + 2c_6 + c_7)\hat{w}_1^{n+1} + (12c_1 - \hat{c}_1^1 + c_2)\hat{u}_2^{n+1} \\
&\quad - c_3\hat{v}_2^{n+1} - (\hat{c}_3^1 + 4c_5 + c_6)\hat{w}_2^{n+1} - 6c_1\hat{u}_3^{n+1} + c_5\hat{w}_3^{n+1} + c_1\hat{u}_4^{n+1} = \varsigma_1\,(\hat{q}_r)_1^{n+1} + \mathcal{F}(\hat{w}_1) \\
&\quad + \varsigma_2\,\{-10c_1\mathcal{L}(\hat{u}_1) + (2c_3 + c_4)\mathcal{L}(\hat{v}_1) + (7c_5 + 2c_6 + c_7)\mathcal{L}(\hat{w}_1) + (12c_1 + c_2)\mathcal{L}(\hat{u}_2) \\
&\quad - c_3\mathcal{L}(\hat{v}_2) - (4c_5 + c_6)\mathcal{L}(\hat{w}_2) - 6c_1\mathcal{L}(\hat{u}_3) + c_5\mathcal{L}(\hat{w}_3) + c_1\mathcal{L}(\hat{u}_4)\}\,,
\end{aligned}
\tag{5.65}
$$

where $\mathcal{F}(\ )$ and $\mathcal{L}(\ )$ will be defined by Equations (5.75).

<u>For node i such that $2 \leq i \leq (N-1)$</u>,

$$
\begin{aligned}
&-a_4\hat{w}_{i-2}^{n+1} - (a_1 + \hat{a}_1^i)\hat{u}_{i-1}^{n+1} + a_3\hat{v}_{i-1}^{n+1} + (2a_4 - \hat{a}_4^i + a_5)\hat{w}_{i-1}^{n+1} + (2 + 2a_1 + 2\hat{a}_1^i + a_2 + \hat{a}_2^i)\hat{u}_i^{n+1} \\
&\quad - \hat{a}_3^i\hat{v}_i^{n+1} - \hat{a}_5^i\hat{w}_i^{n+1} - (a_1 + \hat{a}_1^i)\hat{u}_{i+1}^{n+1} - a_3\hat{v}_{i+1}^{n+1} - (2a_4 - \hat{a}_4^i + a_5)\hat{w}_{i+1}^{n+1} + a_4\hat{w}_{i+2}^{n+1} \\
&\quad = \varsigma_1\,(\hat{q}_x)_i^{n+1} + \mathcal{F}(\hat{v}_i) + \varsigma_2\,\{-a_4\mathcal{L}(\hat{w}_{i-2}) - a_1\mathcal{L}(\hat{u}_{i-1}) + a_3\mathcal{L}(\hat{v}_{i-1}) + (2a_4 + a_5)\mathcal{L}(\hat{w}_{i-1}) \\
&\quad + (2a_1 + a_2)\mathcal{L}(\hat{u}_i) - a_1\mathcal{L}(\hat{u}_{i+1}) - a_3\mathcal{L}(\hat{v}_{i+1}) - (2a_4 + a_5)\mathcal{L}(\hat{w}_{i+1}) + a_4\mathcal{L}(\hat{w}_{i+2})\}\,,
\end{aligned}
\tag{5.66}
$$

$$
\begin{aligned}
&-b_1\hat{u}_{i-1}^{n+1} - (\hat{b}_1^i + b_2)\hat{v}_{i-1}^{n+1} - b_4\hat{w}_{i-1}^{n+1} + (2 + 2\hat{b}_1^i + 2b_2 + \hat{b}_2^i + b_3)\hat{v}_i^{n+1} + (\hat{b}_3^i + 2b_4 + b_5)\hat{w}_i^{n+1} \\
&+ b_1\hat{u}_{i+1}^{n+1} - (\hat{b}_1^i + b_2)\hat{v}_{i+1}^{n+1} - b_4\hat{w}_{i+1}^{n+1} = \varsigma_1\,(\hat{q}_\theta)_i^{n+1} + \mathcal{F}(\hat{v}_i) + \varsigma_2\,\{-b_1\mathcal{L}(\hat{u}_{i-1}) - b_2\mathcal{L}(\hat{v}_{i-1}) \\
&- b_4\mathcal{L}(\hat{w}_{i-1}) + (2b_2 + b_3)\mathcal{L}(\hat{v}_i) + (2b_4 + b_5)\mathcal{L}(\hat{w}_i) + b_1\mathcal{L}(\hat{u}_{i+1}) - b_2\mathcal{L}(\hat{v}_{i+1}) - b_4\mathcal{L}(\hat{w}_{i+1})\}\,,
\end{aligned}
\tag{5.67}
$$

$$
\begin{aligned}
&c_1\hat{u}_{i-2}^{n+1} + c_5\hat{w}_{i-2}^{n+1} - (2c_1 - \hat{c}_1^i + c_2)\hat{u}_{i-1}^{n+1} - c_3\hat{v}_{i-1}^{n+1} - (\hat{c}_3^i + 4c_5 + c_6)\hat{w}_{i-1}^{n+1} + (\hat{c}_2^i + 2c_3 + c_4)\hat{v}_i^{n+1} \\
&\quad + (2 + 2\hat{c}_3^i + \hat{c}_4^i + 6c_5 + 2c_6 + c_7)\hat{w}_i^{n+1} + (2c_1 - \hat{c}_1^i + c_2)\hat{u}_{i+1}^{n+1} - c_3\hat{v}_{i+1}^{n+1} - (\hat{c}_3^i + 4c_5 + c_6)\hat{w}_{i+1}^{n+1}
\end{aligned}
$$

$$
- c_1\hat{u}_{i+2}^{n+1} + c_5\hat{w}_{i+2}^{n+1} = \zeta_1\,(\hat{q}_r)_i^{n+1} + \mathcal{F}(\hat{w}_i) + \zeta_2\,\{c_1\mathcal{L}(\hat{u}_{i-2}) + c_5\mathcal{L}(\hat{w}_{i-2}) - (2c_1 + c_2)\mathcal{L}(\hat{u}_{i-1})
- c_3\mathcal{L}(\hat{v}_{i-1}) - (4c_5 + c_6)\mathcal{L}(\hat{w}_{i-1}) + (2c_3 + c_4)\mathcal{L}(\hat{v}_i) + (6c_5 + 2c_6 + c_7)\mathcal{L}(\hat{w}_i)
+ (2c_1 + c_2)\mathcal{L}(\hat{u}_{i+1}) - c_3\mathcal{L}(\hat{v}_{i+1}) - (4c_5 + c_6)\mathcal{L}(\hat{w}_{i+1}) - c_1\mathcal{L}(\hat{u}_{i+2}) + c_5\mathcal{L}(\hat{w}_{i+2})\}\,. \tag{5.68}
$$

For node N,

$$
a_4\hat{w}_{N-3}^{n+1} - 6a_4\hat{w}_{N-2}^{n+1} - (a_1 + \hat{a}_1^N)\hat{u}_{N-1}^{n+1} + a_3\hat{v}_{N-1}^{n+1} + (12a_4 - \hat{a}_4^N + a_5)\hat{w}_{N-1}^{n+1}
+ (2 + 2a_1 + 2\hat{a}_1^N + a_2 + \hat{a}_2^N)\hat{u}_N^{n+1} - \hat{a}_3^N\hat{v}_N^{n+1} - (10a_4 + \hat{a}_5^N)\hat{w}_N^{n+1} - (a_1 + \hat{a}_1^N)\hat{u}_{N+1}^{n+1}
- a_3\hat{v}_{N+1}^{n+1} + (3a_4 + \hat{a}_4^N - a_5)\hat{w}_{N+1}^{n+1} = \zeta_1\,(\hat{q}_x)_N^{n+1} + \mathcal{F}(\hat{u}_N) + \zeta_2\,\{a_4\mathcal{L}(\hat{w}_{N-3}) - 6a_4\mathcal{L}(\hat{w}_{N-2})
- a_1\mathcal{L}(\hat{u}_{N-1}) + a_3\mathcal{L}(\hat{v}_{N-1}) + (12a_4 + a_5)\mathcal{L}(\hat{w}_{N-1}) + (2a_1 + a_2)\mathcal{L}(\hat{u}_N) - 10a_4\mathcal{L}(\hat{w}_N)
- a_1\mathcal{L}(\hat{u}_{N+1}) - a_3\mathcal{L}(\hat{v}_{N+1}) + (3a_4 - a_5)\mathcal{L}(\hat{w}_{N+1})\}\,, \tag{5.69}
$$

$$
-b_1\hat{u}_{N-1}^{n+1} - (\hat{b}_1^N + b_2)\hat{v}_{N-1}^{n+1} - b_4\hat{w}_{N-1}^{n+1} + (2 + 2\hat{b}_1^N + 2b_2 + \hat{b}_2^N + b_3)\hat{v}_N^{n+1} + (\hat{b}_3^N + 2b_4 + b_5)\hat{w}_N^{n+1}
+ b_1\hat{u}_{N+1}^{n+1} - (\hat{b}_1^N + b_2)\hat{v}_{N+1}^{n+1} - b_4\hat{w}_{N+1}^{n+1} = \zeta_1\,(\hat{q}_\theta)_N^{n+1} + \mathcal{F}(\hat{v}_N) + \zeta_2\,\{-b_1\mathcal{L}(\hat{u}_{N-1})
- b_2\mathcal{L}(\hat{v}_{N-1}) - b_4\mathcal{L}(\hat{w}_{N-1}) + (2b_2 + b_3)\mathcal{L}(\hat{v}_N) + (2b_4 + b_5)\mathcal{L}(\hat{w}_N)
+ b_1\mathcal{L}(\hat{u}_{N+1}) - b_2\mathcal{L}(\hat{v}_{N+1}) - b_4\mathcal{L}(\hat{w}_{N+1})\}\,, \tag{5.70}
$$

$$
(\hat{c}_1^N - c_8)\hat{u}_{N-1}^{n+1} - (\hat{c}_3^N + c_9)\hat{w}_{N-1}^{n+1} + (\hat{c}_2^N + c_4)\hat{v}_N^{n+1} + (2 + 2\hat{c}_3^N + \hat{c}_4^N + c_7 + 2c_9)\hat{w}_N^{n+1}
- (\hat{c}_1^N - c_8)\hat{u}_{N+1}^{n+1} - (\hat{c}_3^N + c_9)\hat{w}_{N+1}^{n+1} = \zeta_1\,(\hat{q}_r)_N^{n+1} + \mathcal{F}(\hat{w}_N) + \zeta_2\,\{-c_8\mathcal{L}(\hat{u}_{N-1})
- c_9\mathcal{L}(\hat{w}_{N-1}) + c_4\mathcal{L}(\hat{v}_N) + (c_7 + 2c_9)\mathcal{L}(\hat{w}_N) + c_8\mathcal{L}(\hat{u}_{N+1}) - c_9\mathcal{L}(\hat{w}_{N+1})\}\,; \tag{5.71}
$$

there are also the following equations resulting from the free–end boundary conditions:

$$
- d_1\hat{u}_{N-1}^{n+1} - d_3\hat{w}_{N-1}^{n+1} + d_2\hat{v}_N^{n+1} + (2d_3 + d_4)\hat{w}_N^{n+1} + d_1\hat{u}_{N+1}^{n+1} - d_3\hat{w}_{N+1}^{n+1} = 0, \tag{5.72}
$$

$$
- d_6\hat{v}_{N-1}^{n+1} - d_7\hat{w}_{N-1}^{n+1} - d_5\hat{u}_N^{n+1} + d_6\hat{v}_{N+1}^{n+1} + d_7\hat{w}_{N+1}^{n+1} = 0, \tag{5.73}
$$

$$
d_5\hat{u}_{N-1}^{n+1} + d_8\hat{w}_{N-1}^{n+1} - d_2\hat{v}_N^{n+1} - (2d_8 + d_9)\hat{w}_N^{n+1} - d_5\hat{u}_{N+1}^{n+1} + d_8\hat{w}_{N+1}^{n+1} = 0. \tag{5.74}
$$

In the foregoing, Equations (5.63)–(5.71), $\mathcal{F}(\;)$ and $\mathcal{L}(\;)$ are two short–hand notations, and they are defined as

$$
\mathcal{F}(\;) = 5(\;)^n - 4(\;)^{n-1} + (\;)^{n-2}, \qquad \mathcal{L}(\;) = 4(\;)^n - (\;)^{n-1}. \tag{5.75}
$$

Equations (5.63)–(5.74) are subsequently assembled into the global matrix equation of the form

$$[A]\{X^{n+1}\} = \{R^{n+1}\}$$

or equivalently,

$$\{X^{n+1}\} = [A]^{-1}\{R^{n+1}\}, \tag{5.76}$$

where $[A]$ is a constant coefficient matrix of size $3(N+1)$ by $3(N+1)$; as a result, $[A]^{-1}$ will be calculated only once in the first time step and then reused over and over in all subsequent time steps; $\{X^{n+1}\}$ is a vector of size $3(N+1)$, containing unknown nodal displacements at the time level $(n+1)$, that is

$$\{X^{n+1}\}^{\mathrm{T}} = \{\ \ldots \mid \underbrace{\hat{u}_i^{n+1}\ \ \hat{v}_i^{n+1}\ \ \hat{w}_i^{n+1}}_{\text{at node } i} \mid \ldots\} \qquad \text{for } 1 \le i \le (N+1).$$

Initially, the displacements at node $(N+1)$ which is beyond the free end of the shell are not known at $t = 0, -\Delta t$ and $-2(\Delta t)$; here, they are linearly extrapolated from those at nodes N and $(N-1)$ (the reason for doing this will become obvious in the next paragraph). $\{R^{n+1}\}$ is a vector of size $3(N+1)$ and is a function of $\{Q^{n+1}\}$, $\{X^n\}$, $\{X^{n-1}\}$ and $\{X^{n-2}\}$, where

$$\{Q^{n+1}\}^{\mathrm{T}} = \{\ \ldots \mid \underbrace{(\hat{q}_x)_i^{n+1}\ \ (\hat{q}_\theta)_i^{n+1}\ \ (\hat{q}_r)_i^{n+1}}_{\text{at node } i} \mid \ldots \mid \underbrace{0 \quad 0 \quad 0}_{\text{at node } (N+1)}\} \qquad \text{for } 1 \le i \le N.$$

The elements of $\{Q^{n+1}\}$ will be determined in Section 5.3.4.

As may be expected, the present time integration procedure is not self-starting; for the first time step $(n = 0)$, the vectors $\{X^0\}$, $\{X^{-1}\}$ and $\{X^{-2}\}$, corresponding to $t = 0$, $-\Delta t$ and $-2(\Delta t)$, respectively, are needed in order to determine $\{X^1\}$ according to Equation (5.76). These vectors will be evaluated below using the theory presented in Chapter 2; from the functional forms (2.31) taken for the shell displacements, it is seen that

$$\{X^{-2}\} = e^{-2i\Omega\Delta t}\{X^0\}, \quad \{X^{-1}\} = e^{-i\Omega\Delta t}\{X^0\}, \quad \{X^1\} = e^{i\Omega\Delta t}\{X^0\}, \tag{5.77}$$

where $\{X^0\}$ corresponds to the initial conditions.

It should be pointed out that the theory in Chapter 2 gave frequencies of oscillation and mode shapes of the shell, but not the actual displacements. Thus, the magnitudes of the elements of $\{X^0\}$ for the present analysis have to be arbitrarily imposed; after calculation from (2.31), normalized $\{X^0\}$ is scaled down by a factor of 1/100 of the annular gap width, i.e.

$$\{X^0\} \;=\; \left[\frac{\varepsilon_o - \varepsilon_i}{100}\right]\{X^0\}. \tag{5.78}$$

5.3.3 Solution to the Linearized Navier–Stokes Equations

The solution of the linearized Navier–Stokes equations is much more complex than that of the shell equations, principally because it is not possible in this case to reduce the problem to one involving only one spatial independent variable, as will be seen in the following.

5.3.3.1 Numerical Formulation

For purposes of solving the linearized Navier–Stokes and continuity equations [Equations (5.21)–(5.24)], v_r, v_θ, v_x and p are taken to be of the form

$$\begin{Bmatrix} v_r(x,\theta,r,t) \\ v_\theta(x,\theta,r,t) \\ v_x(x,\theta,r,t) \\ p(x,\theta,r,t) \end{Bmatrix} = \sum_{n=1}^{\infty} \begin{Bmatrix} \bar{v}_r(x,r,t)\cos n\theta \\ \bar{v}_\theta(x,r,t)\sin n\theta \\ \bar{v}_x(x,r,t)\cos n\theta \\ \bar{p}(x,r,t)\cos n\theta \end{Bmatrix}, \tag{5.79}$$

which are then substituted into Equations (5.21)–(5.24), yielding

$$\sum_{n=1}^{\infty}\left\{\frac{\partial \bar{v}_r}{\partial t} + G_r(\bar{v}_r,\bar{v}_\theta,\bar{v}_x,\bar{p})\right\}\cos n\theta \;=\; 0, \tag{5.80}$$

$$\sum_{n=1}^{\infty}\left\{\frac{\partial \bar{v}_\theta}{\partial t} + G_\theta(\bar{v}_r,\bar{v}_\theta,\bar{v}_x,\bar{p})\right\}\sin n\theta \;=\; 0, \tag{5.81}$$

$$\sum_{n=1}^{\infty}\left\{\frac{\partial \bar{v}_x}{\partial t} + G_x(\bar{v}_r,\bar{v}_\theta,\bar{v}_x,\bar{p})\right\}\cos n\theta \;=\; 0, \tag{5.82}$$

$$\sum_{n=1}^{\infty} G_\nabla(\bar{v}_r,\bar{v}_\theta,\bar{v}_x)\cos n\theta \;=\; 0, \tag{5.83}$$

where

$$G_r(\bar{v}_r,\bar{v}_\theta,\bar{v}_x,\bar{p}) \;=\; U(r)\frac{\partial v_r}{\partial x} + \frac{\partial \bar{p}}{\partial r} - 2\frac{\mathrm{d}\nu}{\mathrm{d}r}\frac{\partial \bar{v}_r}{\partial r}$$

$$
\begin{aligned}
& \quad -\nu\left\{\frac{\partial^2\bar{v}_r}{\partial x}+\frac{1}{r}\frac{\partial}{\partial r}\left(r\frac{\partial\bar{v}_r}{\partial r}\right)-\frac{(1+n^2)}{r^2}\bar{v}_r-\frac{2n}{r^2}\bar{v}_\theta\right\}, \\
G_\theta(\bar{v}_r,\bar{v}_\theta,\bar{v}_x,\bar{p}) &= U(r)\frac{\partial v_\theta}{\partial x}-\frac{n}{r}\bar{p}-\frac{\mathrm{d}\nu}{\mathrm{d}r}\left(\frac{\partial\bar{v}_\theta}{\partial r}-\frac{n}{r}\bar{v}_r\right) \\
& \quad -\nu\left\{\frac{\partial^2\bar{v}_\theta}{\partial x^2}+\frac{1}{r}\frac{\partial}{\partial r}\left(r\frac{\partial\bar{v}_\theta}{\partial r}\right)-\frac{1+n^2}{r^2}\bar{v}_\theta-\frac{2n}{r^2}\bar{v}_r\right\}, \\
G_x(\bar{v}_r,\bar{v}_\theta,\bar{v}_x,\bar{p}) &= U(r)\frac{\partial v_x}{\partial x}+U'(r)\bar{v}_r+\frac{\partial p}{\partial x}-\frac{\mathrm{d}\nu}{\mathrm{d}r}\left(\frac{\partial\bar{v}_x}{\partial r}+\frac{\partial\bar{v}_r}{\partial x}\right) \\
& \quad -\nu\left\{\frac{\partial^2\bar{v}_x}{\partial x^2}+\frac{1}{r}\frac{\partial}{\partial r}\left(r\frac{\partial\bar{v}_x}{\partial r}\right)-\frac{n^2}{x^2}\bar{v}_x\right\}, \\
G_\nabla(\bar{v}_r,\bar{v}_\theta,\bar{v}_x) &= \frac{1}{r}\frac{\partial}{\partial r}(r\bar{v}_r)+\frac{n}{r}\bar{v}_\theta+\frac{\partial\bar{v}_x}{\partial x}.
\end{aligned}
$$

As $\sin n\theta$ and $\cos n\theta$ are generally not zero, their coefficients in the infinite series (5.80)–(5.83) must vanish, or equivalently

$$\frac{\partial\bar{\mathbf{v}}}{\partial t}+\mathbf{G}(\bar{\mathbf{v}},\bar{p}) = 0, \tag{5.84}$$

$$G_\nabla(\bar{\mathbf{v}}) = 0, \tag{5.85}$$

where $\bar{\mathbf{v}}=(\bar{v}_r,\bar{v}_\theta,\bar{v}_x)$, and $\mathbf{G}(\bar{\mathbf{v}},\bar{p})=[G_r(\bar{\mathbf{v}},\bar{p}),G_\theta(\bar{\mathbf{v}},\bar{p}),G_x(\bar{\mathbf{v}},\bar{p})]$; Equation (5.84) thus represents three equations corresponding to the r–, θ– and x–coordinate.

As was mentioned in Section 5.3.1, the numerical method developed by Soh and Goodrich (1988) will be adopted in this study to solve Equation (5.84) with the velocity components satisfying the constraint (5.85). Since the background of the method was fully discussed by the authors, it will not be repeated here; nevertheless, every step of the solution procedure will be explained below in detail.

To be consistent with the fully implicit scheme employed in Section 5.3.2 for time derivatives, the two–point backward difference approximation is now used to discretize Equation (5.84) in physical time

$$\frac{\bar{\mathbf{v}}^{n+1}-\bar{\mathbf{v}}^n}{\Delta t}+\mathbf{G}(\bar{\mathbf{v}}^{n+1},\bar{p}^{n+1}) = 0, \tag{5.86}$$

which has first–order accuracy in time. Since the continuity equation (5.85) should be satisfied in every time step,

$$G_\nabla(\bar{\mathbf{v}}^{n+1}) = 0. \tag{5.87}$$

It is noted that, by means of the new notations

$$\hat{\mathbf{v}}^{n+1} = \bar{\mathbf{v}}^{n+1} - \bar{\mathbf{v}}^{n}, \qquad \hat{p}^{n+1} = \bar{p}^{n+1} - \bar{p}^{n}, \tag{5.88}$$

Equations (5.86) and (5.87) may be rewritten as

$$\hat{\mathbf{v}}^{n+1} + \Delta t\, \mathbf{G}(\hat{\mathbf{v}}^{n+1}, \hat{p}^{n+1}) = -\Delta t\, \mathbf{G}(\bar{\mathbf{v}}^{n}, \bar{p}^{n}), \tag{5.89}$$

$$G_{\nabla}(\hat{\mathbf{v}}^{n+1}) = 0, \tag{5.90}$$

since $\mathbf{G}(\ )$ and $G_{\nabla}(\ )$ are *linear* operators.

For the solution of Equation (5.89) satisfying the divergence–free constraint (5.90) on the perturbation velocity, a continuous auxiliary system in pseudo–time and involving an artificial compressibility is introduced

$$\frac{\partial \hat{\mathbf{v}}}{\partial \tau} + \hat{\mathbf{v}} + \Delta t\, \mathbf{G}(\hat{\mathbf{v}}, \hat{p}) = -\Delta t\, \mathbf{G}(\bar{\mathbf{v}}^{n}, \bar{p}^{n}), \tag{5.91}$$

$$\beta \frac{\partial \hat{p}}{\partial \tau} + G_{\nabla}(\hat{\mathbf{v}}) = 0, \tag{5.92}$$

where τ is a *pseudo–time* which should be distinguished from the *physical time* t, β is the artificial compressibility coefficient, and $\hat{\mathbf{v}} = \bar{\mathbf{v}}^{*} - \bar{\mathbf{v}}^{n}$, $\hat{p} = \bar{p}^{*} - \bar{p}^{n}$; here, the asterisk denotes a transient value in pseudo–time. It is seen from Equations (5.91) and (5.92) that, as the steady state is reached in pseudo–time, $\partial \hat{\mathbf{v}}/\partial \tau$ and $\partial \hat{p}/\partial \tau$ are both virtually zero; hence, $\hat{\mathbf{v}}$ and $\hat{p}$ become $\hat{\mathbf{v}}^{n+1}$ and $\hat{p}^{n+1}$, respectively. Evidently, the solution of the set (5.89) and (5.90) in each physical time step is practically the same as the steady solution of the set (5.91) and (5.92) in pseudo–time. Equations (5.91) and (5.92) therefore have no physical meaning until reaching the steady state in pseudo–time.

Equations (5.91) and (5.92) may be written in a more compact form as

$$\frac{\partial \mathbf{\Pi}}{\partial \tau} + (\mathbf{A}_r + \mathbf{A}_x + \mathbf{A}_\theta)\mathbf{\Pi} = \mathbf{R}, \tag{5.93}$$

where $\mathbf{R}$ is kept constant at its value at the physical–time level n, and

$$\mathbf{\Pi} = \left\{ \begin{array}{c} \hat{v}_r \\ \hat{v}_\theta \\ \hat{v}_x \\ \hat{p} \end{array} \right\}, \qquad \mathbf{R} = \left\{ \begin{array}{c} -\alpha G_r(\bar{\mathbf{v}}^n, \bar{p}^n) \\ -\alpha G_\theta(\bar{\mathbf{v}}^n, \bar{p}^n) \\ -\alpha G_x(\bar{\mathbf{v}}^n, \bar{p}^n) \\ 0 \end{array} \right\}, \qquad \alpha = \Delta t,$$

and

$$\mathbf{A}_r = \alpha \begin{bmatrix} \frac{1}{\alpha} - 2\frac{\mathrm{d}\nu}{\mathrm{d}r}\frac{\partial}{\partial r} - \frac{\nu}{r}\frac{\partial}{\partial r}\left(r\frac{\partial}{\partial r}\right) & 0 & 0 & \frac{\partial}{\partial r} \\ 0 & -\frac{\mathrm{d}\nu}{\mathrm{d}r}\frac{\partial}{\partial r} - \frac{\nu}{r}\frac{\partial}{\partial r}\left(r\frac{\partial}{\partial r}\right) & 0 & 0 \\ 0 & 0 & -\frac{\mathrm{d}\nu}{\mathrm{d}r}\frac{\partial}{\partial r} - \frac{\nu}{r}\frac{\partial}{\partial r}\left(r\frac{\partial}{\partial r}\right) & 0 \\ \frac{1}{\alpha\beta}\left(\frac{1}{r} + \frac{\partial}{\partial r}\right) & 0 & 0 & 0 \end{bmatrix},$$

$$\mathbf{A}_x = \alpha \begin{bmatrix} U(r)\frac{\partial}{\partial x} - \nu\frac{\partial^2}{\partial x^2} & \frac{2\nu n}{r^2} & 0 & 0 \\ 0 & U(r)\frac{\partial}{\partial x} - \nu\frac{\partial^2}{\partial x^2} & 0 & 0 \\ -\frac{\mathrm{d}\nu}{\mathrm{d}r}\frac{\partial}{\partial x} & 0 & \frac{1}{\alpha} + U(r)\frac{\partial}{\partial x} - \nu\frac{\partial^2}{\partial x^2} & \frac{\partial}{\partial x} \\ 0 & 0 & \frac{1}{\alpha\beta}\frac{\partial}{\partial x} & 0 \end{bmatrix},$$

$$\mathbf{A}_\theta = \alpha \begin{bmatrix} \frac{\nu(1+n^2)}{r^2} & 0 & 0 & 0 \\ \frac{n}{r}\left(\frac{\mathrm{d}\nu}{\mathrm{d}r} + \frac{2\nu}{r}\right) & \frac{1}{\alpha} + \frac{\nu(1+n^2)}{r^2} & 0 & -\frac{n}{r} \\ U'(r) & 0 & \frac{\nu n^2}{r^2} & 0 \\ 0 & \frac{1}{\alpha\beta}\frac{n}{r} & 0 & 0 \end{bmatrix}.$$

Equation (5.93) may be integrated in pseudo–time through two intermediate steps denoted by * and **:

$$\begin{aligned} \frac{\mathbf{\Pi}^* - \mathbf{\Pi}^k}{\Delta\tau} + \mathbf{A}_r\mathbf{\Pi}^* + (\mathbf{A}_x + \mathbf{A}_\theta)\mathbf{\Pi}^k &= \mathbf{R}, \\ \frac{\mathbf{\Pi}^{**} - \mathbf{\Pi}^k}{\Delta\tau} + \mathbf{A}_r\mathbf{\Pi}^* + \mathbf{A}_x\mathbf{\Pi}^{**} + \mathbf{A}_\theta\mathbf{\Pi}^k &= \mathbf{R}, \\ \frac{\mathbf{\Pi}^{k+1} - \mathbf{\Pi}^k}{\Delta\tau} + \mathbf{A}_r\mathbf{\Pi}^* + \mathbf{A}_x\mathbf{\Pi}^{**} + \mathbf{A}_\theta\mathbf{\Pi}^{k+1} &= \mathbf{R}. \end{aligned}$$

Briley and McDonald (1980) introduced a compact form of the above equations, which is called the "delta form",

$$(\mathbf{I} + \Delta\tau\mathbf{A}_r)\tilde{\mathbf{\Pi}} = \Delta\tau\left[\mathbf{R} - (\mathbf{A}_r + \mathbf{A}_x + \mathbf{A}_\theta)\mathbf{\Pi}^k\right], \tag{5.94}$$

$$(\mathbf{I} + \Delta\tau\mathbf{A}_x)\check{\mathbf{\Pi}} = \tilde{\mathbf{\Pi}}, \tag{5.95}$$

$$(\mathbf{I} + \Delta\tau\mathbf{A}_\theta)\Delta\mathbf{\Pi} = \check{\mathbf{\Pi}}, \tag{5.96}$$

where $\tilde{\mathbf{\Pi}} = \mathbf{\Pi}^* - \mathbf{\Pi}^k$, $\check{\mathbf{\Pi}} = \mathbf{\Pi}^{**} - \mathbf{\Pi}^k$, $\Delta\mathbf{\Pi} = \mathbf{\Pi}^{k+1} - \mathbf{\Pi}^k$, $\mathbf{I}$ is the identity matrix of size 4×4, and k denotes a certain pseudo–time step. The method of solution represented by Equations (5.94)–(5.96) is commonly referred to as the ADI (Alternating Direction Implicit) scheme, and is carried out on a staggered grid (further discussion on the staggered grid is given in Appendix H). Equations (5.94), (5.95) and (5.96) are called the r–, x– and θ–sweep, respectively. In the staggered grid, $\hat{v}_r$ is coupled with the pressure $\hat{p}$ during the r–sweep. Similarly, $\hat{v}_x$ and $\hat{v}_\theta$ are coupled with $\hat{p}$ in the x– and θ–sweep, respectively.

5.3.3.2 Initial and Boundary Conditions

Since the physical–time system (5.89)–(5.90) and the pseudo–time system (5.91)–(5.92) are both initial boundary value problems, initial and boundary conditions must be specified to complete these systems. For the problem under consideration, the initial flow variables for the systems (5.89)–(5.90) and (5.91)–(5.92) are taken to be zero:

$$\bar{\mathrm{v}} = \bar{p} = 0 \quad \text{at } t = 0, \qquad \hat{\mathrm{v}} = \hat{p} = 0 \quad \text{at } \tau = 0. \tag{5.97}$$

At the inlet ($\xi = 0$), the flow is assumed to be undisturbed; in essence, flow perturbations are zero, or equivalently

$$\bar{\mathrm{v}} = \hat{\mathrm{v}} = \bar{p} = \hat{p} = 0 \qquad \text{at } \xi = 0. \tag{5.98}$$

At the exit ($\xi = 1$), flow perturbations must tend to die out according to any of the realistic outflow models described in Chapter 2. Explanations on how to impose this boundary condition will be given when the x–sweep is considered (Section 5.3.3.3).

Because the staggered grid is being used, the pressure boundary conditions are not needed at the physical boundaries, which are a rigid wall and a flexible (moving) wall in the present problem; this is a great advantage of this method. In the following analysis, η is the nondimensionalized radial variable, $\eta = r/L$, as defined in Equations (5.40). Thus, at $\eta = \varepsilon_o$ (rigid wall), the velocity boundary conditions are

$$\bar{\mathrm{v}} = \hat{\mathrm{v}} = 0, \tag{5.99}$$

while at $\eta = \varepsilon_i$ (moving wall),

$$\bar{\mathrm{v}}^n = \left(\frac{\partial \bar{\mathrm{u}}}{\partial t}\right)^n = \frac{L}{2\Delta t}(\hat{\mathrm{u}}^{n-2} - 4\hat{\mathrm{u}}^{n-1} + 3\hat{\mathrm{u}}^n) \quad + O[(\Delta t)^2], \tag{5.100}$$

where $\hat{\mathbf{u}} = (\hat{u}, \hat{v}, \hat{w})$ is a vector whose components are the shell displacements, and

$$\hat{\mathbf{v}}^{n+1} = \bar{\mathbf{v}}^{n+1} - \bar{\mathbf{v}}^{n}; \tag{5.101}$$

nevertheless, $\bar{\mathbf{v}}^{n+1}$ is not known at the beginning of the physical–time step $(n+1)$, and hence an *iterative* procedure has to be employed here. First of all, the right–hand side of Equation (5.101) is approximated from the known quantities in previous time steps: $\bar{\mathbf{v}}^{n-2}$, $\bar{\mathbf{v}}^{n-1}$ and $\bar{\mathbf{v}}^{n}$. This can be achieved by expanding Equation (5.101) in a Taylor series about n,

$$\begin{aligned}
\hat{\mathbf{v}}^{n+1} &= \left\{\bar{\mathbf{v}}^{n} + \Delta t\left(\frac{\partial \bar{\mathbf{v}}}{\partial t}\right)^{n} + \frac{(\Delta t)^2}{2}\left(\frac{\partial^2 \bar{\mathbf{v}}}{\partial t^2}\right)^{n} \quad + \mathcal{O}[(\Delta t)^3]\right\} - \bar{\mathbf{v}}^{n} \\
&= \Delta t\left(\frac{\partial \bar{\mathbf{v}}}{\partial t}\right)^{n} + \frac{(\Delta t)^2}{2}\left(\frac{\partial^2 \bar{\mathbf{v}}}{\partial t^2}\right)^{n} \quad + \mathcal{O}[(\Delta t)^3] \\
&= \Delta t\left\{\frac{\bar{\mathbf{v}}^{n-2} - 4\bar{\mathbf{v}}^{n-1} + 3\bar{\mathbf{v}}^{n}}{2\Delta t}\right\} + \frac{(\Delta t)^2}{2}\left\{\frac{\bar{\mathbf{v}}^{n-2} - 2\bar{\mathbf{v}}^{n-1} + \bar{\mathbf{v}}^{n}}{(\Delta t)^2}\right\} \quad + \mathcal{O}[(\Delta t)^3],
\end{aligned}$$

or

$$\hat{\mathbf{v}}^{n+1} = \bar{\mathbf{v}}^{n-2} - 3\bar{\mathbf{v}}^{n-1} + 2\bar{\mathbf{v}}^{n} \quad + \mathcal{O}[(\Delta t)^3]. \tag{5.102}$$

Then, from the approximation (5.102), $\hat{\mathbf{u}}^{n+1}$ is obtained [through the solution of Equation (5.76)], thus allowing $\bar{\mathbf{v}}^{n+1}$ and $\hat{\mathbf{v}}^{n+1}$ to be recalculated according to Equations (5.100) and (5.101), respectively. A new value of $\hat{\mathbf{u}}^{n+1}$ is again obtained, and the same procedure is repeated until the change in $\hat{\mathbf{u}}^{n+1}$ between any two successive iterations is negligibly small. Numerically, this condition is considered to be achieved when, between any two successive iterations,

$$\text{Max}\left\{\frac{\Delta \hat{u}_{i_1}^{n+1}}{\hat{u}_{i_1}^{n+1}}, \frac{\Delta \hat{v}_{i_2}^{n+1}}{\hat{v}_{i_2}^{n+1}}, \frac{\Delta \hat{w}_{i_3}^{n+1}}{\hat{w}_{i_3}^{n+1}}\right\} \le 10^{-3}, \tag{5.103}$$

where i_1, i_2 and i_3 are integers, representing the numbers of some nodes on the shell such that $1 \le i_1, i_2, i_3 \le (N+1)$.

For $n = 0$, Equations (5.100) and (5.102) become

$$\bar{\mathbf{v}}^{0} = \frac{L}{2\Delta t}(\hat{\mathbf{u}}^{-2} - 4\hat{\mathbf{u}}^{-1} + 3\hat{\mathbf{u}}^{0}) \quad + \mathcal{O}[(\Delta t)^2] \tag{5.104}$$

and

$$\hat{\mathbf{v}}^{1} = \bar{\mathbf{v}}^{1} - \bar{\mathbf{v}}^{0}; \tag{5.105}$$

here, according to Equation (5.100), $\bar{\mathbf{v}}^1$ is given by

$$\bar{\mathbf{v}}^1 = \frac{L}{2\Delta t}(\hat{\mathbf{u}}^{-1} - 4\hat{\mathbf{u}}^0 + 3\hat{\mathbf{u}}^1) \quad + O[(\Delta t)^2]; \tag{5.106}$$

in Equations (5.104) and (5.106), $\hat{\mathbf{u}}^{-2}, \ldots, \hat{\mathbf{u}}^1$ were given in Equations (5.77).

5.3.3.3 Evaluation of the r, x, and θ Sweeps

Equations (5.94)–(5.96) show that the r– and x–sweep represent two sets of differential equations which indeed have to be treated differently, whereas the θ–sweep is simply a set of linear algebraic equations. During the r–sweep, the values of each intermediate flow variable at all the grid points aligned in the r–direction for a given i are solved for simultaneously, as i is incremented (by one) from its smallest value to its largest one. Similarly, the x–sweep involves solving simultaneously for the values of each intermediate flow variable at all the grid points aligned in the x–direction for a given j, as j is incremented. The range in which i or j is incremented may vary slightly from one flow variable to another, since the flow variables are not defined at the same location in the staggered mesh. In this section, the r, x and θ sweeps will be considered in the same order as indicated by Equations (5.94)–(5.96).

<u>r–Sweep</u>

If the right–hand side of Equation (5.94) is denoted by $\mathbf{S} = \{S_r \ S_\theta \ S_x \ S_\nabla\}^{\mathrm{T}}$, then the r–sweep can be written in full as

$$\left\{(1+\Delta\tau) - \frac{\alpha\Delta\tau}{L^2}\left[2\frac{\mathrm{d}\nu}{\mathrm{d}\eta}\frac{\partial}{\partial\eta} + \frac{\nu}{\eta}\frac{\partial}{\partial\eta}\left(\eta\frac{\partial}{\partial\eta}\right)\right]\right\}\tilde{v}_r + \frac{\alpha\Delta\tau}{L}\frac{\partial\tilde{p}}{\partial\eta} = S_r, \tag{5.107}$$

$$\left\{1 - \frac{\alpha\Delta\tau}{L^2}\left[\frac{\mathrm{d}\nu}{\mathrm{d}\eta}\frac{\partial}{\partial\eta} + \frac{\nu}{\eta}\frac{\partial}{\partial\eta}\left(\eta\frac{\partial}{\partial\eta}\right)\right]\right\}\tilde{v}_\theta = S_\theta, \tag{5.108}$$

$$\left\{1 - \frac{\alpha\Delta\tau}{L^2}\left[\frac{\mathrm{d}\nu}{\mathrm{d}\eta}\frac{\partial}{\partial\eta} + \frac{\nu}{\eta}\frac{\partial}{\partial\eta}\left(\eta\frac{\partial}{\partial\eta}\right)\right]\right\}\tilde{v}_x = S_x, \tag{5.109}$$

$$\frac{\Delta\tau}{L\beta}\frac{1}{\eta}\frac{\partial}{\partial\eta}(\eta\tilde{v}_r) + \tilde{p} = S_\nabla, \tag{5.110}$$

where η is defined as r/L; the difference expressions for S_r, S_θ, S_x and S_∇ are given in Appendix G. In this r–sweep, the solution is carried out first for Equation (5.108), then for Equation (5.109), and finally for Equations (5.107) and (5.110) together.

With the substitution of the appropriate difference expressions in Appendix H for the partial derivatives in Equation (5.108), it is found that

for $3 \leq j \leq (M-2)$,

$$\frac{1}{\Delta\eta_j^r}\left\{\left(\frac{\mathrm{d}\nu}{\mathrm{d}\eta}\right)_j^x(1-\mathrm{d}\eta_j^x) - \frac{\nu_j^x\eta_{j-1}^r}{\eta_j^x\Delta\eta_j^x}\right\}(\tilde{v}_\theta)_{i,j-1}$$
$$+\left\{\frac{L^2}{\alpha\Delta\tau} + \frac{1}{\Delta\eta_j^r}\left[\frac{\nu_j^x}{\eta_j^x}\left(\frac{\eta_j^r}{\Delta\eta_{j+1}^x} + \frac{\eta_{j-1}^r}{\Delta\eta_j^x}\right) - (1-\mathrm{d}\eta_j^x - \mathrm{d}_{j+1}^x)\left(\frac{\mathrm{d}\nu}{\mathrm{d}\eta}\right)_j^x\right]\right\}(\tilde{v}_\theta)_{i,j}$$
$$-\frac{1}{\Delta\eta_j^r}\left\{\mathrm{d}\eta_{j+1}^x\left(\frac{\mathrm{d}\nu}{\mathrm{d}\eta}\right)_j^x + \frac{\nu_j^x\eta_j^r}{\eta_j^x\Delta\eta_{j+1}^x}\right\}(\tilde{v}_\theta)_{i,j+1} = \left(\frac{L^2}{\alpha\Delta\tau}\right)(S_\theta)_{i,j}; \tag{5.111}$$

for $j = 2$,

$$\left\{\frac{L^2}{\alpha\Delta\tau} - \frac{1-\mathrm{d}\eta_3^x}{\Delta\eta_2^r}\left(\frac{\mathrm{d}\nu}{\mathrm{d}\eta}\right)_2^x - \nu_2^x\left(b_F + \frac{1-\mathrm{d}\eta_3^x}{\eta_2^x\Delta\eta_2^r}\right)\right\}(\tilde{v}_\theta)_{i,2}$$
$$-\left\{\frac{\mathrm{d}\eta_3^x}{\Delta\eta_2^r}\left(\frac{\mathrm{d}\nu}{\mathrm{d}\eta}\right)_2^x + \nu_2^x\left(c_F + \frac{\mathrm{d}\eta_3^x}{\eta_2^x\Delta\eta_2^r}\right)\right\}(\tilde{v}_\theta)_{i,3} = \left(\frac{L^2}{\alpha\Delta\tau}\right)(S_\theta)_{i,2}; \tag{5.112}$$

and for $j = j^* = (M-1)$,

$$\left\{\frac{1-\mathrm{d}\eta_{j^*}^x}{\Delta\eta_{j^*}^r}\left(\frac{\mathrm{d}\nu}{\mathrm{d}\eta}\right)_{j^*}^x - \nu_{j^*}^x\left(a_R - \frac{1-\mathrm{d}\eta_{j^*}^x}{\eta_{j^*}^x\Delta\eta_{j^*}^r}\right)\right\}(\tilde{v}_\theta)_{i,j^*-1}$$
$$+\left\{\frac{L^2}{\alpha\Delta\tau} + \frac{\mathrm{d}\eta_{j^*}^x}{\Delta\eta_{j^*}^r}\left(\frac{\mathrm{d}\nu}{\mathrm{d}\eta}\right)_{j^*}^x - \nu_{j^*}^x\left(b_R - \frac{\mathrm{d}\eta_{j^*}^x}{\eta_{j^*}^x\Delta\eta_{j^*}^r}\right)\right\}(\tilde{v}_\theta)_{i,j^*} = \left(\frac{L^2}{\alpha\Delta\tau}\right)(S_\theta)_{i,j^*}. \tag{5.113}$$

For the above equations as well as for subsequent equations, M denotes the total number of $(\hat{v}_\theta)_{i,j}$ grid points for a given i, including the two $[(\hat{v}_\theta)_{i,1}$ and $(\hat{v}_\theta)_{i,M}]$ outside the computational domain (Figure 5.2). In the derivation of Equations (5.112)–(5.113), attention has been given to the fact that the values of $\hat{v}_\theta$ at the two physical boundaries are prescribed and remain unchanged during the pseudo–time integration; as a result, $\Delta\hat{v}_\theta = \check{v}_\theta = \tilde{v}_\theta = 0$ at the physical boundaries. Equations (5.111)–(5.113) constitute a tridiagonal system of linear algebraic equations, which are solved for each i, such that $2 \leq i \leq (N+1)$ as depicted by Figure 5.2. It is worthwhile to mention here that a rapid solver (Anderson *et al.* 1984) is used to solve all the tridiagonal systems of linear algebraic equations in the present work.

Since (i) Equations (5.108) and (5.109) are of the same form and (ii) $(\tilde{v}_\theta)_{i,j}$ and $(\tilde{v}_x)_{i,j}$ have the same η–coordinate in the staggered mesh, the difference representations of Equation (5.109) for $1 \leq i \leq N$ may be obtained from Equations (5.111)–(5.113) by replacing the subscript θ by x; thus, for $3 \leq j \leq (M-2)$,

$$\frac{1}{\Delta\eta_j^r}\left\{\left(\frac{\mathrm{d}\nu}{\mathrm{d}\eta}\right)_j^z(1-\mathrm{d}\eta_j^z) - \frac{\nu_j^z\eta_{j-1}^r}{\eta_j^z\Delta\eta_j^z}\right\}(\tilde{v}_z)_{i,j-1}$$
$$+\left\{\frac{L^2}{\alpha\Delta\tau} + \frac{1}{\Delta\eta_j^r}\left[\frac{\nu_j^z}{\eta_j^z}\left(\frac{\eta_j^r}{\Delta\eta_{j+1}^z} + \frac{\eta_{j-1}^r}{\Delta\eta_j^z}\right) - (1-\mathrm{d}\eta_j^z - \mathrm{d}_{j+1}^z)\left(\frac{\mathrm{d}\nu}{\mathrm{d}\eta}\right)_j^z\right]\right\}(\tilde{v}_z)_{i,j}$$
$$-\frac{1}{\Delta\eta_j^r}\left\{\mathrm{d}\eta_{j+1}^z\left(\frac{\mathrm{d}\nu}{\mathrm{d}\eta}\right)_j^z + \frac{\nu_j^z\eta_j^r}{\eta_j^z\Delta\eta_{j+1}^z}\right\}(\tilde{v}_z)_{i,j+1} = \left(\frac{L^2}{\alpha\Delta\tau}\right)(S_z)_{i,j}; \tag{5.114}$$

for $j = 2$,

$$\left\{\frac{L^2}{\alpha\Delta\tau} - \frac{1-\mathrm{d}\eta_3^z}{\Delta\eta_2^r}\left(\frac{\mathrm{d}\nu}{\mathrm{d}\eta}\right)_2^z - \nu_2^z\left(b_F + \frac{1-\mathrm{d}\eta_3^z}{\eta_2^z\Delta\eta_2^r}\right)\right\}(\tilde{v}_z)_{i,2}$$
$$-\left\{\frac{\mathrm{d}\eta_3^z}{\Delta\eta_2^r}\left(\frac{\mathrm{d}\nu}{\mathrm{d}\eta}\right)_2^z + \nu_2^z\left(c_F + \frac{\mathrm{d}\eta_3^z}{\eta_2^z\Delta\eta_2^r}\right)\right\}(\tilde{v}_z)_{i,3} = \left(\frac{L^2}{\alpha\Delta\tau}\right)(S_z)_{i,2}; \tag{5.115}$$

and for $j = j^* = (M-1)$,

$$\left\{\frac{1-\mathrm{d}\eta_{j^*}^z}{\Delta\eta_{j^*}^r}\left(\frac{\mathrm{d}\nu}{\mathrm{d}\eta}\right)_{j^*}^z - \nu_{j^*}^z\left(a_R - \frac{1-\mathrm{d}\eta_{j^*}^z}{\eta_{j^*}^z\Delta\eta_{j^*}^r}\right)\right\}(\tilde{v}_z)_{i,j^*-1} \tag{5.116}$$

$$+\left\{\frac{L^2}{\alpha\Delta\tau} + \frac{\mathrm{d}\eta_{j^*}^z}{\Delta\eta_{j^*}^r}\left(\frac{\mathrm{d}\nu}{\mathrm{d}\eta}\right)_{j^*}^z - \nu_{j^*}^z\left(b_R - \frac{\mathrm{d}\eta_{j^*}^z}{\eta_{j^*}^z\Delta\eta_{j^*}^r}\right)\right\}(\tilde{v}_z)_{i,j^*} = \left(\frac{L^2}{\alpha\Delta\tau}\right)(S_z)_{i,j^*}. \tag{5.117}$$

The determination of $\tilde{v}_r$ and $\tilde{p}$ is somewhat more involved, as these two variables are coupled in Equations (5.107) and (5.110), the difference representations of which are found to be

$$\left\{\frac{2(1-\mathrm{d}\eta_j^r)}{\Delta\eta_{j+1}^z}\left(\frac{\mathrm{d}\nu}{\mathrm{d}\eta}\right)_j^r - \frac{\nu_j^r\eta_j^z}{\eta_j^r\Delta\eta_j^r\Delta\eta_{j+1}^z}\right\}(\tilde{v}_r)_{i,j-1} + \left\{\frac{L^2}{\alpha\Delta\tau}(1+\Delta\tau) - \frac{2(1-\mathrm{d}\eta_j^r - \mathrm{d}\eta_{j+1}^r)}{\Delta\eta_{j+1}^z}\left(\frac{\mathrm{d}\nu}{\mathrm{d}\eta}\right)_j^r\right.$$
$$\left.+\frac{\nu_j^r}{\eta_j^r\Delta\eta_{j+1}^z}\left(\frac{\eta_{j+1}^z}{\Delta\eta_{j+1}^r} + \frac{\eta_j^z}{\Delta\eta_j^r}\right)\right\}(\tilde{v}_r)_{i,j} - \left\{\frac{2\mathrm{d}\eta_{j+1}^r}{\Delta\eta_{j+1}^z}\left(\frac{\mathrm{d}\nu}{\mathrm{d}\eta}\right)_j^r + \frac{\nu_j^r\eta_j^r}{\eta_{j+1}^z\Delta\eta_{j+1}^r\Delta\eta_{j+1}^z}\right\}(\tilde{v}_r)_{i,j+1}$$
$$+\frac{L}{\Delta\eta_{j+1}^z}\left[(\tilde{p})_{i,j+1} - (\tilde{p})_{i,j}\right] = \left(\frac{L^2}{\alpha\Delta\tau}\right)(S_r)_{i,j} \tag{5.118}$$

and

$$\frac{1}{\eta_j^z\Delta\eta_j^r}\left(\frac{\Delta\tau}{L\beta}\right)\left[\eta_j^r(\tilde{v}_r)_{i,j} - \eta_{j-1}^r(\tilde{v}_r)_{i,j-1}\right] + (\tilde{p})_{i,j} = (S_\nabla)_{i,j}, \tag{5.119}$$

respectively, after all the derivatives in the two equations have been replaced by their difference expressions in Appendix H. Subtracting Equation (5.119) for $j = j$ from the same equation for $j = j+1$ and then multiplying the resulting equation by $(L/\Delta\eta_{j+1}^z)$ yields

$$\frac{\Delta\tau}{\beta\Delta\eta_{j+1}^z}\left\{\frac{\eta_{j-1}^r}{\eta_j^z\Delta\eta_j^r}(\tilde{v}_r)_{i,j-1} - \eta_j^r\left[\frac{1}{\eta_{j+1}^z\Delta\eta_{j+1}^r} + \frac{1}{\eta_j^z\Delta\eta_j^r}\right](\tilde{v}_r)_{i,j} + \frac{\eta_{j+1}^r}{\eta_{j+1}^z\Delta\eta_{j+1}^r}(\tilde{v}_r)_{i,j+1}\right\}$$

$$+\frac{L}{\Delta\eta^x_{j+1}}\Big[(\tilde{p})_{i,j+1}-(\tilde{p})_{i,j}\Big] \;=\; \frac{L}{\Delta\eta^x_{j+1}}\Big[(S_\nabla)_{i,j+1}-(S_\nabla)_{i,j}\Big], \tag{5.120}$$

which is then subtracted from Equation (5.118), giving

$$\begin{aligned}
&\left\{2(1-\mathrm{d}\eta^r_j)\left(\frac{\mathrm{d}\nu}{\mathrm{d}\eta}\right)^r_j-\frac{\nu^r_j\eta^x_j}{\eta^r_j\Delta\eta^r_j}-\frac{\Delta\tau}{\beta}\left[\frac{\eta^r_{j-1}}{\eta^x_j\Delta\eta^r_j}\right]\right\}(\tilde{v}_r)_{i,j-1}+\left\{\frac{L^2}{\alpha\Delta\tau}(1+\Delta\tau)\Delta\eta^x_{j+1}\right.\\
&-\left.2(1-\mathrm{d}\eta^r_j-\mathrm{d}\eta^r_{j+1})\left(\frac{\mathrm{d}\nu}{\mathrm{d}\eta}\right)^r_j+\frac{\nu^r_j}{\eta^r_j}\left[\frac{\eta^x_{j+1}}{\Delta\eta^r_{j+1}}+\frac{\eta^x_j}{\Delta\eta^r_j}\right]+\frac{\eta^r_j\Delta\tau}{\beta}\left[\frac{1}{\eta^x_{j+1}\Delta\eta^r_{j+1}}+\frac{1}{\eta^x_j\Delta\eta^r_j}\right]\right\}(\tilde{v}_r)_{i,j}\\
&-\left\{2\mathrm{d}\eta^r_{j+1}\left(\frac{\mathrm{d}\nu}{\mathrm{d}\eta}\right)^r_j+\frac{\nu^r_j\eta^x_{j+1}}{\eta^r_j\Delta\eta^r_{j+1}}+\frac{\Delta\tau}{\beta}\left[\frac{\eta^r_{j+1}}{\eta^x_{j+1}\Delta\eta^r_{j+1}}\right]\right\}(\tilde{v}_r)_{i,j+1}\\
&=\Delta\eta^x_{j+1}\left(\frac{L^2}{\alpha\Delta\tau}\right)(S_r)_{i,j}-L\Big[(S_\nabla)_{i,j+1}-(S_\nabla)_{i,j}\Big].
\end{aligned} \tag{5.121}$$

Equation (5.121) can now be solved for $(\tilde{v}_r)_{i,j}$, for $2\leq j\leq(M-2)$ with i incremented such that $2\leq i\leq(N+1)$, using the tridiagonal matrix solver, and $(\tilde{p})_{i,j}$ is subsequently obtained from Equation (5.119) for $2\leq j\leq(M-1)$ and $2\leq i\leq(N+1)$,

$$(\tilde{p})_{i,j} \;=\; (S_\nabla)_{i,j}-\frac{1}{\eta^x_j\Delta\eta^r_j}\left(\frac{\Delta\tau}{L\beta}\right)\Big[\eta^r_j(\tilde{v}_r)_{i,j}-\eta^r_{j-1}(\tilde{v}_r)_{i,j-1}\Big]. \tag{5.122}$$

<u>x–Sweep</u>

The x–sweep, characterized by Equation (5.95), involves the following equations

$$\left\{1+\frac{\alpha\Delta\tau}{L^2}\left[LU(\eta)\frac{\partial}{\partial\xi}-\nu\frac{\partial^2}{\partial\xi^2}\right]\right\}\breve{v}_r \;+\; \frac{\alpha\Delta\tau}{L^2}\left(\frac{2n\nu}{\eta^2}\right)\breve{v}_\theta \;=\; \tilde{v}_r, \tag{5.123}$$

$$\left\{1+\frac{\alpha\Delta\tau}{L^2}\left[LU(\eta)\frac{\partial}{\partial\xi}-\nu\frac{\partial^2}{\partial\xi^2}\right]\right\}\breve{v}_\theta \;=\; \tilde{v}_\theta, \tag{5.124}$$

$$\left\{(1+\Delta\tau)+\frac{\alpha\Delta\tau}{L^2}\left[LU(\eta)\frac{\partial}{\partial\xi}-\nu\frac{\partial^2}{\partial\xi^2}\right]\right\}\breve{v}_x \;-\; \frac{\alpha\Delta\tau}{L^2}\left(\frac{\mathrm{d}\nu}{\mathrm{d}\eta}\right)\frac{\partial\breve{v}_r}{\partial\xi} \;+\; \left(\frac{\alpha\Delta\tau}{L}\right)\frac{\partial\breve{p}}{\partial\xi} \;=\; \tilde{v}_x, \tag{5.125}$$

$$\left(\frac{\Delta\tau}{L\beta}\right)\frac{\partial\breve{v}_x}{\partial\xi} \;+\; \breve{p} \;=\; \tilde{p}, \tag{5.126}$$

where $\tilde{v}_r$, $\tilde{v}_\theta$, $\tilde{v}_x$ and $\tilde{p}$ have all been determined in the r–sweep. Here, the sequence in which Equations (5.123)–(5.126) are solved is quite obvious: the only equation that can possibly be solved first is (5.124), then Equation (5.123) for $\breve{v}_r$ since $\breve{v}_\theta$ is already known, and then Equations (5.125) and (5.126) together since $\breve{v}_x$ and $\breve{p}$ are not only coupled in these equations but also dependent on $\breve{v}_r$. In the x–sweep, the diffusion terms (i.e. $\partial^2/\partial\xi^2$) are approximated by the three–point central difference expression whereas the two–point backward difference representation is used for the convective terms (i.e.

$\partial/\partial\xi$). It should also be reiterated that Equations (5.123)–(5.126) are approximated at the locations of $(\breve{v}_r)_{i,j}$, $(\breve{v}_\theta)_{i,j}$, $(\breve{v}_x)_{i,j}$ and $(\hat{p})_{i,j}$, respectively, in the staggered mesh.

Accordingly, for $3 \leq i \leq N$, Equation (5.124) is represented by

$$-\left[\frac{LU(\eta_j^x)}{\Delta\xi} + \frac{\nu_j^x}{(\Delta\xi)^2}\right](\breve{v}_\theta)_{i-1,j} + \left[\frac{L^2}{\alpha\Delta\tau} + \frac{LU(\eta_j^x)}{\Delta\xi} + \frac{2\nu_j^x}{(\Delta\xi)^2}\right](\breve{v}_\theta)_{i,j}$$
$$- \left[\frac{\nu_j^x}{(\Delta\xi)^2}\right](\breve{v}_\theta)_{i+1,j} = \left(\frac{L^2}{\alpha\Delta\tau}\right)(\tilde{v}_\theta)_{i,j}, \qquad (5.127)$$

which can be simplified for $i = 2$,

$$\left[\frac{L^2}{\alpha\Delta\tau} + \frac{LU(\eta_j^x)}{\Delta\xi} + \frac{2\nu_j^x}{(\Delta\xi)^2}\right](\breve{v}_\theta)_{2,j} - \left[\frac{\nu_j^x}{(\Delta\xi)^2}\right](\breve{v}_\theta)_{3,j} = \left(\frac{L^2}{\alpha\Delta\tau}\right)(\tilde{v}_\theta)_{2,j}, \qquad (5.128)$$

because $(\breve{v}_\theta)_{1,j} = 0$ is imposed at the inlet of the flow (Section 5.3.3.2); for $i = N+1$, Equation (5.127) becomes

$$-\left[\frac{LU(\eta_j^x)}{\Delta\xi} + \frac{\nu_j^x}{(\Delta\xi)^2}\right](\breve{v}_\theta)_{N,j} + \left[\frac{L^2}{\alpha\Delta\tau} + \frac{LU(\eta_j^x)}{\Delta\xi} + \frac{2\nu_j^x}{(\Delta\xi)^2}\right](\breve{v}_\theta)_{N+1,j}$$
$$- \left[\frac{\nu_j^x}{(\Delta\xi)^2}\right](\breve{v}_\theta)_{N+2,j} = \left(\frac{L^2}{\alpha\Delta\tau}\right)(\tilde{v}_\theta)_{N+1,j}. \qquad (5.129)$$

Here, the value of $(\breve{v}_\theta)_{N+2,j}$ represents the boundary condition at the exit of the flow, and must be such that $\breve{v}_\theta$ would vanish somewhere downstream [i.e. $\breve{v}_\theta = 0$ at $\xi = \ell$, $\ell > 1$] as prescribed by any of the realistic flow models discussed in Chapter 2. It may be shown that

$$(\breve{v}_\theta)_{N+2,j} = A(\breve{v}_\theta)_{N,j} - B(\breve{v}_\theta)_{N+1,j}, \qquad (5.130)$$

where the constants A and B depend on the particular flow model adopted and are given in Appendix B. With the boundary condition (5.130) imposed, Equation (5.129) turns out to be

$$-\left[\frac{LU(\eta_j^x)}{\Delta\xi} + (1+A)\frac{\nu_j^x}{\Delta\xi^2}\right](\breve{v}_\theta)_{N,j} + \left[\frac{L^2}{\alpha\Delta\tau} + \frac{LU(\eta_j^x)}{\Delta\xi} + (2+B)\frac{\nu_j^x}{(\Delta\xi)^2}\right](\breve{v}_\theta)_{N+1,j}$$
$$= \left(\frac{L^2}{\alpha\Delta\tau}\right)(\tilde{v}_\theta)_{N+1,j}. \qquad (5.131)$$

It is seen that Equations (5.127), (5.128), and (5.131) form another tridiagonal system, which is then solved for $2 \leq i \leq (N+1)$ with j incremented such that $2 \leq j \leq (M-1)$.

The above procedure is also applied to Equation (5.123) with $2 \leq j \leq (M-2)$, resulting in the following equations:

for $3 \le i \le N$,

$$-\left[\frac{LU(\eta_j^r)}{\Delta\xi} + \frac{\nu_j^r}{(\Delta\xi)^2}\right](\breve{v}_r)_{i-1,j} + \left[\frac{L^2}{\alpha\Delta\tau} + \frac{LU(\eta_j^r)}{\Delta\xi} + \frac{2\nu_j^r}{(\Delta\xi)^2}\right](\breve{v}_r)_{i,j} - \left[\frac{\nu_j^r}{(\Delta\xi)^2}\right](\breve{v}_r)_{i+1,j}$$

$$= \left(\frac{L^2}{\alpha\Delta\tau}\right)(\tilde{v}_r)_{i,j} - \left[\frac{2n\nu_j^r}{(\eta_j^r)^2}\right]\left[\mathrm{d}\eta_{j+1}^x(\breve{v}_\theta)_{i,j+1} + (1 - \mathrm{d}\eta_{j+1}^x)(\breve{v}_\theta)_{i,j}\right]; \tag{5.132}$$

for $i = 2$

$$\left[\frac{L^2}{\alpha\Delta\tau} + \frac{LU(\eta_j^r)}{\Delta\xi} + \frac{2\nu_j^r}{(\Delta\xi)^2}\right](\breve{v}_r)_{2,j} - \left[\frac{\nu_j^r}{\Delta\xi^2}\right](\breve{v}_r)_{3,j} = \left[\frac{L^2}{\alpha\Delta\tau}\right](\tilde{v}_r)_{2,j}$$

$$- \left(\frac{2n\nu_j^r}{(\eta_j^r)^2}\right)\left[\mathrm{d}\eta_{j+1}^x(\breve{v}_\theta)_{2,j+1} + (1 - \mathrm{d}\eta_{j+1}^x)(\breve{v}_\theta)_{2,j}\right]; \tag{5.133}$$

for $i = (N+1)$,

$$-\left[\frac{LU(\eta_j^r)}{\Delta\xi} + (1+A)\frac{\nu_j^r}{(\Delta\xi)^2}\right](\breve{v}_r)_{N,j} + \left[\frac{L^2}{\alpha\Delta\tau} + \frac{LU(\eta_j^r)}{\Delta\xi} + (2+B)\frac{2\nu_j^r}{(\Delta\xi)^2}\right](\breve{v}_r)_{N+1,j}$$

$$= \left(\frac{L^2}{\alpha\Delta\tau}\right)(\tilde{v}_r)_{N+1,j} - \left[\frac{2n\nu_j^r}{(\nu_j^r)^2}\right]\left[\mathrm{d}\eta_{j+1}^x(\breve{v}_\theta)_{N+1,j+1} + (1 - \mathrm{d}\eta_{j+1}^x)(\breve{v}_\theta)_{N+1,j}\right]. \tag{5.134}$$

The solution of Equations (5.125) and (5.126) involves the decoupling of $\breve{v}_x$ and $\breve{p}$. First of all, the discretization of Equation (5.125) gives

$$-\left[\frac{LU(\eta_j^x)}{\Delta\xi} + \frac{\nu_j^x}{(\Delta\xi)^2}\right](\breve{v}_x)_{i-1,j} + \left[\frac{L^2}{\alpha\Delta\tau}(1+\Delta\tau) + \frac{LU(\eta_j^x)}{\Delta\xi} + \frac{2\nu_j^x}{(\Delta\xi)^2}\right](\breve{v}_x)_{i,j}$$

$$- \left[\frac{\nu_j^x}{(\Delta\xi)^2}\right](\breve{v}_x)_{i+1,j} + \frac{L}{\Delta\xi}\left[(\breve{p})_{i+1,j} - (\breve{p})_{i,j}\right] = \left(\frac{L^2}{\alpha\Delta\tau}\right)(\tilde{v}_x)_{i,j}$$

$$+ \frac{1}{\Delta\xi}\left(\frac{\mathrm{d}\nu}{\mathrm{d}\eta}\right)_j^x\left\{\mathrm{d}\eta_j^r\left[(\breve{v}_r)_{i+1,j} - (\breve{v}_r)_{i,j}\right] + (1 - \mathrm{d}\eta_j^r)\left[(\breve{v}_r)_{i+1,j-1} - (\breve{v}_r)_{i,j-1}\right]\right\}, \tag{5.135}$$

while it follows from Equation (5.126) that

$$\frac{1}{\Delta\xi}\left(\frac{\Delta\tau}{L\beta}\right)\left[(\breve{v}_x)_{i,j} - (\breve{v}_x)_{i-1,j}\right] + (\breve{p})_{i,j} = (\tilde{p})_{i,j}. \tag{5.136}$$

Subtracting Equation (5.136) for $i = i$ from the same equation for $i = i + 1$ and then multiplying the resulting equation by $(L/\Delta\xi)$ gives

$$\frac{\Delta\tau}{\beta(\Delta\xi)^2}\left[(\breve{v}_x)_{i-1,j} - 2(\breve{v}_x)_{i,j} + (\breve{v}_x)_{i+1,j}\right] + \frac{L}{\Delta\xi}\left[(\breve{p})_{i+1,j} - (\breve{p})_{i,j}\right] = \frac{L}{\Delta\xi}\left[(\tilde{p})_{i+1,j} - (\tilde{p})_{i,j}\right], \tag{5.137}$$

which is then subtracted from Equation (5.135), yielding the following relationship for $2 \le i \le (N-1)$,

$$-\left\{\frac{LU(\eta_j^x)}{\Delta\xi} + \frac{1}{(\Delta\xi)^2}\left[\nu_j^x + \frac{\Delta\tau}{\beta}\right]\right\}(\breve{v}_x)_{i-1,j} + \left\{\frac{L^2}{\alpha\Delta\tau}(1+\Delta\tau) + \frac{2}{(\Delta\xi)^2}\left[\nu_j^x + \frac{\Delta\tau}{\beta}\right]\right.$$

$$+\frac{LU(\eta_j^x)}{\Delta\xi}\Bigg\}(\breve{v}_x)_{i,j} \;-\; \frac{1}{(\Delta\xi)^2}\Big[\nu_j^x + \frac{\Delta\tau}{\beta}\Big](\breve{v}_x)_{i+1,j} \;=\; \Big(\frac{L^2}{\alpha\Delta\tau}\Big)(\tilde{v}_x)_{i,j} \;-\; \Big(\frac{L}{\Delta\xi}\Big)\Big[(\tilde{p})_{i+1,j} - (\tilde{p})_{i,j}\Big]$$
$$+\;\frac{1}{\Delta\xi}\Big(\frac{\mathrm{d}\nu}{\mathrm{d}\eta}\Big)_j^x\Big\{\mathrm{d}\eta_j^r\Big[(\breve{v}_r)_{i+1,j} - (\breve{v}_r)_{i,j}\Big] + (1-\mathrm{d}\eta_j^r)\Big[(\breve{v}_r)_{i+1,j-1} - (\breve{v}_r)_{i,j-1}\Big]\Big\}. \tag{5.138}$$

Similarly, it is found that, for $i = 1$,

$$\Bigg\{\frac{L^2}{\alpha\Delta\tau}(1+\Delta\tau) + \frac{1}{(\Delta\xi)^2}\Big[2\nu_j^x + \frac{\Delta\tau}{\beta}\Big] + \frac{LU(\eta_j^x)}{\Delta\xi}\Bigg\}(\breve{v}_x)_{1,j} \;-\; \frac{1}{(\Delta\xi)^2}\Big[\nu_j^x + \frac{\Delta\tau}{\beta}\Big](\breve{v}_x)_{2,j}$$
$$=\;\Big(\frac{L^2}{\alpha\Delta\tau}\Big)(\tilde{v}_x)_{1,j} \;-\; \Big(\frac{L}{\Delta\xi}\Big)(\tilde{p})_{2,j} \;+\; \frac{1}{\Delta\xi}\Big(\frac{\mathrm{d}\nu}{\mathrm{d}\eta}\Big)_j^x\Big[\mathrm{d}\eta_j^r(\breve{v}_r)_{2,j} + (1-\mathrm{d}\eta_j^r)(\breve{v}_r)_{2,j-1}\Big], \tag{5.139}$$

and for $i = N$,

$$-\Bigg\{\frac{LU(\eta_j^x)}{\Delta\xi} + \frac{(1+A)}{(\Delta\xi)^2}\Big[\nu_j^x + \frac{\Delta\tau}{\beta}\Big]\Bigg\}(\breve{v}_x)_{N-1,j} \;+\; \Bigg\{\frac{L^2}{\alpha\Delta\tau} + \frac{(2+B)}{(\Delta\xi)^2}\Big[\nu_j^x + \frac{\Delta\tau}{\beta}\Big]$$
$$+\;\frac{LU(\eta_j^x)}{\Delta\xi}\Bigg\}(\breve{v}_x)_{N,j} \;=\; \frac{L^2}{\alpha\Delta\tau}(\tilde{v}_x)_{N,j} \;-\; \frac{L}{\Delta\xi}\Big[(\tilde{p})_{N+1,j} - (\tilde{p})_{N,j}\Big]$$
$$+\;\frac{1}{\Delta\xi}\Big(\frac{\mathrm{d}\nu}{\mathrm{d}\eta}\Big)_j^x\Big\{\mathrm{d}\eta_j^r\Big[(\breve{v}_r)_{N+1,j} - (\breve{v}_r)_{N,j}\Big] \;+\; (1-\mathrm{d}\eta_j^r)\Big[(\breve{v}_r)_{N+1,j-1} - (\breve{v}_r)_{N,j-1}\Big]\Big\}, \tag{5.140}$$

where the boundary conditions $(\breve{v}_x)_{0,j} = 0$ and $(\breve{v}_x)_{N+1,j} = A(\breve{v}_x)_{N-1,j} - B(\breve{v}_x)_{N,j}$ have been imposed. Here, Equations (5.138)–(5.140) also form a tridiagonal system with j incremented from 2 to $(M-1)$. For the same range of j, the pressure $\breve{p}$ is calculated subsequently from Equation (5.136): for $2 \le i \le N$,

$$(\breve{p})_{i,j} \;=\; (\tilde{p})_{i,j} \;-\; \frac{1}{\Delta\xi}\Big(\frac{\Delta\tau}{L\beta}\Big)\Big[(\breve{v}_x)_{i,j} - (\breve{v}_x)_{i-1,j}\Big], \tag{5.141}$$

and for $i = (N+1)$,

$$(\breve{p})_{N+1,j} \;=\; (\tilde{p})_{N+1,j} \;-\; \frac{1}{\Delta\xi}\Big(\frac{\Delta\tau}{L\beta}\Big)\Big[A(\breve{v}_x)_{N-1,j} - (1+B)(\breve{v}_x)_{N,j}\Big]. \tag{5.142}$$

<u>θ–Sweep</u>

The θ–sweep, characterized by Equation (5.96), covers the following equations

$$\Bigg\{1 + \frac{\alpha\Delta\tau}{L^2}\Bigg[\frac{\nu(1+n^2)}{\eta^2}\Bigg]\Bigg\}\Delta\hat{v}_r \;=\; \breve{v}_r, \tag{5.143}$$

$$\frac{\alpha\Delta\tau}{L^2}\Big(\frac{n}{\eta}\Big)\Big[\frac{\mathrm{d}\nu}{\mathrm{d}\eta} + \frac{2\nu}{\eta}\Big]\Delta\hat{v}_r + \Bigg\{(1+\Delta\tau) + \frac{\alpha\Delta\tau}{L^2}\Bigg[\frac{\nu(1+n^2)}{\eta^2}\Bigg]\Bigg\}\Delta\hat{v}_\theta - \frac{\alpha\Delta\tau}{L}\Big(\frac{n}{\eta}\Big)\Delta\hat{p} \;=\; \breve{v}_\theta, \tag{5.144}$$

$$\frac{\alpha\Delta\tau}{L}\Big(\frac{\mathrm{d}U}{\mathrm{d}\eta}\Big)\Delta\hat{v}_r \;+\; \Bigg\{1 + \frac{\alpha\Delta\tau}{L^2}\Big(\frac{\nu n^2}{\eta^2}\Big)\Bigg\}\Delta\hat{v}_x \;=\; \breve{v}_x, \tag{5.145}$$

$$\frac{\Delta\tau}{L\beta}\Big(\frac{n}{\eta}\Big)\Delta\hat{v}_\theta \;+\; \Delta\hat{p} \;=\; \breve{p}, \tag{5.146}$$

where $\breve{v}_r$, $\breve{v}_\theta$, $\breve{v}_x$, and $\breve{p}$ have been determined in the x–sweep. In the θ–sweep, $\Delta\hat{v}_\theta$ is coupled with $\Delta\hat{p}$, and the sequence in which Equations (5.143)–(5.146) are solved is still selective: (5.143), then (5.145), and finally (5.144) and (5.146) together; nevertheless, no tridiagonal systems of linear algebraic equations are generated.

For $2 \le i \le (N+1)$ and $2 \le j \le (M-2)$, Equation (5.143) is represented by

$$\left\{1 + \frac{\alpha\Delta\tau}{L^2}\left[\frac{\nu_j^r(1+n^2)}{(\eta_j^r)^2}\right]\right\}(\Delta\hat{v}_r)_{i,j} \;=\; (\breve{v}_r)_{i,j}. \tag{5.147}$$

Similarly, for $1 \le i \le N$ and $2 \le j \le (M-1)$, Equation (5.145) becomes

$$\begin{aligned}\left\{1 + \frac{\alpha\Delta\tau}{L^2}\left[\frac{\nu_j^x n^2}{(\eta_j^x)^2}\right]\right\}(\Delta\hat{v}_x)_{i,j} \;&=\; (\breve{v}_x)_{i,j} \;-\; \frac{\alpha\Delta\tau}{2L}\left(\frac{\mathrm{d}U}{\mathrm{d}\eta}\right)_j^x\Big\{\mathrm{d}\eta_j^r\left[(\Delta\hat{v}_r)_{i,j} + (\Delta\hat{v}_r)_{i+1,j}\right] \\ &+\; (1-\mathrm{d}\eta_j^r)\left[(\Delta\hat{v}_r)_{i,j-1} + (\Delta\hat{v}_r)_{i+1,j-1}\right]\Big\}.\end{aligned} \tag{5.148}$$

Equations (5.147) and (5.148) can both be solved directly for $(\Delta\hat{v}_r)_{i,j}$ and $(\Delta\hat{v}_x)_{i,j}$, respectively. On the other hand, the difference expression of Equation (5.144) contains $(\Delta\hat{v}_\theta)_{i,j}$ and $(\Delta\hat{p})_{i,j}$

$$\begin{aligned}&\frac{\alpha\Delta\tau}{L^2}\left(\frac{n}{\eta_j^x}\right)\left[\left(\frac{\mathrm{d}\nu}{\mathrm{d}\eta}\right)_j^x + \frac{2\nu_j^x}{\nu_j^x}\right]\left[\mathrm{d}\eta_j^r(\Delta\hat{v}_r)_{i,j} + (1-\mathrm{d}\eta_j^r)(\Delta\hat{v}_r)_{i,j-1}\right] \\ +\; &\left\{(1+\Delta\tau) + \frac{\alpha\Delta\tau}{L^2}\left[\frac{\nu_j^x(1+n^2)}{(\eta_j^x)^2}\right]\right\}(\Delta\hat{v}_\theta)_{i,j} \;-\; \frac{\alpha\Delta\tau}{L}\left(\frac{n}{\eta_j^x}\right)(\Delta\hat{p})_{i,j} \;=\; (\breve{v}_\theta)_{i,j}.\end{aligned} \tag{5.149}$$

As expected, the elimination of $(\Delta p)_{i,j}$ from the above equation requires the difference expression of Equation (5.146),

$$\frac{\Delta\tau}{L\beta}\left(\frac{n}{\eta_j^x}\right)(\Delta\hat{v}_\theta)_{i,j} \;+\; (\Delta\hat{p})_{i,j} \;=\; (\breve{p})_{i,j}, \tag{5.150}$$

which is multiplied by $(\alpha\Delta\tau/L)(n/\eta_j^x)$ and then subtracted from Equation (5.149), giving

$$\begin{aligned}&\left\{(1+\Delta\tau) + \frac{1}{(\eta_j^x)^2}\left(\frac{\alpha\Delta\tau}{L^2}\right)\left[\nu_j^x(1+n^2) + \frac{n^2\Delta\tau}{\beta}\right]\right\}(\Delta\hat{v}_\theta)_{i,j} \;=\; (\breve{v}_\theta)_{i,j} \;+\; \frac{\alpha\Delta\tau}{L}\left(\frac{n}{\eta_j^x}\right)(\breve{p})_{i,j} \\ -\; &\frac{\alpha\Delta\tau}{L^2}\left(\frac{n}{\eta_j^x}\right)\left[\left(\frac{\mathrm{d}\nu}{\mathrm{d}\eta}\right)_j^x + \frac{2\nu_j^x}{\nu_j^x}\right]\left[\mathrm{d}\eta_j^r(\Delta\hat{v}_r)_{i,j} + (1-\mathrm{d}\eta_j^r)(\Delta\hat{v}_r)_{i,j-1}\right]\end{aligned} \tag{5.151}$$

for $2 \le i \le (N+1)$ and $2 \le j \le (M-1)$. The pressure Δp is calculated subsequently from Equation (5.150) for the same ranges of i and j as for $\Delta\hat{v}_\theta$,

$$(\Delta\hat{p})_{i,j} \;=\; (\breve{p})_{i,j} \;-\; \frac{\Delta\tau}{L\beta}\left(\frac{n}{\eta_j^x}\right)(\Delta\hat{v}_\theta)_{i,j}. \tag{5.152}$$

Once $(\Delta\hat{v}_r)_{i,j}$, $(\Delta\hat{v}_\theta)_{i,j}$, $(\Delta\hat{v}_x)_{i,j}$, and $(\Delta\hat{p})_{i,j}$ have been determined and so have $(\hat{v}_r^{k+1})_{i,j}$, $(\hat{v}_\theta^{k+1})_{i,j}$, $(\hat{v}_x^{k+1})_{i,j}$, and $(\hat{p}^{k+1})_{i,j}$ according to $\mathbf{\Pi}^{k+1} = \mathbf{\Pi}^k + \Delta\mathbf{\Pi}$ as defined in Equation (5.96), the next pseudo–time step is advanced. In principle, this process continues until

$$(\Delta\hat{v}_r)_{i,j} = (\Delta\hat{v}_\theta)_{i,j} = (\Delta\hat{v}_x)_{i,j} = (\Delta\hat{p})_{i,j} = 0, \tag{5.153}$$

at which time the steady solution in pseudo–time has been obtained. The next physical-time step can then be advanced after $\bar{\mathbf{v}}^{n+1}$ and $\bar{p}^{n+1}$ have been updated according to Equation (5.88). In the actual numerical calculations to be conducted, the condition (5.153) is considered to be achieved when

$$\mathrm{Max}\left\{\frac{(\Delta\hat{v}_r)_{i_1,j_1}}{(\hat{v}_r^{k+1})_{i_1,j_1}}, \frac{(\Delta\hat{v}_\theta)_{i_2,j_2}}{(\hat{v}_\theta^{k+1})_{i_2,j_2}}, \frac{(\Delta\hat{v}_x)_{i_3,j_3}}{(\hat{v}_x^{k+1})_{i_3,j_3}}, \frac{(\Delta\hat{p})_{i_4,j_4}}{(\hat{p}^{k+1})_{i_4,j_4}}\right\} \leq 10^{-3}, \tag{5.154}$$

where i_1, j_1, ..., i_4, j_4 may take on any (integer) value as long as the location of the corresponding flow variable is within the computational domain considered.

5.3.4 Determination of the Unsteady Viscous Forces

If (i) the functional forms taken for the unsteady viscous forces, Equation (5.31), and for the flow perturbations, Equation (5.79), are substituted into the relationships between these forces and perturbations, Equations (5.27)–(5.29), and (ii) the coefficients of $\sin n\theta$ or $\cos n\theta$ in the series on the two sides of each of the resulting identities are equated, then the following equations will be obtained

$$\bar{q}_x = \rho\nu\left\{\frac{\partial\bar{v}_r}{\partial x} + \frac{\partial\bar{v}_x}{\partial r}\right\}\Bigg|_{ss}, \tag{5.155}$$

$$\bar{q}_\theta = \rho\nu\left\{r\frac{\partial}{\partial r}\left(\frac{\bar{v}_\theta}{r}\right) - \frac{n}{r}\bar{v}_r\right\}\Bigg|_{ss}, \tag{5.156}$$

$$\bar{q}_r = \rho\nu\left\{-\frac{\bar{p}}{\nu} + 2\frac{\partial\bar{v}_r}{\partial r}\right\}\Bigg|_{ss}. \tag{5.157}$$

For the convenience of solving the shell equations of motion, Equations (5.155)–(5.157) are now nondimensionalized according to Equation (5.40), thus producing

$$\hat{q}_x = G\left\{\frac{\partial\bar{v}_r}{\partial\xi} + \frac{\partial\bar{v}_x}{\partial\eta}\right\}\Bigg|_{ss}, \tag{5.158}$$

$$\hat{q}_\theta = G\left\{\eta\frac{\partial}{\partial\eta}\left(\frac{\bar{v}_\theta}{\eta}\right) - \frac{n}{\eta}\bar{v}_r\right\}\Bigg|_{ss}, \tag{5.159}$$

$$\hat{q}_r = G\left\{-\frac{\bar{p}}{\nu} + 2\frac{\partial \bar{v}_r}{\partial \eta}\right\}\bigg|_{ss}. \tag{5.160}$$

where $G = (\gamma\rho\nu)/(\rho_s h L^2)$ with $\nu = \nu_m$ at the shell surface.

The difference representations of Equations (5.158)–(5.160) can be obtained by replacing $\partial/\partial\xi$ by the two-point central difference approximation and $\hat{v}_r$ and $\hat{v}_x$ by the difference expressions derived in Appendix F. According to the numbering of the nodes on the shell and of the locations of the flow variables in the staggered mesh, the following expressions are obtained:

$$\begin{aligned}(\hat{q}_x^{n+1})_i &= \frac{G}{2\Delta\xi}\left\{(\bar{v}_r^{n+1})_{i+2,F} - (\bar{v}_r^{n+1})_{i,F}\right\} + \frac{G}{2}\left\{\breve{a}\left[(\bar{v}_x^{n+1})_{i,F} + (\bar{v}_x^{n+1})_{i+1,F}\right]\right. \\ &\quad \left. + \breve{b}\left[(\bar{v}_x^{n+1})_{i,2} + (\bar{v}_x^{n+1})_{i+1,2}\right] + \breve{c}\left[(\bar{v}_x^{n+1})_{i,3} + (\bar{v}_x^{n+1})_{i+1,3}\right]\right\},\end{aligned} \tag{5.161}$$

$$(\hat{q}_\theta^{n+1})_i = G\left\{\left(\breve{a} - \frac{1}{\eta_1^r}\right)(\bar{v}_\theta^{n+1})_{i+1,F} + \breve{b}(\bar{v}_\theta^{n+1})_{i+1,2} + \breve{c}(\bar{v}_\theta^{n+1})_{i+1,3} - \frac{n}{\eta_1^r}(\bar{v}_r^{n+1})_{i+1,F}\right\}, \tag{5.162}$$

$$\begin{aligned}(\hat{q}_r^{n+1})_i &= -G\left(\frac{L}{\nu}\right)\left\{\left(1 + \frac{\Delta\tilde{\eta}}{\Delta\eta_3^x}\right)\bar{p}_{i+1,2}^{n+1} - \frac{\Delta\tilde{\eta}}{\Delta\eta_3^x}\bar{p}_{i+1,3}^{n+1}\right\} \\ &\quad + 2G\left\{\bar{a}(\bar{v}_r^{n+1})_{i+1,F} + \bar{b}(\bar{v}_r^{n+1})_{i+1,2} + \bar{c}(\bar{v}_r^{n+1})_{i+1,3}\right\},\end{aligned} \tag{5.163}$$

where $\breve{a}$, $\bar{a}$, ..., $\breve{c}$ and $\bar{c}$ are constants given in Appendix F.

5.3.5 Remarks on the Moving Boundary

Since shell motions are assumed to be sufficiently small, the width of the annular gap may be considered to vary neither with ξ (uniform gap) nor with time t; nondimensionally, it is taken to be $(\varepsilon_o - \varepsilon_i)$ for which the shell is motionless. (This, as will shortly be seen, is unsatisfactory, but its consideration is instructive.) Hence, η_j could be calculated from Equation (H.1), and the resulting staggered mesh becomes fixed throughout the physical–time integration. Thus, when the shell is in motion, the flow velocities $U(\eta)$ at some of the grid points that were initially in contact with the undeformed shell surface may no longer be zero due to a rapid increase in $U(\eta)$ in the vicinity of the shell wall.

In earlier stages of developing the theory, the use of this fixed grid had led to the results that were virtually identical, both qualitatively and quantitatively, to those obtained with the theory in Chapter 2 but *without* the unsteady fluid forces included. As such, the only type of instability obtained was divergence, which is evidently due to the flow pressurization required to push the fluid through the annular gap. Furthermore, the discrepancy between the predictions of $\bar{U}_c^*$ given by the two theories was found to be 3.9% (based on $\bar{U}_c^* = 33\,\mathrm{m/s}$ by the theory of Chapter 2) for $g/a = 1/10$, 1.1% ($\bar{U}_c^* = 90\,\mathrm{m/s}$) for $g/a = 1/4$, and 0.8% ($\bar{U}_c^* = 141\,\mathrm{m/s}$) for $g/a = 1$. (*With* the unsteady fluid forces included, the results for $\bar{U}_c^*$ were much lower, as will be seen later in Figure 5.6.) The foregoing comparison has shown that the unsteady viscous forces were completely missing when the fixed grid was used.

The actual grid, on the other hand, continuously deforms with the moving shell, such that they always remain in contact; this requires the continual recalculation of (i) the coordinates of, and (ii) $U(\eta)$ at, all spatial locations of the flow variables, as the time integration progresses. Hence, all the coefficients of the tridiagonal systems of linear algebraic equations presented earlier (Section 5.3.3.3) would need to be reevaluated at the beginning of all iterations (see Section 5.3.3.2) within every physical–time step, for a large number of time steps. Consequently, the amount of computing time associated with the use of the actual grid is prohibitively enormous, considering the very limited funding and resources available for this research. It might be of interest to mention that the programming effort involved in such a procedure would also be equally substantial.

The calculations to be presented in Section 5.4.2 adopted what may be considered as an approximation to the actual grid; Section 5.4.1 will briefly discuss the computing cost associated with this approximate scheme. The approximation involves the use of the fixed grid; nevertheless, at the beginning of every iteration within each physical–time step, the flow velocities $U(\eta)$ at all the grid points that were initially in contact with the motionless shell–wall are updated. For a given ξ_i, $U(\eta)$ is determined from the velocity profile defined on $[\varepsilon_i + \hat{w}_i, \varepsilon_o]$, where $\hat{w}_i$ is the instantaneous radial displacement of the shell at $\xi = \xi_i$. This approximation was found to recover the unsteady viscous forces, which were missing when the purely fixed grid was used.

5.3.6 Summary

Section 5.3 has presented in detail (i) the numerical solution of Flügge's shell equations and of the unsteady linearized Navier–Stokes equations, and (ii) the evaluation of the time-dependent viscous forces acting on the shell. The finite-difference method was applied to discretize Flügge's equations into linear algebraic equations. Similarly, a factored ADI (Alternating Direction Implicit) finite-difference method was used to solve the linearized Navier–Stokes equations with the flow field represented by a staggered mesh of flow variables; the divergence-free velocity constraint was satisfied at each physical-time step by means of a time-marching method in pseudo-time with artificial compressibility.

5.4 Numerical Results

5.4.1 Numerical Procedure

The purpose of this section is to explain the procedure involved in running the computer program encoding the theory presented earlier in this chapter.

First of all, the initial displacements of the shell have to be provided as input; it is recalled that the shell mode shape is characterized by the axial wave number m and the circumferential wave number n. Once m and n have been chosen, the theory in Chapter 2 is used to obtain the corresponding eigenfrequency and eigenvector (for $\bar{U}_o = 0$), from which the displacements of the shell in early physical-time steps ($t = -2\Delta t$, Δt, 0, Δt) can be calculated.

Next, the pseudo-time step $\Delta\tau$ and the artificial compressibility coefficient β have to be selected. For simple 2-D inflow-outflow problems, optimum values of $\Delta\tau$ and β may be approximated analytically (Soh and Goodrich 1988). However, given the complex nature of the *fluid-shell coupling* problem here under consideration, no relationship is known to exist which would suggest proper values for $\Delta\tau$ and β. As far as the present analysis was concerned, for a particular configuration of the system and for a given average flow velocity U_a, the optimum values of $\Delta\tau$ and β were determined via series of numerical experiments: firstly, some good guesses were made for $\Delta\tau$ and β (the very first good guesses were found accidentally!); secondly, β was kept unchanged while the computer program was run for various values of $\Delta\tau$ until convergence (the steady solution) was obtained with the lowest number of pseudo-time steps; in turn, with the newly found optimum value of $\Delta\tau$ fixed, the program was again run for various values of β until convergence was obtained with the lowest number of pseudo-time steps. If the number of pseudo-time steps required for convergence were plotted versus $\Delta\tau$ (for a given β) or β (for a given $\Delta\tau$), then the curve would be found to be quasi-parabolic.

In general, the optimum values of $\Delta\tau$ and β vary from one physical-time step to another; nevertheless, it is not feasible to determine them for every single time step. What was actually done was that the optimum values of $\Delta\tau$ and β found for the first time step, in which the program had been run on the McGill IBM mainframe computer, were used for all subsequent time steps, in which the program was run on the CRAY X-MP 2/8 computer. As a result, convergence was achieved with as few as 35 pseudo-time steps in the first physical-time step but with as many as 150 pseudo-time steps in subsequent physical-time steps.

For each configuration of the system considered, the program was run for a total of $40T_o$ or 960 physical-time steps with $\Delta t = T_o/24$, where T_o is the period of oscillation of the shell at time $t = 0$ (for given m and n). Here, although the time interval over which numerical time integration is performed is selected arbitrarily, it must be long enough to ensure that a conclusion regarding stability of the system at a given average flow velocity U_a can be drawn from a displacement-time plot generated from the computer run. For systems having their parameters listed in Section 5.4.2, each run on the CRAY computer was found to take from 1600 to 2400 CPU seconds.

5.4.2 Numerical Results

Due to a tremendous amount of computing time required for each computer run in searching for the optimum values of $\Delta\tau$ and β and especially in carrying out the time integration for a large number of time steps, it was not feasible for the present analysis to cover all the cases as were presented in Chapter 2 or 3. (Besides, since the financial support for this research was limited, the use of the CRAY computer was restricted to time donated by the CRAY Research Inc.; once the computer left Montréal, no more free computing time was available.) Instead, numerical results were obtained for a limited number of geometries, with attention being paid to the unsteady viscous effects of the annular flow on the stability of a system having a narrow annular gap; hence, for the same length of the flexible shell, considered were systems of various annular gap widths, for more than half of which the corresponding experimental results had been obtained.

For comparative purposes, the present analysis was conducted for systems with the same material properties and geometries as those tested in Chapter 4, namely

$$E = 2.8246 \times 10^6\,\mathrm{N/m^2},\ \nu = 0.47,\ \rho_s = 1.1588 \times 10^3\,\mathrm{kg/m^3},\ \mu = 0.01948,$$

$$\mathcal{U} = 55.934\,\mathrm{m/s};\ \text{for air at } 21.1^\circ\mathrm{C}\ (70^\circ\mathrm{F}):\ \rho_{air} = 1.205\,\mathrm{kg/m^3},$$

$\nu_m = 15.178 \times 10^{-6}\,\mathrm{m^2/s};\ a = 24.$[illegible]$4\,\mathrm{mm},\ h = 1.37\,\mathrm{mm},\ L/a = 8,$

$$b = 28.02\,\mathrm{mm}\ (1/10\text{–gap}),\ b = 32.63\,\mathrm{mm}\ (1/4\text{–gap}), \tag{5.164}$$

$$b = 38.1\,\mathrm{mm}\ (1/2\text{–gap}),\ b = 44.45\,\mathrm{mm}\ (3/4\text{–gap}),\ b = 50.93\,\mathrm{mm}\ (1/1\text{–gap});$$

non–uniform staggered mesh: $\gamma_s = 4,\ N = 30,\ M = 20$ for the 1/10– and 1/4–gap, $M = 30$ for the 1/2–, 3/4– and 1/1–gap.

For clarity, it should be recalled that ν is Poisson's ratio; μ is the structural damping coefficient; the term "g/a–gap" refers to the system with annular gap width $g/a = [b - (a + h/2)]/a$; γ_s is the parameter that controls how much the staggered mesh is stretched in the η–direction; M and N determine how finely the flow field is discretized in the η– and ξ–direction, respectively; $\mathcal{U} \equiv [E/\rho(1-\nu^2)]^{1/2}$ is the reference flow velocity, from which a nondimensionalized average flow velocity $\bar{U}$ can be defined, $\bar{U} = U_a/\mathcal{U}$.

Section 5.2 indicated that internal dissipation within the shell was taken to be represented by viscoelastic damping; the viscoelastic damping coefficient χ was found by equating the energy dissipated by the viscoelastic damping to that of the structural damping characterized by μ, which is constant and frequency–independent. The value of μ shown in (5.164) was measured as part of the experimental work presented in Chapter 4.

With the same procedure of analysis as adopted in Chapter 2, some preliminary calculations were first carried out to check some important part of the computer program developed herein. Theoretically, in the absence of internal dissipation, the present method of solution and that in Chapter 2 should give similar predictions for the frequency of oscillation of the shell *in vacuo* for a certain mode shape (i.e. for a certain combination of m and n). In Figure 5.3, the nondimensionalized radial shell displacement $\hat{w}$ at $\xi = 1$ is plotted against the number of time steps for (a) $\Delta t = T_o/24$ and (b) $\Delta t = T_o/48$. In both cases, the shell was excited in $m = 2$ and $n = 2$. It is found that (i) $f = 27.7\,\text{Hz}$ (between $t_1 = 160\Delta t$ and $t_2 = 801\Delta t$) for $\Delta t = T_o/24$, (ii) $f = 28.4\,\text{Hz}$ (between $t_1 = 313\Delta t$ and $t_2 = 1608\Delta t$) for $\Delta t = T_o/48$, and (iii) $f = 26.5\,\text{Hz}$ by the theory of Chapter 2. The smallness of the discrepancies between these calculated values of f may be considered to validate the segment of the computer program. The damping-like effect, clearly seen in Figure 5.3(a) and characterized by a reduction in the amplitude of $\hat{w}$, is due to the *discrete* time integration currently used. A comparison of Figures 5.3(a) and 5.3(b) indicates that such an effect becomes diminished as Δt is reduced. There is little doubt that $\Delta t = T_o/48$ is sufficiently small; nevertheless, the use of this time stepsize would have significantly increased the number of time steps required for each computer run. For this reason, $\Delta t = T_o/24$ was used for all subsequent calculations as mentioned in Section 5.4.1.

Regardless of how the shell was excited initially, if the average flow velocity were below some critical value, shell motions would die out with time due to the presence of material damping and fluid damping. However, if the flow velocity were greater than a critical value, shell motions would become continually larger, signifying a loss of stability. In the present work, both types of instabilities were observed: divergence (static instability), as illustrated in Figure 5.4 for the 1/10–gap system, and flutter (oscillatory instability), as in Figure 5.5 for the 1/2–gap system. Again, plotted in these figures is the nondimensionalized radial shell displacement at $\xi = 1$ versus the number of time steps; the shell was excited in $m = 2$ and $n = 2$ in the case of Figure 5.4 and in $m = 1$ and $n = 2$ in the case of Figure 5.5. It is seen from Figures 5.4(a) and 5.4(b) that when $\tilde{U}$ is 0.35 or 0.40, the displacement becomes rapidly diminished after about 400 time steps; on the contrary, when $\bar{U}$ is 0.45 as in Figure 5.4(c), the displacement sharply increases without any limit (i.e. divergence) after about 320 time steps. A similar trend is also found in Figures 5.5(a) and 5.5(b), for which $\bar{U}$ is 0.90 and 0.95, respectively—the displacement exhibits a harmonic pattern with a diminishing amplitude; however, with $\bar{U}$ incremented to 1.00, the displacement still retains its harmonic nature, but the amplitude keeps on increasing with time (i.e. flutter). Needless to say, the critical flow velocities depicted by Figures 5.4 and 5.5 are within (0.40,0.45) and (0.95,1.00), respectively.

For a particular annular gap, the overall critical flow velocity $\bar{U}_c^*$ of the system is the lowest of those obtained for different combinations of m and n; i.e., $\bar{U}_c^*$ is the value of $\bar{U}$ at which the system first loses stability either by divergence or by flutter. The significance of unsteady viscous effects on the stability of a system can then be revealed by plotting $\bar{U}_c^*$ for various annular gap widths g/a. Presented in Figure 5.6 are available experimental measurements and the analytical results given by the present theory, shown as the cross-hatched curve, and by the theory in Chapter 2, the solid curve. The thickness of the cross-hatched curve represents the range in which the predicted value of $\bar{U}_c^*$ fell, since computer runs were made with $\bar{U}$ incremented by 0.05 until instability was encountered. In general, with the chosen mesh size of the staggered grid (prescribed by the listed γ_s, M and N), there is excellent agreement between the numerical results and experiment, at least for $0.1 \leq g/a \leq 0.5$. A comparison between the cross-hatched curve and the solid one shows that, for $g/a \leq 0.8$, the unsteady viscous forces have a destabilizing effect on the system, lowering the value of $\bar{U}_c^*$ predicted by the previous theory (potential theory with steady viscous effects taken into account); the widest gap between the two curves appears to be at $g/a = 0.5$. As g/a becomes smaller, the predictions of $\bar{U}_c^*$ given by the two theories are seen to approach each other, thus narrowing down their discrepancy. This observation therefore implies that the unsteady viscous effects tend to be diminished and become *less* important with decreasing g/a. The effects are in fact more significant with moderate g/a, which is of the order of 0.5 for the present system parameters.

With the numerical results obtained so far, the present theory has proved to be quite promising; nevertheless, it should be borne in mind that the foregoing analysis has been based on the results for $L/a = 8$. In the light of the fact that the degree of agreement between the previous theory and experiment varied not only with g/a but also with L/a (Chapter 4), it is certainly desired to investigate such variations, if any, of the present theory by performing the same type of calculations as in Figure 5.6 for a wide range of L/a; the numerical aspect of the analysis also needs to be undertaken, namely the convergence study of $\bar{U}_c^*$ as each of γ_s, M and N is varied. These suggested studies should be carried out whenever the necessary computing resources become available.

5.5 Conclusion

A new analytical model has been introduced for the study of instabilities of the system involving a cantilevered flexible cylindrical shell confined in a coaxial rigid cylinder and subjected to an incompressible viscous flow in the annular region. This model took into account both steady and unsteady types of viscosity–related fluid forces exerted on the shell. The main aim of the analysis conducted was to examine the unsteady viscous effects on the stability of the system, especially when the annular gap was relatively small.

In the new model, shell motions were also described by Flügge's modified shell equations (Païdoussis, Misra and Chan 1985), which were solved numerically by the finite–difference method. The unsteady viscous forces, acting as forcing functions in the shell equations, were determined from the velocity and pressure perturbations in the flow. These perturbations were governed by the linearized, unsteady Navier–Stokes equations, the solution of which was obtained using a time–marching finite–difference method with artificial compressibility on a staggered grid. This method involves (i) introducing a pseudo time between two physical time steps and (ii) using a factored ADI (Alternating Direction Implicit) scheme to solve for the flow variables in the grid. In the analysis, the actual grid changing continuously to remain in contact with the moving physical boundary was approximated by a fixed grid, in which the mean axial flow velocities at all spatial locations on the boundary grid line were updated in every iteration within each physical time step.

It was found that numerical results obtained for a particular set of system parameters are in excellent agreement with experiment; the unsteady viscous effects tend to be diminished with diminishing annular gap width, provided that the gap is sufficiently small ($g/a < 0.5$, approximately). Nevertheless, effects of a number of important system parameters still remain to be explored in future work.

Chapter 6

Conclusion

6.1 Contributions of the Thesis

This thesis presented two new analytical models for the study of the stability of clamped–free coaxial cylindrical shells subjected to internal and/or annular incompressible viscous fluid flow. A substantial amount of experimental work was also conducted to verify the analytical results obtained and hence validate such models.

In the first model, Flügge's shell equations were used to describe the shell motions; the complexity of the free–end boundary conditions of the shells was dealt with by the *extended* form of the Galerkin method in solving the governing equations of motion. The unsteady fluid–dynamic forces in these equations were formulated from potential flow theory: the perturbation pressures on the shells were determined from the perturbation velocity potentials via the unsteady Bernoulli equation; those velocity potentials were governed by the Laplace equation, which was solved by the Fourier transform method. As the downstream end of the shells was unsupported, different so–called outflow models were examined in modelling the decay of flow perturbations beyond the free end. Also incorporated into the equations of motion were the *time–independent* viscosity–related effects, which result from (i) flow pressurization necessary to keep the fluid flowing and (ii) shear stress on the shell due to surface traction. Such steady viscous effects were evaluated for cantilevered shells using the same procedure previously proposed by Païdoussis, Misra and Chan (1985) for the system of clamped–clamped shells.

The theory was first used to solve test problems involving cantilevered cylindrical shells: (i) the natural frequencies of a shell *in vacuo* and (ii) the critical flow velocity of another shell conveying fluid. In both problems, predictions were found to be in excellent agreement with experimental results available in the literature. The theory was then applied to investigate the dynamical behaviour of a cantilevered steel shell located coaxially inside a rigid cylinder; the system had water flowing within the shell and/or in the annular region. The following main findings were obtained:

- In the case of internal flow, only in beam–like motions of the shell ($n = 1$) are steady viscous effects truly negligible; for shell–type motions ($n \geq 2$), flow pressurization and skin friction stabilize the shell by a considerable amount, especially if the shell is long. The presence of the quiescent annular fluid lowers the natural frequencies by increasing the effective inertia of the system. A reduction in the annular gap destabilizes the system by increasing the virtual mass of the annular fluid and hence reducing the effective stiffness of the system. With the system parameters taken for the analysis, loss of stability is not always by flutter. For some large n, divergence occurs first, followed by single– or coupled–mode flutter; nevertheless, loss of stability is always by single–mode flutter in the most critical mode, i.e. the mode associated with the lowest critical flow velocity, U_{ic}^*. In connection with the Fourier transform method employed in the theory, the utilization of an outflow model is not only desirable, but essential.

- In the case of annular flow, the system may lose stability either by flutter directly, or by divergence, followed by flutter at a higher flow. Unless the annular gap is relatively wide and n is very low, the principal effect of the steady viscous forces is to severely destabilize the system. This is due to the fact that pressurization of the annular flow results in inward–directed, crushing compressive loads acting on the shell. The inclusion of internal dissipation in the analysis rectifies the physical paradox that the critical flow velocity, U_{oc}, becomes progressively smaller with increasing n in the absence of dissipative forces. As the annular gap is reduced, U_{oc}^* becomes smaller since inviscid and pressurization forces become larger; this trend is expected to level off or even become reversed once unsteady viscous effects are taken into account. The value of U_{oc}^* is decreased as length of the shell, L, is increased or its thickness, h_i, is reduced; this finding also holds for the case of internal flow and for systems with other end boundary conditions (for instance, clamped–clamped).

- Each flow by itself, whether internal or annular, is capable of leading to instability of the system. However, if one of the two flows is present and the system is stable, the addition of the second flow does not necessarily bring it closer to instability. Furthermore, there are certain ranges of one flow for which stability can only be achieved provided that the other flow is neither too low nor too high. This intricate dynamical behaviour stems from the nonconservative nature of the cantilevered system. With a shell clamped at both ends, the system loses stability more easily when conveying counter–current flows than when conveying co–current flows.

The theory was generally well supported by the experimental part of the thesis, at least for the results of natural frequencies and of overall critical flow velocities of the system under various flow and geometric conditions. Both types of instability, divergence and flutter, predicted by theory were also observed experimentally.

In the second analytical model, much attention was given to the unsteady viscous effects of the *annular flow* on the stability of the system with narrow annular gaps. Such effects, which had been neglected in previous studies, were evaluated in a formal manner for the first time. Although the model also used Flügge's shell equations to describe the shell motions, it formulated the unsteady fluid–dynamic forces on the shell from the flow perturbations governed by the linearized, unsteady Navier–Stokes equations subject to the divergence–free velocity constraint. Such flow perturbations, namely the perturbed pressure and components of the perturbed flow velocity, were shell–motion induced; they were determined by solving the linearized Navier–Stokes equations with a time–marching, factored ADI (Alternating Direction Implicit) finite–difference method on a staggered grid (Soh and Goodrich 1988). This method involves introducing a pseudo–time between two physical–time levels. The momentum equations are first disthen rewritten in a continuous pseudo–time derivative form. The continuity equation is preconditioned with a pseudo–time derivative of the pressure multiplied by an "artificial compressibility" coefficient. The actual solution at the advanced physical–time level is the same as the steady solution of the preconditioned equations in the pseudo–time. For the problem under consideration, the choice of the artificial compressibility coefficient and of the pseudo–time stepsize played a crucial role in determining how fast the steady state in pseudo–time was reached in each physical–time step. Optimum values of the two parameters had to be found through many numerical experiments. For compatibility between the methods of solution, the finite–difference method was also used to solve Flügge's shell equations, modified to take into account flow pressurization and basic loads pre–stressing the shell. Thus, the second model in effect treated both steady and unsteady types of viscous forces due to the annular flow.

The new theory agreed quite well with experiment in terms of the overall critical flow velocities for various annular gaps of the system; the shell had the same length in all cases considered. For sufficiently small widths of the annular gap, the unsteady viscous effects of the annular flow were found to be destabilizing; they became diminished as the gap was reduced. This observation by no means rules out the possibility that the unsteady viscous forces stabilize the system with a very narrow annular passage. This can only be confirmed with further calculations and analysis.

6.2 Suggestions for Future Work

In the development of the first analytical model, it was shown that the use of an outflow model in the Fourier transform method is very essential, and that a realistic outflow model depends not only on the displacement, but also on the *slope* of the downstream end of the shell(s). Therefore, the stability of the system of pinned–pinned coaxial cylindrical shells conveying fluid should be re–examined; it was previously studied without the inclusion of any outflow model.

With the second model, only a limited set of calculations was presented: the effect of varying annular gap on the overall stability of the system for a certain length of the of varying annular gap on the overall stability of the system for a certain length of the shell. Once computing resources are available, it is important to study such an effect for a wide range of shell lengths; in addition, the possibility that the unsteady viscous effects are stabilizing for the system with an extremely narrow annular passage should also be investigated. There is an important numerical aspect of the model, which should be considered in future work as well. This is particularly concerned with the computational domain of the annular region: the effect of varying the parameter controlling the concentration of nodes in the vicinity of large gradients (physical walls), of varying the number of nodes in the radial direction, and of varying the number of nodes in the axial direction. Furthermore, all calculations in Chapter 5 were carried out with a fixed mesh, in which the coordinates of the nodes (i.e. locations of flow variables) remains unchanged even if the shell is in motion. In order to use a more realistic mesh, which continuously deforms with the moving shell, further research needs to be done on how to re–evaluate the coefficients of the flow variables in the tridiagonal systems of linear equations (in the factored ADI method) without substantially increasing the amount of computing time required. Once the model is completely validated and possibly improved, it is worthwhile to undertake similar studies of the unsteady viscous effects on systems of coaxial shells with other boundary conditions, such as clamped–clamped and pinned–pinned.

Bibliography

[1] ALTMAN, W. and De OLIVEIRA, M.G. Vibration and stability of cantilevered cylindrical shell panels under follower forces. *Journal of Sound and Vibration*, **122**, 291–298.

[2] ANDERSON, G.L. 1972 A comparison of approximate methods for solving non-conservative problems of elastic stability. *Journal of Sound and Vibration*, **22**, 159–168.

[3] ANDERSON, D.A., TANNEHILL, J.C. and PLETCHER, R.H., 1984 *Computational Fluid Mechanics and Heat Transfer*, New York: Hemisphere Publishing Corporation.

[4] ARNOLD, R.N. and WARBURTON, G.B. 1949 Flexural vibrations of the walls of thin cylindrical shells having freely supported ends. *Proceedings of the Royal Society of London*, **197**, 238–256.

[5] ASHLEY, H. and HAVILAND, G. 1950 Bending vibrations of a pipeline containing flowing fluid. *Journal of Applied Mechanics*, **17**, 229–232.

[6] AU–YANG, M.K. 1976 Free vibration of fluid–coupled coaxial cylindrical shells of different lengths. *Journal of Applied Mechanics*, **98**, 480–484.

[7] BEAN, H.S. 1971 Fluid meters—their theory and applications. *Report of ASME Research Committee on Fluid Meters*, 6th edition.

[8] BENJAMIN, T.B. 1961a Dynamics of a system of articulated pipes conveying fluid – I. Theory. *Proceedings of the Royal Society (London)*, **261**(A), 457–486.

[9] BENJAMIN, T.B. 1961b Dynamics of a system of articulated pipes conveying fluid – II. Experiments. *Proceedings of the Royal Society (London)*, **261**(A), 487–499.

[10] BISHOP, R.E.D. and JOHNSON, D.C. 1960 *Mechanics of Vibration*. Cambridge: Cambridge University Press.

[11] BOURRIÈRES, F.J. 1939 Sur un phénomène d'oscillation auto–entretenue en mécanique des fluides réels. *Publications Scientifiques et Techniques du Ministère de l'Air*, No. 147.

[12] BOUSSINESQ, J. 1877 Théorie de l'écoulement tourbillant. *Mém. prés. Acad. Sci.*, **XXIII**, 46.

[13] BRACEWELL, R.N. 1974 *The Fourier transform and its applications*. New York: McGraw–Hill Book Company, 2nd edition.

[14] BRIGHTON, J.A. and JONES, J.B. 1964 Fully developed turbulent flow in annuli. *ASME Journal of Basic Engineering*, **86**, 835–844.

[15] BRILEY, W.R. and McDONALD, H. 1980 On the structure and use of linearized block implicit schemes. *Journal of Computational Physics*, **34**, 54–73.

[16] BROWN, S.J. and LIEB, B.W. 1980 A comparison of experimental and theoretical vibration results for narrow gap, fluid–coupled, coaxial flexible cylinders. *American Society of Mechanical Engineers*, Paper No. 80–C2/PVP–104.

[17] CHEN, S.S. 1974 Dynamics of a rod–shell system conveying fluid. *Nuclear Engineering and Design*, **30**, 223–233.

[18] CHEN, S.S. 1975 Vibration of nuclear fuel bundles. *Nuclear Engineering and Design*, **35**, 399–422.

[19] CHEN, S.S. and ROSENBERG, G.S. 1975 Dynamics of a coupled shell–fluid system. *Nuclear Engineering and Design*, **32**, 302–310.

[20] CHEN, S.S. and JENDRZEJCZYK, J.A. 1978 Experiments on fluidelastic vibration of cantilevered tube bundles. *Journal of Mechanical Design*, **100**, 540–548.

[21] CHUNG, H., TURULA, P., MULCAHY, T.M. and JENDRZEJCZYK, J.A. 1981 Analysis of a cylindrical shell vibrating in a cylindrical fluid region. *Nuclear Engineering and Design*, **63**, 109–120.

[22] DOWELL, E.H. 1966 Flutter of infinitely long plates and shells. Part II: cylindrical shells. *AIAA Journal*, **4**, 1510–1518.

[23] DOWELL, E.H. and WIDNALL, S.E. 1966 Generalized aerodynamic forces on an oscillating cylindrical shell. *Quarterly of Applied Mathematics*, **XXIV**, 1–17.

[24] EL CHEBAIR, A., MISRA, A.K. and PAÏDOUSSIS, M.P. 1990 Theoretical study of the effect of unsteady viscous forces on inner– and annular–flow–induced instabilities of cylindrical shells. *Journal of Sound and Vibration*, **138**, 457–478.

[25] EL CHEBAIR, A., PAÏDOUSSIS, M.P. and MISRA, A.K. 1989 Experimental study of annular flow–induced instabilities of cylindrical shells. *Journal of Fluids and Structures*, **3**, 349–364.

[26] EVENSEN, D.A. 1974 Nonlinear vibrations of circular cylindrical shells. In *Thin-Shell Structures: Theory, Experiment, and Design* (eds Y.C. Fung & E.E. Sechler), pp. 133–155. New Jersey: Prentice Hall. (Also NASA TN D–4090, 1967.)

[27] EVENSEN, D.A. and OLSON, M.D. 1968 Circumferentially travelling wave flutter of a circular cylindrical shell. *AIAA Journal*, **6**, 1522–1527.

[28] FEODOS'EV, V.P. 1951 Vibrations and stability of a pipe when liquid flows through it. *Inzhenernyi Sbornik*, **10**, 169–170.

[29] FLÜGGE, W. 1960 *Stresses in Shells*. Berlin: Springer–Verlag.

[30] GILL, P.A.T. 1972 Vibrations of clamped–free circular cylindrical shells. *Journal of Sound and Vibration*, **25**, 501–502.

[31] GREGORY, R.W. and PAÏDOUSSIS, M.P. 1966a Unstable oscillation of tubular cantilevers conveying fluid – I. Theory. *Proceedings of the Royal Society (London)*, **293**(A), 512–527.

[32] GREGORY, R.W. and PAÏDOUSSIS, M.P. 1966b Unstable oscillation of tubular cantilevers conveying fluid – II. Experiments. *Proceedings of the Royal Society (London)*, **293**(A), 528–542.

[33] GROTBERG, J.B. and DAVIS, S.H. 1980 Fluid dynamic flapping of a collapsible channel: sound generation and flow limitation. *Journal of Biomechanics*, **13**, 219–230.

[34] HANNOYER, M.J. and PAÏDOUSSIS, M.P. 1978 Instabilities of tubular beams simultaneously subjected to internal and external axial flows. *ASME Journal of Mechanical Design*, **100**, 328–336.

[35] HANNOYER, M.J. and PAÏDOUSSIS, M.P. 1979a Dynamics of slender tapered beams with internal or external axial flow. Part 1: Theory. *Journal of Applied Mechanics*, **46**, 45–51.

[36] HANNOYER, M.J. and PAÏDOUSSIS, M.P. 1979b Dynamics of slender tapered beams with internal or external axial flow. Part 2: Experiments. *Journal of Applied Mechanics*, **46**, 52–57.

[37] HARLOW, F.H. and WELCH, J.E. 1965 Numerical calculation of time–dependent viscous incompressible flow of fluid with free surface. *Physics of Fluids*, **8**, 2182–2189.

[38] HOBSON, D.E. 1982 Fluid–elastic instabilities caused by flow in annulus. In *Proceedings of the 3rd International Conference on Vibration of Nuclear Plant*, pp. 440–463. Keswick, UK.

[39] HOLMES, P.J. 1978 Pipes supported at both ends cannot flutter. *Journal of Applied Mechanics*, **45**, 619–622.

[40] HOUSNER, G.W. 1952 Bending vibrations of a pipe line containing flowing fluid. *Journal of Applied Mechanics*, **19**, 205–208.

[41] JENDRZEJCZYK, J.A. and CHEN, S.S. 1985 Experiments on tubes conveying fluid. *Thin-Walled Structures*, **3**, 109–134.

[42] KNUDSEN, J.G. and KATZ, D.L. 1958 *Fluid Dynamics and Heat Transfer*. New York: McGraw–Hill Book Company.

[43] KRAJCINOVIC, D. 1974 Vibrations of two coaxial cylindrical shells containing fluid. *Nuclear Engineering and Design*, **30**, 242–248.

[44] LAUFER, J. 1953 The structure of turbulence in fully–developed pipe flow. NACA Technical Note 2954.

[45] LIU, H.S. and MOTE, C.D. 1974 Dynamic Response of Pipes Transporting Fluids *Journal of Engineering for Industry*, **96**, 591–596.

[46] MATEESCU, D. and PAÏDOUSSIS, M.P. 1985 The unsteady potential flow in an axially variable annulus and its effect on the dynamics of the oscillating rigid center–body. *Journal of Fluids Engineering*, **107**, 421–427.

[47] MATEESCU, D. and PAÏDOUSSIS, M.P. 1987 Unsteady viscous effects on the annular–flow–induced instabilities of a rigid cylindrical body in a narrow duct. *Journal of Fluids and Structures*, **1**, 197–215.

[48] MATEESCU, D., PAÏDOUSSIS, M.P. and BÉLANGER, F. 1988 Unsteady pressure measurements on an oscillating cylinder in narrow annular flow. *Journal of Fluids and Structures*, **2**, 615–628.

[49] MATEESCU, D., PAÏDOUSSIS, M.P. and BÉLANGER, F. 1991a Computational solutions based on a finite difference formulation for unsteady internal flows. In *Proceedings of the 29th Aerospace Sciences Meeting*, Paper No. AIAA 91–0724. Reno, Nevada.

[50] MATEESCU, D., PAÏDOUSSIS, M.P. and BÉLANGER, F. 1991b A theoretical model compared with experiments for the unsteady pressure on a cylinder oscillating in turbulent annular flow. To appear.

[51] MULCAHY, T.M. 1983 Leakage flow–induced vibrations of reactor components. *Shock and Vibration Digest*, **15**, 11-18.

[52] MURDOCK, J.W. 1976 *Fluid Mechanics and its Applications*. Boston: Houghton Mifflin Company.

[53] NAGULESWARAN, S. and WILLIAMS, C.J.H. 1968 Lateral vibration of a pipe conveying a fluid. *Journal of Mechanical Engineering Science*, **10**, 228–238.

[54] NIORDSON, F.I. 1953 Vibrations of a cylindrical tube containing flowing fluid. *Kungliga Tekniska Högskolans Handlingar (Stockholm)*, No. 73.

[55] PAÏDOUSSIS, M.P. 1966a Dynamics of flexible slender cylinders in axial flow. Part I: Theory. *Journal of Fluid Mechanics*, **26**, 717–736.

[56] PAÏDOUSSIS, M.P. 1966b Dynamics of flexible slender cylinders in axial flow. Part II: Experiments. *Journal of Fluid Mechanics*, **26**, 737–751.

[57] PAÏDOUSSIS, M.P. 1970 Dynamics of tubular cantilevers conveying fluid. *Journal of Mechanical Engineering Science*, **12**, 85–103.

[58] PAÏDOUSSIS, M.P. 1973 Dynamics of cylindrical structures subjected to axial flow. *Journal of Sound and Vibration*, **29**, 365–385.

[59] PAÏDOUSSIS, M.P. 1975 Flutter of conservative systems of pipes conveying incompressible fluid. *I. Mech. E. Journal of Mechanical Engineering Science*, **17**, 19–25.

[60] PAÏDOUSSIS, M.P. 1979 The dynamics of clusters of flexible cylinders in axial flow: theory and experiments. *Journal of Sound and Vibration*, **65**, 391–417.

[61] PAÏDOUSSIS, M.P. 1980 Flow–induced vibrations in nuclear reactors and heat exchangers. Practical experiences and state of knowledge. In *Practical Experiences with Flow–Induced Vibrations* (eds E. Naudascher and D. Rockwell), pp. 1–81. Berlin: Springer–Verlag.

[62] PAÏDOUSSIS, M.P. 1987 Flow–induced instabilities of cylindrical structures. *Applied Mechanics Reviews*, **40**, 163–175.

[63] PAÏDOUSSIS, M.P., CHAN, S.P. and MISRA, A.K. 1984 Dynamics and stability of coaxial cylindrical shells containing flowing fluid. *Journal of Sound and Vibration*, **97**, 201–235.

[64] PAÏDOUSSIS, M.P., CURLING, L.R. and GAGNON, J.O. 1982 Experiments on fluidelastic instability of cylinder clusters in axial flow. *Journal of Fluids Engineering*, **104**, 342–349.

[65] PAÏDOUSSIS, M.P. and DEKSNIS, E.B. 1970 Articulated models of cantilevers conveying fluid: the study of a paradox. *Journal of Mechanical Engineering Science*, **12**, 288–300.

[66] PAÏDOUSSIS, M.P. and DENISE, J.–P. 1970 Instabilities of cylindrical shells containing flow. M.E.R.L. TN. 70–5, Department of Mechanical Engineering, McGill University.

[67] PAÏDOUSSIS, M.P. and DENISE, J.–P. 1971 Flutter of cylindrical shells conveying fluid. *Journal of Sound and Vibration*, **16**, 459–461.

[68] PAÏDOUSSIS, M.P. and DENISE, J.–P. 1972 Flutter of thin cylindrical shells conveying fluid. *Journal of Sound and Vibration*, **20**, 9–26.

[69] PAÏDOUSSIS, M.P. AND ISSID, N.T. 1974 Dynamic stability of pipes conveying fluid. *Journal of Sound and Vibration*, **33**, 267–294.

[70] PAÏDOUSSIS, M.P., LUU, T.P. and LAITHIER, B.E. 1986 Dynamics of finite-length tubular beams conveying fluid. *Journal of Sound and Vibration*, **106**, 311–331.

[71] PAÏDOUSSIS, M.P., MATEESCU, D. and SIM, W.G. 1990 Dynamics and stability of a flexible cylinder in a narrow coaxial cylindrical duct, subjected to annular flow. *Journal of Applied Mechanics* (in press).

[72] PAÏDOUSSIS, M.P., MISRA, A.K. and CHAN, S.P. 1985 Dynamics and stability of coaxial cylindrical shells conveying viscous fluid. *Journal of Applied Mechanics*, **52**, 389–396.

[73] PAÏDOUSSIS, M.P., NGUYEN, V.B. and MISRA, A.K. 1991 A theoretical study of the stability of cantilevered coaxial cylindrical shells conveying fluid. *Journal of Fluids and Structures*, **5**, 127–164.

[74] PAÏDOUSSIS, M.P. and OSTOJA–STARZEWSKI, M. 1981 Dynamics of a flexible cylinder in subsonic axial flow. *AIAA Journal*, **19**, 1467–1475.

[75] PAÏDOUSSIS, M.P. and PETTIGREW, M.J. 1979 Dynamics of flexible cylinders in axisymmetrically confined axial flow. *Journal of Applied Mechanics*, **46**, 37–44.

[76] PAÏDOUSSIS, M.P. and SUSS, S. 1977 Stability of a cluster of flexible cylinders in bounded axial flow. *Journal of Applied Mechanics*, **44**, 401–408.

[77] PAÏDOUSSIS, M.P. and des TROIS MAISONS, P.E. 1969 Free vibration of a heavy, damped cantilever in a plane inclined to the vertical. M.E.R.L. Report No. 69–6, Department of Mechanical Engineering, McGill University.

[78] PATANKAR, S.V. 1980 *Numerical Heat Transfer and Fluid Flow.* New York: Hemisphere Publishing Corporation.

[79] PHAM, T.T. and MISRA, A.K. 1981 Dynamic stability of cylindrical shells subjected to axial flow and a linearly varying axial load. *Proceedings of the 8th Canadian Congress of Applied Mechanics, Moncton, New Brunswick*, pp. 143–144.

[80] PRANDTL, L. 1925 Über die ausgebildete turbulenz. *ZAMM*, **5**, 136–139.

[81] RAYLEIGH, L. 1945 *Theory of Sound.* New York: Dover Pubications.

[82] RODI, W. 1980 Turbulence models and their applications in hydraulics—a state-of-the-art review. IAHR Section on Fundamentals of Division II: Experimental and Mathematical Fluid Dynamics. Delft: IAHR.

[83] SCHLICHTING, H. 1968 *Boundary-Layer Theory.* New York: McGraw-Hill Book Co., 6th edition.

[84] SHARMA, C.B. 1974 Calculation of natural frequencies of fixed-free circular cylindrical shells. *Journal of Sound and Vibration*, **35**, 55–76.

[85] SHARMA, C.B. 1978 Calculation of integrals involving characteristic beam functions. *Journal of Sound and Vibration*, **56**, 475–480.

[86] SHAYO, L.K. and ELLEN, C.H. 1974 The stability of finite length circular cross-section pipes conveying inviscid fluid. *Journal of Sound and Vibration*, **37**, 535–545.

[87] SHAYO, L.K. and ELLEN, C.H. 1978 Theoretical studies of internal flow-induced instabilities of cantilevered pipes. *Journal of Sound and Vibration*, **54**, 463–474.

[88] SOH, W.Y. and GOODRICH, J.W. 1988 Unsteady solution of incompressible Navier-Stokes equations. *Journal of Computational Physics*, **79**, 113–134.

[89] TIMOSHENKO, S. and WOINOWSKY-KRIEGER, S. 1959 *Theory of Plates and Shells.* New York: McGraw-Hill Book Company, 2nd edition.

[90] VINOKUR, M. 1983 On one-dimensional stretching functions for finite-difference calculations. *Journal of Computational Physics*, **50**, 215–234.

[91] WEAVER, D.S. and UNNY, T.E. 1973 On the dynamic stability of fluid conveying pipes. *Journal of Applied Mechanics*, **40**, 48–52.

[92] WEBSTER, P.M., SAWATZKY, R.P., HOFFSTEIN, V., LEBLANC, R., HINCHEY, M.J. and SULLIVAN, P.A. 1985 Wall motion in expiratory flow limitation: choke and flutter. *Journal of Applied Physiology*, **59**, 1304–1312.

[93] WEPPELINK, H. 1979 Free vibrations of finite circular cylindrical shells and tubes with and without a surrounding fluid. Ph.D. Thesis, Technische Hogeschool Twente, Enschede, The Netherlands.

[94] WILLS, A.P. 1931 *Vector and Tensor Analysis.* New York: Prentice-Hall, Inc.

[95] YEH, T.T. and CHEN, S.S. 1977 Dynamics of a cylindrical shell system coupled by viscous fluid. *Journal of the Acoustical Society of America*, **62**, 262–270.

[96] ZIADA, S., BÜHLMANN, E.T. and BOLLETER, U. 1988 Model tests on shell flutter due to flow on both sides. *Journal of Fluids and Structures*, **2**, 177–196.

Table 2.1

Comparison between natural frequencies of a cantilevered shell, as measured by Gill (1972) and as calculated by Sharma's (1974) sextic approximation and by this theory with different numbers of admissible functions M, for different circumferential and axial mode numbers, n and m, respectively.

n	Experiments or Theory		Natural Frequencies (Hz)			
			$m = 1$	$m = 2$	$m = 3$	$m = 4$
2	Gill (1972)		293.0	827.0	1894.8	—
	Sharma (1974)		318.0	1006.4	2356.5	3882.3
	Present Theory	$M = 4$	312.4	953.3	2246.7	3818.3
		$M = 6$	312.0	946.3	2225.8	3734.7
		$M = 8$	311.8	942.9	2214.7	3701.7
		$M = 10$	311.6	940.9	2207.9	3683.4
3	Gill (1972)		760.0	886.0	1371.0	2155.0
	Sharma (1974)		769.7	927.7	1504.2	2403.6
	Present Theory	$M = 4$	755.5	906.5	1461.7	2361.9
		$M = 6$	755.4	905.0	1454.9	2331.6
		$M = 8$	755.4	904.3	1451.2	2318.2
		$M = 10$	755.4	903.8	1449.0	2310.6
4	Gill (1972)		1451.0	1503.0	1673.0	2045.0
	Sharma (1974)		1465.3	1523.3	1726.1	2148.5
	Present Theory	$M = 4$	1438.3	1494.6	1693.1	2116.5
		$M = 6$	1438.3	1494.1	1690.9	2103.8
		$M = 8$	1438.2	1493.8	1689.7	2098.4
		$M = 10$	1438.2	1493.7	1688.9	2095.4

Table 2.2

Comparison between critical flow velocities $\bar{U}_{ic}$ of a cantilevered shell, as calculated by Païdoussis and Denise (1972) and by the present theory with different integration stepsizes $\Delta\bar{\alpha}$, for different circumferential mode numbers n and three different flow models; the axial mode number m shown in each case is associated with instability.

n	Model	Critical Flow Velocity, $\bar{U}_{ic}$						
		Present Theory						Païdoussis & Denise (1972)
		$\Delta\bar{\alpha} = 4.0$	m	$\Delta\bar{\alpha} = 2.0$	m	$\Delta\bar{\alpha} = 1.0$	m	
1	1	0.911096	2	0.890955	2	0.890971	2	0.959
	2	1.095842	2	0.980529	2	0.980665	2	
	3	1.066014	2	0.974488	2	0.974496	2	
2	1	0.374694	2	0.367785	2	0.367785	2	0.452
	2	0.475056	2	0.420881	2	0.420882	2	
	3	0.456199	2	0.418705	2	0.418705	2	
3	1	0.405467	3	0.406670	3	0.406670	3	0.524
	2	0.423276	3	0.466205	3	0.466203	3	
	3	0.453574	3	0.467168	3	0.467168	3	

Table 2.3

Comparison between critical flow velocities $\bar{U}_{ic}$ of a cantilevered shell, as calculated by Païdoussis and Denise (1972) and by the present theory with different integration domains $(-z, z)$, for different circumferential mode numbers n and three different flow models; the axial mode number m shown in each case is associated with instability.

n	Model	Critical Flow Velocity, $\bar{U}_{ic}$								
		Present Theory								Païdoussis & Denise (1972)
		$(-150,150)$	m	$(-200,200)$	m	$(-250,250)$	m	$(-300,300)$	m	
1	1	0.890971	2	0.890955	2	0.890948	2	0.890945	2	0.959
	2	0.980526	2	0.980529	2	0.980534	2	0.980539	2	
	3	0.974459	2	0.974488	2	0.974502	2	0.974509	2	
2	1	0.367808	2	0.367785	2	0.367774	2	0.367769	2	0.452
	2	0.420876	2	0.420881	2	0.420888	2	0.420894	2	
	3	0.418670	2	0.418705	2	0.418721	2	0.418730	2	
3	1	0.406738	3	0.406670	3	0.406639	3	0.406622	3	0.524
	2	0.466193	3	0.466205	3	0.466218	3	0.466230	3	
	3	0.467105	3	0.467168	3	0.467198	3	0.467214	3	

Table 2.4

Comparison between critical flow velocities $\bar{U}_{ic}$ of a cantilevered shell, as calculated by Païdoussis and Denise (1972) and by the present theory with different number of admissible functions M, for different circumferential mode numbers n and three different flow models; the axial mode number m shown in each case is associated with instability.

n	Model	Critical Flow Velocity, $\bar{U}_{ic}$								
		Present Theory								Païdoussis & Denise (1972)
		$M=4$	m	$M=6$	m	$M=8$	m	$M=10$	m	
1	1	0.890955	2	0.885828	2	0.883633	2	0.882477	2	0.959
	2	0.980529	2	0.970659	2	0.966729	2	0.964672	2	
	3	0.974488	2	0.965498	2	0.961962	2	0.960117	2	
2	1	0.367785	2	0.366099	2	0.365230	2	0.364690	2	0.452
	2	0.420881	2	0.419166	2	0.418412	2	0.418124	2	
	3	0.418705	2	0.417027	2	0.416304	2	0.416019	2	
3	1	0.406670	3	0.405667	3	0.405351	3	0.405209	3	0.524
	2	0.466205	3	0.464739	3	0.465733	2	0.467141	2	
	3	0.467168	3	0.463316	3	0.464220	2	0.465516	2	

Table 2.5

The effect of the out–flow model used in the calculations on $\bar{U}_{ic}$; the calculations were conducted for $n = 2$, with $\Delta\bar{\alpha} = 4.0$, $(-z, z) = (-200, 200)$, $M = 4$, $\ell = 3$.

Model	$\bar{U}_{ic}$	Type of Instability
0	0.1311	Divergence
	0.9505	Coupled–mode flutter
1	0.3747	Single–mode flutter
2	0.4751	Single–mode flutter
3	0.4562	Single–mode flutter

Table 2.6

The effect of length ℓ on the critical flow velocity, $\bar{U}_{ic}$, for different circumferential mode numbers n and three different flow models; here, $\Delta\bar{\alpha} = 4.0$, $(-z, z) = (-200, 200)$, $M = 4$. An asterisk signifies that $\bar{U}_{ic} < 0.1$.

n	Model	Critical Flow Velocity, $\bar{U}_{ic}$			
		$\ell = 2.0$	$\ell = 3.0$	$\ell = 4.0$	$\ell = 10^2$
1	1	0.8530	0.9111	0.8623	0.8911
	2	0.8966	1.0958	*	0.6570
	3	0.8996	1.0660	0.8992	1.0134
2	1	0.3505	0.3747	0.3618	0.3642
	2	0.3737	0.4751	*	0.2090
	3	0.3847	0.4565	0.4452	0.3853
3	1	0.4164	0.4054	0.4082	0.4189
	2	0.4927	0.4233	*	*
	3	0.4726	0.4536	0.4197	*
4	1	0.4445	0.4526	0.4752	*
	2	*	0.5484	*	*
	3	0.4774	0.5273	1.0221	*

Table 2.7

The effect of varying the length–to–radius ratio of a cantilevered shell on the critical flow velocity, $\bar{U}_{ic}$, for different circumferential mode numbers n and three different flow models; the axial mode number m shown in each case is associated with instability. The calculations were conducted with $\Delta\bar{\alpha}$, $(-z, z) = (-200, 200)$, $M = 4$ and $\ell = 3.0$.

n	L/a	Critical Flow Velocity, $\bar{U}_{ic}$					
		Model 1	m	Model 2	m	Model 3	m
1	5	1.552088	2	1.605623	2	1.608831	2
	10	1.060300	2	1.145292	2	1.139270	2
	15	0.794790	2	0.882841	2	0.877991	2
	20	0.625826	2	0.705826	2	0.702593	2
2	5	0.765242	2	0.827623	2	0.823093	2
	10	0.452692	2	0.510982	2	0.508065	2
	15	0.327084	2	0.378561	2	0.376519	2
	20	0.286602	2	0.345992	2	0.344017	2
3	5	0.493430	2	0.551185	2	0.547451	2
	10	0.506881	2	0.519440	2	0.519359	2
	15	0.365939	3	0.432463	2	0.430596	3
	20	0.400745	4	0.459856	3	0.459928	3

Table 2.8

The critical flow velocities, $\bar{U}_{ic}$, with n = 1–8 for the 1/10–gap system subjected to internal flow according to the inviscid and viscous (i.e., including steady viscous effects) versions of the theory, with the axial mode number m involved in each case. Cases in which stability is first lost by divergence, for a particular n, are marked by †.

n	Critical Flow Velocity, $\bar{U}_{ic}$			
	Inviscid Theory	m	Viscous Theory	m
1	0.06899	2	0.06904	2
2	0.03107	2	0.03261	2
3	0.02772	3	0.03117	3
4	0.02705	4	0.03356	4
5	0.02990	5	0.03488	4
6	0.02911†	1	0.04808	4
	0.03115	1		
7	0.03427†	1	0.11065	4
	0.03895	1		
8	0.04359†	1	0.41368	3
	0.05185	1		

Table 2.9

The critical flow velocities, $\bar{U}_{ic}$, associated with n = 1–9 for the 1/10– and 1/100–gap systems subjected to internal flow according to inviscid theory, with the axial mode number m involved in each case. Cases in which stability is first lost by divergence, for a particular n, are marked by †.

n	Critical Flow Velocity, $\bar{U}_{ic}$			
	$\frac{1}{10}$–Gap	m	$\frac{1}{100}$–Gap	m
1	0.06899	2	0.06439	2
2	0.03107	2	0.02657	1
3	0.02772	3	0.01565	1
4	0.02705	4	0.01739	2
5	0.02990	5	0.01881	3
6	0.02911†	1	0.02093	4
	0.03115	1		
7	0.03427†	1	0.02316	5
	0.03895	1		
8	0.04359†	1	0.03662†	1
	0.05185	1	0.04423	1,2
9	0.05634†	1	0.04645†	1
	0.06839	1	0.05855	1,2

Table 2.10

The effect of varying the length–to–radius ratio on the overall critical flow velocity, $\bar{U}^{*}_{ic}$, for the 1/10–gap system subjected to internal flow, according to the inviscid and viscous (i.e., including steady viscous effects) versions of the theory; the circumferential mode number n associated with $\bar{U}^{*}_{ic}$ is shown in each case.

L/a	Critical Flow Velocity, $\bar{U}^{*}_{ic}$			
	Inviscid Theory	n	Viscous Theory	n
5	0.03484	5	0.03842	4
10	0.02827	4	0.03241	3
15	0.02242	3	0.02741	2
20	0.01956	2	0.02838	3
25	0.01895	2	0.02717	3
30	0.01869	2	0.02841	2

Table 2.11

Critical annular flow velocities, $\bar{U}_{oc}$, with different n for the 1/10–gap system, according to the inviscid and viscous versions of the theory; "S" stands for single–mode flutter, "C" for coupled–mode flutter, and "D" for divergence. The identification of the mode number m at instability for some of the results with dissipation ($\mu_i \neq 0$) was not clear–cut; hence, no value of m is given.

n	Inviscid Theory ($\mu_i = 0$)			Viscous Theory ($\mu_i = 0$)			Viscous Theory ($\mu_i = 5 \times 10^{-3}$)		
	$\bar{U}_{oc}$	Instability Type	m	$\bar{U}_{oc}$	Instability Type	m	$\bar{U}_{oc}$	Instability Type	m
1	0.06672	S	4	0.06656	S	4	0.06508	S	4
2	0.03429	S	3	0.00361	D	1	0.00361	D	1
				0.0151	C	1	0.0151	C	1
3	0.02461	S	3	0.00288	D	1	0.00284	D	1
				0.0102	C	2	0.0102	C	1
4	0.02534	S	4	0.00294	D	1	0.0086	C	—
				0.0108	C	1			
5	0.02559	S	3	0.00306	C	1	0.0080	C	—
6	0.02130	D	1	0.00208	C	1	0.0087	C	—
	0.02284	C	1						
7	0.02650	D	1	0.00140	C	1	0.00173	C	—
	0.03000	C	1						
8	0.03526	D	1	0.00107	C	1	> 0.1	C	—
	0.04179	C	1						

Table 2.12

The effect of steady viscous forces and structural damping on stability with $n = 1$, showing that they can be either stabilizing or destabilizing, depending on the gap size.

Gap Size,	Critical Flow Velocity, $\bar{U}_{oc}$		
$(b-a)/a$	Inviscid	Viscous ($\mu_i = 0$)	Viscous ($\mu_i = 5 \times 10^{-3}$)
1/10	0.06672	0.06656	0.06508
1/2	0.10099	0.10272	0.10253

Table 4.1

The effect of annular fluid on the critical internal flow velocity, $\bar{U}^*_{ic}$, for different lengths of a cantilevered silicone rubber shell. The fluid is air.

$(b-a)/a$	Critical Flow Velocity, $\bar{U}^*_{ic}$ (m/s)		
	$L/a=8$	$L/a=7$	$L/a=6$
1.5	63.71 ± 2.66%	70.30 ± 1.17%	78.03 ± 0.60%
∞	63.25 ± 1.71%	70.11 ± 0.99%	78.08 ± 0.47%

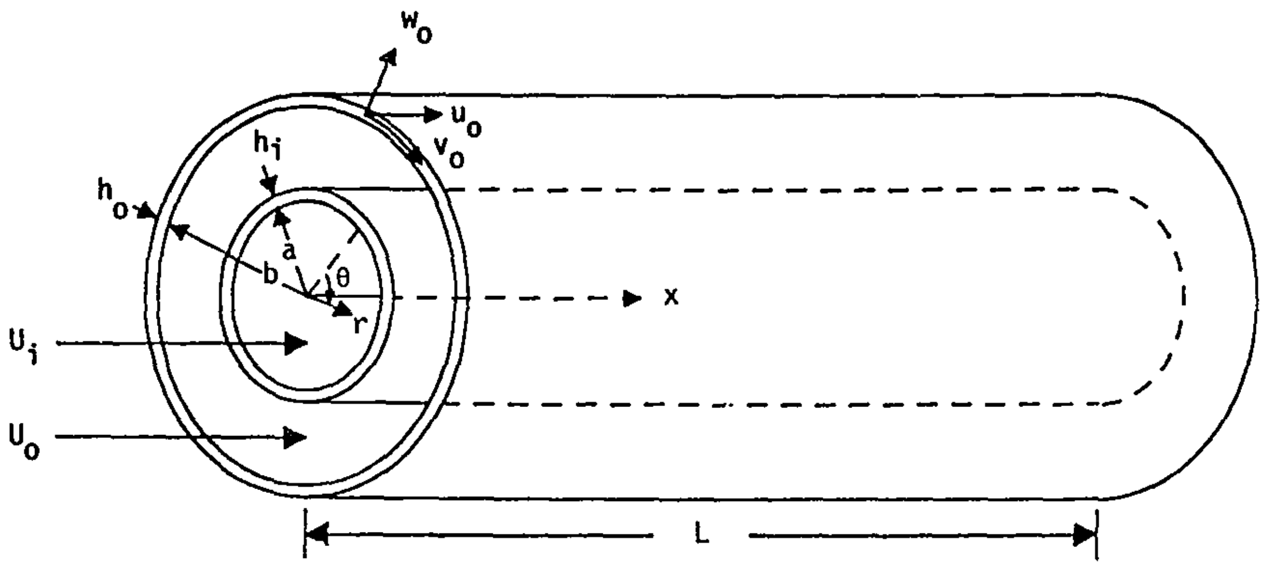

Figure 2.1: Schematic of the system under consideration.

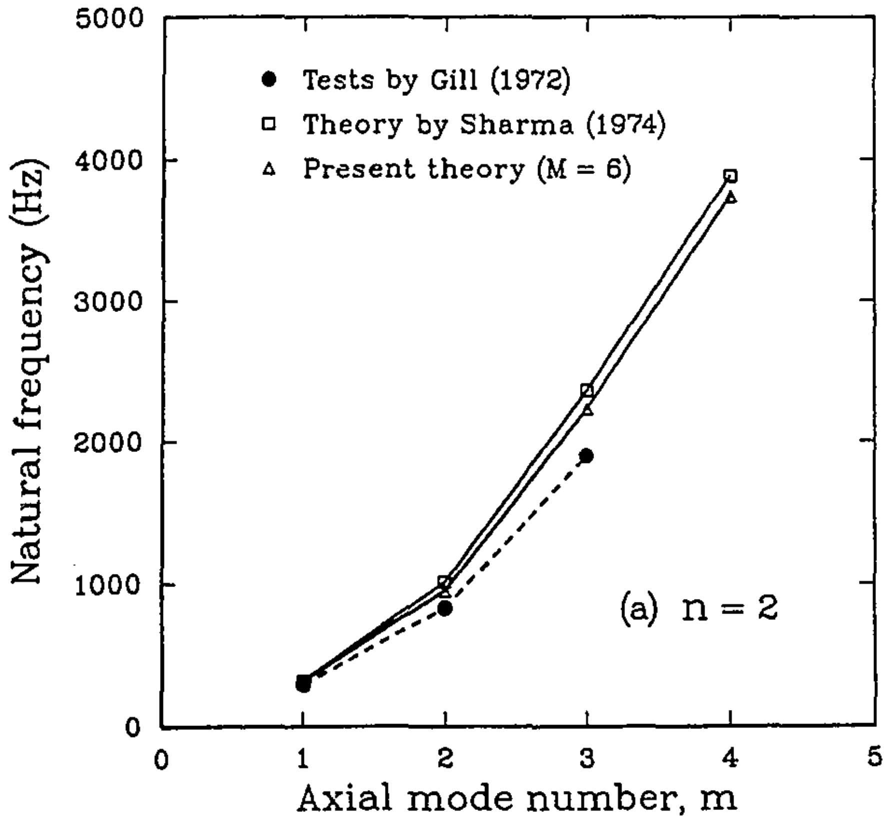

Figure 2.2: Comparison of the *in vacuo* natural frequencies calculated by this theory with Gill's (1972) measurements and Sharma's (1974) sextic-approximation calculations; the shell parameters are given in Section 2.4.2. (a) $n = 2$; (b) $n = 3$; (c) $n = 4$.

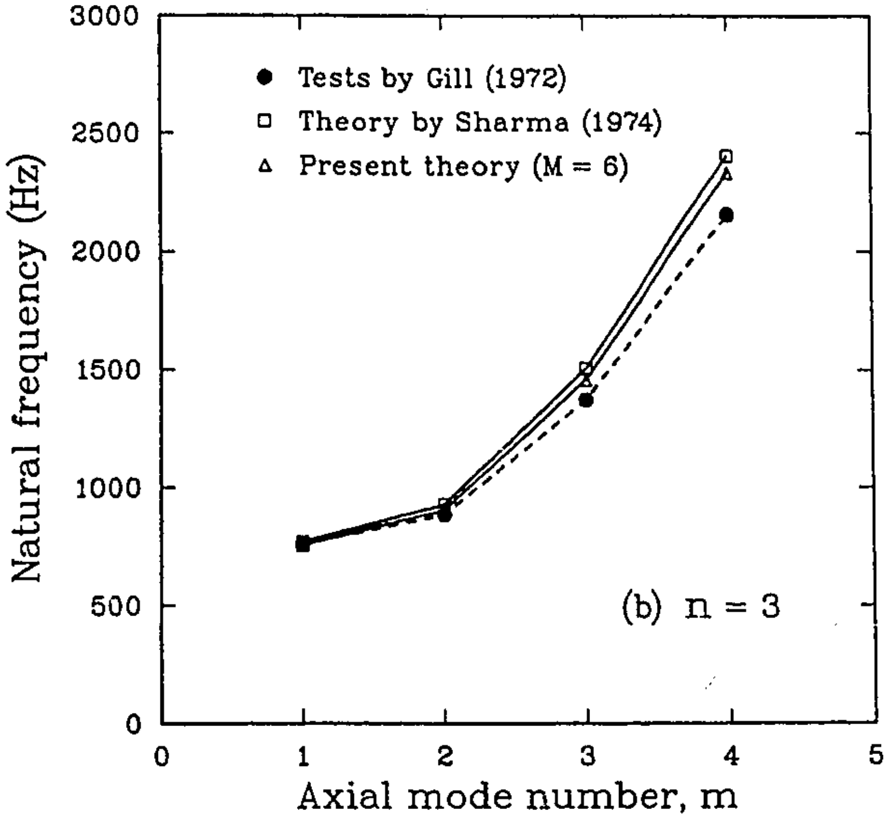

Figure 2.2 (continued): Part (b).

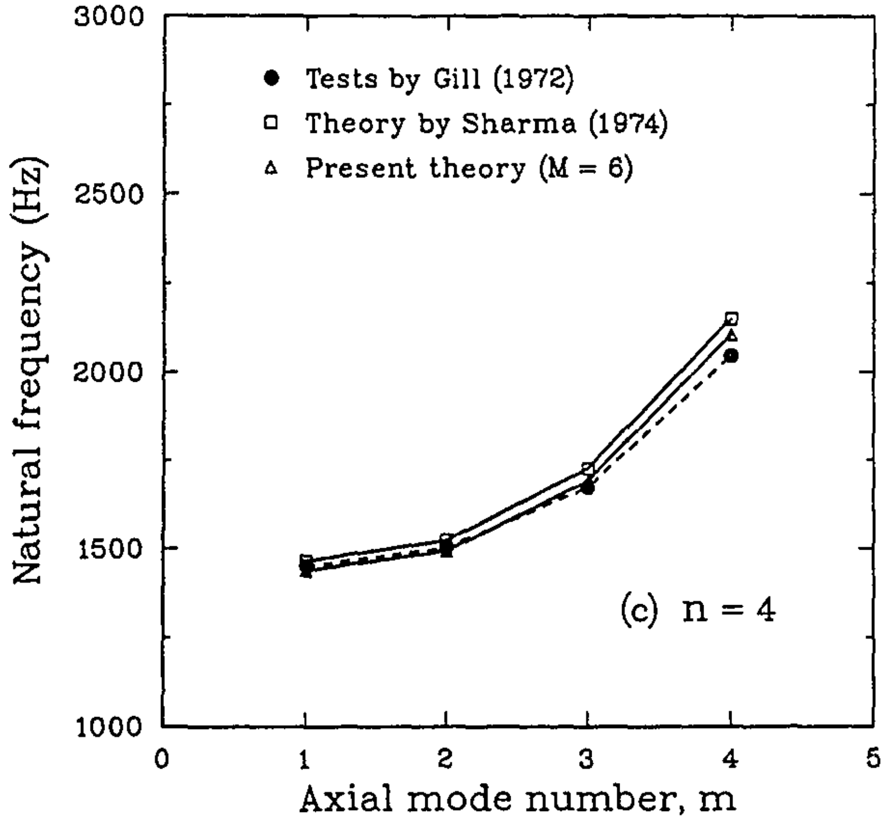

Figure 2.2 (continued): Part (c).

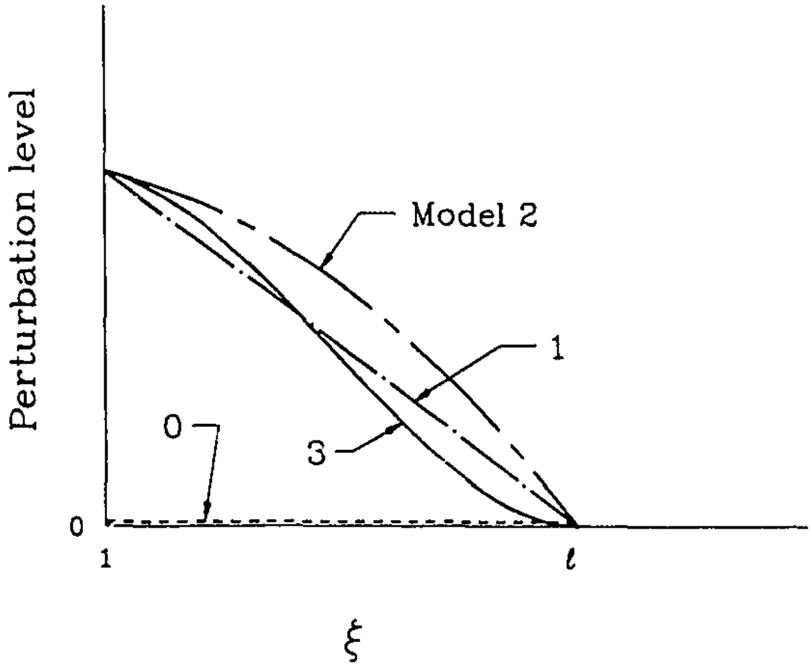

Figure 2.3: The so–called "out–flow" models considered in this theory for the decay of perturbations beyond the free end of the shells; Model 0 effectively corresponds to no model at all. $\xi \equiv x/L = 1$ corresponds to the free end of the shell; $\xi = \ell(\equiv L'/L)$ is the point where perturbations are assumed to vanish.

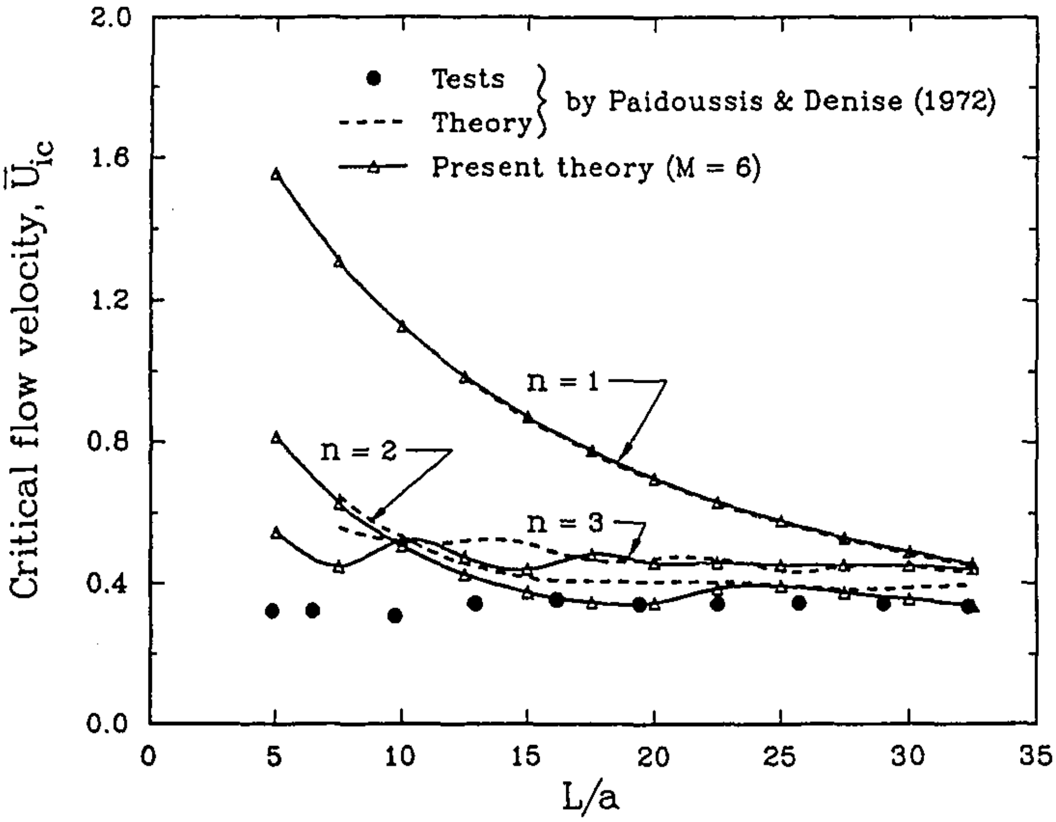

Figure 2.4: Comparison of the dimensionless critical flow velocities, $\bar{U}_{ic}$, calculated by the present theory with Païdoussis and Denise's (1972) theoretical and experimental values, for a cantilevered elastomer shell conveying air flow; the system parameters are given in Section 2.4.3.

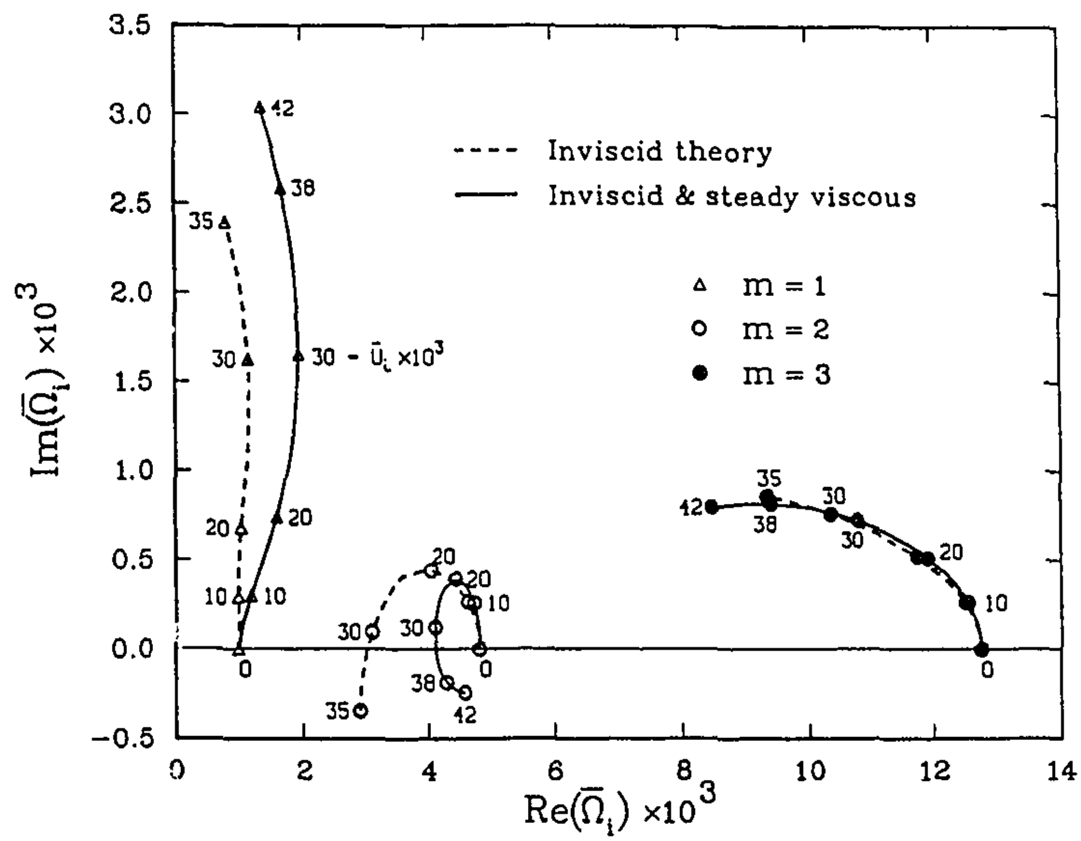

Figure 2.5: Typical Argand diagram involving the real, $\mathrm{Re}(\bar{\Omega}_i)$, and imaginary, $\mathrm{Im}(\bar{\Omega}_i)$, parts of the dimensionless eigenfrequencies of the so-called 1/10-gap system, consisting of a cantilevered steel shell surrounded by quiescent annular fluid (water) while conveying internal water flow, as the dimensionless flow velocity $\bar{U}_i$ is varied; the system parameters are given in Section 2.5.1. These calculations were carried out for $n = 2$, $m = 1, 2, 3$; - - - - , inviscid theory; ——, with steady viscous terms taken into account.

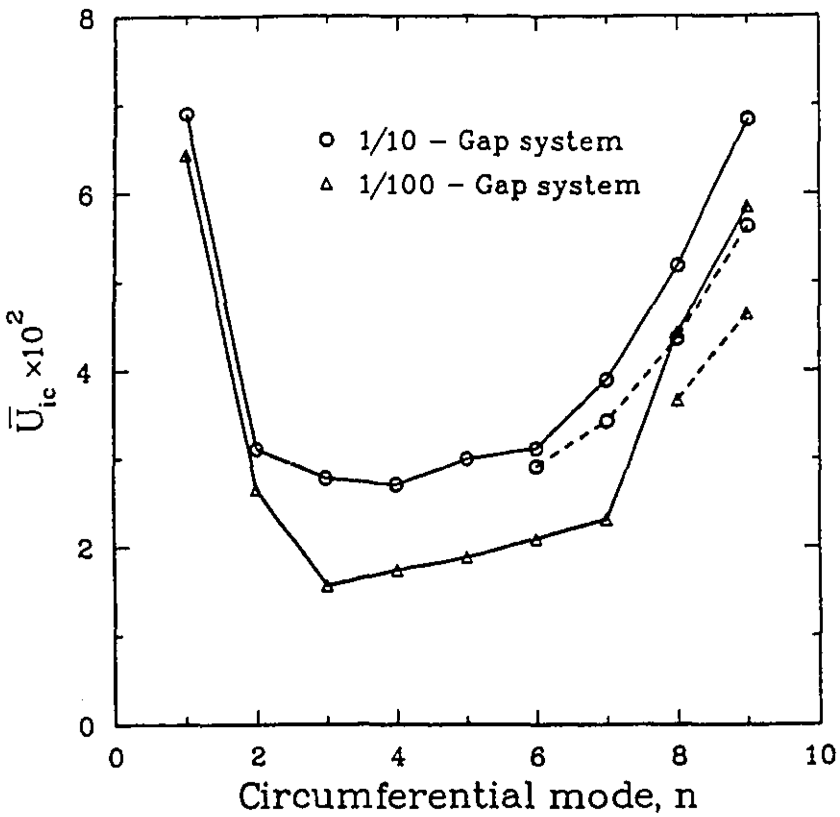

Figure 2.6: The dimensionless critical flow velocity $\bar{U}_{ic}$ of a cantilevered steel shell, surrounded by quiescent annular fluid (water) while conveying internal water flow, as a function of n for two different annular gaps; the system parameters are given in Section 2.5.1. These calculations were done with the inviscid theory; ——, flutter boundary; - - - -, divergence boundary (for the modes in which stability is first lost by divergence). Note: "1/k-gap" system means one where (annular gap) / (inner-shell radius) = 1/k.

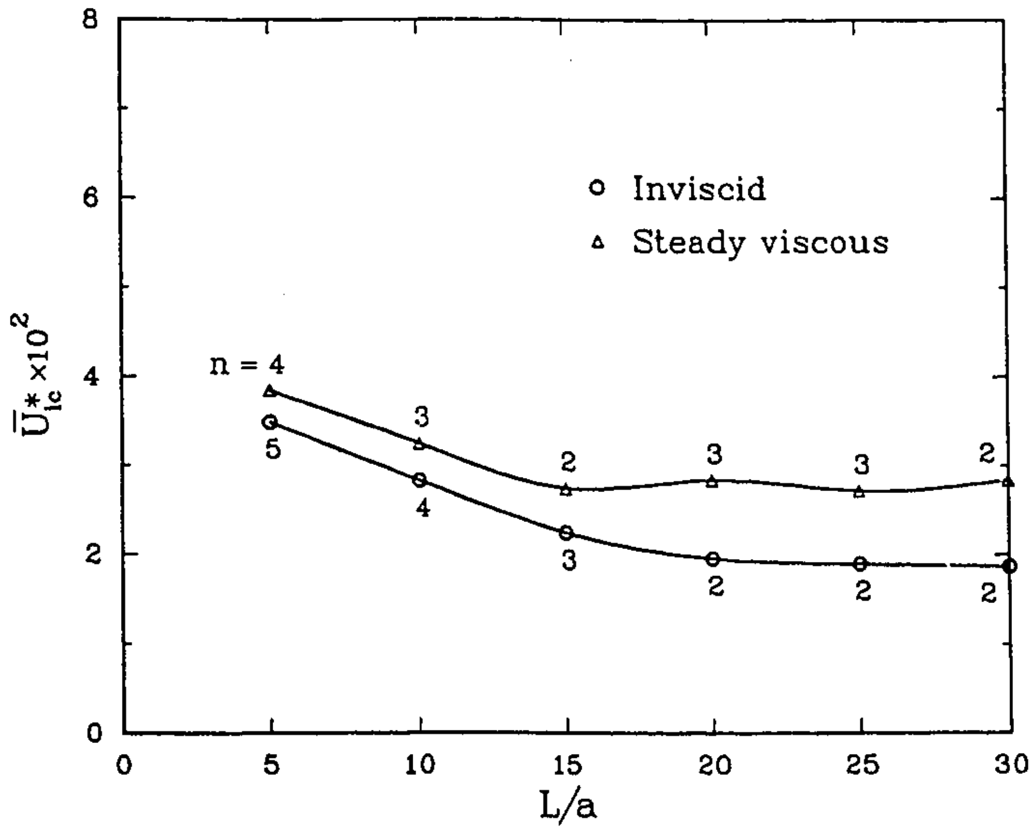

Figure 2.7: The effect of L/a on the overall (lowest) critical dimensionless flow velocity, $\bar{U}^*_{lc}$, for the 1/10–gap system conveying internal water flow and quiescent annular fluid (water); the circumferential mode number, n, associated with first loss of stability is shown in the figure. ○, inviscid flow; △, with steady viscous effects taken into account.

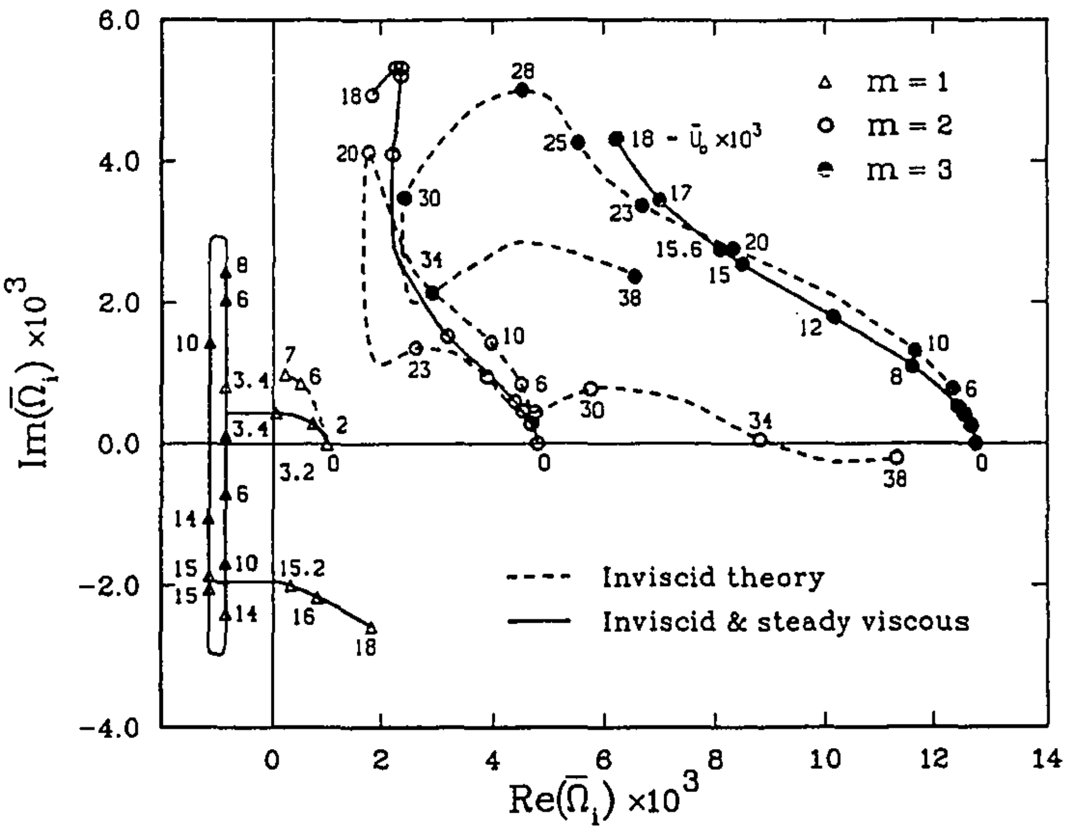

Figure 2.8: Typical Argand diagram for the dimensionless eigenfrequencies $\bar{\Omega}_i$ of the 1/10–gap system conveying annular water flow and quiescent internal fluid (water), as the dimensionless flow velocity $\bar{U}_o$ is varied; the system parameters are given in Section 2.5.1. These calculations were carried out for $n = 2$, $m = 1,2,3$; - - - - , inviscid theory; ——, with steady viscous effects taken into account.

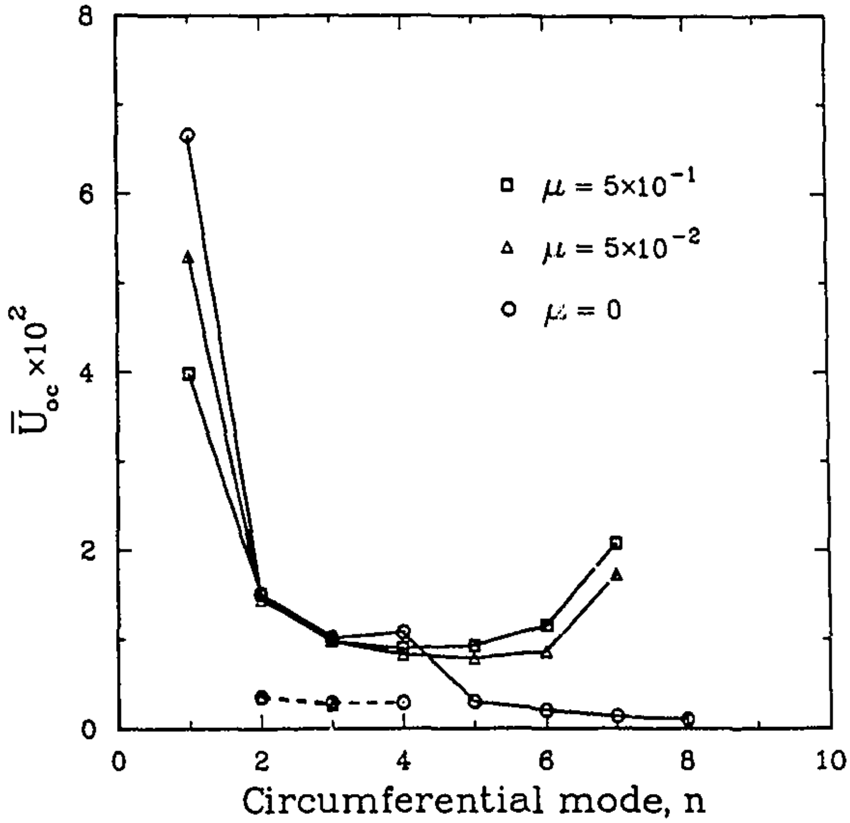

Figure 2.9: The effect of structural damping (variable μ_i) on stability of the 1/10–gap system with annular water flow according to the viscous version of the theory, showing the emergence of a minimum $\bar{U}_{oc}$ for flutter, at $n = 5$ when $\mu_i \neq 0$; - - - - , divergence boundary; —— , flutter boundary.

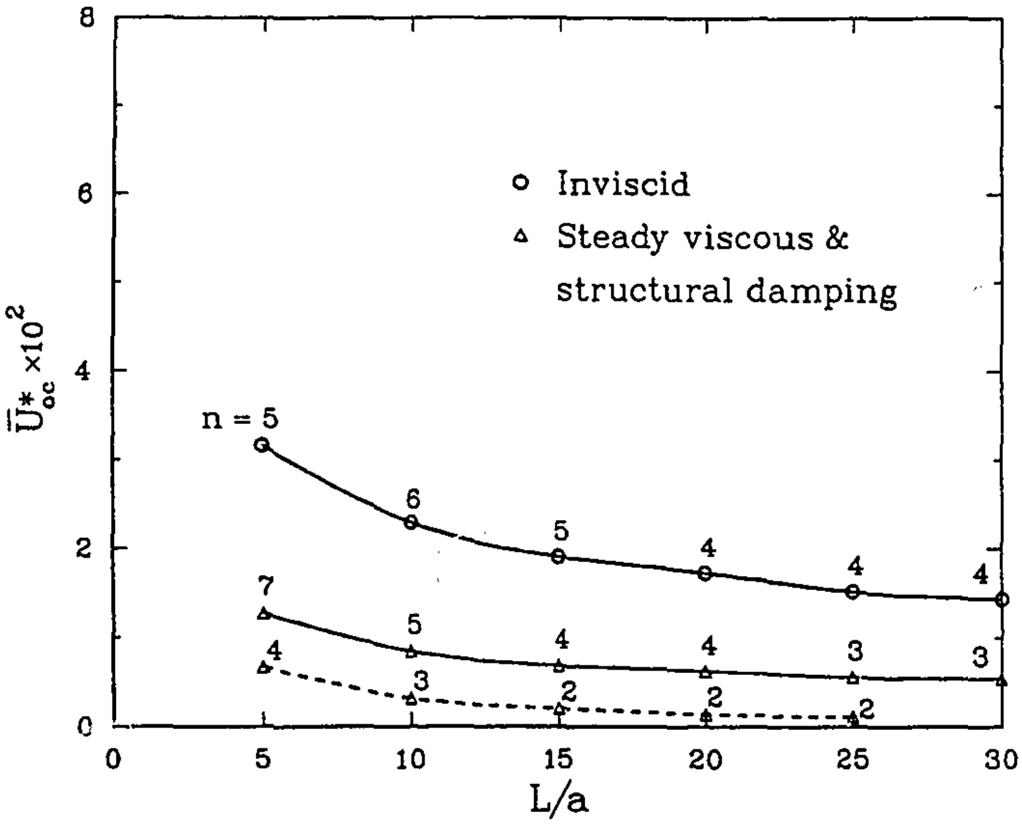

Figure 2.10: The effect of L/a on the overall (lowest) critical dimensionless flow velocity, $\bar{U}^*_{oc}$, for the 1/10–gap system conveying annular water flow and quiescent internal fluid (water); the circumferential mode number, n, associated with first loss of stability is shown for each value of L/a for which calculations were conducted. - - - - , divergence boundary; ——, flutter boundary. The viscous results were obtained with $\mu_i = 5\times10^{-3}$.

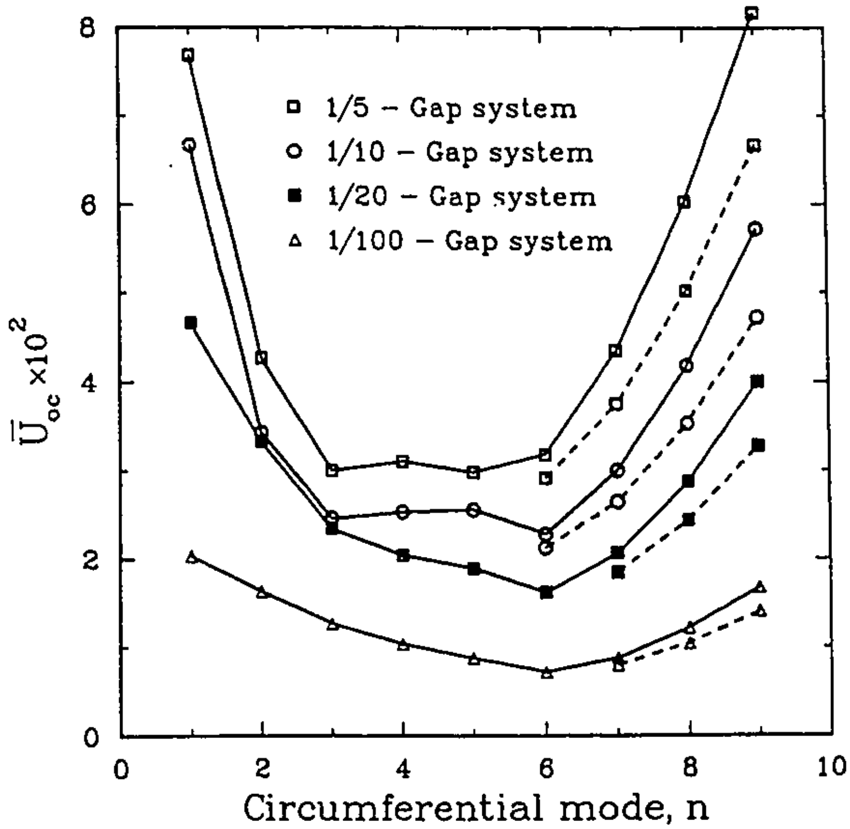

Figure 2.11: The effect of annular gap size on the critical annular flow velocity $\bar{U}_{oc}$ according to the inviscid theory as n is varied. In cases where divergence precedes flutter, the divergence boundaries (- - - -) are also shown.

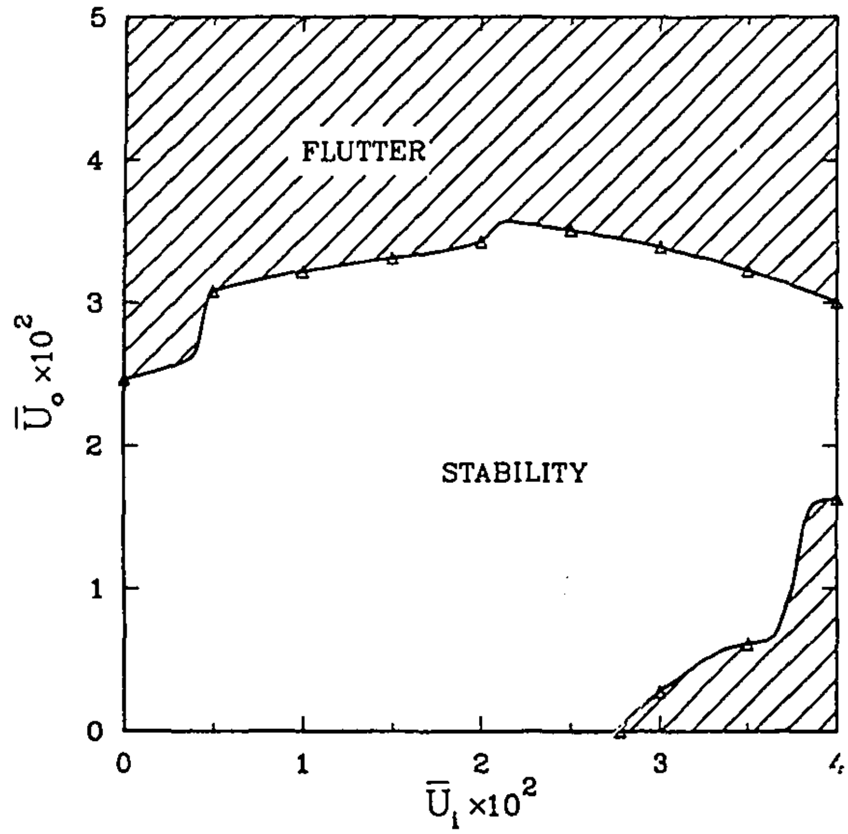

Figure 2.12: Stability map with $n = 3$ for the 1/10–gap system simultaneously subjected to internal and annular flows according to the inviscid theory.

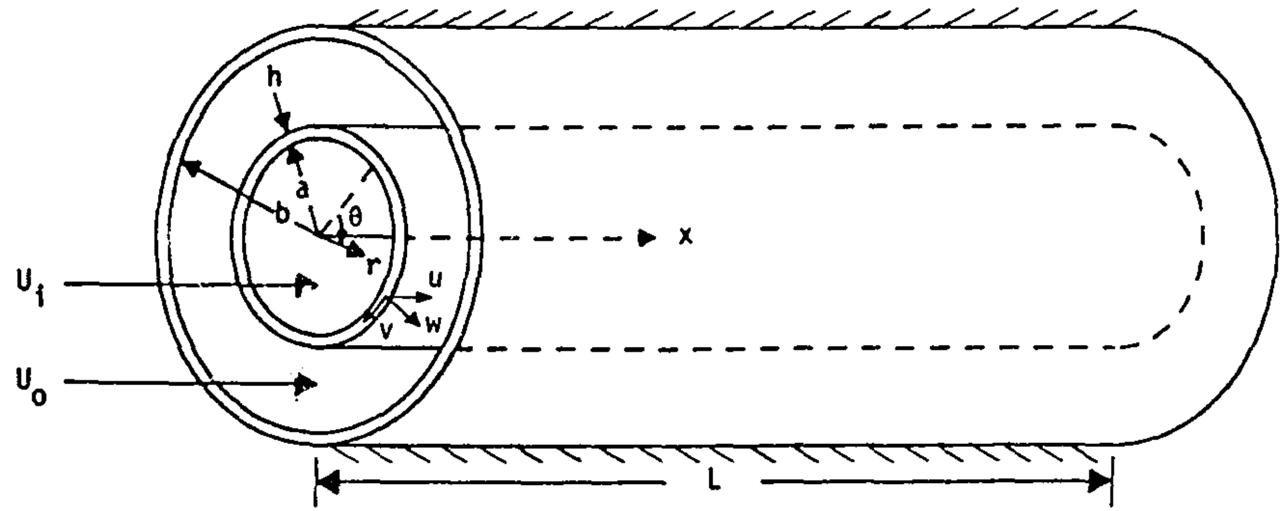

Figure 3.1: Schematic of the system under consideration.

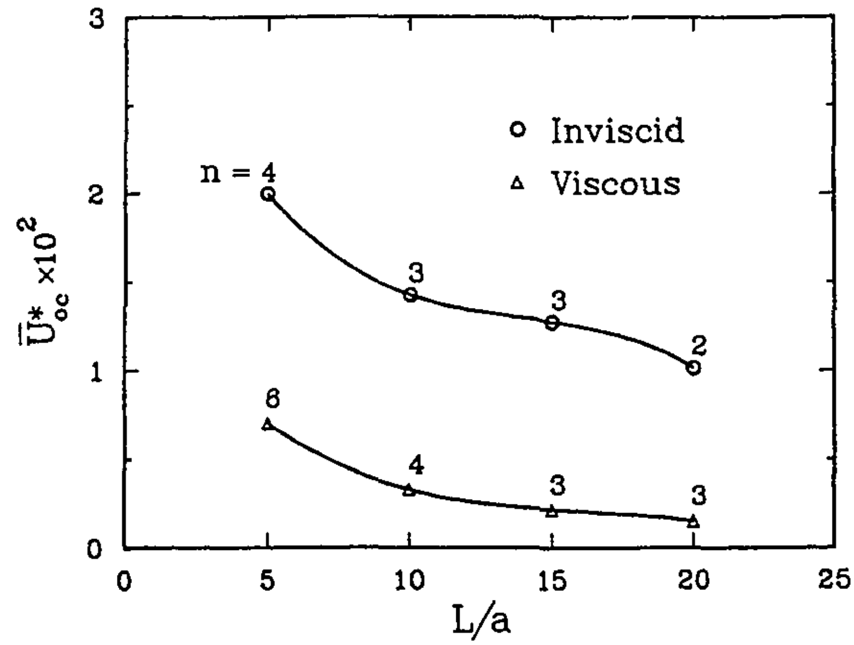

Figure 3.2: The overall (lowest) critical dimensionless annular flow velocity, $\bar{U}^*_{oc}$, in the $\frac{1}{10}$-gap system as a function of the dimensionless length of the shell L/a, with the circumferential mode, n, associated with first loss of stability indicated in the figure; ○, inviscid flow; △, with steady viscous effects taken into account. The shell is clamped at both ends and the inner fluid is stagnant.

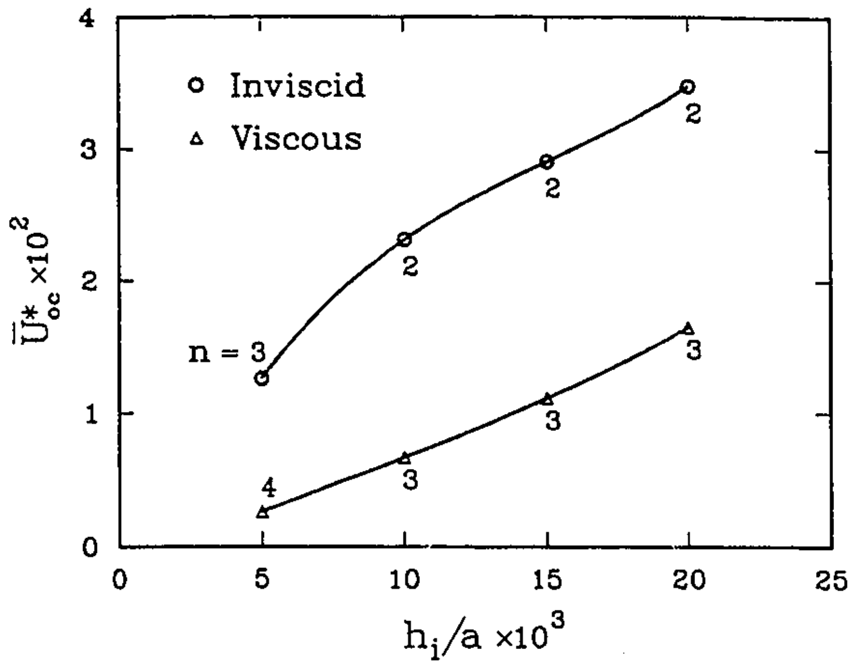

Figure 3.3: The overall critical dimensionless annular flow velocity, $\bar{U}^*_{oc}$, in the $\frac{1}{10}$-gap system as a function of the dimensionless wall-thickness of the shell h_i/a, with the circumferential mode, n, associated with first loss of stability indicated in the figure; $\bigcirc$, inviscid flow; $\triangle$, with steady viscous effects taken into account. The shell is clamped at both ends and the inner fluid is stagnant.

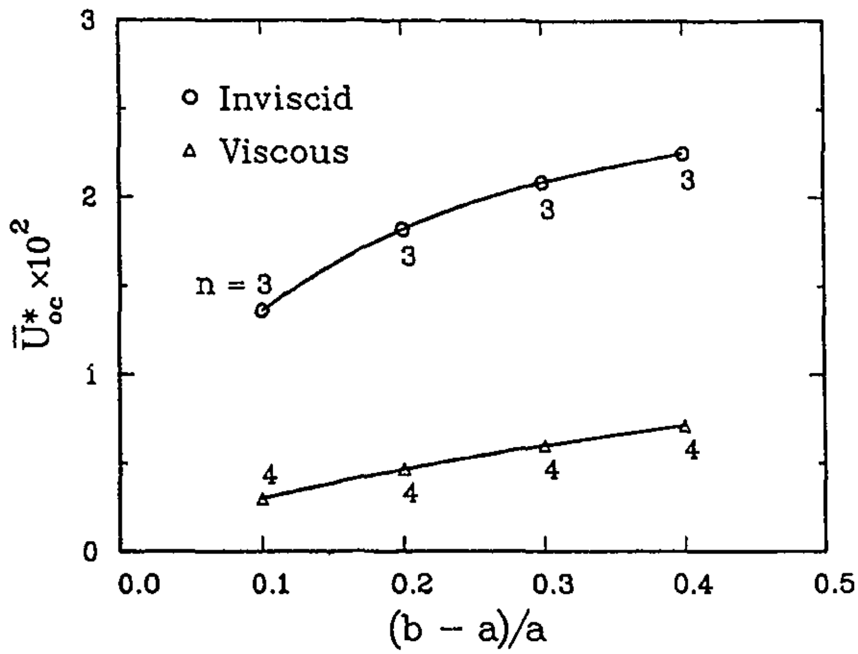

Figure 3.4: The overall critical dimensionless annular flow velocity, $\bar{U}^*_{oc}$, as a function of the dimensionless annular gap $(b-a)/a$, with the circumferential mode, n, associated with first loss of stability marked in the figure; ○, inviscid flow; △, with steady viscous effects taken into account. The shell is clamped at both ends and the inner fluid is stagnant.

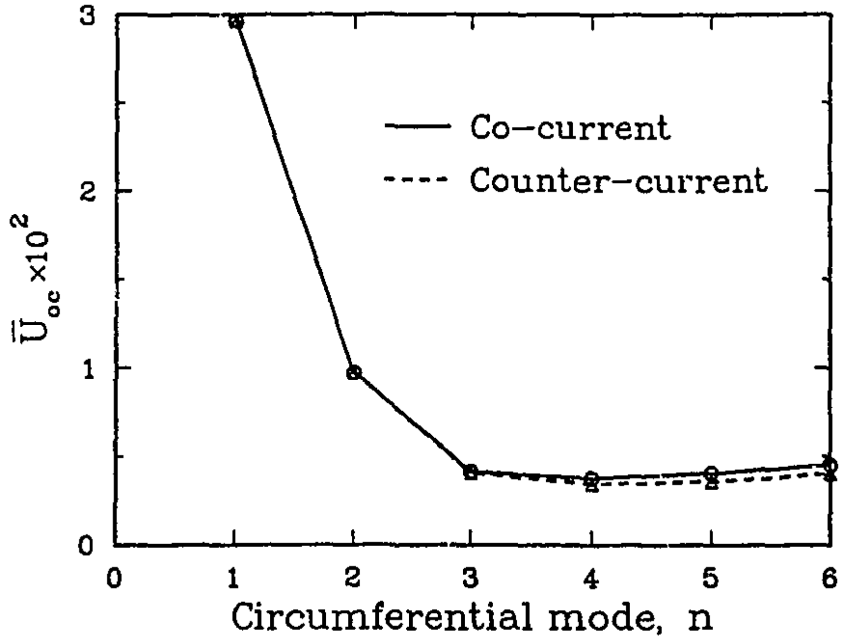

Figure 3.5: The critical dimensionless annular flow velocity, $\bar{U}_{oc}$, in the $\frac{1}{10}$-gap system as a function of the circumferential mode, n; ——, flows in the same direction; - - - -, flows in opposite directions. The shell is clamped at both ends and the inner flow velocity is constant ($\bar{U}_i = 0.01$).

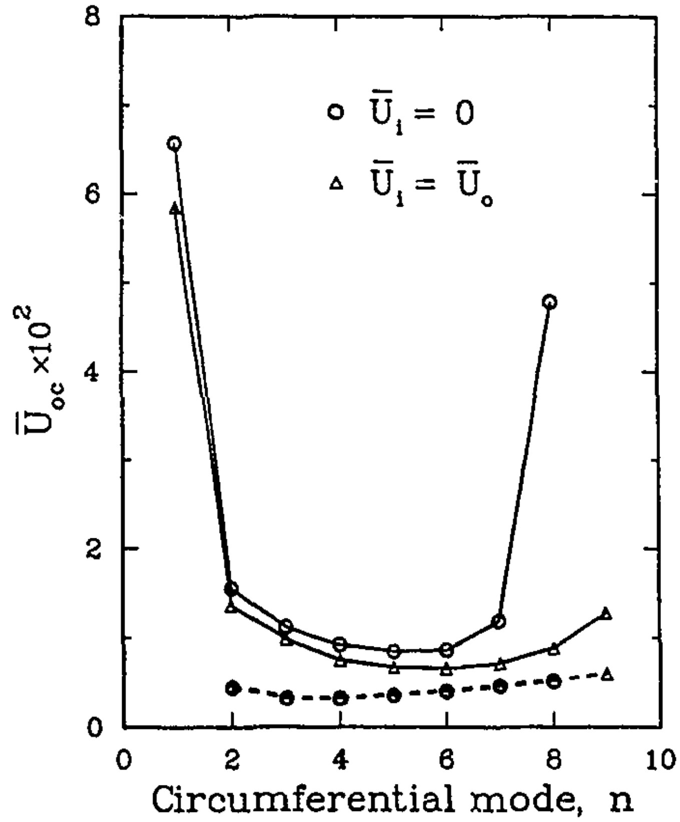

Figure 3.6: The critical dimensionless annular flow velocity, $\bar{U}_{oc}$, in the $\frac{1}{10}$-gap system as a function of the circumferential mode, n, for two different inner flow velocities; $\bigcirc$, $\bar{U}_i = 0$; $\triangle$, $\bar{U}_i = \bar{U}_o$; - - - - , divergence boundary; —— , flutter boundary. The divergence boundaries for the two values of $\bar{U}_i$ are generally coincident. The shell is cantilevered.

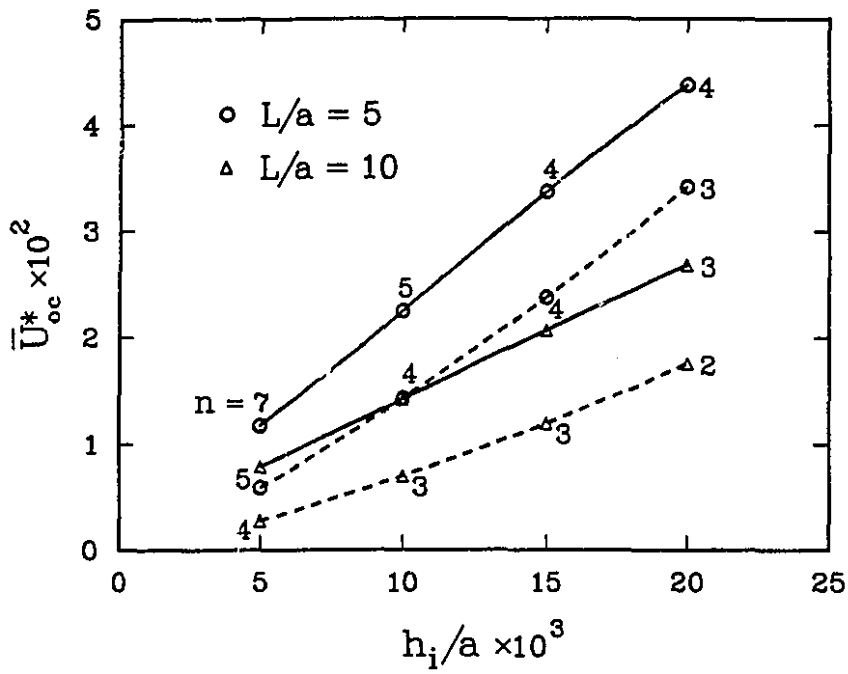

Figure 3.7: The overall critical dimensionless annular flow velocity, $\bar{U}^*_{oc}$, in the $\frac{1}{10}$-gap system as a function of h_i/a for two different shell lengths, with the circumferential mode, n, associated with first loss of stability marked in the figure; $\bigcirc, L/a = 5$; $\triangle, L/a = 10$; - - - -, divergence boundary; ——, flutter boundary. The shell is cantilevered and the inner fluid is stagnant.

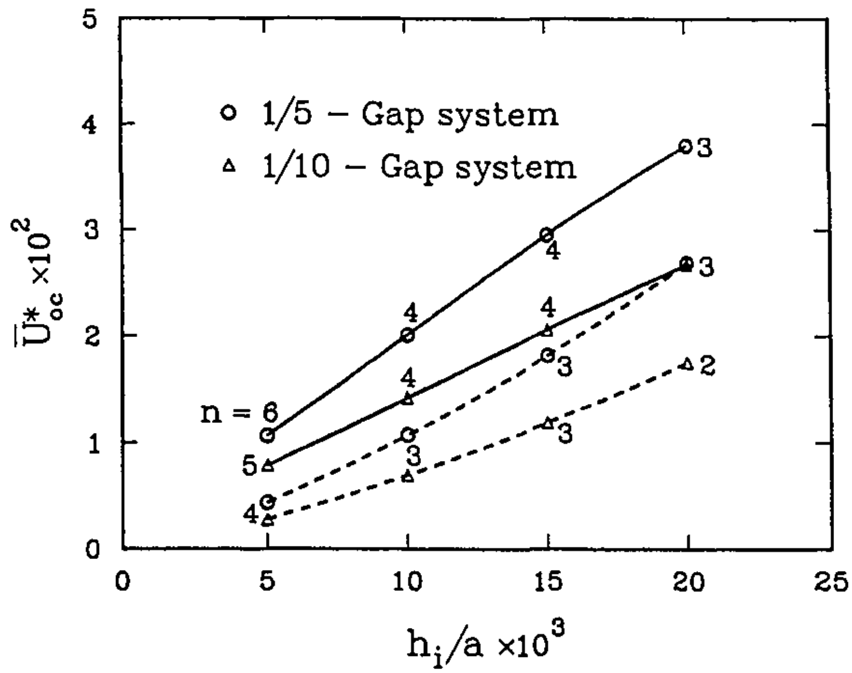

Figure 3.8: The overall critical dimensionless annular flow velocity, $\bar{U}^*_{oc}$, as a function of h_i/a for two different annular widths ($L/a = 10$), with the circumferential mode, n, associated with first loss of stability marked in the figure; ○, $(b-a)/a = 1/5$; △, $(b-a)/a = 1/10$; - - - - , divergence boundary; ——– , flutter boundary. The shell is cantilevered and the inner fluid is stagnant.

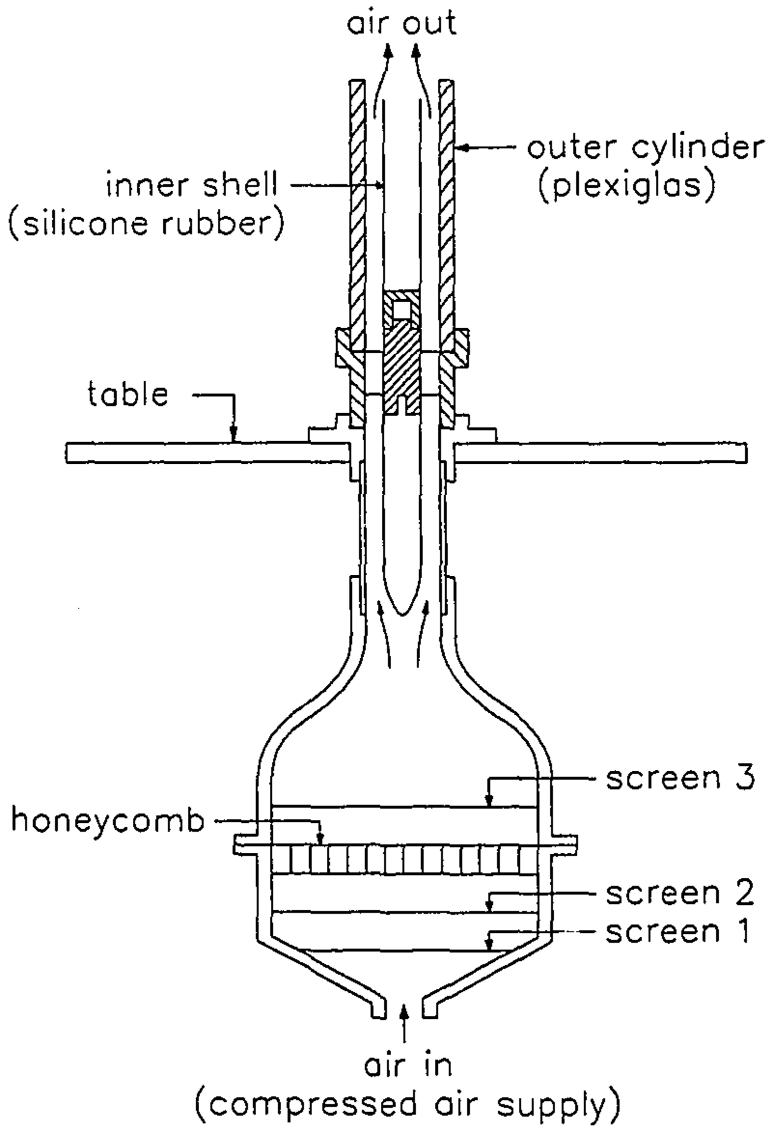

Figure 4.1: Schematic of the test apparatus involving *annular* flow.

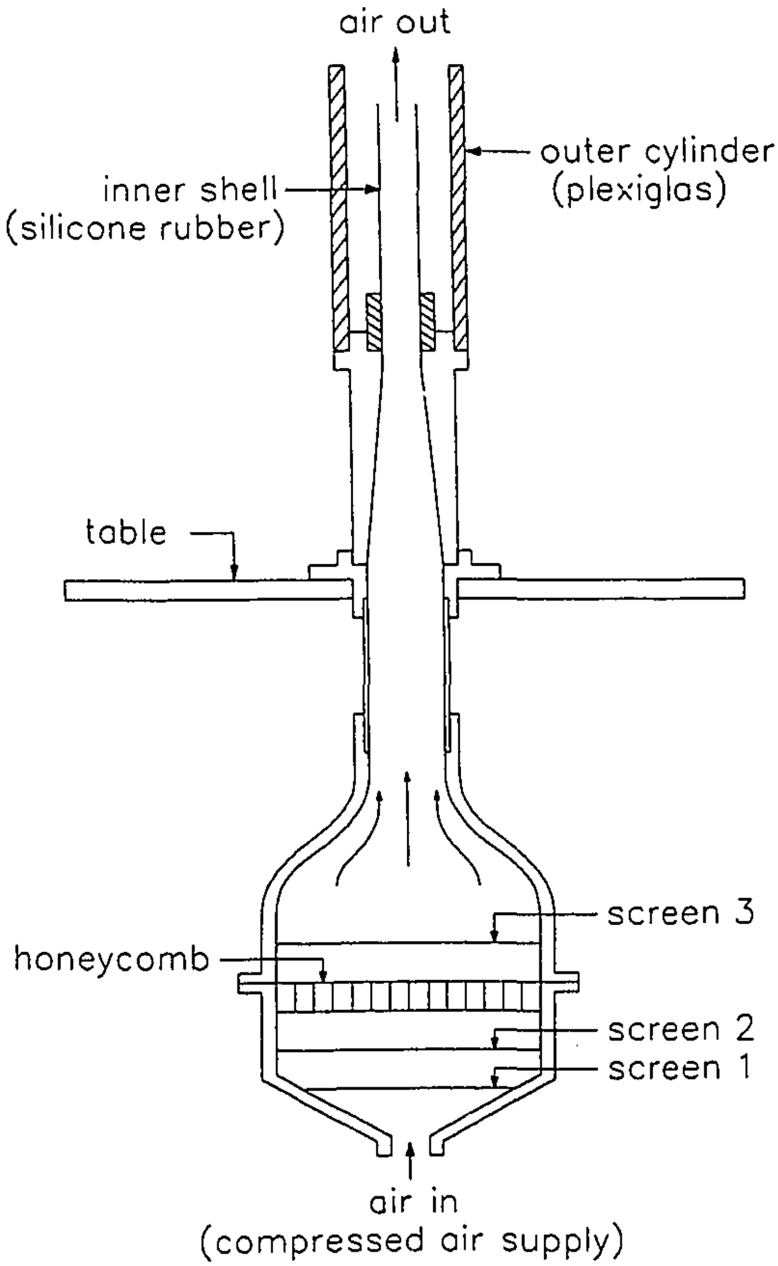

Figure 4.2: Schematic of the test apparatus involving *internal* flow.

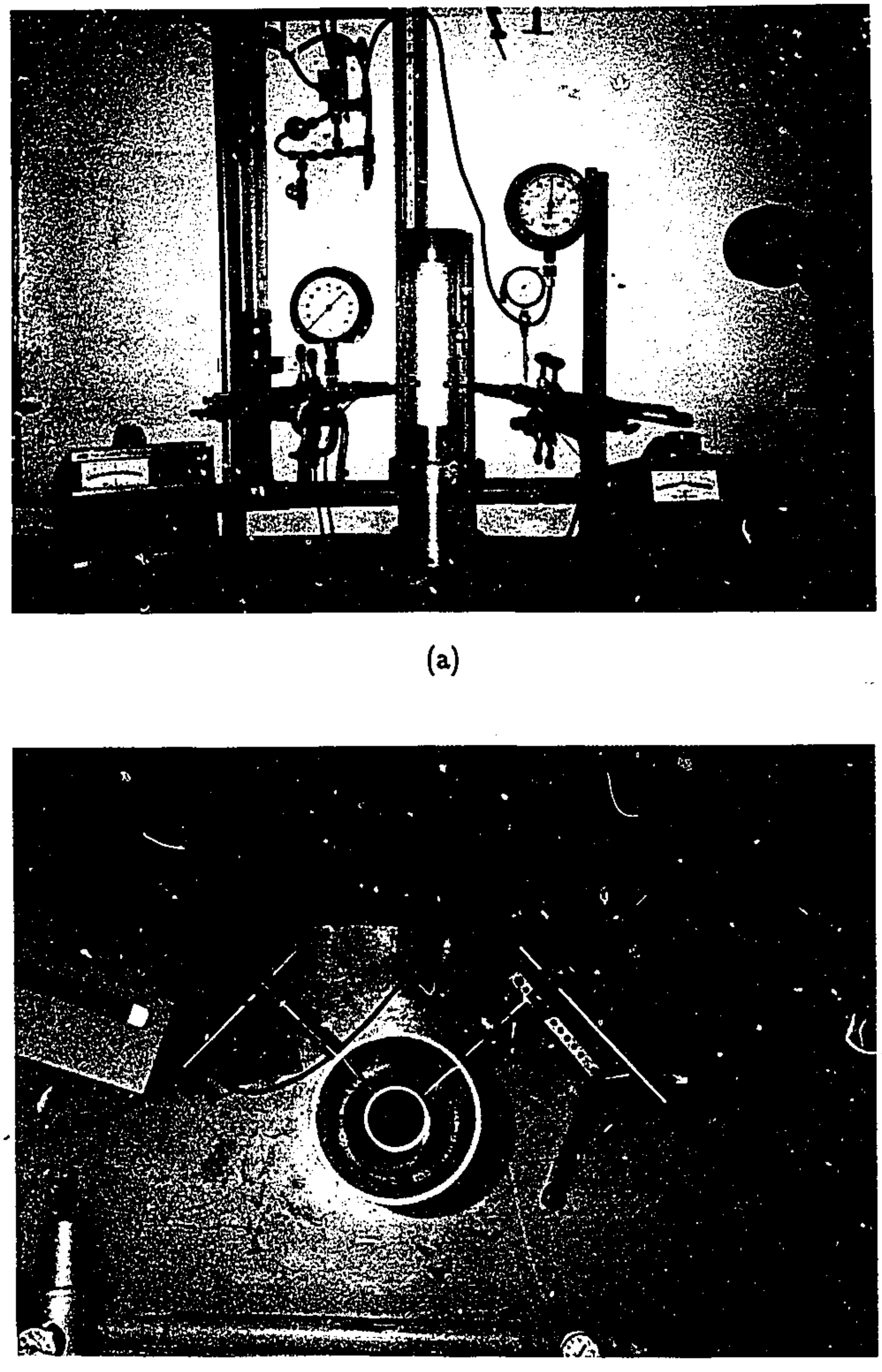

(a)

(b)

Figure 4.3: Photographs of a silicone rubber shell inside a plexiglas cylinder with two mounted fotonic sensors: (a) side view, (b) top view.

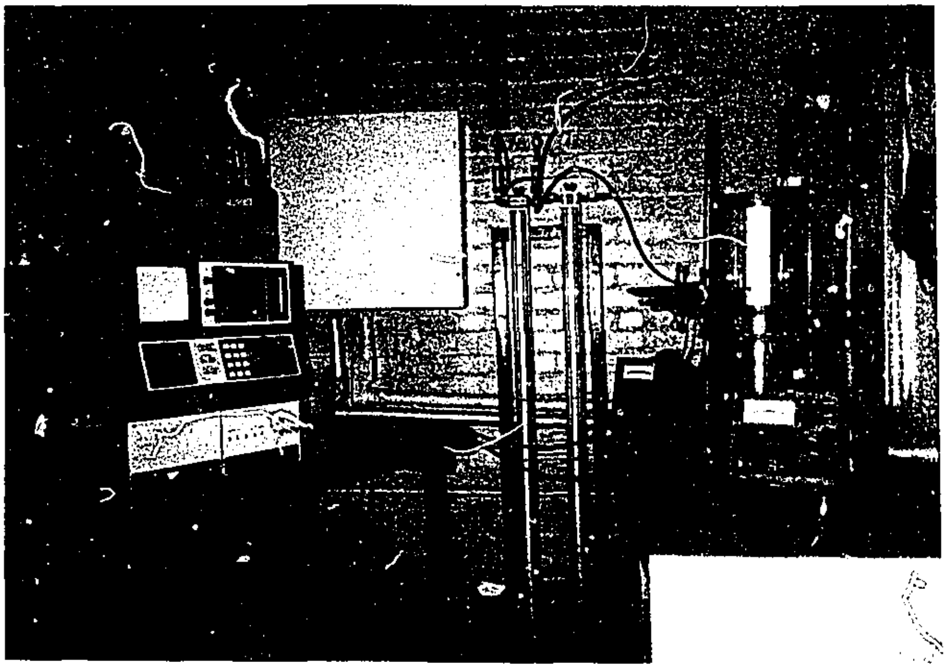

Figure 4.4: Photograph of the entire experimental setup.

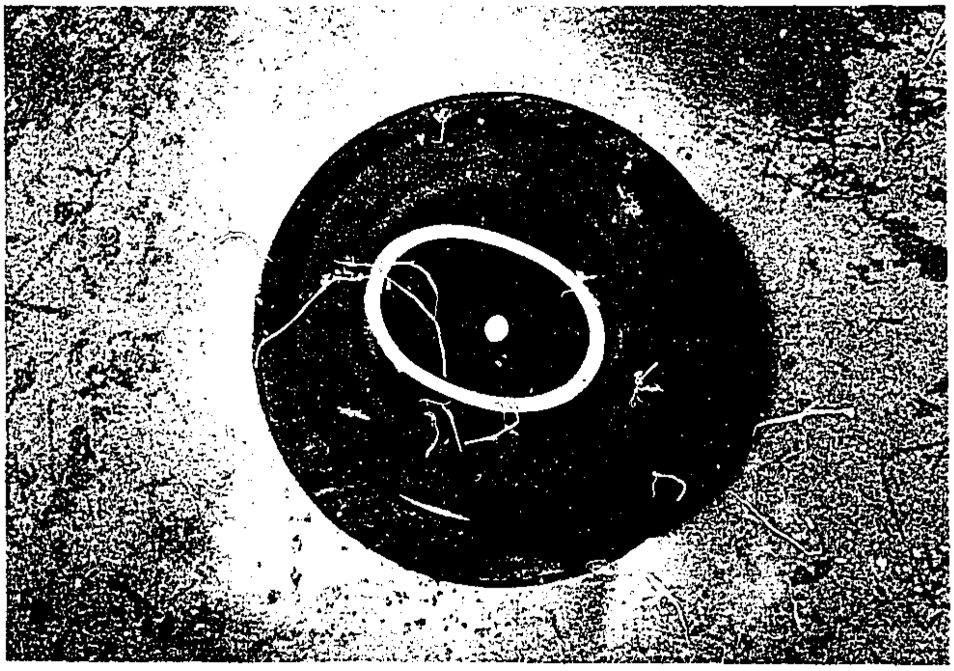

Figure 4.5: Photograph of the free–end cross section of the shell fluttering in $n = 2$.

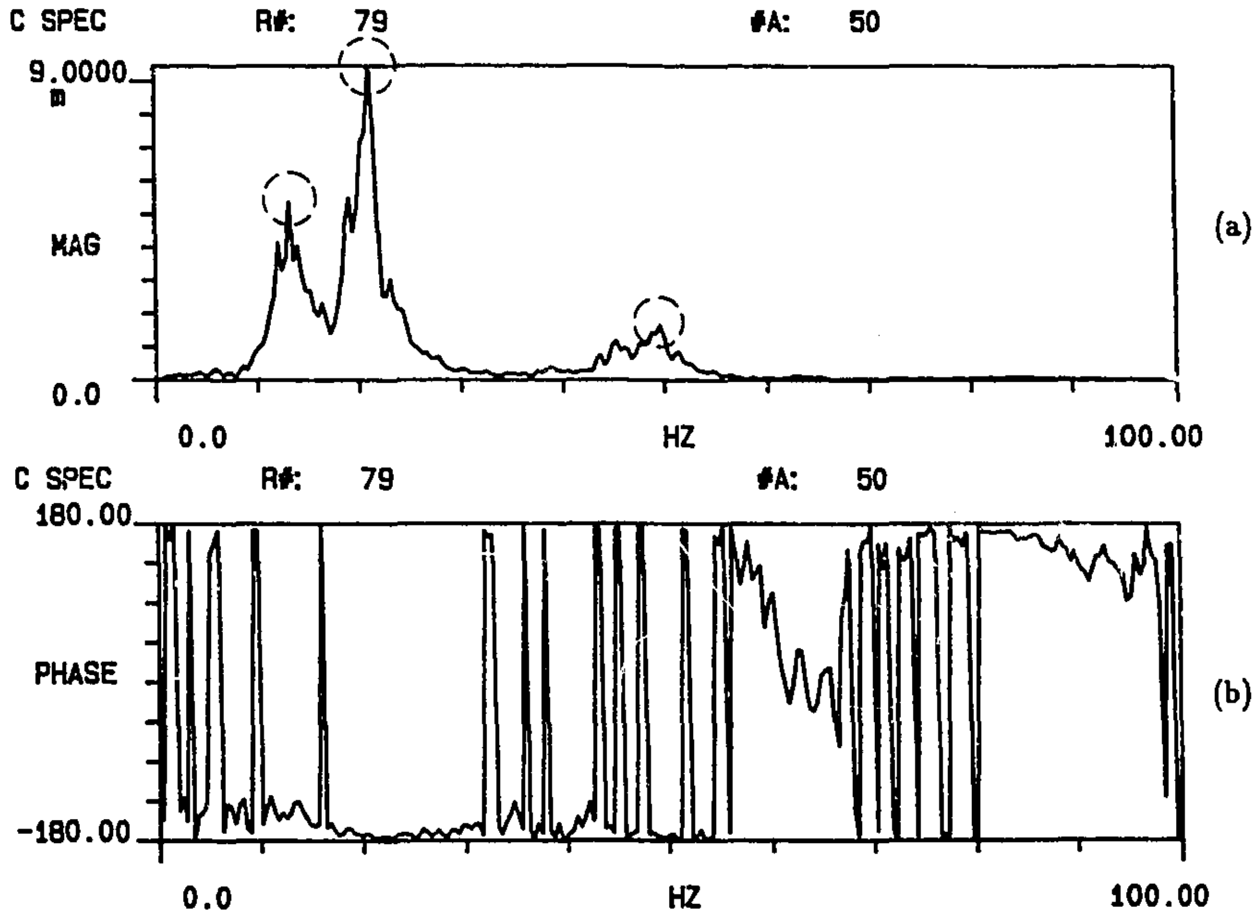

Figure 4.6: A typical cross spectral density (CSD): (a) amplitude of the shell motion(s) versus the frequency(ies) of oscillation, and (b) phase difference of the shell motions at the locations of the two fotonic sensors.

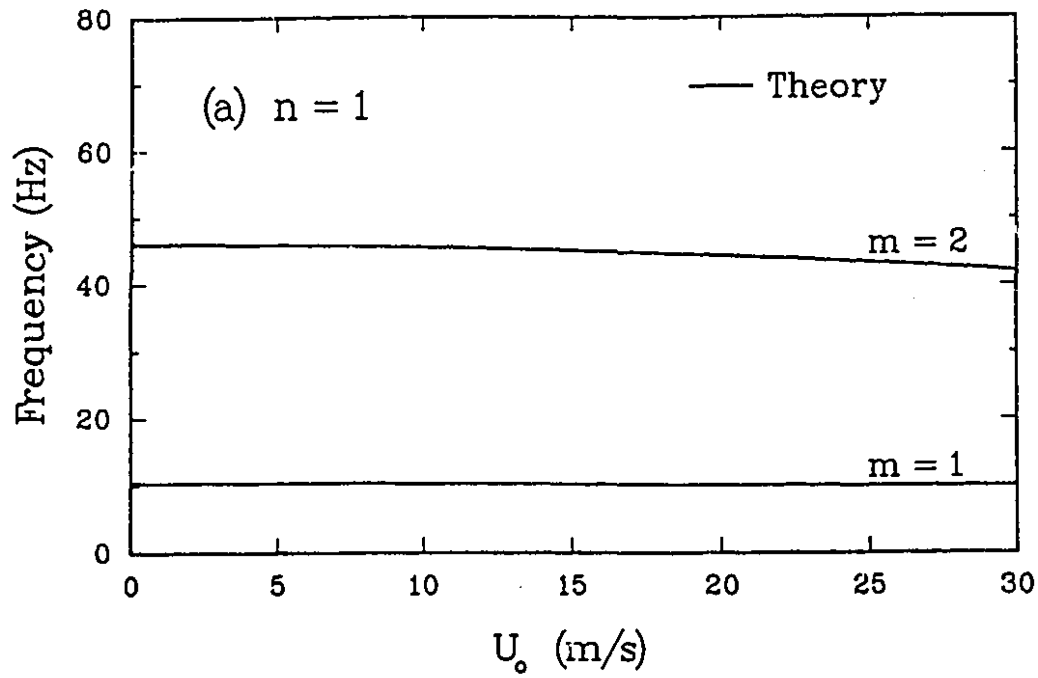

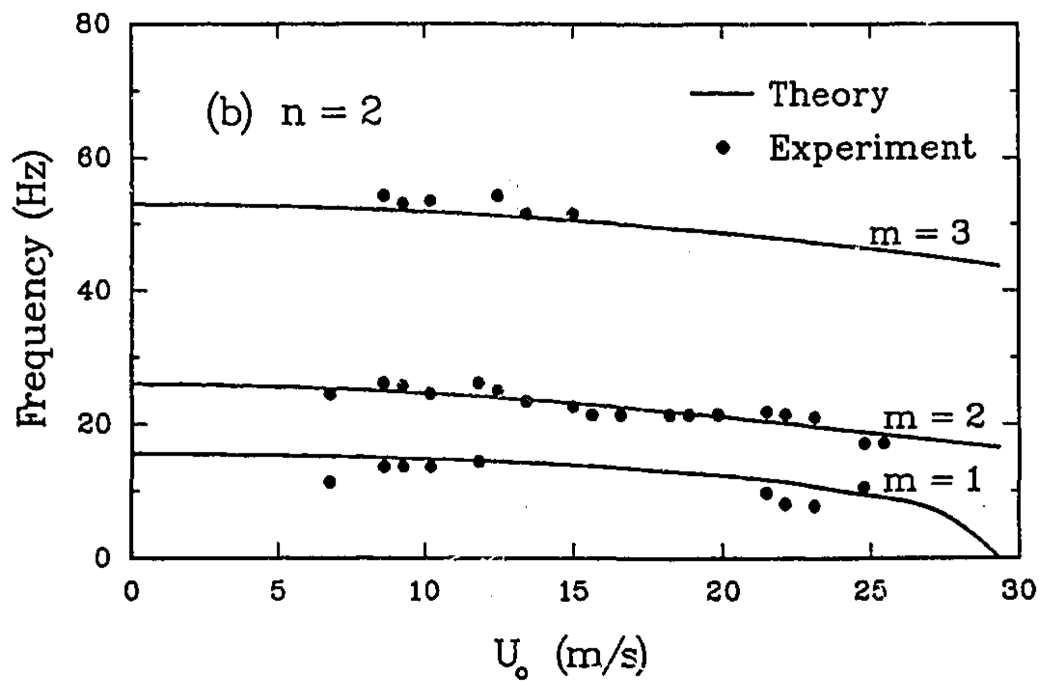

Figure 4.7: Predicted and measured frequencies of the shell at various annular flow velocities: (a) $n = 1$, (b) $n = 2$. The system has $g/a = 1/10$, $L/a = 8$.

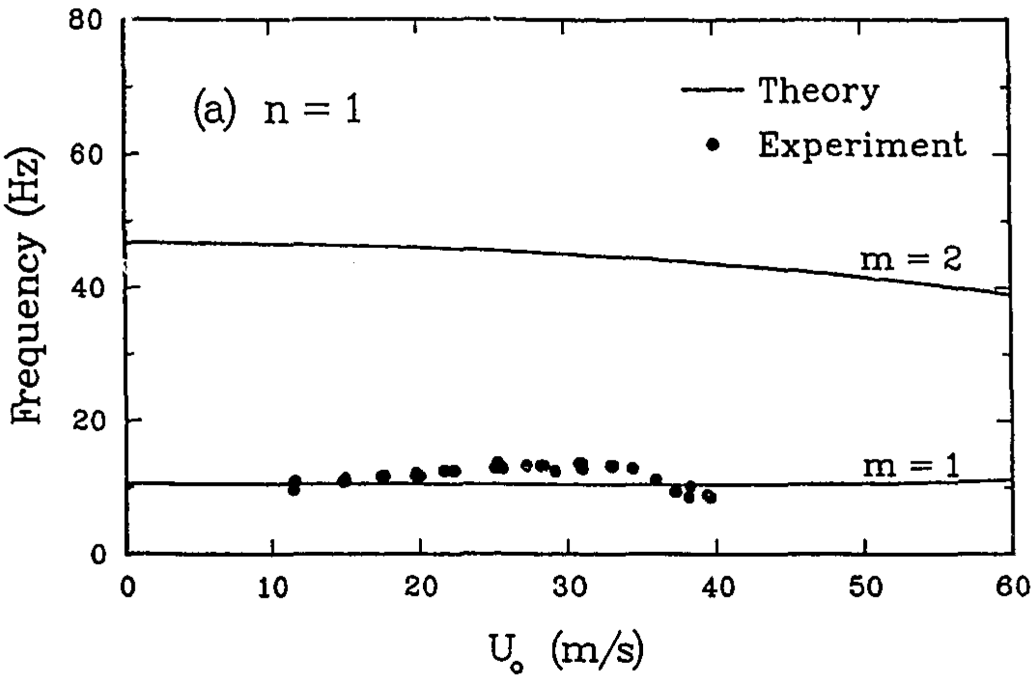

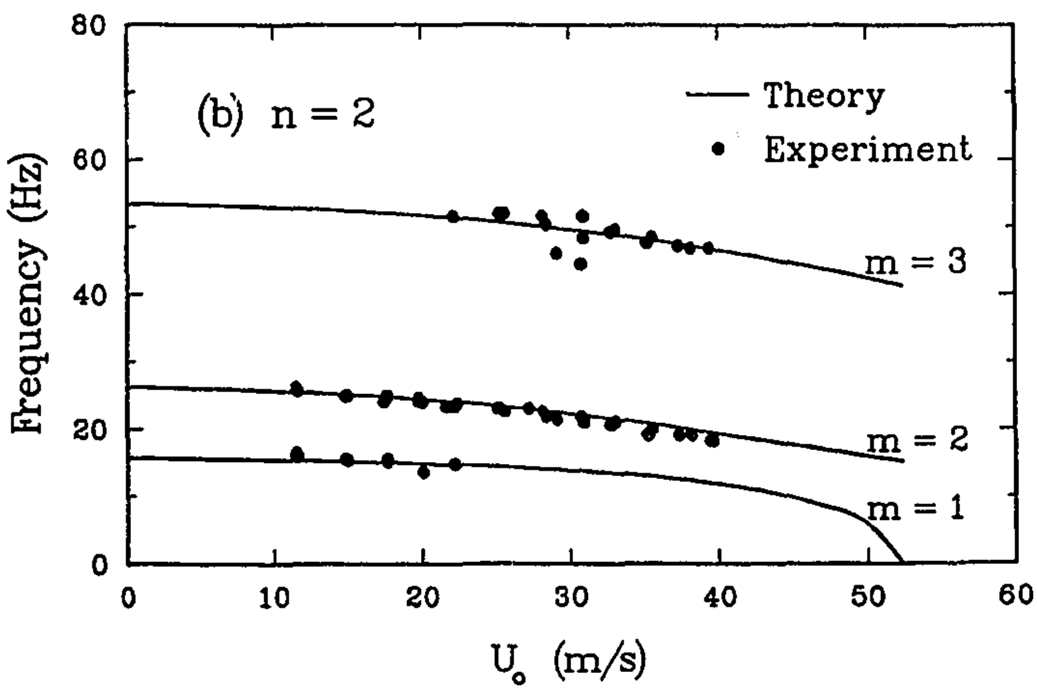

Figure 4.8: Predicted and measured frequencies of the shell at various annular flow velocities: (a) $n = 1$, (b) $n = 2$, and (c) $n = 3$. The system has $g/a = 1/4$, $L/a = 8$.

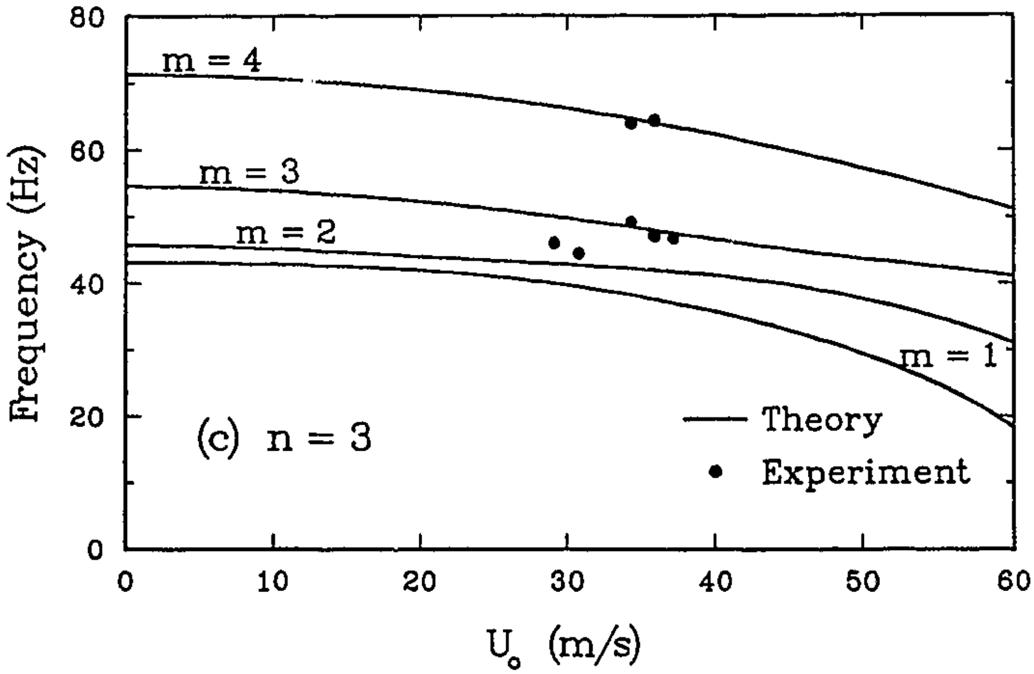

Figure 4.8 (continued): Part (c).

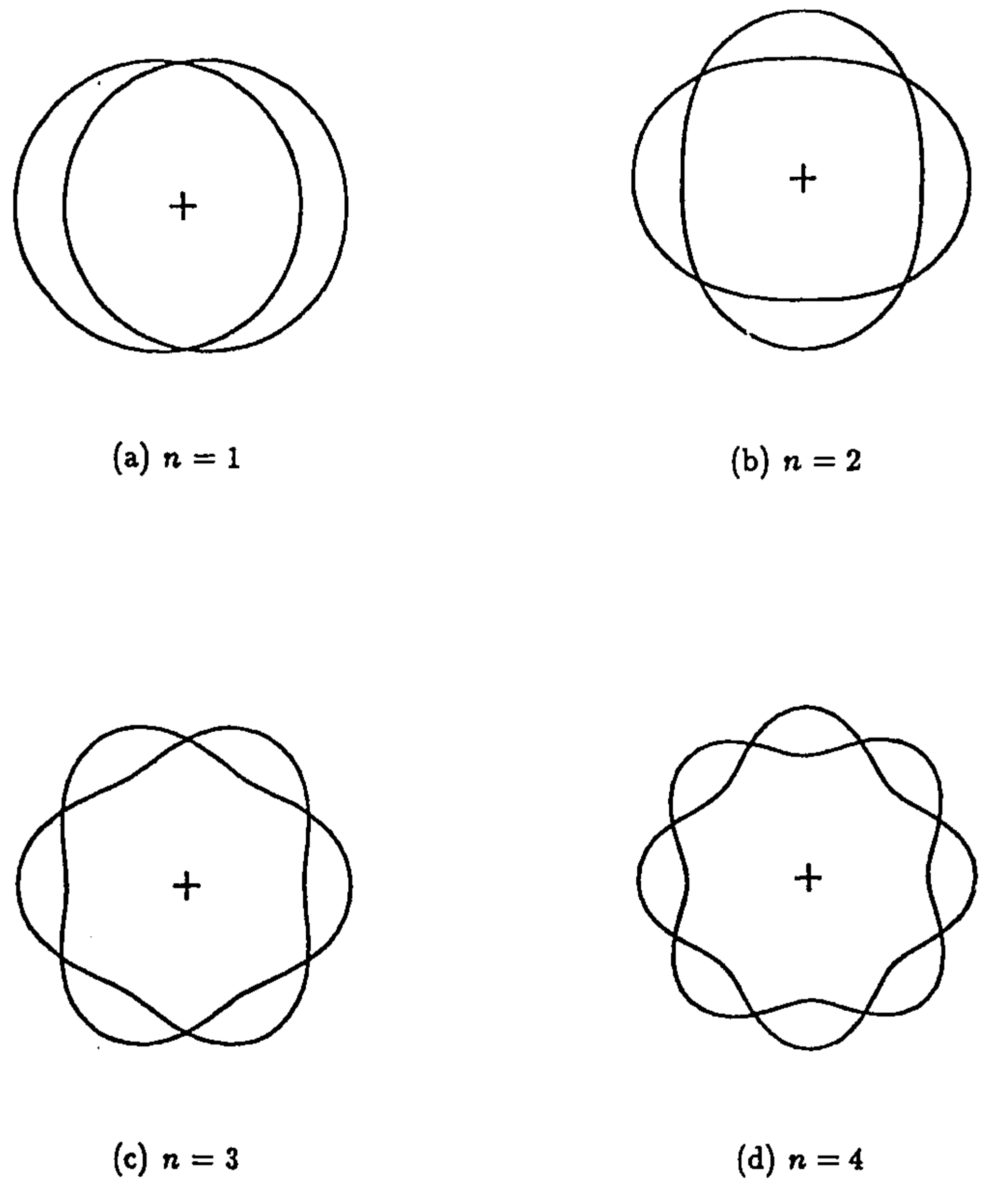

(a) $n = 1$ (b) $n = 2$

(c) $n = 3$ (d) $n = 4$

Figure 4.9: Cross section of the shell vibrating in (a) $n = 1$, (b) $n = 2$, (c) $n = 3$, and (d) $n = 4$.

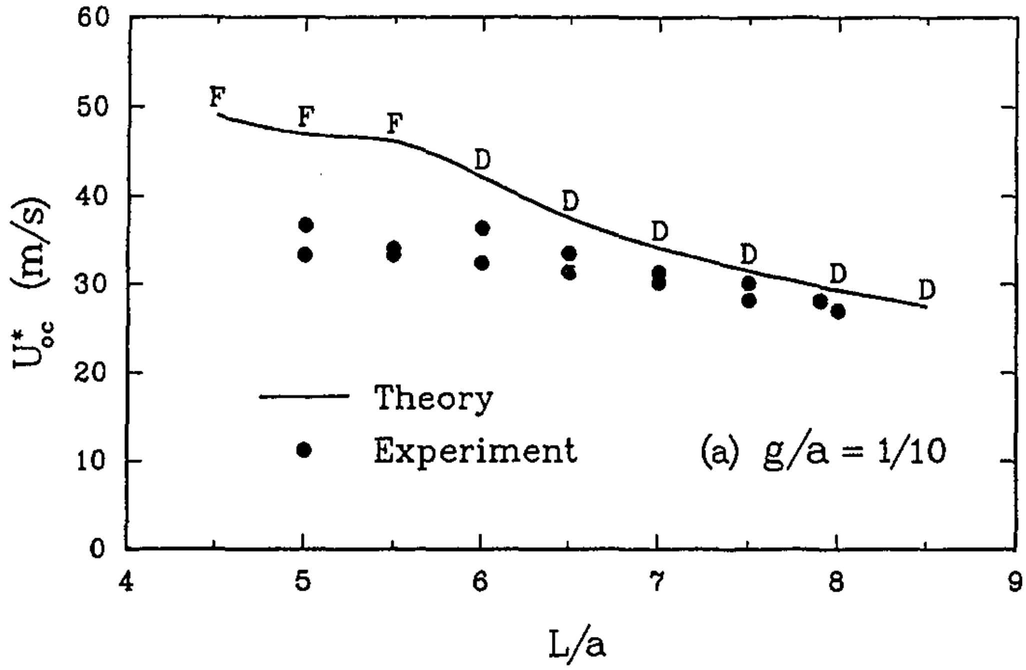

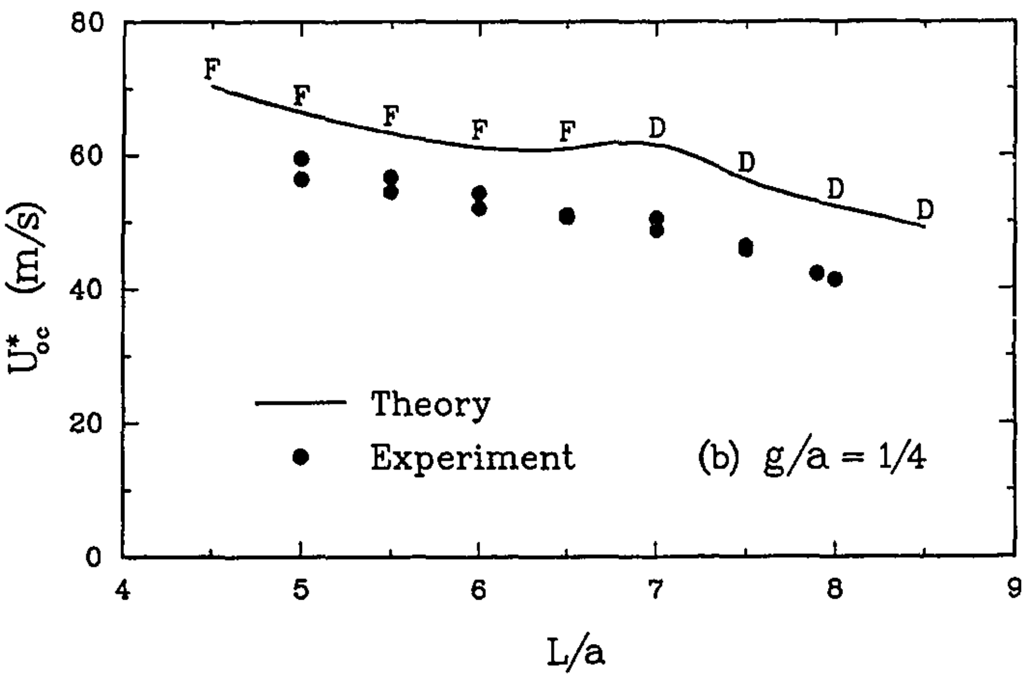

Figure 4.10: Overall critical annular flow velocity, U^*_{oc}, as a function of length-to-radius ratio of the shell, L/a, for (a) $g/a = 1/10$, (b) $g/a = 1/4$, and (c) $g/a = 1/2$.

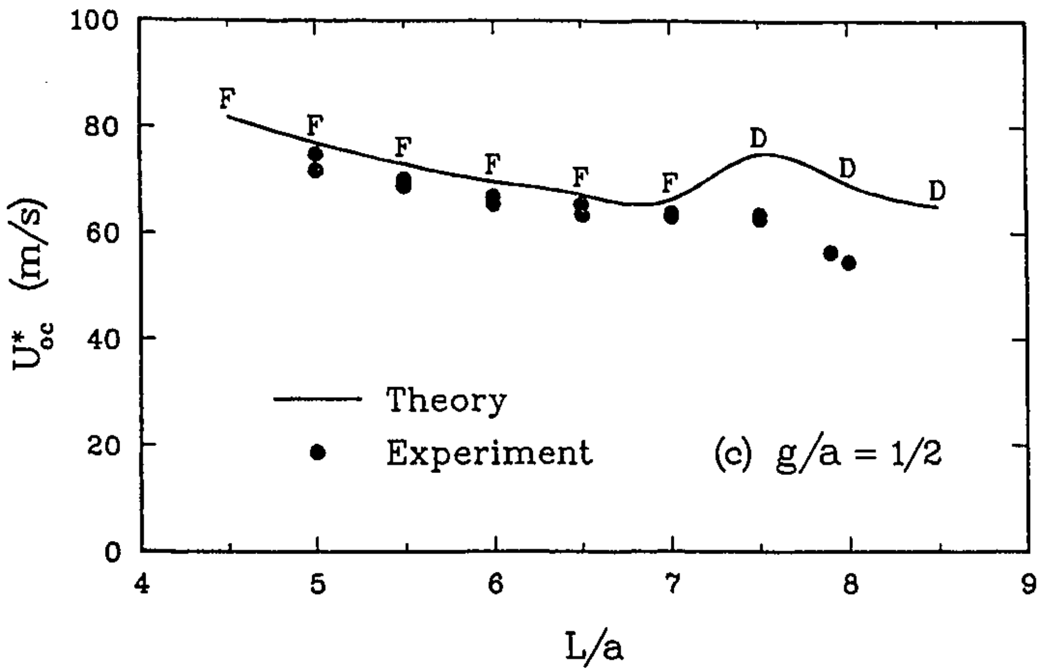

Figure 4.10 (continued): Part (c).

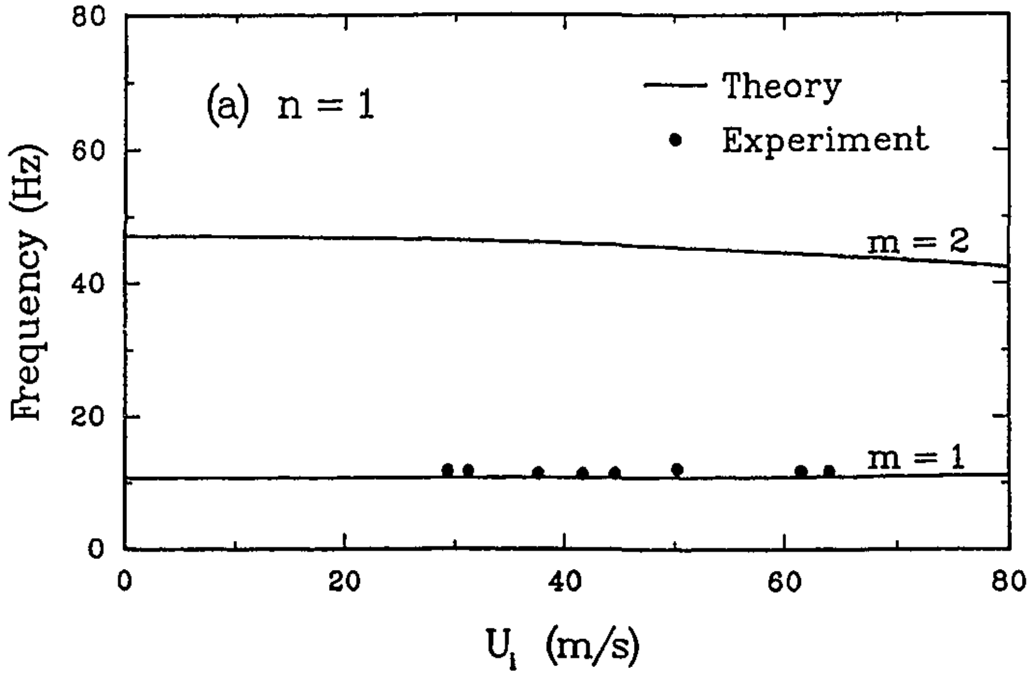

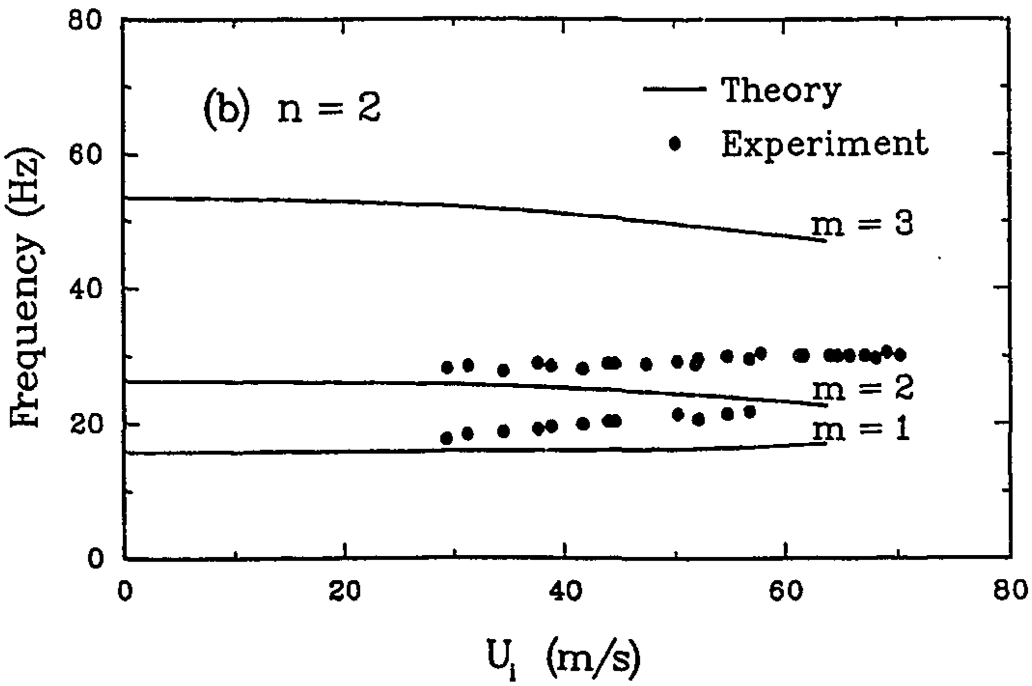

Figure 4.11: Predicted and measured frequencies of the shell at various internal flow velocities: (a) $n = 1$, (b) $n = 2$, and (c) $n = 3$. The system has $g/a = 1.5$, $L/a = 8$.

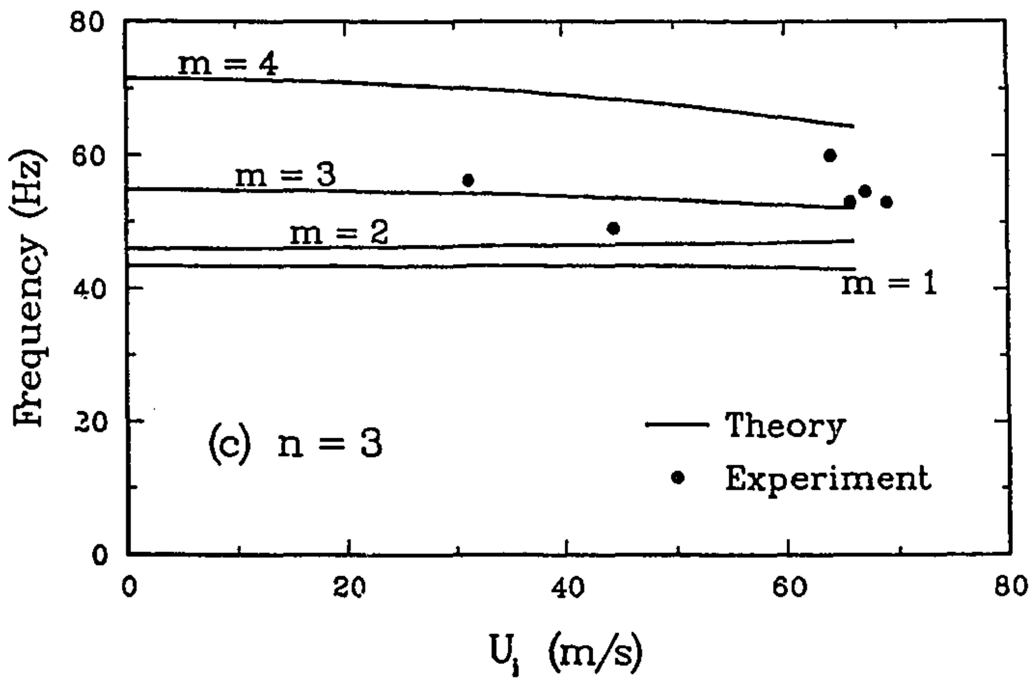

Figure 4.11 (continued): Part (c).

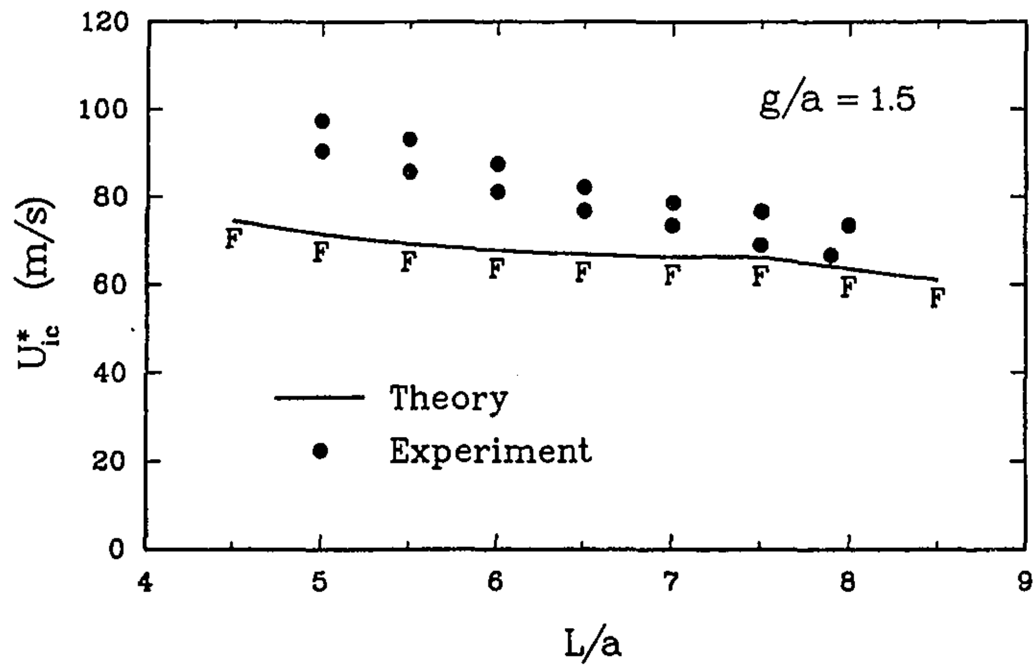

Figure 4.12: Overall critical internal flow velocity, U^*_{ic}, as a function of length-to-radius ratio of the shell, L/a, for $g/a = 1.5$.

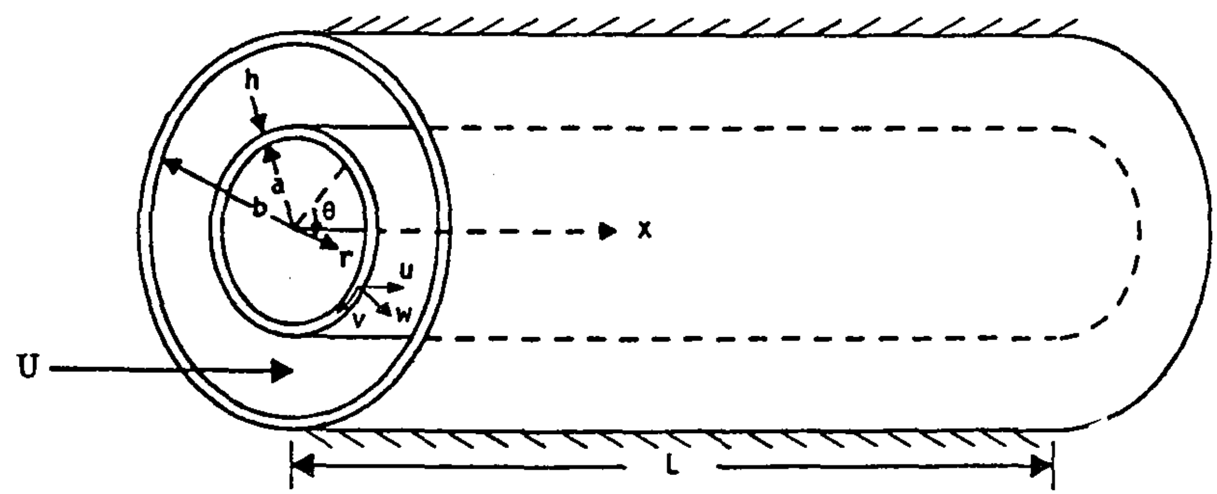

Figure 5.1: Schematic of the system under consideration.

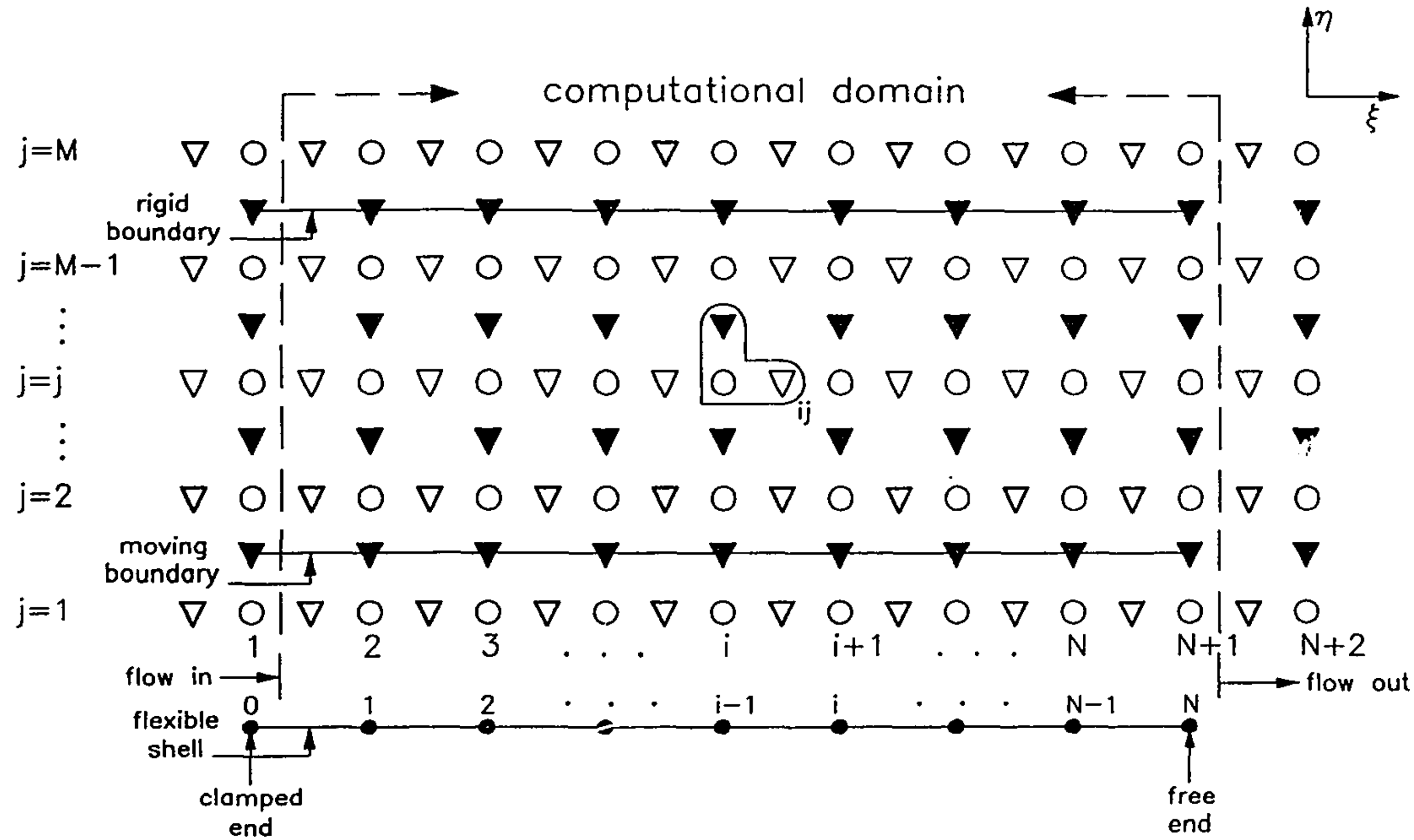

Figure 5.2: Schematic of the arrangement of (i) flow variables in the present staggered mesh and (ii) nodes on the flexible shell. ▼ : $\mathcal{V}_r$; ▽ : $\mathcal{V}_x$; ○ : $\mathcal{P}$, $\mathcal{V}_\theta$; • : nodes on the shell.

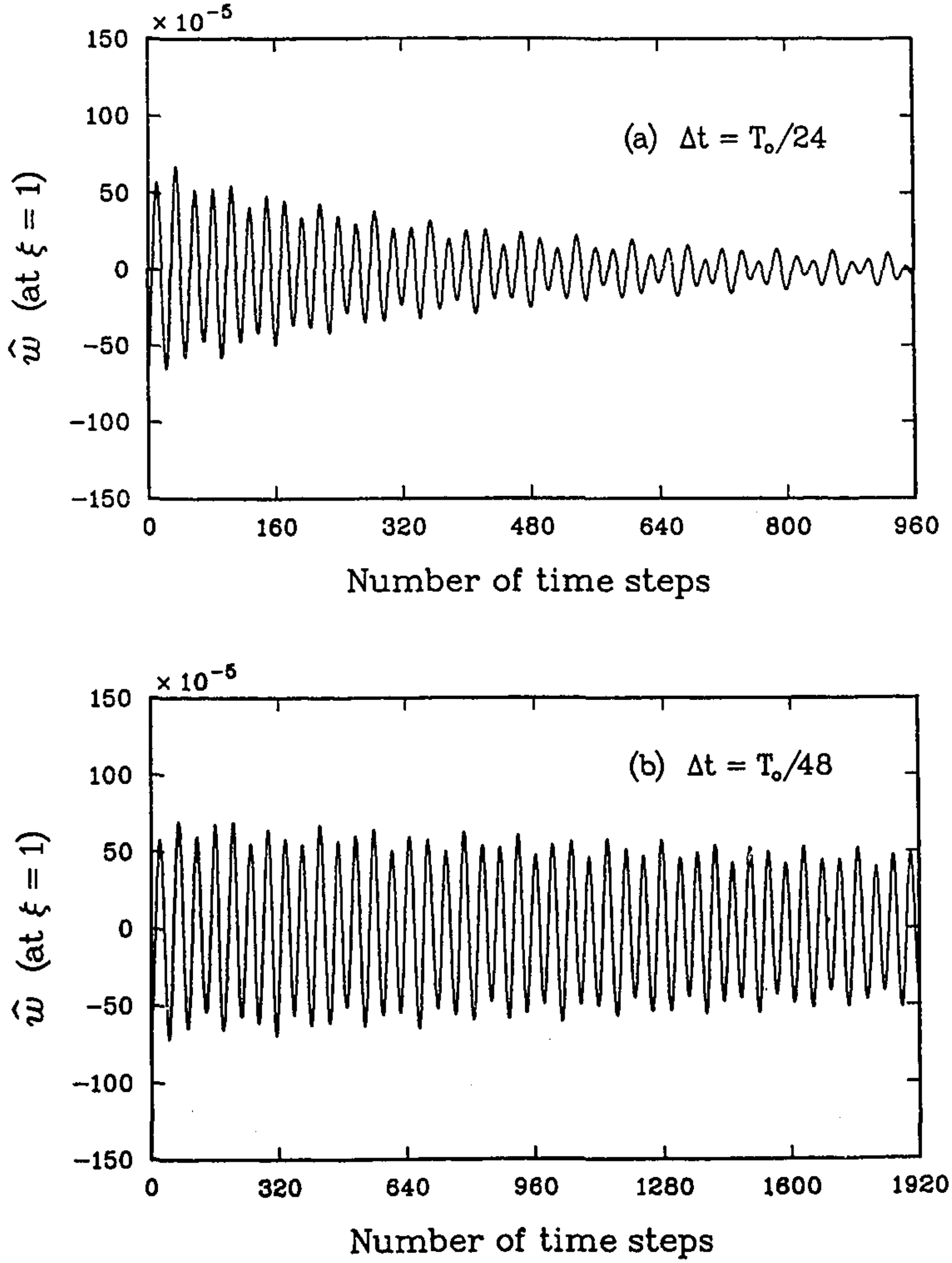

Figure 5.3: Radial displacement of the shell at $\xi = 1$ as a function of time, initially excited in $m = 2$ (axial mode) and $n = 2$ (circumferential mode). The shell oscillates *in vacuo* and in the absence of internal dissipation. (a) : $\Delta t = T_o/24$; (b) : $\Delta t = T_o/48$.

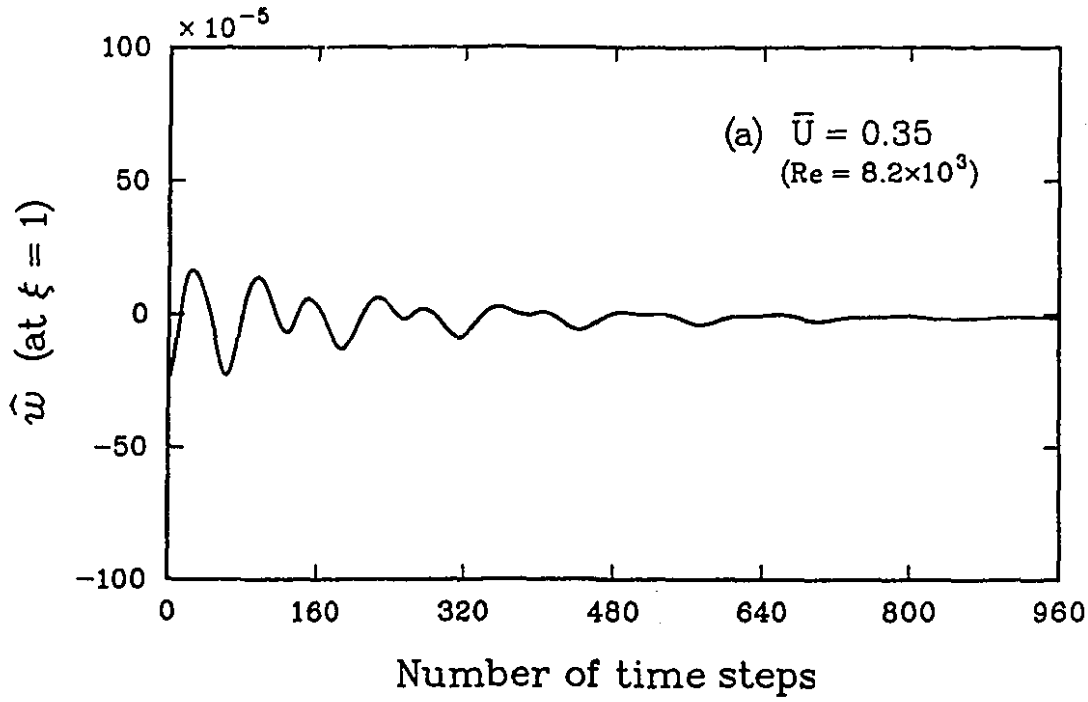

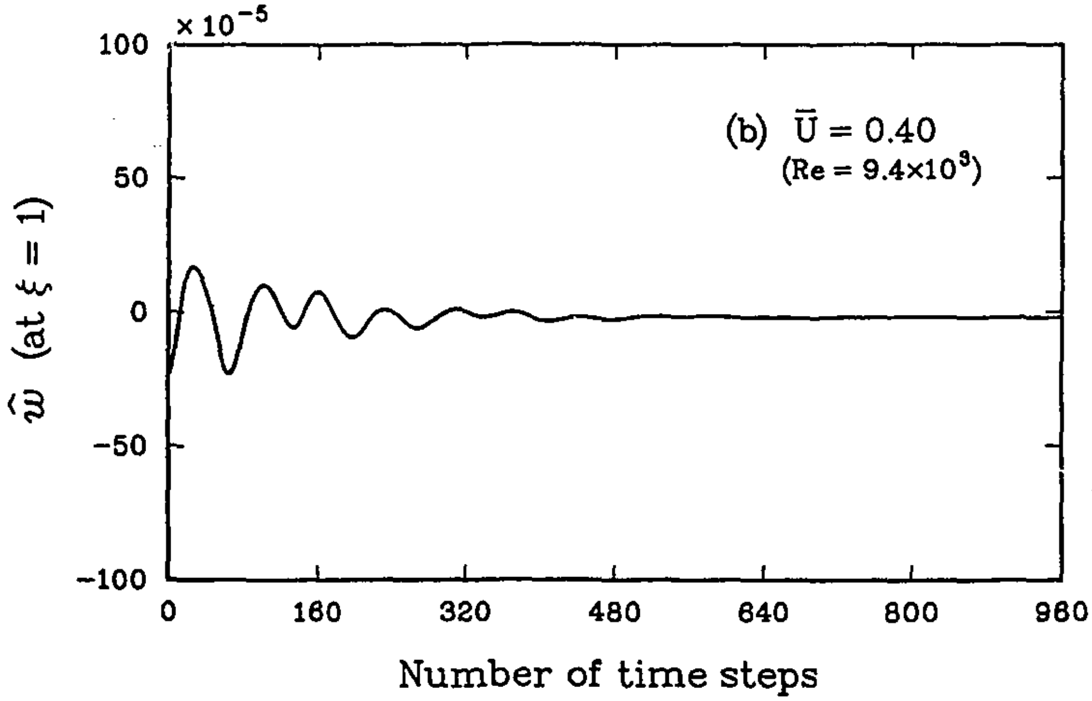

Figure 5.4: Radial displacement of the shell at $\xi = 1$ as a function of time in the 1/10-gap system, initially excited in $m = 2$ (axial mode) and $n = 2$ (circumferential mode). (a) : $\bar{U} = 0.35$; (b) : $\bar{U} = 0.40$; (c) : $\bar{U} = 0.45$.

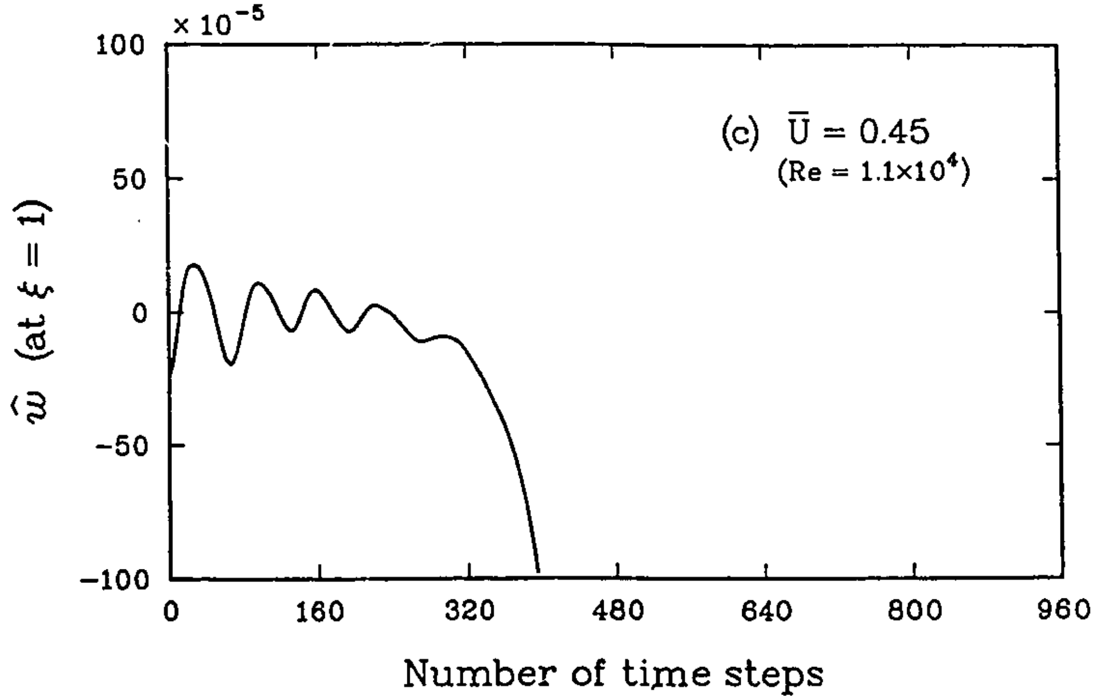

Figure 5.4 (continued): Part (c).

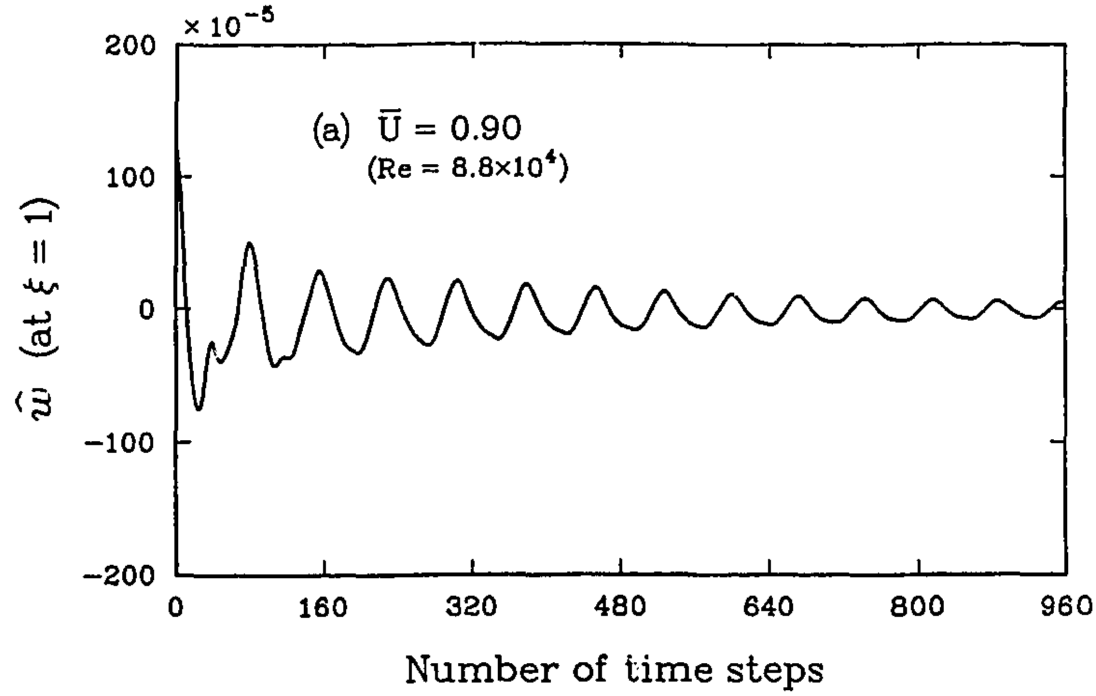

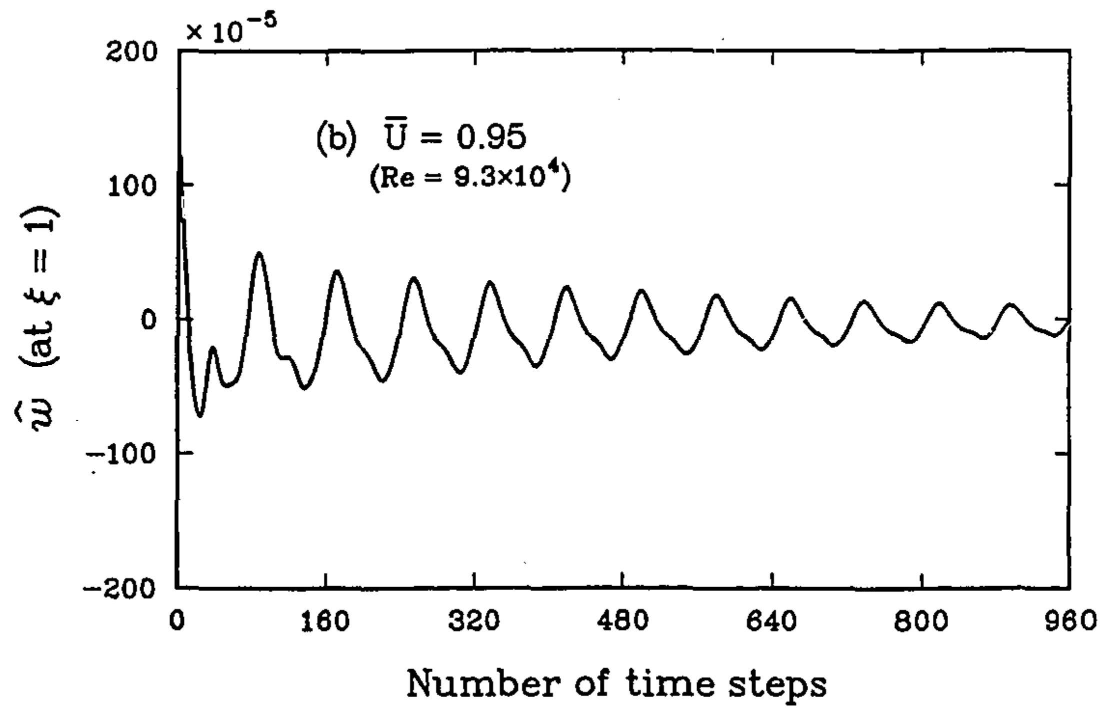

Figure 5.5: Radial displacement of the shell at $\xi = 1$ as a function of time in the 1/2-gap system, initially excited in $m = 1$ (axial mode) and $n = 2$ (circumferential mode). (a) : $\bar{U} = 0.90$; (b) : $\bar{U} = 0.95$; (c) : $\bar{U} = 1.00$.

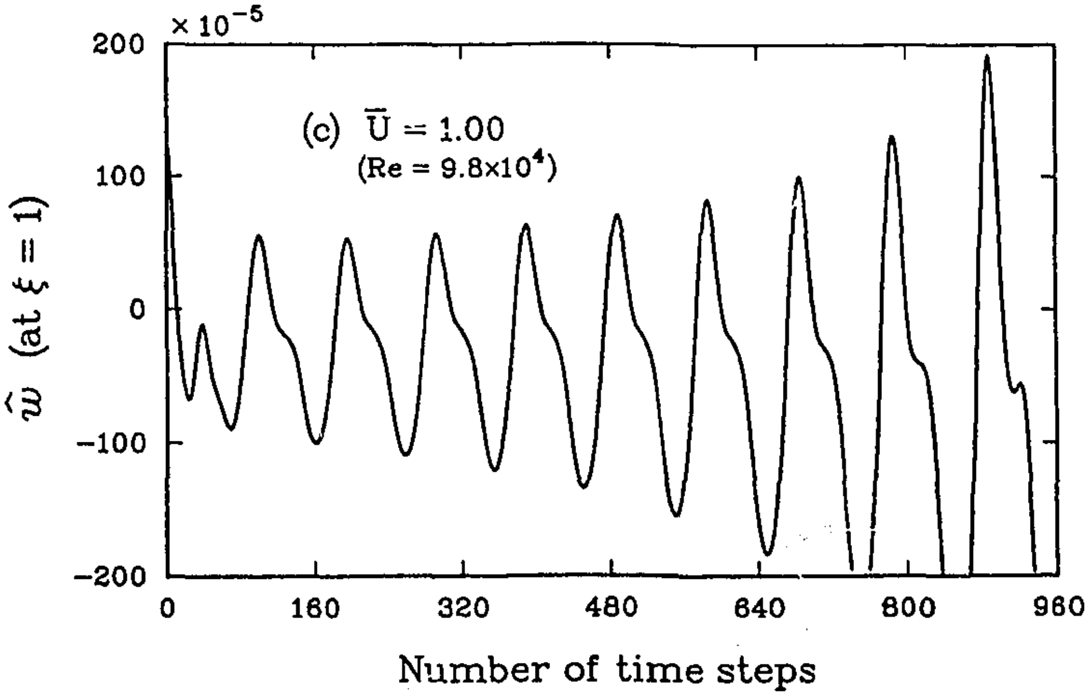

Figure 5.5 (continued): Part (c).

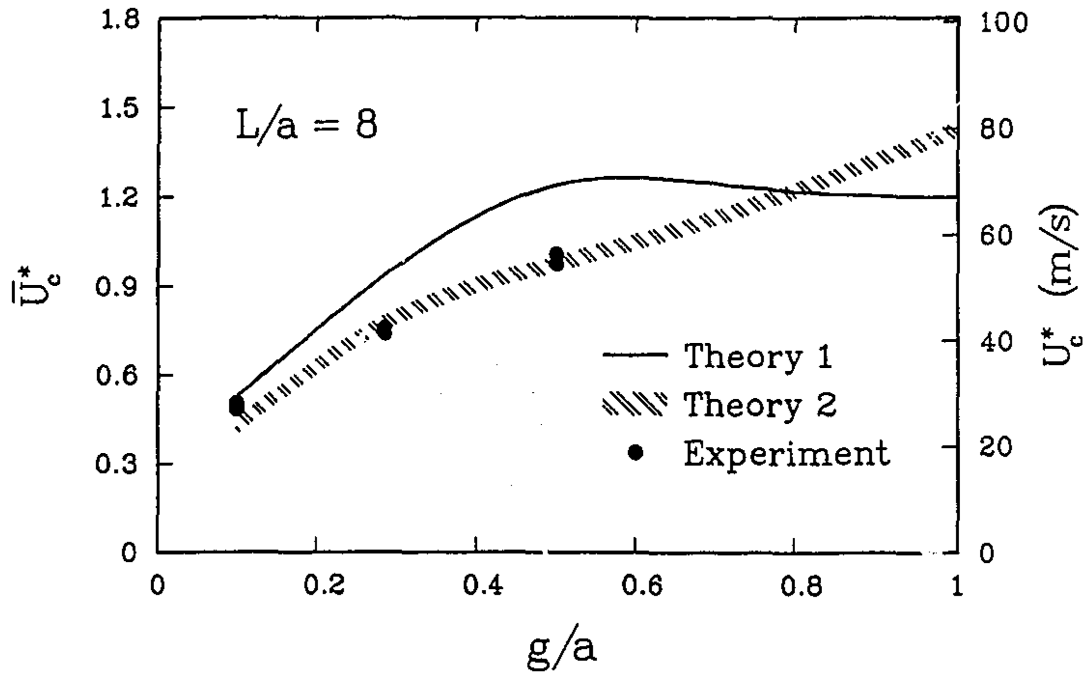

Figure 5.6: The effect of annular gap width on the overall critical flow velocity, $\bar{U}_c^*$. Theory 1 : inviscid theory with steady viscous effects included (Chapter 2); Theory 2 : theory of Chapter 5.

Appendix A

Expression for $H_{km}(\bar{\alpha})$

$H_{km}(\bar{\alpha})$ was defined in Equation (2.65) as

$$H_{km}(\bar{\alpha}) \; = \; H_k(-\bar{\alpha})H_m(\bar{\alpha}), \tag{A.1}$$

where k and m are indices such that $1 \leq k, m \leq M$, and

$$H_j(\bar{\alpha}) = \int_0^1 \Phi_j(\xi)\, e^{i\bar{\alpha}\xi}\, \mathrm{d}\xi. \tag{A.2}$$

In the above integral, $\Phi_j(\xi)$ are beam eigenfunctions, which have a general form

$$\Phi_j(\xi) = (\cosh\lambda_j\xi - \cos\lambda_j\xi) - \sigma_j(\sinh\lambda_j\xi - \sin\lambda_j\xi), \tag{A.3}$$

and satisfy the equation

$$\Phi_j''''(\xi) = \lambda_j^4\Phi_j(\xi), \tag{A.4}$$

where primes denote differentiation with respect to the argument of the function, ξ; for a cantilevered beam, the constants σ_j are

$$\sigma_j = \frac{\cosh\lambda_j + \cos\lambda_j}{\sinh\lambda_j + \sin\lambda_j}, \tag{A.5}$$

and the eigenvalues λ_j are the roots of the transcendental equation

$$\cosh\lambda_j \cos\lambda_j + 1 = 0. \tag{A.6}$$

By successive integration by parts, it is found that

$$H_j(\bar{\alpha}) = \frac{1}{\lambda_j^4 - \bar{\alpha}^4}\left[\Phi_j'''(\xi) - (i\bar{\alpha})\Phi_j''(\xi) + (i\bar{\alpha})^2\Phi_j'(\xi) - (i\bar{\alpha})^3\Phi_j(\xi)\right] e^{i\bar{\alpha}\xi}\Bigg|_0^1, \tag{A.7}$$

and using the boundary conditions of a cantilevered beam, i.e. ,

$$\begin{aligned} \Phi_j(0) &= 0, & \Phi_j(1) &= 2(-1)^{j+1}, \\ \Phi_j'(0) &= 0, & \Phi_j'(1) &= 2\lambda_j\sigma_j(-1)^{j+1}, \\ \Phi_j''(0) &= 2\lambda_j^2, & \Phi_j''(1) &= 0, \\ \Phi_j'''(0) &= 2\lambda_j^3\sigma_j, & \Phi_j'''(1) &= 0, \end{aligned}$$

gives the following expression for $H_j(\bar{\alpha})$:

$$H_j(\bar{\alpha}) = \frac{2}{\lambda_j^4 - \bar{\alpha}^4}\left[\bar{\alpha}^2 e^{i\bar{\alpha}}(i\bar{\alpha} - \lambda_j\sigma_j)(-1)^{j+1} + \lambda_j^2(i\bar{\alpha} + \lambda_j\sigma_j)\right]. \tag{A.8}$$

It is noted that $H_j(\bar{\alpha})$ becomes undefined when

$$\bar{\alpha} = \bar{\alpha}^* \equiv \pm\lambda_j,\ \pm i\lambda_j, \tag{A.9}$$

because the right–hand side of (A.8) has the form 0/0; in such cases, applying L'Hôpital's rule to Equation (A.8) yields

$$H_j(\bar{\alpha}^*) = \frac{1}{2(\bar{\alpha}^*)^3}\left\{e^{i\bar{\alpha}^*}\left[(\bar{\alpha}^*)^3 + i(\lambda_j\sigma_j - 3)(\bar{\alpha}^*)^2 + 2\lambda_j\sigma_j\bar{\alpha}^*\right](-1)^{j+1} - i\lambda_j^2\right\}. \tag{A.10}$$

Appendix B

Out–Flow Models: Description

As a note, the analyses in Sections B.1 and B.2 are related to the Fourier transform method in Chapter 2 and to the finite–difference method in Chapter 5, respectively.

B.1 In the Fourier Transform Method

B.1.1 Introduction

These "models" effectively prescribe the manner in which flow perturbations beyond the free end of the shells decay to naught, by dissipation and diffusion. Another interpretation of these flow models is to imagine that beyond the free end there exists a "collector pipe" (Shayo and Ellen 1978), which at its upstream end generally moves in synchronism with the shell free end so as to "collect" the fluid and quieten it down over a certain distance. However, the first interpretation is considered to be the correct one.

The functional form of each model is given by $R_m(\xi)$, defined over $1 \leq \xi \leq \ell$, where ℓ is the location at which flow perturbations vanish. $R_m(\xi)$ may be considered as an extension of the beam eigenfunctions (the admissible functions), $\Phi_m(\xi)$, beyond $\xi = 1$. In the process of obtaining the generalized fluid forces acting on the shells (Chapter 2), another function $N_{km}(\bar{\alpha})$ closely related to $R_m(\xi)$ was defined [Equation (2.66)],

$$N_{km}(\bar{\alpha}) = H_k(-\bar{\alpha})N_m(\bar{\alpha}), \tag{B.1}$$

where

$$H_k(-\bar{\alpha}) = \int_0^1 \Phi_k(\xi)\, e^{-i\bar{\alpha}\xi}\, d\xi, \qquad N_m(\bar{\alpha}) = \int_1^{\ell} R_m(\xi)\, e^{i\bar{\alpha}\xi}\, d\xi. \tag{B.2}$$

It should be recalled that $H_k(-\bar{\alpha})$ was completely determined in Appendix A; thus, what still remains to be done in this appendix is to evaluate $N_m(\bar{\alpha})$ corresponding to each flow model.

B.1.2 Model 0: No Model

This is a trivial model in which flow perturbations are assumed to go to zero immediately upon exit from the shell (Figure 2.3); i.e., $R_m(\xi) = 0$ and hence $N_m(\bar{\alpha}) = 0$.

B.1.3 Model 1: Straight Decay Model

- In this model, first introduced by Shayo and Ellen (1978), flow perturbations are considered to decay linearly between 1 and ℓ. The model was originally visualized as a collector pipe, unconnected to the shell, yet following its motion. The characteristic function of this model thus must satisfy the boundary conditions:

$$R_m(\xi)\Big|_{\xi=1} = \Phi_m(1), \qquad R_m(\xi)\Big|_{\xi=\ell} = 0, \tag{B.3}$$

  from which $R_m(\xi)$ takes the form

$$R_m(\xi) = \begin{cases} \Phi_m(1)(\ell-\xi)/(\ell-1) & \text{for } 1 \le \xi \le \ell, \\ 0 & \text{for } \xi > \ell. \end{cases} \tag{B.4}$$

- $N_m(\bar{\alpha})$, defined in (B.2), can easily be found by integration by parts

$$\begin{aligned} N_m(\bar{\alpha}) &= \frac{\Phi_m(1)}{(\ell-1)} \int_1^{\ell} (\ell-\xi)\, e^{i\bar{\alpha}\xi}\, d\xi, \\ &= \frac{\Phi_m(1)}{(\ell-1)\bar{\alpha}^2} \left\{ e^{i\bar{\alpha}} \left[1 + i\bar{\alpha}(\ell-1)\right] - e^{i\bar{\alpha}\ell} \right\}. \end{aligned} \tag{B.5}$$

  For $\bar{\alpha} = 0$, L'Hôpital's rule gives

$$N_m(0) = \frac{1}{2}\Phi_m(1)(\ell-1). \tag{B.6}$$

  Since the value of ℓ is artificially imposed, it is of interest to evaluate $N_m(\bar{\alpha})$ as ℓ approaches ∞,

$$\lim_{\ell\to\infty} N_m(\bar{\alpha}) = \lim_{\ell\to\infty} \frac{\Phi_m(1)}{\bar{\alpha}^2} \left\{ e^{i\bar{\alpha}} \left[\frac{1}{(\ell-1)} + i\bar{\alpha}\right] - \frac{e^{i\bar{\alpha}\ell}}{(\ell-1)} \right\} = \Phi_m(1)\left(\frac{i}{\bar{\alpha}}\right) e^{i\bar{\alpha}}; \tag{B.7}$$

in finding $\lim_{\ell\to\infty} N_m(\bar{\alpha})$, attention has been given to the fact that the term $e^{i\bar{\alpha}\ell}$ is a harmonic function, related to trigonometric functions by Euler's identity,

$$e^{i\bar{\alpha}\ell} = \cos\bar{\alpha}\ell + i\sin\bar{\alpha}\ell, \tag{B.8}$$

and hence $|e^{i\bar{\alpha}\ell}| = 1$.

B.1.4 Model 2: Curved Decay Model

- In Model 1 there exists a discontinuity in the slope of the fluid flow at $\xi = 1$. To improve this, Païdoussis, Luu and Laithier (1986) have refined matters by requiring that flow perturbations have the same slope across $\xi = 1$. Thus, three boundary conditions need be imposed on $R_m(\xi)$:

$$R_m(\bar{\alpha})\Big|_{\xi=1} = \Phi_m(1), \quad R'_m(\bar{\alpha})\Big|_{\xi=1} = \Phi'_m(1), \quad R_m(\bar{\alpha})\Big|_{\xi=\ell} = 0. \tag{B.9}$$

  Using a quadratic polynomial fit, $R_m(\xi)$ is found to be given by

$$R_m(\xi) = \Phi_m(1)\left\{1 - \frac{(\xi-1)^2}{(\ell-1)^2}\right\} + \Phi'_m(1)\left\{(\xi-1) - \frac{(\xi-1)^2}{(\ell-1)}\right\} \tag{B.10}$$

  for $1 \le \xi \le \ell$ and, as before, $R_m(\xi) = 0$ for $\xi > \ell$.

- For the evaluation of $N_m(\bar{\alpha})$, it is convenient to define the following functions

$$\hat{N}_0(\bar{\alpha}) = \int_1^\ell e^{i\bar{\alpha}\xi}\,\mathrm{d}\xi = \frac{1}{i\bar{\alpha}}\left\{e^{i\bar{\alpha}\ell} - e^{i\bar{\alpha}}\right\}, \tag{B.11}$$

$$\hat{N}_1(\bar{\alpha}) = \int_1^\ell (\xi-1)\,e^{i\bar{\alpha}\xi}\,\mathrm{d}\xi = \frac{1}{\bar{\alpha}^2}\left\{[1 - i\bar{\alpha}(\ell-1)]\,e^{i\bar{\alpha}\ell} - e^{i\bar{\alpha}}\right\}, \tag{B.12}$$

$$\hat{N}_2(\bar{\alpha}) = \int_1^\ell (\xi-1)^2\,e^{i\bar{\alpha}\xi}\,\mathrm{d}\xi = \frac{1}{\bar{\alpha}^3}\left\{\left[2i + 2\bar{\alpha}(\ell-1) - i\bar{\alpha}^2(\ell-1)^2\right]e^{i\bar{\alpha}\ell} - 2ie^{i\bar{\alpha}}\right\}. \tag{B.13}$$

  For $\bar{\alpha} = 0$, applying L'Hôpital's rule to (B.11)–(B.13) yields

$$\hat{N}_0(0) = (\ell-1), \tag{B.14}$$

$$\hat{N}_1(0) = \frac{1}{2}(\ell-1)^2, \tag{B.15}$$

$$\hat{N}_2(0) = \frac{1}{3}(\ell-1)^3. \tag{B.16}$$

  Substituting (B.10) into the second equation of (B.2) and taking (B.11)–(B.13) into account results in

$$N_m(\bar{\alpha}) = \Phi_m(1)\left\{\hat{N}_0(\bar{\alpha}) - \frac{\hat{N}_2(\bar{\alpha})}{(\ell-1)^2}\right\} + \Phi'_m(1)\left\{\hat{N}_1(\bar{\alpha}) - \frac{\hat{N}_2(\bar{\alpha})}{(\ell-1)}\right\}. \tag{B.17}$$

The limiting value of $N_m(\bar{\alpha})$ as ℓ approaches ∞ is given by

$$\begin{aligned}\lim_{\ell\to\infty} N_m(\bar{\alpha}) &= \Phi_m(1)\lim_{\ell\to\infty}\left\{\hat{N}_0(\bar{\alpha}) - \frac{\hat{N}_2(\bar{\alpha})}{(\ell-1)^2}\right\} + \Phi_m'(1)\lim_{\ell\to\infty}\left\{\hat{N}_1(\bar{\alpha}) - \frac{\hat{N}_2(\bar{\alpha})}{(\ell-1)}\right\} \\ &= \Phi_m(1)\left(\frac{i}{\bar{\alpha}}\right)e^{i\bar{\alpha}} + \Phi_m'(1)\lim_{\ell\to\infty}\left\{\hat{N}_1(\bar{\alpha}) - \frac{\hat{N}_2(\bar{\alpha})}{(\ell-1)}\right\}. \end{aligned} \tag{B.18}$$

From Euler's identity in (B.8), it is seen that

$$\lim_{\ell\to\infty}(\ell-1)e^{i\bar{\alpha}\ell} = \lim_{\ell\to\infty}(\ell-1)\cos\bar{\alpha}\ell + i\lim_{\ell\to\infty}(\ell-1)\sin\bar{\alpha}\ell \tag{B.19}$$

does not exist, thus leading to the non–existence of the limit on the right–hand side of (B.18), which in turn gives rise to the non–existence of $\lim_{\ell\to\infty} N_m(\bar{\alpha})$. The resolution of this will be discussed in Section B.1.6.

B.1.5 Model 3: Refined Curved Model

- This is a refinement to Model 2, by requiring further that the slope of the perturbation curve also vanish at $\xi = \ell$, thus imposing a total of four boundary conditions on $R_m(\xi)$,

$$R_m(\xi)\Big|_{\xi=1} = \Phi_m(1),\quad R_m'(\xi)\Big|_{\xi=1} = \Phi_m'(1),\quad R_m(\xi)\Big|_{\xi=\ell} = 0,\quad R_m'(\xi)\Big|_{\xi=\ell} = 0. \tag{B.20}$$

Hence, with a cubic polynomial fit, $R_m(\xi)$ is obtained, $R_m(\xi) = 0$ for $\xi > \ell$ and

$$\begin{aligned} R_m(\xi) &= \frac{\Phi_m(1)}{(\ell-1)^3}\left\{2\xi^3 - 3(\ell+1)\xi^2 + 6\ell\xi + \ell^2(\ell-3)\right\} \\ &+ \frac{\Phi_m'(1)}{(\ell-1)^2}\left\{\xi^3 - (2\ell+1)\xi^2 + \ell(\ell+2)\xi - \ell^2\right\} \quad \text{for } 1 \le \xi \le \ell. \end{aligned} \tag{B.21}$$

- As done for Model 2, the following functions are defined

$$\hat{N}_0(\bar{\alpha}) = \int_1^\ell e^{i\bar{\alpha}\xi}\,\mathrm{d}\xi = \frac{1}{i\bar{\alpha}}\left\{e^{i\bar{\alpha}\ell} - e^{i\bar{\alpha}}\right\}, \tag{B.22}$$

$$\hat{N}_1(\bar{\alpha}) = \int_1^\ell \xi\, e^{i\bar{\alpha}\xi}\,\mathrm{d}\xi = \frac{1}{\bar{\alpha}^2}\left\{e^{i\bar{\alpha}\ell}(1-i\bar{\alpha}\ell) - e^{i\bar{\alpha}}(1-i\bar{\alpha})\right\}, \tag{B.23}$$

$$\hat{N}_2(\bar{\alpha}) = \int_1^\ell \xi^2\, e^{i\bar{\alpha}\xi}\,\mathrm{d}\xi = \frac{1}{\bar{\alpha}^3}\left\{e^{i\bar{\alpha}\ell}\left[2(i+\bar{\alpha}\ell) - i\bar{\alpha}^2\ell^2\right] - e^{i\bar{\alpha}}\left[2(i+\bar{\alpha}) - i\bar{\alpha}^2\right]\right\}, \tag{B.24}$$

$$\begin{aligned}\hat{N}_3(\bar{\alpha}) &= \int_1^\ell \xi^3\, e^{i\bar{\alpha}\xi}\,\mathrm{d}\xi = \frac{1}{\bar{\alpha}^4}\left\{e^{i\bar{\alpha}\ell}\left[\bar{\alpha}^2\ell^2(3-i\bar{\alpha}\ell) + 6(i\bar{\alpha}\ell-1)\right]\right. \\ &\qquad \left. - e^{i\bar{\alpha}}\left[\bar{\alpha}^2(3-i\bar{\alpha}) + 6(i\bar{\alpha}-1)\right]\right\}, \end{aligned} \tag{B.25}$$

and for $\bar{\alpha} = 0$, L'Hôpital's rule gives

$$\hat{N}_0(0) = (\ell - 1), \tag{B.26}$$

$$\hat{N}_1(0) = \frac{1}{2}(\ell^2 - 1), \tag{B.27}$$

$$\hat{N}_2(0) = \frac{1}{3}(\ell^3 - 1), \tag{B.28}$$

$$\hat{N}_3(0) = \frac{1}{4}(\ell^4 - 1). \tag{B.29}$$

Finally, $N_m(\bar{\alpha})$ for Model 3 is determined from (B.2), together with (B.21) and (B.22)–(B.25),

$$\begin{aligned} N_m(\bar{\alpha}) &= \frac{\Phi_m(1)}{(\ell - 1)^3}\Big\{2\hat{N}_3(\bar{\alpha}) - 3(\ell + 1)\hat{N}_2(\bar{\alpha}) + 6\ell\hat{N}_1(\bar{\alpha}) + \ell^2(\ell - 3)\hat{N}_0(\bar{\alpha})\Big\} \\ &+ \frac{\Phi'_m(1)}{(\ell - 1)^2}\Big\{\hat{N}_3(\bar{\alpha}) - (2\ell + 1)\hat{N}_2(\bar{\alpha}) + \ell(\ell + 2)\hat{N}_1(\bar{\alpha}) - \ell^2\hat{N}_0(\bar{\alpha})\Big\}. \end{aligned} \tag{B.30}$$

The limiting value of $N_m(\bar{\alpha})$ is found the same way as was done in Equation (B.18), namely

$$\begin{aligned} \lim_{\ell \to \infty} N_m(\bar{\alpha}) &= \Phi_m(1)\Big(\frac{i}{\bar{\alpha}}\Big)e^{i\bar{\alpha}} \\ &+ \Phi'_m(1)\lim_{\ell \to \infty}\left\{\frac{\hat{N}_3(\bar{\alpha}) - (2\ell + 1)\hat{N}_2(\bar{\alpha}) + \ell(\ell + 2)\hat{N}_1(\bar{\alpha}) - \ell^2\hat{N}_0(\bar{\alpha})}{(\ell - 1)^2}\right\}, \end{aligned} \tag{B.31}$$

which does not exist due to the non-existence of $\lim_{\ell \to \infty} \ell e^{i\bar{\alpha}\ell}$. Further discussion on this matter will be given in the immediately following section.

B.1.6 Remarks

A comparison of Equations (B.7), (B.18) and (B.31) shows that the non-existence of $\lim_{\ell \to \infty} N_m(\bar{\alpha})$ in Models 2 and 3 is attributed to the presence of the term(s) associated with $\Phi'_m(1)$. Since it is the dependence on $\Phi'_m(1)$ that makes Models 2 and 3 more realistic than Model 1, ℓ should be taken to be *finite* so as to produce physically reasonable results. Further discussion on the magnitude of ℓ was given in Chapter 2 (Section 2.4.4.2).

B.2 In the Finite–Difference Method

The aim of this Section is to find the expressions represented by the constants A and B in Equation (5.130) [Chapter 5]. Here, for practical purposes, only Models 1–3 will be considered.

It is noted that the characteristic functions $R_m(\xi)$ of flow models as were found in Section B.1 could all be expressed in the following general form

$$R_m(\xi) \;=\; C_1(\xi,\ell)\Phi_m(1) \;+\; C_2(\xi,\ell)\Phi_m'(1), \tag{B.32}$$

where $R_m(\xi)$ generally has a non–zero value for $1 \le \xi \le \ell$ and,

- for Model 1,

$$C_1(\xi,\ell) \;=\; \frac{\ell-\xi}{\ell-1}, \qquad C_1(\xi,\ell) \;=\; 0; \tag{B.33}$$

- for Model 2,

$$C_1(\xi,\ell) \;=\; \left\{1-\frac{(\xi-1)^2}{(\ell-1)^2}\right\}, \quad C_2(\xi,\ell) \;=\; \left\{(\xi-1)-\frac{(\xi-1)^2}{(\ell-1)}\right\}; \tag{B.34}$$

- for Model 3,

$$\begin{aligned} C_1(\xi,\ell) \;&=\; \frac{1}{(\ell-1)^3}\left\{2\xi^3-3(\ell+1)\xi^2+6\ell\xi+\ell^2(\ell-3)\right\}, \\ C_2(\xi,\ell) \;&=\; \frac{1}{(\ell-1)^2}\left\{\xi^3-(2\ell+1)\xi^2+\ell(\ell+2)\xi-\ell^2\right\}. \end{aligned} \tag{B.35}$$

If $\mathcal{V}(\xi)$ stands for a component of the perturbation velocity, then $\mathcal{V}(\xi)$ can also be written in the form of Equation (B.32) for $1 \le \xi \le \ell$,

$$\begin{aligned} \mathcal{V}(\xi) \;&=\; C_1(\xi,\ell)\mathcal{V}(1) \;+\; C_2(\xi,\ell)\mathcal{V}'(1) \\ &=\; C_1(\xi,\ell)\mathcal{V}_{i^*,j} \;+\; C_2(\xi,\ell)\left[\frac{\mathcal{V}_{i^*,j}-\mathcal{V}_{i^*-1,j}}{\Delta\xi}\right] \\ &=\; -\left[\frac{C_2(\xi,\ell)}{\Delta\xi}\right]\mathcal{V}_{i^*-1,j} \;+\; \left[C_1(\xi,\ell)+\frac{C_2(\xi,\ell)}{\Delta\xi}\right]\mathcal{V}_{i^*,j}, \end{aligned} \tag{B.36}$$

where $\mathcal{V}(1)$ has been replaced by $\mathcal{V}_{i^*,j}$, and $\mathcal{V}'(1)$ by the two–point backward difference approximation, with i^* denoting the last spatial location of $\mathcal{V}$ in the computational domain for a given j; thus, $i^* = N$ for $\mathcal{V} \equiv \mathcal{V}_x$, and $i^* = (N+1)$ for $\mathcal{V} \equiv \mathcal{V}_r$ or $\mathcal{V}_\theta$. Since the grid is uniform in the ξ–direction, the ξ–coordinate of $\mathcal{V}_{i^*+1,j}$ being just outside the domain (Figure 5.2) would be $\xi = \xi^* = (1 + \Delta\xi)$. According to Equation (B.36),

$$\mathcal{V}_{i^*+1,j} = -\left[\frac{C_2(\xi^*, \ell)}{\Delta\xi}\right]\mathcal{V}_{i^*-1,j} + \left[C_1(\xi^*, \ell) + \frac{C_2(\xi^*, \ell)}{\Delta\xi}\right]\mathcal{V}_{i^*,j},$$

or

$$\mathcal{V}_{i^*+1,j} = A\mathcal{V}_{i^*-1,j} - B\mathcal{V}_{i^*,j}, \tag{B.37}$$

where

$$A = -\left[\frac{C_2(\xi^*, \ell)}{\Delta\xi}\right], \qquad B = -\left[C_1(\xi^*, \ell) + \frac{C_2(\xi^*, \ell)}{\Delta\xi}\right]. \tag{B.38}$$

Appendix C

Definition of [M], [C] and [K]

The following are the elements of [M], [C] and [K].

<u>Matrix</u> [M]

$$M_{km}^{1,1} = \varepsilon_i^2 b_{km}; \;\; M_{km}^{2,2} = \delta_{km}; \;\; M_{km}^{3,3} = \delta_{km} + q_{km}^{(1)}; \;\; M_{km}^{3,6} = r_{km}^{(1)};$$

$$M_{km}^{4,4} = \varepsilon_o^2 b/\Omega_r^2; \;\; M_{km}^{5,5} = \delta_{km}/\Omega_r^2; \;\; M_{km}^{6,3} = s_{km}^{(1)}; \;\; M_{km}^{6,6} = \delta_{km}/\Omega_r^2 + t_{km}^{(1)}.$$

The remaining elements are zeros.

<u>Matrix</u> [C]

$$C_{km}^{3,3} = 2q_{km}^{(2)}; \;\; C_{km}^{3,6} = 2r_{km}^{(2)}; \;\; C_{km}^{6,3} = 2s_{km}^{(2)}; \;\; C_{km}^{6,6} = 2t_{km}^{(2)}.$$

The remaining elements are zeros.

<u>Matrix</u> [K]: $\quad$ $[\mathrm{K}] = [\mathrm{K}_1] + [\mathrm{K}_2] + [\mathrm{K}_3]$

Each constituent part of [K] has a different physical basis. Matrix $[\mathrm{K}_1]$ results from the strain energy associated with the standard Flügge's shell theory; matrix $[\mathrm{K}_2]$ accounts for the free–end boundary conditions, whereas matrix $[\mathrm{K}_3]$ represents a change in the *effective* stiffness of the system due to steady viscous effects of the flowing fluid.

The elements of $[\mathrm{K}_1]$ are:

$$K_{1km}^{1,1} = -\tfrac{1}{2}n(1+k_i)(1-\nu_i)\varepsilon_i^2 b_{km} + \varepsilon_i^4 d_{km}; \;\; K_{1km}^{1,2} = \tfrac{1}{2}n(1+\nu_i)\varepsilon_i^2 b_{km};$$

$$K_{1km}^{1,3} = \left\{\nu_i - \tfrac{1}{2}n^2 k_i(1-\nu_i)\right\}\varepsilon_i^2 b_{km} - k_i\varepsilon_i^4 d_{km}; \;\; K_{1km}^{2,1} = -\tfrac{1}{2}n^2(1+\nu_i)\varepsilon_i^2 c_{km};$$

$$K_{1km}^{2,2} = -n^2\delta_{km} + \tfrac{1}{2}(1+3k_i)(1-\nu_i)\varepsilon_i^2 c_{km}; \;\; K_{1km}^{2,3} = \tfrac{1}{2}nk_i\,(3-\nu_i)\varepsilon_i^2 c_{km} - n\delta_{km};$$

$$K_{1km}^{3,1} = \left\{\tfrac{1}{2}n^2 k_i(1-\nu_i) - \nu_i\right\}\varepsilon_i^2 c_{km} + k_i\varepsilon_i^4\lambda_m^4\delta_{km}; \;\; K_{1km}^{3,2} = K_{1km}^{2,3}$$

$$K^{3,3}_{1km} = -[k_i(n^2-1)^2 + k_i\varepsilon_i^4\lambda_m^4 + 1]\delta_{km} + 2k_in^2\varepsilon_i^2c_{km} + q^{(3)}_{km};\;\; K^{3,6}_{1km} = r^{(3)}_{km};$$

$$K^{4,4}_{1km} = -\tfrac{1}{2}n^2(1+k_o)(1-\nu_o)\varepsilon_o^2b_{km} + \varepsilon_o^4d_{km};\;\; K^{4,5}_{1km} = \tfrac{1}{2}n(1+\nu_o)\varepsilon_o^2b_{km};$$

$$K^{4,6}_{1km} = \left\{\nu_o - \tfrac{1}{2}n^2k_o(1-\nu_o)\right\}\varepsilon_o^2b - k_o\varepsilon_o^4d_{km};\;\; K^{5,4}_{1km} = -\tfrac{1}{2}n(1+\nu_o)\varepsilon_o^2c_{km};$$

$$K^{5,5}_{1km} = -n^2\delta_{km} + \tfrac{1}{2}(1+3k_o)(1-\nu_o)\varepsilon_o^2c_{km};\;\; K^{5,6}_{1km} = \tfrac{1}{2}nk_o(3-\nu_o)\varepsilon_o^2c_{km} - n\delta_{km};$$

$$K^{6,3}_{1km} = s^{(3)}_{km};\;\; K^{6,4}_{1km} = \left\{\tfrac{1}{2}n^2k_o(1-\nu_o) - \nu_o\right\}\varepsilon_o^2c_{km} + k_o\varepsilon_o^4\lambda^4_{km}\delta_{km};\;\; K^{6,5}_{1km} = K^{5,6}_{1km};$$

$$K^{6,6}_{1km} = -\left\{k_o(n^2-1)^2 + k_o\varepsilon_o^4\lambda_m^4 + 1\right\}\delta_{km} + 2k_on^2\varepsilon_o^2c_{km} + t^{(3)}_{km}.$$

The remaining elements are zeros.

The elements of [K_2] are:

$$K^{1,2}_{2km} = -\nu_in\varepsilon_i^2e_{km};\;\; K^{1,3}_{2km} = -\nu_i\varepsilon_i^2e_{km};\;\; K^{2,1}_{2km} = \tfrac{1}{2}n\varepsilon_i^2(1-\nu_i)f_{km};$$

$$K^{2,2}_{2km} = -\tfrac{1}{2}\varepsilon_i^2(1+3k_i)(1-\nu_i)f_{km};\;\; K^{2,3}_{2km} = -\tfrac{3}{2}nk_i\varepsilon_i^2(1-\nu_i)f_{km};$$

$$K^{3,1}_{2km} = -\tfrac{1}{2}n^2\varepsilon_i^2k_i(1-\nu_i)f_{km};\;\; K^{3,2}_{2km} = nk_i\varepsilon_i^2\left[\nu_ie_{km} - \tfrac{1}{2}(3-\nu_i)f_{km}\right];$$

$$K^{3,3}_{2km} = n^2k_i\varepsilon_i^2\left[\nu_ie_{km} - (2-\nu_i)f_{km}\right];\;\; K^{4,5}_{2km} = -\nu_on\varepsilon_o^2e_{km};\;\; K^{4,6}_{2km} = -\nu_o\varepsilon_o^2e_{km};$$

$$K^{5,4}_{2km} = \tfrac{1}{2}n\varepsilon_o^2(1-\nu_o)f_{km};\;\; K^{5,5}_{2km} = -\tfrac{1}{2}\varepsilon_o^2(1+3k_o)(1-\nu_o)f_{km};$$

$$K^{5,6}_{2km} = -\tfrac{3}{2}nk_o\varepsilon_o^2(1-\nu_o)f_{km};\;\; K^{6,4}_{2km} = -\tfrac{1}{2}n^2\varepsilon_o^2k_o(1-\nu_o)f_{km};$$

$$K^{6,5}_{2km} = nk_o\varepsilon_o^2\left[\nu_oe_{km} - \tfrac{1}{2}(3-\nu_o)f_{km}\right];\;\; K^{6,6}_{2km} = n^2k_o\varepsilon_o^2\left[\nu_oe_{km} - (2-\nu_o)f_{km}\right].$$

The remaining elements are zeros.

The elements of matrix [K_3] are:

$$K^{1,1}_{3km} = \varepsilon_i^4\left[\hat{A}_{1i}\hat{d}_{km} + \hat{B}_{1i}d_{km}\right] - n^2\varepsilon_i^2\left[\hat{A}_{3i}\hat{b}_{km} + \hat{B}_{3i}b_{km}\right];$$

$$K^{1,2}_{3km} = n\hat{B}_{2i}\varepsilon_ia_{km};\;\; K^{1,3}_{3km} = \hat{B}_{2i}\varepsilon_ia_{km} - \varepsilon_i^2\left[\hat{A}_{3i}\hat{b}_{km} + \hat{B}_{3i}b_{km}\right];$$

$$K^{2,2}_{3km} = \varepsilon_i^2\left[\hat{A}_{1i}\hat{c}_{km} + \hat{B}_{1i}c_{km}\right] - n^2\left[\hat{A}_{3i}\hat{a}_{km} + \hat{B}_{3i}\delta_{km}\right];$$

$$K^{2,3}_{3km} = -n\left[\hat{A}_{3i}\hat{a}_{km} + \hat{B}_{3i}\delta_{km}\right];\;\; K^{3,1}_{3km} = \varepsilon_i^2\left[\hat{A}_{3i}\hat{c}_{km} + \hat{B}_{3i}c_{km}\right];$$

$$K^{3,2}_{3km} = K^{2,3}_{3km};\;\; K^{3,3}_{3km} = \varepsilon_i^2\left[\hat{A}_{1i}\hat{c}_{km} + \hat{B}_{1i}c_{km}\right] - n^2\left[\hat{A}_{3i}\hat{a}_{km} + \hat{B}_{3i}\delta_{km}\right];$$

$$K^{4,4}_{3km} = \varepsilon_o^4\left[\hat{A}_{1o}\hat{d}_{km} + \hat{B}_{1o}d_{km}\right] - n^2\varepsilon_o^2\left[\hat{A}_{3o}\hat{b}_{km} + \hat{B}_{3o}b_{km}\right];$$

$$K^{4,5}_{3km} = n\hat{B}_{2o}\varepsilon_oa_{km};\;\; K^{4,6}_{3km} = \hat{B}_{2o}\varepsilon_oa_{km} - \varepsilon_o^2\left[\hat{A}_{3o}\hat{b}_{km} + \hat{B}_{3o}b_{km}\right];$$

$$K^{5,5}_{3km} = \varepsilon_o^2\left[\hat{A}_{1o}\hat{c}_{km} + \hat{B}_{1o}c_{km}\right] - n^2\left[\hat{A}_{3o}\hat{a}_{km} + \hat{B}_{3o}\delta_{km}\right];$$

$$K^{5,6}_{3km} = -n\left[\hat{A}_{3o}\hat{a}_{km} + \hat{B}_{3o}\delta_{km}\right]; \;\; K^{6,4}_{3km} = \varepsilon_o^2\left[\hat{A}_{3o}\hat{c}_{km} + \hat{B}_{3o}c_{km}\right];$$

$$K^{6,5}_{3km} = K^{5,6}_{3km}; \;\; K^{6,6}_{3km} = \varepsilon_o^2\left[\hat{A}_{1o}\hat{c}_{km} + \hat{B}_{1o}c_{km}\right] - n^2\left[\hat{A}_{3o}\hat{a}_{km} + \hat{B}_{3o}\delta_{km}\right].$$

The remaining elements are zeros.

In the above matrix elements, $\hat{A}$'s and $\hat{B}$'s are constants defined in (2.100), while

$$\begin{aligned} a_{km} &= \int_0^1 \Phi_k'(\xi)\,\Phi_m(\xi)\,\mathrm{d}\xi, & \hat{a}_{km} &= \int_0^1 \xi\,\Phi_k(\xi)\,\Phi_m(\xi)\,\mathrm{d}\xi, \\ b_{km} &= \int_0^1 \Phi_k'(\xi)\,\Phi_m'(\xi)\,\mathrm{d}\xi, & \hat{b}_{km} &= \int_0^1 \xi\,\Phi_k'(\xi)\,\Phi_m'(\xi)\,\mathrm{d}\xi, \\ c_{km} &= \int_0^1 \Phi_k(\xi)\,\Phi_m''(\xi)\,\mathrm{d}\xi, & \hat{c}_{km} &= \int_0^1 \xi\,\Phi_k(\xi)\,\Phi_m''(\xi)\,\mathrm{d}\xi, \\ d_{km} &= \int_0^1 \Phi_k'(\xi)\,\Phi_m'''(\xi)\,\mathrm{d}\xi, & \hat{d}_{km} &= \int_0^1 \xi\,\Phi_k'(\xi)\,\Phi_m'''(\xi)\,\mathrm{d}\xi, \end{aligned}$$

all of which are evaluated in Appendix D, and

$$\begin{aligned} \delta_{km} &= \int_0^1 \Phi_k(\xi)\,\Phi_m(\xi)\,\mathrm{d}\xi = \begin{cases} 0 & \text{if } k \neq m, \\ 1 & \text{if } k = m, \end{cases} \\ e_{km} &= \Phi_k'(1)\Phi_m(1) = 4\lambda_k\sigma_k(-1)^{k+m}, \\ f_{km} &= e_{mk}, \end{aligned}$$

where f_{km} has been used to denote e_{mk} for the sake of clarity, and $\Phi_m(\xi)$ are the eigenfunctions of a cantilevered beam,

$$\Phi_m(\xi) = (\cosh\lambda_m\xi - \cos\lambda_m\xi) - \sigma_m(\sinh\lambda_m\xi - \sin\lambda_m\xi),$$

with

$$\xi = x/L, \;\; \cosh\lambda_m\cos\lambda_m + 1 = 0, \;\; \sigma_m = (\cosh\lambda_m + \cos\lambda_m)/(\sinh\lambda_m + \sin\lambda_m).$$

In the above expressions, primes denote differentiation with respect to the argument of the function, ξ.

Vector {X}

$$\{\mathrm{X}\}^{\mathrm{T}} = \{\bar{A}_m\;\bar{B}_m\;\bar{C}_m\;\bar{D}_m\;\bar{E}_m\;\bar{F}_m\}.$$

It should be noted that, since k and m are indices such that $1 \leq k, m \leq M$, each element of [M], [C], or [K] is in effect an $M \times M$ submatrix of scalars, and each element of {X} is a subvector of M (scalar) elements.

Appendix D

Integrals Involving Beam Eigenfunctions

A number of definite integrals involving beam eigenfunctions were encountered in Chapter 2 (Section 2.3.4), as the extended Galerkin method was utilized to solve the equations of motion. Such integrals were denoted by the following constants in Appendix C:

$$\begin{aligned}
a_{km} &= \int_0^1 \frac{\mathrm{d}\Phi_k}{\mathrm{d}\xi}\,\Phi_m\,\mathrm{d}\xi, & \hat{a}_{km} &= \int_0^1 \xi\,\Phi_k\,\Phi_m\,\mathrm{d}\xi,\\
b_{km} &= \int_0^1 \frac{\mathrm{d}\Phi_k}{\mathrm{d}\xi}\,\frac{\mathrm{d}\Phi_m}{\mathrm{d}\xi}\,\mathrm{d}\xi, & \hat{b}_{km} &= \int_0^1 \xi\,\frac{\mathrm{d}\Phi_k}{\mathrm{d}\xi}\,\frac{\mathrm{d}\Phi_m}{\mathrm{d}\xi}\,\mathrm{d}\xi,\\
c_{km} &= \int_0^1 \Phi_k\,\frac{\mathrm{d}^2\Phi_m}{\mathrm{d}\xi^2}\,\mathrm{d}\xi, & \hat{c}_{km} &= \int_0^1 \xi\,\Phi_k\,\frac{\mathrm{d}^2\Phi_m}{\mathrm{d}\xi^2}\,\mathrm{d}\xi,\\
d_{km} &= \int_0^1 \frac{\mathrm{d}\Phi_k}{\mathrm{d}\xi}\,\frac{\mathrm{d}^3\Phi_m}{\mathrm{d}\xi^3}\,\mathrm{d}\xi, & \hat{d}_{km} &= \int_0^1 \xi\,\frac{\mathrm{d}\Phi_k}{\mathrm{d}\xi}\,\frac{\mathrm{d}^3\Phi_m}{\mathrm{d}\xi^3}\,\mathrm{d}\xi,
\end{aligned}$$

where $\xi = x/L$ is a dimensionless length variable, defined in (2.55).

The above integrals will be evaluated using the same procedure as introduced by Gregory and Païdoussis (1966a); nevertheless, Sharma's (1978) notation will be adopted here. Consideration is now given to two eigenfunctions $\Phi_k(\lambda_k\xi)$ and $\Psi_m(\alpha_m\xi)$, satisfying the relationship

$$\Phi_k''''(\lambda_k\xi) = \Phi_k(\lambda_k\xi), \qquad \Psi_m''''(\alpha_m\xi) = \Psi_m(\alpha_m\xi), \tag{D.1}$$

where primes denote differentiation with respect to the arguments of the functions. Here, it should be pointed out that, although the definition of primes in this appendix is the same as that in the previous appendices, the *current* arguments of the functions Φ_m and Ψ_m are different: $\lambda_k\xi$ for Φ_m and $\alpha_m\xi$ for Ψ_m (in the previous appendices, ξ was the argument of Φ_m). By integration by parts, it follows that

$$(\alpha_m^4 - \lambda_k^4)\int_0^1 \Phi_k\Psi_m\,\mathrm{d}\xi = \left\{\alpha_m^3\Phi_k\Psi_m''' - \lambda_k\alpha_m^2\Phi_k'\Psi_m'' + \lambda_k^2\alpha_m\Phi_k''\Psi_m' - \lambda_k^3\Phi_k'''\Psi_m\right\}\Big|_0^1, \quad \text{(D.2)}$$

$$(\alpha_m^4 - \lambda_k^4)\int_0^1 \Phi_k'\Psi_m\,\mathrm{d}\xi = \left\{\alpha_m^3\Phi_k'\Psi_m''' - \lambda_k\alpha_m^2\Phi_k''\Psi_m'' + \lambda_k^2\alpha_m\Phi_k'''\Psi_m' - \lambda_k^3\Phi_k\Psi_m\right\}\Big|_0^1, \quad \text{(D.3)}$$

$$(\alpha_m^4 - \lambda_k^4)\int_0^1 \Phi_k\Psi_m''\,\mathrm{d}\xi = \left\{\alpha_m^3\Phi_k\Psi_m' - \lambda_k\alpha_m^2\Phi_k'\Psi_m + \lambda_k^2\alpha_m\Phi_k''\Psi_m''' - \lambda_k^3\Phi_k'''\Psi_m''\right\}\Big|_0^1, \quad \text{(D.4)}$$

$$(\alpha_m^4 - \lambda_k^4)\int_0^1 \Phi_k'\Psi_m'''\,\mathrm{d}\xi = \left\{\alpha_m^3\Phi_k'\Psi_m'' - \lambda_k\alpha_m^2\Phi_k''\Psi_m' + \lambda_k^2\alpha_m\Phi_k'''\Psi_m - \lambda_k^3\Phi_k\Psi_m'''\right\}\Big|_0^1, \quad \text{(D.5)}$$

$$\begin{aligned}(\alpha_m^4 - \lambda_k^4)\int_0^1 \xi\,\Phi_k\Psi_m\,\mathrm{d}\xi &= \Big\{\xi\alpha_m^3\Phi_k\Psi_m''' - \xi\lambda_k\alpha_m^2\Phi_k'\Psi_m'' + \xi\lambda_k^2\alpha_m\Phi_k''\Psi_m' - \xi\lambda_k^3\Phi_k'''\Psi_m \\ &\quad + 3\alpha_m^2\Phi_k\Psi_m'' - 2\lambda_k\alpha_m\Phi_k'\Psi_m' + \lambda_k^2\Phi_k''\Psi_m\Big\}\Big|_0^1 - 4\alpha_m^3\int_0^1 \Phi_k\Psi_m'''\,\mathrm{d}\xi, \quad \text{(D.6)}\end{aligned}$$

$$\begin{aligned}(\alpha_m^4 - \lambda_k^4)\int_0^1 \xi\,\Phi_k'\Psi_m'\,\mathrm{d}\xi &= \Big\{\xi\alpha_m^3\Phi_k'\Psi_m - \xi\lambda_k\alpha_m^2\Phi_k''\Psi_m''' + \xi\lambda_k^2\alpha_m\Phi_k'''\Psi_m'' - \xi\lambda_k^3\Phi_k\Psi_m' \\ &\quad + 3\alpha_m^2\Phi_k'\Psi_m''' - 2\lambda_k\alpha_m\Phi_k''\Psi_m'' + \lambda_k^2\Phi_k'''\Psi_m'\Big\}\Big|_0^1 - 4\alpha_m^3\int_0^1 \Phi_k'\Psi_m\,\mathrm{d}\xi, \quad \text{(D.7)}\end{aligned}$$

$$\begin{aligned}(\alpha_m^4 - \lambda_k^4)\int_0^1 \xi\,\Phi_k\Psi_m''\,\mathrm{d}\xi &= \Big\{\xi\alpha_m^3\Phi_k\Psi_m' - \xi\lambda_k\alpha_m^2\Phi_k'\Psi_m + \xi\lambda_k^2\alpha_m\Phi_k''\Psi_m''' - \xi\lambda_k^3\Phi_k'''\Psi_m'' \\ &\quad + 3\alpha_m^2\Phi_k\Psi_m - 2\lambda_k\alpha_m\Phi_k'\Psi_m''' + \lambda_k^2\Phi_k''\Psi_m''\Big\}\Big|_0^1 - 4\alpha_m^3\int_0^1 \Phi_k\Psi_m'\,\mathrm{d}\xi, \quad \text{(D.8)}\end{aligned}$$

$$\begin{aligned}(\alpha_m^4 - \lambda_k^4)\int_0^1 \xi\,\Phi_k'\Psi_m''\,\mathrm{d}\xi &= \Big\{\xi\alpha_m^3\Phi_k'\Psi_m'' - \xi\lambda_k\alpha_m^2\Phi_k''\Psi_m' + \xi\lambda_k^2\alpha_m\Phi_k'''\Psi_m - \xi\lambda_k^3\Phi_k\Psi_m''' \\ &\quad + 3\alpha_m^2\Phi_k'\Psi_m' - 2\lambda_k\alpha_m\Phi_k''\Psi_m + \lambda_k^2\Phi_k'''\Psi_m'''\Big\}\Big|_0^1 - 4\alpha_m^3\int_0^1 \Phi_k'\Psi_m''\,\mathrm{d}\xi. \quad \text{(D.9)}\end{aligned}$$

When Ψ_k is replaced by Φ_k, both sides of Equations (D.2–D.9) identically vanish and hence the values of the integrals cannot be calculated from these equations. For such a case, the limiting procedure outlined by Rayleigh (1945) will be used; the idea here is that by letting $\alpha_k = \lambda_k + \delta\lambda_k$ then as $\delta\lambda_k$ approaches zero, Ψ_k approaches Φ_k. In this procedure, Ψ_k and its derivatives are approximated as

$$\Psi_k \equiv \Psi_k(\lambda_k + \delta\lambda_k) \simeq \Phi_k + \left(\frac{\mathrm{d}\Phi_k}{\mathrm{d}\lambda_k}\right)\delta\lambda_k, \quad \text{(D.10)}$$

$$\Psi_k' \equiv \Psi_k'(\lambda_k + \delta\lambda_k) \simeq \Phi_k' + \left(\frac{\mathrm{d}\Phi_k'}{\mathrm{d}\lambda_k}\right)\delta\lambda_k, \tag{D.11}$$

$$\Psi_k'' \equiv \Psi_k''(\lambda_k + \delta\lambda_k) \simeq \Phi_k'' + \left(\frac{\mathrm{d}\Phi_k''}{\mathrm{d}\lambda_k}\right)\delta\lambda_k, \tag{D.12}$$

$$\Psi_k''' \equiv \Psi_k'''(\lambda_k + \delta\lambda_k) \simeq \Phi_k''' + \left(\frac{\mathrm{d}\Phi_k'''}{\mathrm{d}\lambda_k}\right)\delta\lambda_k, \tag{D.13}$$

where terms of higher powers of $\delta\lambda_k$ than unity are neglected.

Substituting the above approximations into Equations (D.2)–(D.8) and evaluating the resulting equations as $\delta\lambda_k$ approaches zero gives

$$4\lambda_k \int_0^1 \Phi_k^2\,\mathrm{d}\xi = \left\{3\Phi_k\Phi_k''' + \xi\lambda_k\Phi_k^2 - 2\xi\lambda_k\Phi_k'\Phi_k''' - \Phi_k'\Phi_k'' + \xi\lambda_k(\Phi_k'')^2\right\}\Big|_0^1, \tag{D.14}$$

$$2\lambda_k \int_0^1 \Phi_k'\,\Phi_k\,\mathrm{d}\xi = \left\{2\Phi_k'\Phi_k''' - (\Phi_k'')^2\right\}\Big|_0^1, \tag{D.15}$$

$$4\lambda_k \int_0^1 \Phi_k\,\Phi_k''\,\mathrm{d}\xi = \left\{2\xi\lambda_k\Phi_k\Phi_k'' - \xi\lambda_k(\Phi_k')^2 - \xi\lambda_k(\Phi_k''')^2 + \Phi_k\Phi_k' + \Phi_k''\Phi_k'''\right\}\Big|_0^1, \tag{D.16}$$

$$4\lambda_k \int_0^1 \Phi_k'\,\Phi_k'''\,\mathrm{d}\xi = \left\{2\xi\lambda_k\Phi_k'\Phi_k''' - \xi\lambda_k(\Phi_k'')^2 - \xi\lambda_k\Phi_k^2 + \Phi_k'\Phi_k'' + \Phi_k'''\Phi_k\right\}\Big|_0^1, \tag{D.17}$$

$$\begin{aligned} 8\lambda_k^2 \int_0^1 \xi\,\Phi_k^2\,\mathrm{d}\xi &= \Big\{2\xi\lambda_k\left[3\Phi_k\Phi_k''' - \Phi_k'\Phi_k''\right] + \xi^2\lambda_k^2\left[\Phi_k^2 + (\Phi_k'')^2 - 2\Phi_k'\Phi_k'''\right] \\ &\quad + 4(\Phi_k')^2 - 6\Phi_k\Phi_k''\Big\}\Big|_0^1, \end{aligned} \tag{D.18}$$

$$\begin{aligned} 8\lambda_k^2 \int_0^1 \xi\,(\Phi_k')^2\,\mathrm{d}\xi &= \Big\{2\xi\lambda_k\left[3\Phi_k'\Phi_k - \Phi_k''\Phi_k'''\right] + \xi^2\lambda_k^2\left[(\Phi_k')^2 + (\Phi_k''')^2 - 2\Phi_k''\Phi_k\right] \\ &\quad + 4(\Phi_k'')^2 - 6\Phi_k'\Phi_k'''\Big\}\Big|_0^1, \end{aligned} \tag{D.19}$$

$$\begin{aligned} 8\lambda_k^2 \int_0^1 \xi\,\Phi_k\,\Phi_k''\,\mathrm{d}\xi &= \Big\{2\xi\lambda_k\left[\Phi_k\Phi_k' + \Phi_k''\Phi_k'''\right] + \xi^2\lambda_k^2\left[2\Phi_k\Phi_k'' - (\Phi_k')^2 - (\Phi_k''')^2\right] \\ &\quad + 16\Phi_k'\Phi_k''' - 9\Phi_k^2 - 9(\Phi_k'')^2\Big\}\Big|_0^1, \end{aligned} \tag{D.20}$$

$$\begin{aligned} 8\lambda_k^2 \int_0^1 \xi\,\Phi_k'\,\Phi_k'''\,\mathrm{d}\xi &= \Big\{2\xi\lambda_k\left[\Phi_k'\Phi_k'' + \Phi_k'''\Phi_k\right] + \xi^2\lambda_k^2\left[2\Phi_k'\Phi_k''' - (\Phi_k'')^2 - \Phi_k^2\right] \\ &\quad + 16\Phi_k''\Phi_k - 9(\Phi_k')^2 - 9(\Phi_k''')^2\Big\}\Big|_0^1. \end{aligned} \tag{D.21}$$

For a cantilevered beam, the eigenfunctions are known to be

$$\Phi_m(\lambda_m\xi) = (\cosh\lambda_m\xi - \cos\lambda_m\xi) - \sigma_m(\sinh\lambda_m\xi - \sin\lambda_m\xi), \tag{D.22}$$

where the constants σ_m are defined as

$$\sigma_m = \frac{\cosh\lambda_m + \cos\lambda_m}{\sinh\lambda_m + \sin\lambda_m}, \tag{D.23}$$

and the eigenvalues λ_m are the roots of the transcendental equation

$$\cosh\lambda_m \cos\lambda_m + 1 = 0. \tag{D.24}$$

With the boundary conditions of a cantilevered beam,

$$\begin{aligned}
\Phi_m(\lambda_m\xi)\Big|_{\xi=0} &= 0, & \Phi_m(\lambda_m\xi)\Big|_{\xi=1} &= 2(-1)^{m+1}, \\
\Phi'_m(\lambda_m\xi)\Big|_{\xi=0} &= 0, & \Phi'_m(\lambda_m\xi)\Big|_{\xi=1} &= 2\sigma_m(-1)^{m+1}, \\
\Phi''_m(\lambda_m\xi)\Big|_{\xi=0} &= 2, & \Phi''_m(\lambda_m\xi)\Big|_{\xi=1} &= 0, \\
\Phi'''_m(\lambda_m\xi)\Big|_{\xi=0} &= -2\sigma_m, & \Phi'''_m(\lambda_m\xi)\Big|_{\xi=1} &= 0,
\end{aligned}$$

the integrals in (D.2)–(D.9) and (D.14)–(D.21) may now be evaluated. Finally, the integrals denoted by $a_{km}, \ldots, d_{km}$ and $\hat{a}_{km}, \ldots, \hat{d}_{km}$ in the beginning of this appendix can be inferred from the above–determined integrals and are found to be

$$a_{km} = \begin{cases} \frac{4}{(-1)^{k+m} + (\lambda_m/\lambda_k)^2} & \text{if } k \neq m, \\ 2 & \text{if } k = m; \end{cases}$$

$$b_{km} = \begin{cases} \frac{4\lambda_k\lambda_m}{\lambda_k^4 - \lambda_m^4}\left[(\lambda_k^3\sigma_m - \sigma_k\lambda_m^3)(-1)^{k+m} + (\lambda_k\lambda_m^2\sigma_m - \sigma_k\lambda_k^2\lambda_m)\right] & \text{if } k \neq m, \\ \lambda_m\sigma_m(2 + \lambda_m\sigma_m) & \text{if } k = m; \end{cases}$$

$$c_{km} = \begin{cases} \frac{4(\lambda_k\sigma_k - \lambda_m\sigma_m)}{(\lambda_k/\lambda_m)^2 - (-1)^{k+m}} & \text{if } k \neq m, \\ \lambda_m\sigma_m(2 - \lambda_m\sigma_m) & \text{if } k = m; \end{cases}$$

$$d_{km} = \begin{cases} 0 & \text{if } k \neq m, \\ -\lambda_m^4 & \text{if } k = m; \end{cases}$$

$$\hat{a}_{km} = \begin{cases} \frac{8\lambda_k\lambda_m\sigma_k\sigma_m}{\lambda_k^4 - \lambda_m^4}(-1)^{k+m} + \frac{16\lambda_k\lambda_m^3\sigma_k\sigma_m}{(\lambda_k^4 - \lambda_m^4)^2}\left[\lambda_m^2(-1)^{k+m} - \lambda_k^2\right] & \text{if } k \neq m, \\ \frac{1}{2\lambda_m^2}(\lambda_m^2 + 4\sigma_m^2) & \text{if } k = m; \end{cases}$$

$$\hat{b}_{km} = \begin{cases} \frac{4\lambda_k\lambda_m}{\lambda_k^4-\lambda_m^4}\left[(\lambda_k^3\sigma_m - \sigma_k\lambda_m^3)(-1)^{k+m} - 2\lambda_k\lambda_m\right] + \frac{16\lambda_k^2\lambda_m^4}{(\lambda_k^4-\lambda_m^4)^2}\left[\lambda_k^2(-1)^{k+m} - \lambda_m^2\right] & \text{if } k \neq m, \\ \frac{1}{2}\lambda_m\sigma_m(6+\lambda_m\sigma_m) - 2 & \text{if } k = m; \end{cases}$$

$$\hat{c}_{km} = \begin{cases} \frac{4\lambda_m^2}{\lambda_k^4-\lambda_m^4}\left[\lambda_k^2 + \lambda_m^2(\lambda_k\sigma_k - \lambda_m\sigma_m - 3)(-1)^{k+m}\right] + \frac{16\lambda_m^6}{(\lambda_k^4-\lambda_m^4)^2}\left[\lambda_k^2 - \lambda_m^2(-1)^{k+m}\right] & \text{if } k \neq m, \\ \frac{\lambda_m\sigma_m}{2}(2-\lambda_m\sigma_m) & \text{if } k = m; \end{cases}$$

$$\hat{d}_{km} = \begin{cases} \frac{4\lambda_k\lambda_m^3\sigma_k\sigma_m}{\lambda_k^4-\lambda_m^4}\left[\lambda_k^2 - 3\lambda_m^2(-1)^{k+m}\right] + \frac{16\lambda_k\lambda_m^7\sigma_k\sigma_m}{(\lambda_k^4-\lambda_m^4)^2}\left[\lambda_k^2 - \lambda_m^2(-1)^{k+m}\right] & \text{if } k \neq m, \\ -\frac{\lambda_m^4}{2} & \text{if } k = m. \end{cases}$$

Appendix E

Velocity Profiles and Turbulent Viscosity in Annuli

E.1 Velocity Profiles in annuli

When the flow in an annulus is laminar, the velocity profile therein can be determined analytically and is found to be

$$U(r) = 2U_a\left[\frac{b^2 - r^2 - 2r_m^2\ln(b/r)}{a^2 + b^2 - 2r_m^2}\right], \tag{E.1}$$

where U_a is the average flow velocity, defined as the ratio of the volume flow rate to the cross–sectional area of the annulus; r_m, denoting the radius at which $U(r_m)$ is maximum, is given by

$$r_m = \left\{\frac{b^2 - a^2}{2\ln(b/a)}\right\}^{1/2}. \tag{E.2}$$

Details of the derivation of (E.1) and (E.2) may be found in most text books of Fluid Mechanics (for example, Knudsen and Katz 1958).

On the contrary, when the flow is turbulent, the determination of $U(r)$ and r_m by analytical means is out of the question. With the turbulent velocity profiles obtained from a number of experiments, Knudsen and Katz (1958) showed that

$$U(r) = \begin{cases} 1.14U_a\left[\dfrac{r-a}{r_m - a}\right]^{0.102} & \text{for} \quad a \le r \le r_m, \\ 1.14U_a\left[\dfrac{b-r}{b - r_m}\right]^{0.142} & \text{for} \quad r_m \le r \le b; \end{cases} \tag{E.3}$$

nevertheless, they did not present any results on the variation of r_m with a/b, either implicitly or explicitly. A subsequently study by Brighton and Jones (1963), who devised a new method for measuring accurately r_m, gave extensive experimental measurements on r_m in addition to other quantities of their interest. For the present analysis, the relationships (E.3) are adopted with r_m determined from the multilinear representation of the experimental results reported by Brighton and Jones (1963).

Although there are indications that Equations (E.3) are not valid for Reynolds numbers below 10^4, these equations are currently believed to be the best approximations available to the velocity distributions in annuli with $2.3 \times 10^3 \leq \mathrm{Re} \leq 10^4$; moreover, since the main parameter of interest herein is the critical flow velocity with its corresponding Reynolds number ranging from 7.3×10^3 to 2.7×10^5, Equations (E.3) are perfectly adequate for most of the cases to be tested.

E.2 Turbulent Viscosity in Annuli

The distribution of the turbulent kinematic viscosity ν_t in a flow may be evaluated by a number of turbulence models currently known in the literature. A brief description of these models and their applications have been given by Rodi (1980). Since the velocity profile in an annulus is already given empirically [Equations (E.3)], a simple turbulence model like the mixing–length hypothesis proposed by Prandtl (1925) is deemed to be the most appropriate for the present theory.

It should be recalled that Prandtl's mixing–length hypothesis leads to

$$\nu_t = l^2 \left| \frac{\mathrm{d}U}{\mathrm{d}y} \right|, \tag{E.4}$$

where l is known as Prandtl's mixing length and y is the coordinate measured from the wall, along which the fluid passes in turbulent motion.

For the case of smooth pipes, experiments carried out by Nikuradse showed that the variation of l with y/R can be represented by the empirical relation (Schlichting 1968)

$$\frac{l}{R} = 0.14 - 0.08\left(1 - \frac{y}{R}\right)^2 - 0.06\left(1 - \frac{y}{R}\right)^4, \tag{E.5}$$

where R is the radius of the pipe.

Because of the absence of such a relation for annuli in the literature, Equation (E.5) will have to be adapted to annular flows. As $U(r_m)$ in an annulus corresponds to $U(0)$ in a pipe, Equation (E.5) will take on the following new forms for the flow in an annulus

$$\frac{l}{r_m - a} = 0.14 - 0.08\left[1 - \frac{r-a}{r_m - a}\right]^2 - 0.06\left[1 - \frac{r-a}{r_m - a}\right]^4 \qquad \text{for} \quad a \le r \le r_m, \tag{E.6}$$

and

$$\frac{l}{b - r_m} = 0.14 - 0.08\left[1 - \frac{b-r}{b - r_m}\right]^2 - 0.06\left[1 - \frac{b-r}{b - r_m}\right]^4 \qquad \text{for} \quad r_m \le r \le b. \tag{E.7}$$

As a comparison between the flow in a pipe and that in an annulus, the fluid–structure interface at the pipe surface is similar to that at the outer surface ($r = b$), but *not* at the inner surface ($r = a$), of the annulus; hence, the actual mixing length in the annular flow is closer to the approximation given by Equation (E.7) for $r_m \le r \le b$ than that given by Equation (E.6) for $a \le r \le r_m$.

The evaluation of $\mathrm{d}U/\mathrm{d}y$ in Equation (E.4) is rather straightforward with

$$\frac{\mathrm{d}U}{\mathrm{d}y} = \begin{cases} \dfrac{\mathrm{d}U}{\mathrm{d}(r-a)} = \dfrac{\mathrm{d}U}{\mathrm{d}r} & \text{for} \quad a \le r \le r_m, \\[2ex] \dfrac{\mathrm{d}U}{\mathrm{d}(b-r)} = -\dfrac{\mathrm{d}U}{\mathrm{d}r} & \text{for} \quad r_m \le r \le b, \end{cases} \tag{E.8}$$

where $\mathrm{d}U/\mathrm{d}r$ is obtained by directly differentiating Equations (E.3) with respect to r.

It is noted that, for the velocity distribution given by (E.3), $\mathrm{d}U/\mathrm{d}y$ is always positive because $\mathrm{d}U/\mathrm{d}r$ is positive for $a \le r \le r_m$ and negative for $r_m \le r \le b$; thus, the absolute signs in Equation (E.4) may be removed and the turbulent viscosity ν_t can now be rewritten in terms of (E.6)–(E.8) as

$$\nu_t(r) = \begin{cases} (r_m - a)^2\left\{\dfrac{l}{r_m - a}\right\}^2\left(\dfrac{\mathrm{d}U}{\mathrm{d}r}\right) & \text{for} \quad a \le r \le r_m, \\[2ex] -(b - r_m)^2\left\{\dfrac{l}{b - r_m}\right\}^2\left(\dfrac{\mathrm{d}U}{\mathrm{d}r}\right) & \text{for} \quad r_m \le r \le b. \end{cases} \tag{E.9}$$

Finally, it should be recalled that the total viscosity in the flow is the sum of the molecular and turbulent viscosities, namely

$$\nu(r) = \nu_m + \nu_t(r). \tag{E.10}$$

Appendix F

Finite–Difference Expressions for Derivatives

F.1 In a Uniform Grid

For a function $f(x)$ which is analytic in the neighbourhood of a point x, the forward Taylor series expansion about x gives

$$f(x+h) = f(x) + hf'(x) + \frac{h^2}{2!}f''(x) + \frac{h^3}{3!}f'''(x) + \frac{h^4}{4!}f^{iv}(x) + O(h^5), \qquad \text{(F.1)}$$

which is the basis for deriving difference approximations of any order of accuracy for derivatives of $f(x)$. Here, h is a small increment in x.

In this Appendix, it is desired to express $f'''(x)$ in the following form

$$h^3 f'''(x) = \lambda_1 f(x-h) + \lambda_2 f(x) + \lambda_3 f(x+h) + \lambda_4 f(x+2h) + \lambda_5 f(x+3h), \qquad \text{(F.2)}$$

where $\lambda_1, \ldots, \lambda_5$ are constants to be determined.

Now, expanding the right–hand side of Equation (F.2) in the form of (F.1) gives

$$\begin{aligned} h^3 f'''(x) &= \lambda_1\left[f(x) - hf'(x) + \frac{h^2}{2}f''(x) - \frac{h^3}{6}f'''(x) + \frac{h^4}{24}f^{iv}(x) + O(h^5)\right] \\ &+ \lambda_2 f(x) \\ &+ \lambda_3\left[f(x) + hf'(x) + \frac{h^2}{2}f''(x) + \frac{h^3}{6}f'''(x) + \frac{h^4}{24}f^{iv}(x) + O(h^5)\right] \\ &+ \lambda_4\left[f(x) + 2hf'(x) + 2h^2 f''(x) + \frac{4h^3}{3}f'''(x) + \frac{2h^4}{3}f^{iv}(x) + O(h^5)\right] \end{aligned}$$

$$+ \quad \lambda_5\left[f(x)+3hf'(x)+\frac{9h^2}{2}f''(x)+\frac{9h^3}{2}f'''(x)+\frac{27h^4}{8}f^{iv}(x) \quad +O(h^5)\right]. \qquad (F.3)$$

It should be noted that Equation (F.3) is an identity; thus, the coefficients of $f(x)$, $f'(x)$, ..., $f^{iv}(x)$ on the right-hand of (F.3) must identically equal the corresponding ones on the left-hand side, namely

$$\lambda_1+\lambda_2+\lambda_3+\lambda_4+\lambda_5 = 0, \qquad (F.4)$$

$$-\lambda_1+\lambda_3+2\lambda_4+3\lambda_5 = 0, \qquad (F.5)$$

$$\frac{1}{2}\lambda_1+\frac{1}{2}\lambda_3+2\lambda_4+\frac{9}{2}\lambda_5 = 0, \qquad (F.6)$$

$$-\frac{1}{6}\lambda_1+\frac{1}{6}\lambda_3+\frac{4}{3}\lambda_4+\frac{9}{2}\lambda_5 = 1, \qquad (F.7)$$

$$\frac{1}{24}\lambda_1+\frac{1}{24}\lambda_3+\frac{2}{3}\lambda_4+\frac{27}{8}\lambda_5 = 0. \qquad (F.8)$$

Equation (F.4)–(F.5) are five linear equations with five unknowns; the solution of these equations is found to be

$$\lambda_1=-\frac{3}{2}, \quad \lambda_2=5, \quad \lambda_3=-6, \quad \lambda_4=3, \quad \lambda_5=-\frac{1}{2}. \qquad (F.9)$$

Thus, Equation (F.2) may be rewritten as

$$h^3f'''(x) = -\frac{3}{2}f(x-h)+5f(x)-6f(x+h)+3f(x+2h)-\frac{1}{2}f(x+3h) \quad +O(h^5), \qquad (F.10)$$

or

$$\left(\frac{\partial^3 f}{\partial x^3}\right)_i = \frac{1}{2h^3}\left[-f_{i+3}+6f_{i+2}-12f_{i+1}+10f_i-3f_{i-1}\right] \quad +O(h^2). \qquad (F.11)$$

This is the forward difference representation introduced in (5.59). The backward difference representation in (5.60) can also be obtained from Equation (F.10) by replacing h by $-h$:

$$\left(\frac{\partial^3 f}{\partial x^3}\right)_i = \frac{1}{2h^3}\left[3f_{i+1}-10f_i+12f_{i-1}-6f_{i-2}+f_{i-3}\right] \quad +O(h^2). \qquad (F.12)$$

F.2 In a Non-Uniform Grid

F.2.1 Near a Flexible Wall

Figure 5.2 shows the local area near a flexible wall in the staggered grid. The aim of this section is to express $\left(\frac{\partial \mathcal{V}_\theta}{\partial \eta}\right)_{i,2}$ as a linear function of $(\mathcal{V}_\theta)_{i,F}$ which is the value of $\mathcal{V}_\theta$

at the wall, $(\mathcal{V}_\theta)_{i,2}$, and $(\mathcal{V}_\theta)_{i,3}$; in other words,

$$\left(\frac{\partial^2 \mathcal{V}_\theta}{\partial \eta^2}\right)_{i,2} = a_F(\mathcal{V}_\theta)_{i,F} + b_F(\mathcal{V}_\theta)_{i,2} + c_F(\mathcal{V}_\theta)_{i,3}, \tag{F.13}$$

where a_F, b_F, and c_F are constants which will be determined in the same way as was done in Section F.1. Therefore, all the terms on the right-hand side of Equation (F.13) are first expanded in Taylor series about η_2^z, giving

$$\begin{aligned}\left(\frac{\partial^2 \mathcal{V}_\theta}{\partial \eta^2}\right)_{i,2} &= a_F\left\{(\mathcal{V}_\theta)_{i,2} - \Delta\tilde{\eta}\left(\frac{\partial \mathcal{V}_\theta}{\partial \eta}\right)_{i,2} + \frac{(\Delta\tilde{\eta})^2}{2}\left(\frac{\partial^2 \mathcal{V}_\theta}{\partial \eta^2}\right)_{i,2} + O[(\Delta\tilde{\eta})^3]\right\} \\ &+ b_F(\mathcal{V}_\theta)_{i,2} \\ &+ c_F\left\{(\mathcal{V}_\theta)_{i,2} + \Delta\eta_3^z\left(\frac{\partial \mathcal{V}_\theta}{\partial \eta}\right)_{i,2} + \frac{(\Delta\eta_3^z)^2}{2}\left(\frac{\partial^2 \mathcal{V}_\theta}{\partial \eta^2}\right)_{i,2} + O[(\Delta\eta_3^z)^3]\right\}.\end{aligned} \tag{F.14}$$

where $\Delta\tilde{\eta} = \eta_2^z - \eta_1^r$ and $\Delta\eta_3^z = \eta_3^z - \eta_2^z$. Next, the coefficients of $(\mathcal{V}_\theta)_{i,2}$ and of its derivatives on one side of the identity (F.14) are equated to those on the other side, resulting in

$$a_F + b_F + c_F = 0, \tag{F.15}$$

$$-(\Delta\tilde{\eta})a_F + (\Delta\eta_3^z)c_F = 0, \tag{F.16}$$

$$\left[\frac{(\Delta\tilde{\eta})^2}{2}\right]a_F + \left[\frac{(\Delta\eta_3^z)^2}{2}\right]c_F = 1, \tag{F.17}$$

which constitute a system of three linear equations with three unknowns. The solution of (F.15)–(F.17) is found to be

$$a_F = \frac{2}{\Delta\tilde{\eta}(\Delta\tilde{\eta} + \Delta\eta_3^z)}, \quad b_F = -\frac{2}{\Delta\tilde{\eta}\Delta\eta_3^z}, \quad c_F = \frac{2}{\Delta\eta_3^z(\Delta\tilde{\eta} + \Delta\eta_3^z)}. \tag{F.18}$$

F.2.2 Near a Rigid Wall

Figure 5.2 also shows the local area near a rigid wall in the staggered grid. Here, it is desired to express

$$\left(\frac{\partial^2 \mathcal{V}_\theta}{\partial \eta^2}\right)_{i,j^*} = a_R(\mathcal{V}_\theta)_{i,j^*-1} + b_R(\mathcal{V}_\theta)_{i,j^*} + c_R(\mathcal{V}_\theta)_{i,R}, \tag{F.19}$$

where $j^* = (M-1)$; $(\mathcal{V}_\theta)_{i,R}$ is the value of $\mathcal{V}_\theta$ at the wall; a_R, b_R, and c_R are constants to be determined in the remainder of this section. The right-hand side of Equation (F.19) is now expanded in Taylor series about $\eta^{x}_{j^*}$ with $j^* = (M-1)$, namely

$$\left(\frac{\partial^2 \mathcal{V}_\theta}{\partial \eta^2}\right)_{i,j^*} = a_R\left\{(\mathcal{V}_\theta)_{i,j^*} - \Delta\eta^{x}_{j^*}\left(\frac{\partial \mathcal{V}_\theta}{\partial \eta}\right)_{i,j^*} + \frac{(\Delta\eta^{x}_{j^*})^2}{2}\left(\frac{\partial^2 \mathcal{V}_\theta}{\partial \eta^2}\right)_{i,j^*} + O[(\Delta\eta^{x}_{j^*})^3]\right\}$$

$$+ \; b_R(\mathcal{V}_\theta)_{i,j^*}$$

$$+ \; c_R\left\{(\mathcal{V}_\theta)_{i,j^*} + \Delta\bar{\eta}\left(\frac{\partial \mathcal{V}_\theta}{\partial \eta}\right)_{i,j^*} + \frac{(\Delta\bar{\eta})^2}{2}\left(\frac{\partial^2 \mathcal{V}_\theta}{\partial \eta^2}\right)_{i,j^*} + O[(\Delta\bar{\eta})^3]\right\}, \tag{F.20}$$

where $\Delta\bar{\eta} = \eta^{r}_{j^*} - \eta^{x}_{j^*}$ and $\Delta\eta^{x}_{j^*} = \eta^{x}_{j^*} - \eta^{x}_{j^*-1}$. Equating the corresponding coefficients of $\mathcal{V}_\theta$ and of its derivatives on the two sides of the identity (F.20) leads to

$$a_R + b_R + c_R = 0, \tag{F.21}$$

$$-(\Delta\eta^{x}_{j^*})a_R + (\Delta\bar{\eta})c_R = 0, \tag{F.22}$$

$$\left[\frac{(\Delta\eta^{x}_{j^*})^2}{2}\right]a_R + \left[\frac{(\Delta\bar{\eta})^2}{2}\right]c_R = 1, \tag{F.23}$$

which are three linear equations with three unknowns, hence admitting the solution

$$a_R = \frac{2}{\Delta\eta^{x}_{j^*}(\Delta\bar{\eta} + \Delta\eta^{x}_{j^*})}, \quad b_R = -\frac{2}{\Delta\bar{\eta}\Delta\eta^{x}_{j^*}}, \quad c_R = \frac{2}{\Delta\bar{\eta}(\Delta\bar{\eta} + \Delta\eta^{x}_{j^*})}. \tag{F.24}$$

It is noted that since $(\mathcal{V}_\theta)_{i,R} = 0$ at the rigid wall, Equation (F.19) may be rewritten as

$$\left(\frac{\partial^2 \mathcal{V}_\theta}{\partial \eta^2}\right)_{i,j^*} = a_R(\mathcal{V}_\theta)_{i,j^*-1} + b_R(\mathcal{V}_\theta)_{i,j^*} + O[(\Delta\eta^{x}_{j^*})^3, (\Delta\bar{\eta})^3]. \tag{F.25}$$

F.2.3 At the Flexible Wall

A difference expression for the gradient of $\mathcal{V}_\theta$ may be obtained in the same manner as was done in the last two sections, that is

$$\left(\frac{\partial \mathcal{V}_\theta}{\partial \eta}\right)_{i,F} = \breve{a}(\mathcal{V}_\theta)_{i,F} + \breve{b}(\mathcal{V}_\theta)_{i,2} + \breve{c}(\mathcal{V}_\theta)_{i,3}, \tag{F.26}$$

where the subscript F denotes the value of $\mathcal{V}_\theta$ at the flexible wall; $\breve{a}$, $\breve{b}$, and $\breve{c}$ are constants to be determined below. If the right-hand side of the above equation is expanded in Taylor series about η^{r}_1 (here, $\eta^{r}_1 = \varepsilon_i$),

$$\left(\frac{\partial \mathcal{V}_\theta}{\partial \eta}\right)_{i,F} = \breve{a}(\mathcal{V}_x)_{i,F} + \breve{b}\left\{(\mathcal{V}_\theta)_{i,F} + \Delta\tilde{\eta}\left(\frac{\partial \mathcal{V}_\theta}{\partial \eta}\right)_{i,F} + \frac{(\Delta\tilde{\eta})^2}{2}\left(\frac{\partial^2 \mathcal{V}_\theta}{\partial \eta^2}\right)_{i,F} + O[(\Delta\tilde{\eta})^3]\right\}$$

$$+ \; \breve{c}\left\{(\mathcal{V}_\theta)_{i,F} + \Delta\hat{\eta}\left(\frac{\partial \mathcal{V}_\theta}{\partial \eta}\right)_{i,F} + \frac{(\Delta\hat{\eta})^2}{2}\left(\frac{\partial^2 \mathcal{V}_\theta}{\partial \eta^2}\right)_{i,F} + O[(\Delta\hat{\eta})^3]\right\}, \tag{F.27}$$

with $\Delta\tilde{\eta} = \eta_2^x - \eta_1^r$ and $\Delta\hat{\eta} = \eta_3^x - \eta_1^r$, then

$$\begin{aligned} \breve{a} + \breve{b} + \breve{c} &= 0, && \text{(F.28)} \\ (\Delta\tilde{\eta})\breve{b} + (\Delta\hat{\eta})\breve{c} &= 1, && \text{(F.29)} \\ \left[\frac{(\Delta\tilde{\eta})^2}{2}\right]\breve{b} + \left[\frac{(\Delta\hat{\eta})^2}{2}\right]\breve{c} &= 0. && \text{(F.30)} \end{aligned}$$

The solution of the above equations is found to be

$$\breve{a} = -\frac{\Delta\tilde{\eta} + \Delta\hat{\eta}}{\Delta\tilde{\eta}\Delta\hat{\eta}}, \quad \breve{b} = \frac{\Delta\hat{\eta}}{\Delta\tilde{\eta}(\Delta\hat{\eta} - \Delta\tilde{\eta})}, \quad \breve{c} = -\frac{\Delta\tilde{\eta}}{\Delta\tilde{\eta}(\Delta\hat{\eta} - \Delta\tilde{\eta})}. \tag{F.31}$$

Similarly, for the gradient of $\mathcal{V}_r$,

$$\left(\frac{\partial \mathcal{V}_r}{\partial \eta}\right)_{i,F} = \bar{a}(\mathcal{V}_r)_{i,F} + \bar{b}(\mathcal{V}_r)_{i,2} + \bar{c}(\mathcal{V}_r)_{i,3}. \tag{F.32}$$

where the constants $\bar{a}$, $\bar{b}$, and $\bar{c}$ are also found by expanding the right-hand side of Equation (F.32) in Taylor series about η_1^r. It turns out that

$$\bar{a} = -\frac{\Delta\breve{\eta} + \Delta\eta_2^r}{\Delta\breve{\eta}\Delta\eta_2^r}, \quad \bar{b} = \frac{\Delta\breve{\eta}}{\Delta\eta_2^r(\Delta\breve{\eta} - \Delta\eta_2^r)}, \quad = -\frac{\Delta\eta_2^r}{\Delta\breve{\eta}(\Delta\breve{\eta} - \Delta\eta_2^r)}, \tag{F.33}$$

with $\Delta\eta_2^r = \eta_2^r - \eta_1^r$ and $\Delta\breve{\eta} = \eta_3^r - \eta_1^r$.

Appendix G

Evaluation of $\mathbf{S}_r$, $\mathbf{S}_\theta$, $\mathbf{S}_x$, $\mathbf{S}_\nabla$

In this appendix, the components of $\mathbf{S} = \{S_r \; S_\theta \; S_x \; S_\nabla\}^{\mathrm{T}}$ representing the right–hand side of Equations (5.107)–(5.110) will be evaluated. In all cases, only the final results will be presented with a detailed description of how they could be obtained, as their derivation is rather straightforward but very cumbersome. As S_r, S_θ, S_x, and S_∇ are associated with the r–, θ–, x–momentum equations, and the continuity equation, their expressions will be approximated about the points at which $\bar{v}_r$, $\bar{v}_\theta$, $\bar{v}_x$, and $\bar{p}$, respectively, are defined in the staggered grid. These components will be considered individually in the foregoing–listed order. It is recalled that

$$\mathbf{S} = \Delta\tau\Big[\mathbf{R} - (A_r + A_\theta + A_x)\mathbf{\Pi}^k\Big] = -\Delta\tau\left\{\begin{array}{c} \hat{v}_r^k + \alpha G_r(\hat{v}_r^k + \bar{v}_r^n, \hat{v}_\theta^k + \bar{v}_\theta^n, \hat{v}_x^k + \bar{v}_x^n, \hat{p}^k + \bar{p}^n) \\ \hat{v}_\theta^k + \alpha G_\theta(\hat{v}_r^k + \bar{v}_r^n, \hat{v}_\theta^k + \bar{v}_\theta^n, \hat{v}_x^k + \bar{v}_x^n, \hat{p}^k + \bar{p}^n) \\ \hat{v}_x^k + \alpha G_x(\hat{v}_r^k + \bar{v}_r^n, \hat{v}_\theta^k + \bar{v}_\theta^n, \hat{v}_x^k + \bar{v}_x^n, \hat{p}^k + \bar{p}^n) \\ (1/\beta)G_\nabla(\hat{v}_r^k, \hat{v}_\theta^k, \hat{v}_x^k) \end{array}\right\},$$

where G_r, G_θ, G_x and G_∇ were already defined in conjunction with Equations (5.80)–(5.83).

Thus, S_r may be written in full as

$$\begin{aligned} S_r \;=\; & -\Delta\tau\hat{v}_r^k - \frac{\alpha\Delta\tau}{L^2}\Bigg\{LU(\eta)\frac{\partial(\hat{v}_r^k + \bar{v}_r^n)}{\partial\xi} + L\frac{\partial(\hat{p}^k + \bar{p}^n)}{\partial\eta} - 2\left(\frac{\mathrm{d}\nu}{\mathrm{d}\eta}\right)\frac{\partial(\hat{v}_r^k + \bar{v}_r^n)}{\partial\eta} \\ & - \nu\left[\frac{\partial^2(\hat{v}_r^k + \bar{v}_r^n)}{\partial\xi^2} + \frac{1}{\eta}\frac{\partial}{\partial\eta}\left(\eta\frac{\partial(\hat{v}_r^k + \bar{v}_r^n)}{\partial\eta}\right) - \frac{1+n^2}{\eta^2}(\hat{v}_r^k + \bar{v}_r^n) - \frac{2n}{\eta^2}(\hat{v}_\theta^k + \bar{v}_\theta^n)\right]\Bigg\}. \qquad \text{(G.1)} \end{aligned}$$

In the present numerical procedure, in addition to the use of fully implicit schemes for the time derivatives, the backward differencing is applied to the convective terms (first derivatives with respect to ξ) and the central differencing to the diffusion terms (second derivatives with respect to ξ) in the momentum equations; the reason for doing so is to ensure numerical stability in the solution obtained. Since the grid is non-uniform in the η-direction with a finer grid near the walls (further discussions on the non-uniformity of the grid are given in Appendix H), derivatives of flow variables (v_r, v_θ, v_x and p) with respect to η require a special treatment which is presented in Appendix H. Once all the derivatives in Equation (G.1) have been substituted by appropriate finite-difference representations, it is found that, for $2 \le i \le (N+1)$ and $2 \le j \le (M-2)$,

$$
\begin{aligned}
(S_r)_{ij} \;=\; & -\Delta\tau(\hat{v}_r^k)_{i,j} + \frac{\alpha\Delta\tau}{L^2}\Bigg\{ \frac{1}{\Delta\eta_{j+1}^x}\left[\frac{\nu_j^r\eta_j^x}{\eta_j^r\Delta\eta_j^r} - 2(1-\mathrm{d}\eta_j^r)\left(\frac{\mathrm{d}\nu}{\mathrm{d}\eta}\right)_j^r\right](\hat{v}_r^k+\bar{v}_r^n)_{i,j-1} \\
& + \left[\frac{2(1-\mathrm{d}\eta_j^r-\mathrm{d}\eta_{j+1}^r)}{\Delta\eta_{j+1}^x}\left(\frac{\mathrm{d}\nu}{\mathrm{d}\eta}\right)_j^r - \frac{\nu_j^r}{\eta_j^r\Delta\eta_{j+1}^x}\left(\frac{\eta_{j+1}^x}{\Delta\eta_{j+1}^r}+\frac{\eta_j^x}{\Delta\eta_j^r}\right) - \frac{2\nu_j^r}{\Delta\xi^2} - \frac{LU(\eta_j^r)}{\Delta\xi}\right. \\
& \left. - \frac{\nu_j^r(1+n^2)}{(\eta_j^r)^2}\right](\hat{v}_r^k+\bar{v}_r^n)_{i,j} + \frac{1}{\Delta\eta_{j+1}^x}\left[2\mathrm{d}\eta_{j+1}^r\left(\frac{\mathrm{d}\nu}{\mathrm{d}\eta}\right)_j^r - \frac{\nu_j^r\eta_{j+1}^x}{\eta_j^r\Delta\eta_{j+1}^r}\right](\hat{v}_r^k+\bar{v}_r^n)_{i,j+1} \\
& + \left[\frac{\nu_j^r}{(\Delta\xi)^2} + \frac{LU(\eta_j^r)}{\Delta\xi}\right](\hat{v}_r^k+\bar{v}_r^n)_{i-1,j} + \frac{\nu_j^r}{\Delta\xi^2}(\hat{v}_r^k+\bar{v}_r^n)_{i+1,j} - \frac{2n\nu_j^r}{(\eta_j^r)^2}\Big[\mathrm{d}\eta_{j+1}^x(\hat{v}_\theta^k+\bar{v}_\theta^n)_{i,j+1} \\
& + (1-\mathrm{d}\eta_{j+1}^x)(\hat{v}_\theta^k+\bar{v}_\theta^n)_{i,j}\Big] + \frac{L}{\Delta\eta_{j+1}^x}\Big[(\hat{p}^k+\bar{p}^n)_{i,j} - (\hat{p}^k+\bar{p}^n)_{i,j+1}\Big]\Bigg\}\,,
\end{aligned}
$$

where $(\hat{v}_r^k)_{i,M-1} = 0$ for all pseudo-time levels k and $(\bar{v}_r^n)_{i,M-1} = 0$ for all physical-time levels n because the outer wall is rigid. It should be mentioned here that, in the above equation as well as in the subsequent equations, the following short-hand notation is used

$$
\nu_j^r \equiv \nu(\eta_j^r), \quad \nu_j^x \equiv \nu(\eta_j^x), \quad \left(\frac{\mathrm{d}\nu}{\mathrm{d}\eta}\right)_j^r \equiv \left.\frac{\mathrm{d}\nu}{\mathrm{d}\eta}\right|_{\eta=\eta_j^r}, \quad \left(\frac{\mathrm{d}\nu}{\mathrm{d}\eta}\right)_j^x \equiv \left.\frac{\mathrm{d}\nu}{\mathrm{d}\eta}\right|_{\eta=\eta_j^x}. \tag{G.2}
$$

Similarly, the expression for S_θ has the form

$$
\begin{aligned}
S_\theta \;=\; & -\Delta\tau\hat{v}_\theta^k - \frac{\alpha\Delta\tau}{L^2}\Bigg\{LU(\eta)\frac{\partial(\hat{v}_\theta^k+\bar{v}_\theta^n)}{\partial\xi} + \frac{Ln}{\eta}(\hat{p}^k+\bar{p}^n) - \left(\frac{\mathrm{d}\nu}{\mathrm{d}\eta}\right)\left[\frac{\partial(\hat{v}_\theta^k+\bar{v}_\theta^n)}{\partial\eta} - \frac{n}{\eta}(\hat{v}_r^k+\bar{v}_r^n)\right] \\
& - \nu\left[\frac{\partial^2(\hat{v}_\theta^k+\bar{v}_\theta^n)}{\partial\xi^2} + \frac{1}{\eta}\frac{\partial}{\partial\eta}\left(\eta\frac{\partial(\hat{v}_\theta^k+\bar{v}_\theta^n)}{\partial\eta}\right) - \frac{1+n^2}{\eta^2}(\hat{v}_\theta^k+\bar{v}_\theta^n) - \frac{2n}{\eta^2}(\hat{v}_r^k+\bar{v}_r^n)\right]\Bigg\}\,.
\end{aligned} \tag{G.3}
$$

Due to the relative location of $(v_\theta)_{i,j}$ in the grid, the discretized form of S_θ is different for different values of j, although it remains the same for all i in the computational domain, namely $2 \le i \le (N+1)$. Thus, for $3 \le j \le (M-2)$,

$$
\begin{aligned}
(S_\theta)_{ij} \;=\;& -\Delta\tau(\hat{v}_\theta^k)_{i,j} + \frac{\alpha\Delta\tau}{L^2}\Bigg\{\frac{1}{\Delta\eta_j^r}\left[\frac{\nu_j^x\eta_{j-1}^r}{\eta_j^x\Delta\eta_j^x} - (1-\mathrm{d}\eta_j^x)\left(\frac{\mathrm{d}\nu}{\mathrm{d}\eta}\right)_j^x\right](\hat{v}_\theta^k+\bar{v}_\theta^n)_{i,j-1} \\
&+ \left[\frac{1-\mathrm{d}\eta_j^x-\mathrm{d}\eta_{j+1}^x}{\Delta\eta_j^r}\left(\frac{\mathrm{d}\nu}{\mathrm{d}\eta}\right)_j^x - \frac{\nu_j^x}{\eta_j^x\Delta\eta_j^r}\left(\frac{\eta_j^r}{\Delta\eta_{j+1}^x}+\frac{\eta_{j-1}^r}{\Delta\eta_j^x}\right) - \frac{2\nu_j^x}{\Delta\xi^2} - \frac{LU(\eta_j^x)}{\Delta\xi}\right. \\
&\left. - \frac{\nu_j^x(1+n^2)}{(\eta_j^x)^2}\right](\hat{v}_\theta^k+\bar{v}_\theta^n)_{i,j} + \frac{1}{\Delta\eta_j^r}\left[\mathrm{d}\eta_{j+1}^x\left(\frac{\mathrm{d}\nu}{\mathrm{d}\eta}\right)_j^x + \frac{\nu_j^x\eta_j^r}{\eta_j^x\Delta\eta_{j+1}^x}\right](\hat{v}_\theta^k+\bar{v}_\theta^n)_{i,j+1} \\
&+ \left[\frac{\nu_j^x}{(\Delta\xi)^2}+\frac{LU(\eta_j^x)}{\Delta\xi}\right](\hat{v}_\theta^k+\bar{v}_\theta^n)_{i-1,j} + \frac{\nu_j^x}{\Delta\xi^2}(\hat{v}_\theta^k+\bar{v}_\theta^n)_{i+1,j} \\
&- \frac{n}{\eta_j^x}\left[\frac{2\nu_j^x}{\eta_j^x}+\left(\frac{\mathrm{d}\nu}{\mathrm{d}\eta}\right)_j^x\right]\left[\mathrm{d}\eta_j^r(\hat{v}_r^k+\bar{v}_r^n)_{i,j} + (1-\mathrm{d}\eta_j^r)(\hat{v}_r^k+\bar{v}_r^n)_{i,j-1}\right] + \left(\frac{Ln}{\eta_j^x}\right)(\hat{p}^k+\bar{p}^n)_{i,j}\Bigg\};
\end{aligned}
$$

for $j=2$, which is adjacent to the inner flexible wall,

$$
\begin{aligned}
(S_\theta)_{i,2} \;=\;& -\Delta\tau(\hat{v}_\theta^k)_{i,2} + \frac{\alpha\Delta\tau}{L^2}\Bigg\{\left[\nu_2^x\left(a_F - \frac{1}{\eta_2^x\Delta\eta_2^r}\right) - \frac{1}{\Delta\eta_2^r}\left(\frac{\mathrm{d}\nu}{\mathrm{d}\eta}\right)_2^x\right](\hat{v}_\theta^k+\bar{v}_\theta^n)_{i,w} \\
&+ \left[\nu_2^x\left(b_F + \frac{1-\mathrm{d}\eta_3^x}{\eta_2^x\Delta\eta_2^r}\right) + \frac{1-\mathrm{d}\eta_3^x}{\Delta\eta_2^r}\left(\frac{\mathrm{d}\nu}{\mathrm{d}\eta}\right)_2^x - \frac{2\nu_2^x}{(\Delta\xi)^2} - \frac{LU(\eta_2^x)}{\Delta\xi} - \frac{\nu_2^x(1+n^2)}{(\eta_2^x)^2}\right](\hat{v}_\theta^k+\bar{v}_\theta^n)_{i,2} \\
&+ \left[\nu_2^x\left(c_F + \frac{\mathrm{d}\eta_3^x}{\eta_2^x\Delta\eta_2^r}\right) + \frac{\mathrm{d}\eta_3^x}{\Delta\eta_2^r}\left(\frac{\mathrm{d}\nu}{\mathrm{d}\eta}\right)_2^x\right](\hat{v}_\theta^k+\bar{v}_\theta^n)_{i,3} + \left[\frac{\nu_2^x}{(\Delta\xi)^2}+\frac{LU(\eta_2^x)}{\Delta\xi}\right](\hat{v}_\theta^k+\bar{v}_\theta^n)_{i-1,2} \\
&+ \frac{\nu_2^x}{(\Delta\xi)^2}(\hat{v}_\theta^k+\bar{v}_\theta^n)_{i+1,2} - \frac{n}{\eta_2^x}\left[\frac{2\nu_2^x}{\eta_2^x}+\left(\frac{\mathrm{d}\nu}{\mathrm{d}\eta}\right)_2^x\right]\left[\mathrm{d}\eta_2^r(\hat{v}_r^k+\bar{v}_r^n)_{i,2} + (1-\mathrm{d}\eta_2^r)(\hat{v}_r^k+\bar{v}_r^n)_{i,w}\right] \\
&+ \left(\frac{Ln}{\eta_2^x}\right)(\hat{p}^k+\bar{p}^n)_{i,2}\Bigg\};
\end{aligned}
$$

for $j = j^* = (M-1)$, which is adjacent to the outer rigid wall,

$$
\begin{aligned}
(S_\theta)_{i,j^*} \;=\;& -\Delta\tau(\hat{v}_\theta^k)_{i,j^*} + \frac{\alpha\Delta\tau}{L^2}\Bigg\{\left[\nu_{j^*}^x\left(a_R - \frac{1-\mathrm{d}\eta_{j^*}^x}{\eta_{j^*}^x\Delta\eta_{j^*}^r}\right) - \frac{1-\mathrm{d}\eta_{j^*}^x}{\Delta\eta_{j^*}^r}\left(\frac{\mathrm{d}\nu}{\mathrm{d}\eta}\right)_{j^*}^x\right](\hat{v}_\theta^k+\bar{v}_\theta^n)_{i,j^*-1} \\
&+ \left[\nu_{j^*}^x\left(b_R - \frac{\mathrm{d}\eta_{j^*}^x}{\eta_{j^*}^x\Delta\eta_{j^*}^r}\right) - \frac{\mathrm{d}\eta_{j^*}^x}{\Delta\eta_{j^*}^r}\left(\frac{\mathrm{d}\nu}{\mathrm{d}\eta}\right)_{j^*}^x - \frac{2\nu_{j^*}^x}{(\Delta\xi)^2} - \frac{LU(\eta_{j^*}^x)}{\Delta\xi} - \frac{\nu_{j^*}^x(1+n^2)}{(\eta_{j^*}^x)^2}\right](\hat{v}_\theta^k+\bar{v}_\theta^n)_{i,j^*} \\
&+ \left[\frac{\nu_{j^*}^x}{(\Delta\xi)^2}+\frac{LU(\eta_{j^*}^x)}{\Delta\xi}\right](\hat{v}_\theta^k+\bar{v}_\theta^n)_{i-1,j^*} + \frac{\nu_{j^*}^x}{(\Delta\xi)^2}(\hat{v}_\theta^k+\bar{v}_\theta^n)_{i+1,j^*} \\
&- \frac{n(1-\mathrm{d}\eta_{j^*}^r)}{\eta_{j^*}^x}\left[\frac{2\nu_{j^*}^x}{\eta_{j^*}^x}+\left(\frac{\mathrm{d}\nu}{\mathrm{d}\eta}\right)_{j^*}^x\right](\hat{v}_r^k+\bar{v}_r^n)_{i,j^*-1} + \left(\frac{Ln}{\eta_{j^*}^x}\right)(\hat{p}^k+\bar{p}^n)_{i,j^*}\Bigg\}.
\end{aligned}
$$

The expression for S_x has the form

$$
\begin{aligned}
S_x \;=\;& -\Delta\tau\hat{v}_x^k - \frac{\alpha\Delta\tau}{L^2}\Bigg\{LU(\eta)\frac{\partial(\hat{v}_x^k+\bar{v}_x^n)}{\partial\xi} + L\frac{\partial(\hat{p}^k+\bar{p}^n)}{\partial\xi} - \left(\frac{\mathrm{d}\nu}{\mathrm{d}\eta}\right)\left[\frac{\partial(\hat{v}_x^k+\bar{v}_x^n)}{\partial\eta}+\frac{\partial(\hat{v}_r^k+\bar{v}_r^n)}{\partial\xi}\right] \\
&+ L\left(\frac{\mathrm{d}U}{\mathrm{d}\eta}\right)(\hat{v}_r^k+\bar{v}_r^n) - \nu\left[\frac{\partial^2(\hat{v}_x^k+\bar{v}_x^n)}{\partial\xi^2} + \frac{1}{\eta}\frac{\partial}{\partial\eta}\left(\eta\frac{\partial(\hat{v}_x^k+\bar{v}_x^n)}{\partial\eta}\right) - \frac{n^2}{\eta^2}(\hat{v}_x^k+\bar{v}_x^n)\right]\Bigg\}. \qquad \text{(G.4)}
\end{aligned}
$$

Like S_θ, S_x does not vary with i in the computational domain, here $1 \leq i \leq N$. Thus, for $3 \leq j \leq (M-2)$,

$$
\begin{aligned}
(S_x)_{i,j} \;=\; & -\Delta\tau(\hat{v}_x^k)_{i,j} + \frac{\alpha\Delta\tau}{L^2}\Bigg\{\frac{1}{\Delta\eta_j^r}\Bigg[\frac{\nu_j^x\eta_{j-1}^r}{\eta_j^x\Delta\eta_j^x} - (1-\mathrm{d}\eta_j^x)\Big(\frac{\mathrm{d}\nu}{\mathrm{d}\eta}\Big)_j^x\Bigg](\hat{v}_x^k+\bar{v}_x^n)_{i,j-1} \\
& + \Bigg[\frac{1-\mathrm{d}\eta_j^x-\mathrm{d}\eta_{j+1}^x}{\Delta\eta_j^r}\Big(\frac{\mathrm{d}\nu}{\mathrm{d}\eta}\Big)_j^x - \frac{\nu_j^x}{\eta_j^x\Delta\eta_j^r}\Big(\frac{\eta_j^r}{\Delta\eta_{j+1}^x}+\frac{\eta_{j-1}^r}{\Delta\eta_j^x}\Big) - \frac{2\eta_j^x}{(\Delta\xi)^2} - \frac{LU(\eta_j^x)}{\Delta\xi} \\
& - \frac{\nu_j^x n^2}{(\eta_j^x)^2}\Bigg](\hat{v}_x^k+\bar{v}_x^n)_{i,j} + \frac{1}{\Delta\eta_j^r}\Bigg[\mathrm{d}\eta_{j+1}^x\Big(\frac{\mathrm{d}\nu}{\mathrm{d}\eta}\Big)_j^x + \frac{\nu_j^x\eta_j^r}{\eta_j^x\Delta\eta_{j+1}^x}\Bigg](\hat{v}_x^k+\bar{v}_x^n)_{i,j+1} \\
& + \Bigg[\frac{\nu_j^x}{(\Delta\xi)^2} + \frac{LU(\eta_j^x)}{\Delta\xi}\Bigg](\hat{v}_x^k+\bar{v}_x^n)_{i-1,j} + \frac{\nu_j^x}{(\Delta\xi)^2}(\hat{v}_x^k+\bar{v}_x^n)_{i+1,j} \\
& - \Bigg[\frac{1}{\Delta\xi}\Big(\frac{\mathrm{d}\nu}{\mathrm{d}\eta}\Big)_j^x + \frac{L}{2}\Big(\frac{\mathrm{d}U}{\mathrm{d}\eta}\Big)_j^x\Bigg]\Big[\mathrm{d}\eta_j^r(\hat{v}_r^k+\bar{v}_r^n)_{i,j} + (1-\mathrm{d}\eta_j^r)(\hat{v}_r^k+\bar{v}_r^n)_{i,j-1}\Big] \\
& + \Bigg[\frac{1}{\Delta\xi}\Big(\frac{\mathrm{d}\nu}{\mathrm{d}\eta}\Big)_j^x - \frac{L}{2}\Big(\frac{\mathrm{d}U}{\mathrm{d}\eta}\Big)_j^x\Bigg]\Big[(1-\mathrm{d}\eta_j^r)(\hat{v}_r^k+\bar{v}_r^n)_{i+1,j-1} + \mathrm{d}\eta_j^r(\hat{v}_r^k+\bar{v}_r^n)_{i+1,j}\Big] \\
& + \frac{L}{\Delta\xi}\Big[(\hat{p}^k+\bar{p}^n)_{i,j} - (\hat{p}^k+\bar{p}^n)_{i+1,j}\Big]\Bigg\};
\end{aligned}
$$

for $j = 2$,

$$
\begin{aligned}
(S_x)_{i,2} \;=\; & -\Delta\tau(\hat{v}_x^k)_{i,2} + \frac{\alpha\Delta\tau}{L^2}\Bigg\{\Bigg[\nu_2^x\Big(a_F - \frac{1}{\eta_2^x\Delta\eta_2^r}\Big) - \frac{1}{\Delta\eta_2^r}\Big(\frac{\mathrm{d}\nu}{\mathrm{d}\eta}\Big)_2^x\Bigg](\hat{v}_x^k+\bar{v}_x^n)_{i,w} \\
& + \Bigg[\frac{1-\mathrm{d}\eta_3^x}{\Delta\eta_2^r}\Big(\frac{\mathrm{d}\nu}{\mathrm{d}\eta}\Big)_2^x + \nu_2^x\Big(b_F + \frac{1-\mathrm{d}\eta_3^x}{\eta_2^x\Delta\eta_2^r}\Big) - \frac{2\nu_2^x}{(\Delta\xi)^2} - \frac{LU(\eta_2^x)}{\Delta\xi} - \frac{\nu_2^x n^2}{(\eta_2^x)^2}\Bigg](\hat{v}_x^k+\bar{v}_x^n)_{i,2} \\
& + \Bigg[\frac{\mathrm{d}\eta_3^x}{\Delta\eta_2^r}\Big(\frac{\mathrm{d}\nu}{\mathrm{d}\eta}\Big)_2^x + \nu_2^x\Big(c_F + \frac{\mathrm{d}\eta_3^x}{\eta_2^x\Delta\eta_2^r}\Big)\Bigg](\hat{v}_x^k+\bar{v}_x^n)_{i,3} + \Bigg[\frac{\nu_2^x}{(\Delta\xi)^2} + \frac{LU(\eta_2^x)}{\Delta\xi}\Bigg](\hat{v}_x^k+\bar{v}_x^n)_{i-1,2} \\
& + \frac{\nu_2^x}{(\Delta\xi)^2}(\hat{v}_x^k+\bar{v}_x^n)_{i+1,2} - \Bigg[\frac{1}{\Delta\xi}\Big(\frac{\mathrm{d}\nu}{\mathrm{d}\eta}\Big)_2^x + \frac{L}{2}\Big(\frac{\mathrm{d}U}{\mathrm{d}\eta}\Big)_2^x\Bigg]\Big[\mathrm{d}\eta_2^r(\hat{v}_r^k+\bar{v}_r^n)_{i,2} + (1-\mathrm{d}\eta_2^r)(\hat{v}_r^k+\bar{v}_r^n)_{i,w}\Big] \\
& + \Bigg[\frac{1}{\Delta\xi}\Big(\frac{\mathrm{d}\nu}{\mathrm{d}\eta}\Big)_2^x - \frac{L}{2}\Big(\frac{\mathrm{d}U}{\mathrm{d}\eta}\Big)_2^x\Bigg]\Big[(1-\mathrm{d}\eta_2^r)(\hat{v}_r^k+\bar{v}_r^n)_{i+1,w} + \mathrm{d}\eta_2^r(\hat{v}_r^k+\bar{v}_r^n)_{i+1,2}\Big] \\
& + \frac{L}{\Delta\xi}\Big[(\hat{p}^k+\bar{p}^n)_{i,2} - (\hat{p}^k+\bar{p}^n)_{i+1,2}\Big]\Bigg\};
\end{aligned}
$$

for $j = j^* = (M-1)$,

$$
\begin{aligned}
(S_x)_{i,j^*} \;=\; & -\Delta\tau(\hat{v}_x^k)_{i,j^*} + \frac{\alpha\Delta\tau}{L^2}\Bigg\{\Bigg[\nu_{j^*}^x\Big(a_R - \frac{1-\mathrm{d}\eta_{j^*}^x}{\eta_{j^*}^x\Delta\eta_{j^*}^r}\Big) - \frac{1-\mathrm{d}\eta_{j^*}^x}{\Delta\eta_{j^*}^r}\Big(\frac{\mathrm{d}\nu}{\mathrm{d}\eta}\Big)_{j^*}^x\Bigg](\hat{v}_x^k+\bar{v}_x^n)_{i,j^*-1} \\
& + \Bigg[\nu_{j^*}^x\Big(b_R - \frac{\mathrm{d}\eta_{j^*}^x}{\eta_{j^*}^x\Delta\eta_{j^*}^r}\Big) - \frac{\mathrm{d}\eta_{j^*}^x}{\Delta\eta_{j^*}^r}\Big(\frac{\mathrm{d}\nu}{\mathrm{d}\eta}\Big)_{j^*}^x - \frac{2\nu_{j^*}^x}{(\Delta\xi)^2} - \frac{LU(\eta_{j^*}^x)}{\Delta\xi} - \frac{\nu_{j^*}^x n^2}{(\eta_{j^*}^x)^2}\Bigg](\hat{v}_x^k+\bar{v}_x^n)_{i,j^*}
\end{aligned}
$$

$$+\left[\frac{\nu^x_{j^*}}{(\Delta\xi)^2}+\frac{LU(\eta^x_{j^*})}{\Delta\xi}\right](\hat{v}^k_x+\bar{v}^n_x)_{i-1,j^*}+\frac{\nu^x_{j^*}}{(\Delta\xi)^2}(\hat{v}^k_x+\bar{v}^n_x)_{i+1,j^*}-(1-\mathrm{d}\eta^r_{j^*})\left[\frac{1}{\Delta\xi}\left(\frac{\mathrm{d}\nu}{\mathrm{d}\eta}\right)^x_{j^*}\right.$$

$$\left.+\frac{L}{2}\left(\frac{\mathrm{d}U}{\mathrm{d}\eta}\right)^x_{j^*}\right](\hat{v}^k_r+\bar{v}^n_r)_{i,j^*-1}+(1-\mathrm{d}\eta^r_{j^*})\left[\frac{1}{\Delta\xi}\left(\frac{\mathrm{d}\nu}{\mathrm{d}\eta}\right)^x_{j^*}-\frac{L}{2}\left(\frac{\mathrm{d}U}{\mathrm{d}\eta}\right)^x_{j^*}\right](\hat{v}^k_r+\bar{v}^n_r)_{i+1,j^*-1}$$

$$\left.+\frac{L}{\Delta\xi}\left[(\hat{p}^k+\bar{p}^n)_{i,j^*}-(\hat{p}^k+\bar{p}^n)_{i+1,j^*}\right]\right\}.$$

Finally, the expression for S_∇ has the form

$$S_\nabla=-\frac{\Delta\tau}{L\beta}\left\{\frac{1}{\eta}\frac{\partial}{\partial\eta}\left(\eta\hat{v}^k_r\right)+\left(\frac{n}{\eta}\right)\hat{v}^k_\theta+\frac{\partial\hat{v}^k_x}{\partial\xi}\right\}. \tag{G.5}$$

For $2\le i\le(N+1)$ and $2\le j\le(M-1)$,

$$(S_\nabla)_{i,j}=-\frac{\Delta\tau}{L\beta}\left\{\frac{1}{\eta^x_j\Delta\eta^r_j}\left[\eta^r_j(\hat{v}^k_r)_{i,j}-\eta^r_{j-1}(\hat{v}^k_r)_{i,j-1}\right]+\left(\frac{n}{\eta^x_j}\right)(\hat{v}^k_\theta)_{i,j}+\frac{1}{\Delta\xi}\left[(\hat{v}^k_x)_{i,j}-(\hat{v}^k_x)_{i-1,j}\right]\right\}.$$

Appendix H

Evaluation of Derivatives in a Non–Uniform Staggered Grid

H.1 Generation of a Staggered Grid

As was mentioned in Section 5.2.1, the problem under consideration involves an axisymmetric viscous flow inside the annular region bounded by an outer rigid cylinder and an inner flexible cylindrical shell as shown in Figure 5.1. As a result of the viscous effect of the fluid, flow variables would undergo rapid variations near the physical boundaries (cylinder walls); thus, to capture such variations in the analysis requires a larger number of grid points in the vicinity of the boundaries. An obvious choice here is to employ a two–sided stretching function to generate the grid points in the η–direction. Although quite a few functions may be used for this purpose, the hyperbolic tangent function has been demonstrated to be the best one based on a number of important numerical criteria (Vinokur 1983); therefore, it will be adopted in the present work.

If M denotes the number of unequal intervals into which the nondimensionalized annular gap $(\varepsilon_o - \varepsilon_i)$ is discretized and η_j is the nondimensionalized radial coordinate of a grid point j such that $0 \leq j \leq M$, then the hyperbolic tangent stretching function gives

$$\eta_j \;=\; \varepsilon_i + \left(\frac{\varepsilon_o - \varepsilon_i}{2}\right)\left\{1 + \frac{\tanh\left[\gamma_s\left(j/M - 1/2\right)\right]}{\tanh\left(\gamma_s/2\right)}\right\}, \tag{H.1}$$

where γ_s is a parameter that controls the amount of stretching; the grid becomes uniform as γ_s approaches zero. It is seen from Equation (H.1) that η_0 and η_M are the coordinates of the grid points on the outer surface of the shell and on the inner surface of the rigid cylinder, respectively.

H.2 Flow Variables in the Staggered Grid

The staggered grid was first used by Harlow and Welch (1965) and has proved to have significant advantages over the conventional grid (Patankar 1980).

The idea here is to define a different grid point for each velocity component. For 2–D flow problems, the two velocity components are located either midway between the pressure points if the grid is uniform, or slightly off the midpoint if the grid is non-uniform. For the axisymmetric flow being considered, only two independent variables are needed; nevertheless, there is now a third circumferential velocity component $\mathcal{V}_\theta$ in addition to $\mathcal{V}_x$ and $\mathcal{V}_r$, which may be regarded as being equivalent to the horizontal and vertical velocity components, respectively, in the 2–D problem (the calligraphic letter $\mathcal{V}$ here stands for either $\hat{v}$ or $\bar{v}$ used in Chapter 5; a similar interpretation should also be made for $\mathcal{P}$). One convenient way is to locate $\mathcal{V}_\theta$ at the pressure point, as shown in Figure 5.2. Since the flow variables are defined at different locations, the designation (i, j) in fact identifies a cluster of three distinct spatial locations as indicated by the L–shaped enclosure in Figure 5.2. In this particular staggered grid, $(\mathcal{V}_r)_{i,j}$ is located above $(\mathcal{P})_{i,j}$ while $(\mathcal{V}_x)_{i,j}$ is to the right of $(\mathcal{P})_{i,j}$.

H.3 Evaluation of Derivatives in a Stretched Grid

H.3.1 General Remarks

It is important to mention that the mesh in Figure 5.2 is *uniform* in the ξ–direction but *stretched* in the η–direction, although the mesh was drawn uniform in both directions for the sake of clarity and simplicity. Since finite–difference representations of derivatives for a uniform grid have been well established, the following sections are concerned only with derivatives of dependent variables in a non–uniform grid (η–direction).

In the staggered grid, the $r-$, $\theta-$, and $x-$momentum equations are approximated about the points at which $\mathcal{V}_r$, $\mathcal{V}_\theta$, and $\mathcal{V}_x$, respectively, are defined, whereas the continuity equation is approximated about the point at which $\mathcal{P}$ is defined. One traditional method of evaluating derivatives in a non–uniform grid is to map the grid onto a uniform one and then, by means of the chain rule, substitute central difference expressions for the resulting derivatives; for instance, if f is a dependent variable in a stretched grid with the coordinate η, and $\hat{\eta}$ is the coordinate of a new uniform grid, then $(\partial f/\partial\eta)$ will be approximated as follows

$$\left(\frac{\partial f}{\partial \eta}\right)_j = \frac{(\partial f/\partial\hat{\eta})_j}{(\partial\eta/\partial\hat{\eta})_j} = \frac{(f_{j+1}-f_{j-1})/2\Delta\hat{\eta}}{(\eta_{j+1}-\eta_{j-1})/2\Delta\hat{\eta}} = \frac{f_{j+1}-f_{j-1}}{\eta_{j+1}-\eta_{j-1}}. \tag{H.2}$$

In the staggered grid, a better approximation than (H.2) can be made for $(\partial f/\partial\eta)$, namely

$$\left(\frac{\partial f}{\partial \eta}\right)_j = \frac{f_{j+\frac{1}{2}}-f_{j-\frac{1}{2}}}{\eta_{j+\frac{1}{2}}-\eta_{j-\frac{1}{2}}}, \tag{H.3}$$

where $f_{j+\frac{1}{2}}$ and $f_{j-\frac{1}{2}}$ are the values of f at the two spatial locations adjacent to the one at which f_j is defined. Equation (H.3) is the basis for all derivations in the following sections.

H.3.2 Grid Points far from Physical Boundaries

H.3.2.1 Location of $(\mathcal{V}_r)_{i,j}$

Appearing in the r–momentum equation are derivatives of $\mathcal{V}_r$ and of $\mathcal{P}$ (with respect to η), which are approximated at the location of $(\mathcal{V}_r)_{i,j}$ in the staggered grid. Based on Equation (H.3),

$$\left(\frac{\partial \mathcal{V}_r}{\partial \eta}\right)_{i,j} = \frac{(\mathcal{V}_r)_{i,j+\frac{1}{2}}-(\mathcal{V}_r)_{i,j-\frac{1}{2}}}{\eta^r_{j+\frac{1}{2}}-\eta^r_{j-\frac{1}{2}}} = \frac{(\mathcal{V}_r)_{i,j+\frac{1}{2}}-(\mathcal{V}_r)_{i,j-\frac{1}{2}}}{\eta^x_{j+1}-\eta^x_j}, \tag{H.4}$$

where $(\mathcal{V}_r)_{i,j+\frac{1}{2}}$ and $(\mathcal{V}_r)_{i,j-\frac{1}{2}}$ are the values of $\mathcal{V}_r$ at the locations of $(\mathcal{P})_{i,j+1}$ and $(\mathcal{P})_{i,j}$, respectively; η^r_j and η^x_j denote the η–coordinates of $(\mathcal{V}_r)_{i,j}$ and $(\mathcal{V}_x, \mathcal{V}_\theta, \mathcal{P})_{i,j}$, respectively. $(\mathcal{V}_r)_{i,j-\frac{1}{2}}$ is interpolated between $(\mathcal{V}_r)_{i,j-1}$ and $(\mathcal{V}_r)_{i,j}$ as follows

$$(\mathcal{V}_r)_{i,j-\frac{1}{2}} = (\mathcal{V}_r)_{i,j-1} + \frac{(\mathcal{V}_r)_{i,j}-(\mathcal{V}_r)_{i,j-1}}{\eta^r_j-\eta^r_{j-1}}\left(\eta^x_j-\eta^r_{j-1}\right). \tag{H.5}$$

Here, it is convenient to introduce the following short–hand writing notation

$$\Delta\eta_j^r = \eta_j^r - \eta_{j-1}^r, \quad \Delta\eta_j^z = \eta_j^z - \eta_{j-1}^z, \quad \mathrm{d}\eta_j^r = \frac{\eta_j^z - \eta_{j-1}^r}{\Delta\eta_j^r}, \quad \mathrm{d}\eta_j^z = \frac{\eta_{j-1}^r - \eta_{j-1}^z}{\Delta\eta_j^z}, \tag{H.6}$$

in terms of which Equation (H.5) may be rewritten as

$$(\mathcal{V}_r)_{i,j-\frac{1}{2}} = \mathrm{d}\eta_j^r(\mathcal{V}_r)_{i,j} + (1 - \mathrm{d}\eta_j^r)(\mathcal{V}_r)_{i,j-1}. \tag{H.7}$$

The expression for $(\mathcal{V}_r)_{i,j+\frac{1}{2}}$ can be either derived in the same manner or obtained from Equation (H.5) by replacing the subscript j by $j+1$, namely

$$(\mathcal{V}_r)_{i,j+\frac{1}{2}} = \mathrm{d}\eta_{j+1}^r(\mathcal{V}_r)_{i,j+1} + (1 - \mathrm{d}\eta_{j+1}^r)(\mathcal{V}_r)_{i,j}. \tag{H.8}$$

The results in (H.7) and (H.8) are now substituted into Equation (H.4), yielding

$$\left(\frac{\partial \mathcal{V}_r}{\partial \eta}\right)_{i,j} = \frac{1}{\Delta\eta_{j+1}^z}\Big[\mathrm{d}\eta_{j+1}^r(\mathcal{V}_r)_{i,j+1} + (1 - \mathrm{d}\eta_j^r - \mathrm{d}\eta_{j+1}^r)(\mathcal{V}_r)_{i,j} - (1 - \mathrm{d}\eta_j^r)(\mathcal{V}_r)_{i,j-1}\Big]. \tag{H.9}$$

Similarly, for the second derivative of $\mathcal{V}_r$, Equation (H.3) gives

$$\begin{aligned}
\left[\frac{\partial}{\partial \eta}\left(\eta\frac{\partial \mathcal{V}_r}{\partial \eta}\right)\right]_{i,j} &= \frac{1}{\eta_{j+\frac{1}{2}}^r - \eta_{j-\frac{1}{2}}^r}\left\{\eta_{j+\frac{1}{2}}^r\left(\frac{\partial \mathcal{V}_r}{\partial \eta}\right)_{i,j+\frac{1}{2}} - \eta_{j-\frac{1}{2}}^r\left(\frac{\partial \mathcal{V}_r}{\partial \eta}\right)_{i,j-\frac{1}{2}}\right\} \\
&= \frac{1}{\eta_{j+1}^z - \eta_j^z}\left\{\eta_{j+1}^z\frac{(\mathcal{V}_r)_{i,j+1} - (\mathcal{V}_r)_{i,j}}{\eta_{j+1}^r - \eta_j^r} - \eta_j^z\frac{(\mathcal{V}_r)_{i,j} - (\mathcal{V}_r)_{i,j-1}}{\eta_j^r - \eta_{j-1}^r}\right\} \\
&= \frac{1}{\Delta\eta_{j+1}^z}\left\{\frac{\eta_{j+1}^z}{\Delta\eta_{j+1}^r}(\mathcal{V}_r)_{i,j+1} - \left[\frac{\eta_{j+1}^z}{\Delta\eta_{j+1}^r} + \frac{\eta_j^z}{\Delta\eta_j^r}\right](\mathcal{V}_r)_{i,j} + \frac{\eta_j^z}{\Delta\eta_j^r}(\mathcal{V}_r)_{i,j-1}\right\}.
\end{aligned} \tag{H.10}$$

The last derivative to be approximated at the $(\mathcal{V}_r)_{i,j}$ grid point is that of $\mathcal{P}$,

$$\left(\frac{\partial \mathcal{P}}{\partial \eta}\right)_{i,j} = \frac{(\mathcal{P})_{i,j+1} - (\mathcal{P})_{i,j}}{\eta_{j+1}^z - \eta_j^z} = \frac{1}{\Delta\eta_{j+1}^z}\Big[(\mathcal{P})_{i,j+1} - (\mathcal{P})_{i,j}\Big]. \tag{H.11}$$

H.3.2.2 Location of $(\mathcal{V}_\theta)_{i,j}$

In the θ–momentum equation, only $\mathcal{V}_\theta$ has derivatives which are approximated at the $(\mathcal{V}_\theta)_{i,j}$ grid point. With the same procedure as was carried out in the last section, it is found that

$$\left(\frac{\partial \mathcal{V}_\theta}{\partial \eta}\right)_{i,j} = \frac{1}{\Delta\eta_j^r}\Big[\mathrm{d}\eta_{j+1}^z(\mathcal{V}_\theta)_{i,j+1} + (1 - \mathrm{d}\eta_j^z - \mathrm{d}\eta_{j+1}^z)(\mathcal{V}_\theta)_{i,j} - (1 - \mathrm{d}\eta_j^z)(\mathcal{V}_\theta)_{i,j-1}\Big], \tag{H.12}$$

and

$$\left[\frac{\partial}{\partial \eta}\left(\eta\frac{\partial \mathcal{V}_\theta}{\partial \eta}\right)\right]_{i,j} = \frac{1}{\Delta\eta_j^r}\left\{\frac{\eta_j^r}{\Delta\eta_{j+1}^z}(\mathcal{V}_\theta)_{i,j+1} - \left[\frac{\eta_j^r}{\Delta\eta_{j+1}^z} + \frac{\eta_{j-1}^r}{\Delta\eta_j^z}\right](\mathcal{V}_\theta)_{i,j} + \frac{\eta_{j-1}^r}{\Delta\eta_j^z}(\mathcal{V}_\theta)_{i,j-1}\right\}. \tag{H.13}$$

H.3.2.3 Location of $(\mathcal{V}_x)_{i,j}$

Similar to the case of $(\mathcal{V}_\theta)_{i,j}$, only $\mathcal{V}_x$ has derivatives with respect to η in the x-momentum equation. They are approximated at the $(\mathcal{V}_x)_{i,j}$ grid point and have the same forms as those of $\mathcal{V}_\theta$ since $(\mathcal{V}_x)_{i,j}$ and $(\mathcal{V}_\theta)_{i,j}$ have the same η-coordinate.

$$\left(\frac{\partial \mathcal{V}_x}{\partial \eta}\right)_{i,j} = \frac{1}{\Delta\eta_j^r}\left[\mathrm{d}\eta_{j+1}^x(\mathcal{V}_x)_{i,j+1} + (1 - \mathrm{d}\eta_j^x - \mathrm{d}\eta_{j+1}^x)(\mathcal{V}_x)_{i,j} - (1 - \mathrm{d}\eta_j^x)(\mathcal{V}_x)_{i,j-1}\right], \qquad \text{(H.14)}$$

and

$$\left[\frac{\partial}{\partial \eta}\left(\eta\frac{\partial \mathcal{V}_x}{\partial \eta}\right)\right]_{i,j} = \frac{1}{\Delta\eta_j^r}\left\{\frac{\eta_j^r}{\Delta\eta_{j+1}^x}(\mathcal{V}_x)_{i,j+1} - \left[\frac{\eta_j^r}{\Delta\eta_{j+1}^x} + \frac{\eta_{j-1}^r}{\Delta\eta_j^x}\right](\mathcal{V}_x)_{i,j} + \frac{\eta_{j-1}^r}{\Delta\eta_j^x}(\mathcal{V}_x)_{i,j-1}\right\}. \qquad \text{(H.15)}$$

H.3.2.4 Location of $(\mathcal{P})_{i,j}$

The continuity equation has only one derivative, of $\mathcal{V}_r$, which is approximated at the $(\mathcal{P})_{i,j}$ grid point,

$$\left[\frac{\partial}{\partial \eta}(\eta\mathcal{V}_r)\right]_{i,j} = \frac{\eta_j^r(\mathcal{V}_r)_{i,j} - \eta_{j-1}^r(\mathcal{V}_r)_{i,j-1}}{\eta_j^r - \eta_{j-1}^r} = \frac{1}{\Delta\eta_j^r}\left[\eta_j^r(\mathcal{V}_r)_{i,j} - \eta_{j-1}^r(\mathcal{V}_r)_{i,j-1}\right]. \qquad \text{(H.16)}$$

H.3.2.5 Applicability of the Approximations

In the present staggered grid, the locations of $(\mathcal{V}_r)_{i,1}$ are chosen to be on the flexible physical boundary (Figure 5.2); hence, $(\mathcal{V}_r)_{i,1}$ are shell–motion dependent, generally having non–zero values and theoretically remaining unchanged throughout the pseudo–time integration [more details on $(\mathcal{V}_r)_{i,1}$, $(\mathcal{V}_\theta)_{i,1}$ and $(\mathcal{V}_x)_{i,1}$ were given in Section 5.3.3.2]. On the other hand, the locations of $(\mathcal{V}_r)_{i,M-1}$ are on the rigid physical boundary; $(\mathcal{V}_r)_{i,M-1}$ are zero for all i. With the locations of $(\mathcal{V}_r)_{i,j}$ so arranged, Equations (H.9)–(H.11) are applicable to all the $(\mathcal{V}_r)_{i,j}$ grid points within the computational domain, namely $2 \le j \le (M-2)$; likewise, Equation (H.16) holds for all the $(\mathcal{P})_{i,j}$ grid points with $2 \le j \le (M-1)$. Here, for a given i, M denotes the total number of $(\mathcal{P})_{i,j}$ grid points including the two $[(\mathcal{P})_{i,1}$ and $(\mathcal{P})_{i,M}]$ outside the domain as shown in Figure 5.2.

On the contrary, difficulty arises when Equations (H.12)–(H.15) are used at the boundary grid points of $(\mathcal{V}_\theta)_{i,j}$ and $(\mathcal{V}_x)_{i,j}$, specifically with $j = 2$ or $j = (M-1)$, because these approximations require the value of the dependent variable outside the domain. To overcome this difficulty and also to take into account the boundary conditions at the physical boundaries, a different treatment for the derivatives of $(\mathcal{V}_\theta)_{i,j}$ and $(\mathcal{V}_x)_{i,j}$ at the boundary grid points is needed and will be covered in the coming sections.

H.3.3 Grid Points near the Flexible Physical Boundary

H.3.3.1 Location of $(\mathcal{V}_\theta)_{i,2}$

For the θ–momentum equation, the first derivative of $\mathcal{V}_\theta$ with respect to η is evaluated at the $(\mathcal{V}_\theta)_{i,2}$ grid point in the usual way,

$$\left(\frac{\partial \mathcal{V}_\theta}{\partial \eta}\right)_{i,2} = \frac{(\mathcal{V}_\theta)_{i,\frac{5}{2}} - (\mathcal{V}_\theta)_{i,\frac{1}{2}}}{\eta_2^r - \eta_1^r} \tag{H.17}$$

where $(\mathcal{V}_\theta)_{i,\frac{1}{2}} = (\mathcal{V}_\theta)_{i,F}$, representing the value of $\mathcal{V}_\theta$ at the surface of the flexible shell, is in principle known and prescribed by the history of the shell circumferential motions; $(\mathcal{V}_\theta)_{i,\frac{5}{2}}$, being the value of $\mathcal{V}_\theta$ at the location of $(\mathcal{V}_r)_{i,2}$, is interpolated between $(\mathcal{V}_\theta)_{i,2}$ and $(\mathcal{V}_\theta)_{i,3}$, that is

$$(\mathcal{V}_\theta)_{i,\frac{5}{2}} = \mathrm{d}\eta_3^x(\mathcal{V}_\theta)_{i,3} + (1-\mathrm{d}\eta_3^x)(\mathcal{V}_\theta)_{i,2},$$

from which Equation (H.17) becomes

$$\left(\frac{\partial \mathcal{V}_\theta}{\partial \eta}\right)_{i,2} = \frac{1}{\Delta\eta_2^r}\Big[\mathrm{d}\eta_3^x(\mathcal{V}_\theta)_{i,3} + (1-\mathrm{d}\eta_3^x)(\mathcal{V}_\theta)_{i,2} - (\mathcal{V}_\theta)_{i,F}\Big]. \tag{H.18}$$

The second derivative of $\mathcal{V}_\theta$, in the form that has been considered in this appendix, is first rewritten as

$$\left[\frac{\partial}{\partial \eta}\left(\eta\frac{\partial \mathcal{V}_\theta}{\partial \eta}\right)\right]_{i,2} = \left(\frac{\partial \mathcal{V}_\theta}{\partial \eta}\right)_{i,2} + \eta_2^x\left(\frac{\partial^2 \mathcal{V}_\theta}{\partial \eta^2}\right)_{i,2}; \tag{H.19}$$

the first term of the right–hand side of this expression was just given in (H.18) while the derivative in the second term has the following form

$$\left(\frac{\partial^2 \mathcal{V}_\theta}{\partial \eta^2}\right)_{i,2} = a_F(\mathcal{V}_\theta)_{i,F} + b_F(\mathcal{V}_\theta)_{i,2} + c_F(\mathcal{V}_\theta)_{i,3}, \tag{H.20}$$

where

$$a_F = \frac{2}{\Delta\tilde{\eta}(\Delta\tilde{\eta}+\Delta\eta_3^x)}, \quad b_F = -\frac{2}{\Delta\tilde{\eta}\Delta\eta_3^x}, \quad c_F = \frac{2}{\Delta\eta_3^x(\Delta\tilde{\eta}+\Delta\eta_3^x)}, \quad \Delta\tilde{\eta} = \eta_2^x - \eta_1^r. \tag{H.21}$$

The derivation of Equation (H.20) was given in Appendix F.

H.3.3.2 Location of $(\mathcal{V}_x)_{i,2}$

Since $(\mathcal{V}_x)_{i,2}$ has the same η coordinate as does $(\mathcal{V}_\theta)_{i,2}$, the difference expressions for the derivatives of $\mathcal{V}_x$ at the $(\mathcal{V}_x)_{i,2}$ grid point may be obtained from Equations (H.18)–(H.20) by simply replacing the subscript θ by x, namely

$$\left(\frac{\partial \mathcal{V}_x}{\partial \eta}\right)_{i,2} = \frac{1}{\Delta\eta_2^r}\left[\mathrm{d}\eta_3^x(\mathcal{V}_x)_{i,3} + (1-\mathrm{d}\eta_3^x)(\mathcal{V}_x)_{i,2} - (\mathcal{V}_x)_{i,F}\right], \tag{H.22}$$

where $(\mathcal{V}_x)_{i,F}$ denotes the value of $\mathcal{V}_x$ at the surface of the flexible shell, and

$$\left[\frac{\partial}{\partial\eta}\left(\eta\frac{\partial \mathcal{V}_x}{\partial \eta}\right)\right]_{i,2} = \left(\frac{\partial \mathcal{V}_x}{\partial \eta}\right)_{i,2} + \eta_2^x\left(\frac{\partial^2 \mathcal{V}_x}{\partial \eta^2}\right)_{i,2}, \tag{H.23}$$

where

$$\left(\frac{\partial^2 \mathcal{V}_x}{\partial \eta^2}\right)_{i,2} = a_F(\mathcal{V}_x)_{i,F} + b_F(\mathcal{V}_x)_{i,2} + c_F(\mathcal{V}_x)_{i,3}. \tag{H.24}$$

H.3.4 Grid Points near the Rigid Physical Boundary

H.3.4.1 Location of $(\mathcal{V}_\theta)_{i,M-1}$

The evaluation of the derivatives of $\mathcal{V}_\theta$ at the $(\mathcal{V}_\theta)_{i,j^*}$ grid point with $j^* = (M-1)$ is carried out in the same way as was done in Section H.3.3.1. For the first derivative,

$$\left(\frac{\partial \mathcal{V}_\theta}{\partial \eta}\right)_{i,j^*} = \frac{(\mathcal{V}_\theta)_{i,j^*+\frac{1}{2}} - (\mathcal{V}_\theta)_{i,j^*-\frac{1}{2}}}{\eta_{j^*}^r - \eta_{j^*-1}^r} = \frac{(\mathcal{V}_\theta)_{i,j^*+\frac{1}{2}} - (\mathcal{V}_\theta)_{i,j^*-\frac{1}{2}}}{\Delta\eta_{j^*}^r},$$

where $(\mathcal{V}_\theta)_{i,j^*+\frac{1}{2}} = 0$ is the value of $\mathcal{V}_\theta$ at the rigid physical boundary, and

$$(\mathcal{V}_\theta)_{i,j^*-\frac{1}{2}} = \mathrm{d}\eta_{j^*}^x(\mathcal{V}_\theta)_{i,j^*} + (1-\mathrm{d}\eta_{j^*}^x)(\mathcal{V}_\theta)_{i,j^*-1};$$

hence,

$$\left(\frac{\partial \mathcal{V}_\theta}{\partial \eta}\right)_{i,j^*} = -\frac{1}{\Delta\eta_{j^*}^r}\left[\mathrm{d}\eta_{j^*}^x(\mathcal{V}_\theta)_{i,j^*} + (1-\mathrm{d}\eta_{j^*}^x)(\mathcal{V}_\theta)_{i,j^*-1}\right]. \tag{H.25}$$

For the second derivative,

$$\left[\frac{\partial}{\partial\eta}\left(\eta\frac{\partial \mathcal{V}_\theta}{\partial \eta}\right)\right]_{i,j^*} = \left(\frac{\partial \mathcal{V}_\theta}{\partial \eta}\right)_{i,j^*} + \eta_{j^*}^x\left(\frac{\partial^2 \mathcal{V}_\theta}{\partial \eta^2}\right)_{i,j^*},$$

where

$$\left(\frac{\partial^2 \mathcal{V}_\theta}{\partial \eta^2}\right)_{i,j^*} = a_R(\mathcal{V}_\theta)_{i,j^*-1} + b_R(\mathcal{V}_\theta)_{i,j^*}; \tag{H.26}$$

in the above expression, a_R and b_R were derived in Appendix F and had the following values:

$$a_R = \frac{2}{\Delta\eta^x_{j^*}(\Delta\bar{\eta} + \Delta\eta^x_{j^*})}, \quad b_R = -\frac{2}{\Delta\bar{\eta}\Delta\eta^x_{j^*}}, \quad \Delta\bar{\eta} = \eta^r_{j^*} - \eta^x_{j^*}. \tag{H.27}$$

Hence,

$$\left[\frac{\partial}{\partial\eta}\left(\eta\frac{\partial\mathcal{V}_\theta}{\partial\eta}\right)\right]_{i,j^*} = \left[a_R\eta^x_{j^*} - \frac{1 - \mathrm{d}\eta^x_{j^*}}{\Delta\eta^r_{j^*}}\right](\mathcal{V}_\theta)_{i,j^*-1} + \left[b_R\eta^x_{j^*} - \frac{\mathrm{d}\eta^x_{j^*}}{\Delta\eta^r_{j^*}}\right](\mathcal{V}_\theta)_{i,j^*}. \tag{H.28}$$

H.3.4.2 Location of $(\mathcal{V}_x)_{i,M-1}$

Similarly, the difference representations for the derivatives of $\mathcal{V}_x$ at the $(\mathcal{V}_x)_{i,j^*}$ grid point $[j^* = (M-1)]$ may be obtained from Equations (H.25) and (H.28) by replacing the subscript θ by x; thus, for the first derivative,

$$\left(\frac{\partial\mathcal{V}_x}{\partial\eta}\right)_{i,j^*} = -\frac{1}{\Delta\eta^r_{j^*}}\left[\mathrm{d}\eta^x_{j^*}(\mathcal{V}_x)_{i,j^*} + (1 - \mathrm{d}\eta^x_{j^*})(\mathcal{V}_x)_{i,j^*-1}\right]; \tag{H.29}$$

for the second derivative,

$$\left[\frac{\partial}{\partial\eta}\left(\eta\frac{\partial\mathcal{V}_x}{\partial\eta}\right)\right]_{i,j^*} = \left[a_R\eta^x_{j^*} - \frac{1 - \mathrm{d}\eta^x_{j^*}}{\Delta\eta^r_{j^*}}\right](\mathcal{V}_x)_{i,j^*-1} + \left[b_R\eta^x_{j^*} - \frac{\mathrm{d}\eta^x_{j^*}}{\Delta\eta^r_{j^*}}\right](\mathcal{V}_x)_{i,j^*}. \tag{H.30}$$

Appendix I

Computer Listing

The purpose of Appendix I is *not* to show every single computer program ever written in the course of the thesis. Rather, the appendix describes the programming technique (style, to be exact!) adopted by the author in developing his computer codes; for this reason, only one computer listing will be given and discussed. Nevertheless, interested readers may obtain other listings, related to different parts of the thesis, from the author.

Following is a listing of the computer program developed for Section 2.5. This program was written in FORTRAN 77 (Standard FORTRAN). It has the following characteristics:

- It runs on IBM AT compatible microcomputers with the DOS operating system.
- Most variables used in the program have the same physical meanings as those in the theory.
- All SUBROUTINE and FUNCTION subprograms appear in an alphabetical order according to their names.
- All multi–dimensional arrays have the so–called pseudo dimensions, which change automatically according to the data provided.
- All physical data are read in by the program; i.e. *all* changes in the data are made in the data file, *not* in the computer program.

```
C ... MAIN PROGRAM
C ... CLAMPED-FREE SHELLS USING INVISCID THEORY (WITH OR WITHOUT
C ... STEADY VISCOUS FORCES)
C ... INNER SHELL : FLEXIBLE, OUTER SHELL : RIGID
C ... LAST EDITED: DECEMBER 2, 1991
      IMPLICIT COMPLEX*16(A-H), REAL*8(O-Z)
      COMMON/CONST/PI,RGAMA,IOP1,IOP2
      COMMON/TAPES/JIN,JOUT,JS1,JS2,JS3,JS4,JS5
      COMMON  A(3200)
      OPEN (JIN,FILE='CLFR.INP')
      OPEN (JOUT,FILE='CLFR.DAT')
      OPEN (JS1,FILE='SCR1.FILE',ACCESS='DIRECT',RECL=64)
      OPEN (JS2,FILE='SCR2.FILE',ACCESS='DIRECT',RECL=64)
      OPEN (JS3,FILE='SCR3.FILE',ACCESS='DIRECT',RECL=64)
      REWIND (JS1)
C ... NMAX= 3200 OF COMPLEX*16:  MAXIMUM ALLOWED BY MICROSOFT FORTRAN
      NMAX= 3200
      READ (JIN,1000)  INFO
      WRITE (0,1000)  INFO
      CALL INPUT (NT)
      NR= NT*NT*3
      NS= 3*NT
      NX= 6*NT
      L0= 1
      L1= L0 + NS**2
      L2= L1 + NS**2
      L3= L2 + 2*NR
      L4= L3 + NR
C
      N1= L0 + 2*NR
      N2= N1 + NR
      N3= N2 + NX**2
      N4= N3 + NX
      N5= N4 + NX**2
      N6= N5 + 2*NX
C
      NDIF= MAX0(L4,N6) - NMAX
      IF (NDIF)  20,20,300
   20 IF (INFO)  60,40,60
   40 CALL CLEAR (A(L0),L2-L0)
      CALL MCK (A(L0),A(L1),NT,NS)
      CALL CLFREE (A(L0),A(L1),NT,NS)
      CALL FORCES (A(L2),A(L3),NT,1)
      GO TO 400
   60 CALL FORCES (A(L0),A(N1),NT,2)
      READ (JIN,1000)  NTIMES
      DO 200  ITIME=1,NTIMES
      CALL FORCES (A(L0),A(N1),NT,3)
      IF (IOP1)  120,140,120
  120 CALL CLEAR (A(N2),L1-L0)
      CALL VISFOR (A(N2),NT,NS)
  140 CALL REDUCE (A(N1),A(N2),A(N3),NT,NS,NX)
      CALL EIGCC (A(N2),NX,NX,0,A(N3),A(N4),NX,A(N5),IER)
      CALL OUTPUT (A(N3),A(N5),IER,NX)
  200 CONTINUE
      GO TO 400
  300 WRITE (JOUT,2000) NDIF
  400 CLOSE (JIN)
      CLOSE (JOUT)
      CLOSE (JS1)
      CLOSE (JS2)
      CLOSE (JS3)
      STOP
 1000 FORMAT (I5)
 2000 FORMAT (53H * * *  PROGRAM STOPPED ... ALLOWED STORAGE EXCEEDED ,
     1        10HBY  NDIF =,I5)
      END
C
      COMPLEX*16 FUNCTION  CIN (A,N)
      IMPLICIT COMPLEX*16(A-H), REAL*8(O-Z)
      DOUBLE PRECISION  CDABS,DREAL,DIMAG
      COMMON/CONST/PI,RGAMA,IOP1,IOP2
      IF (CDABS(A).GE.20.D0)  GO TO 140
      AA= 0.5D0*A
      K= 0
      CIN= (0.D0,0.D0)
  100 CNEW= AA**(2*K)/RFAC(K)/RFAC(N + K)
      CIN= CIN + CNEW
      IF (CDABS(CNEW).LT.1.D-10)  GO TO 120
      K= K + 1
      GO TO 100
  120 CIN= CIN*AA**N
      RETURN
  140 CI= (0.D0,1.D0)
      CN1= (4.D0*N**2 - 1.D0)/(8.D0*A)
      CN2= CN1*(4.D0*N**2 - 9.D0)/(16.D0*A)
      CN3= CN2*(4.D0*N**2 - 25.D0)/(24.D0*A)
      CNA= CDEXP(A)/CDSQRT(2.D0*PI*A)
      CNB= CNA*CDEXP(-2.D0*A)
      IF (DIMAG(A))  160,200,180
  160 CIN= CNA*(1.D0-CN1+CN2-CN3)+(-1)**(N+1)*CI*CNB*(1.D0+CN1+CN2+CN3)
      RETURN
  180 CIN= CNA*(1.D0-CN1+CN2-CN3)+(-1)**N*CI*CNB*(1.D0+CN1+CN2+CN3)
      RETURN
  200 IF (DREAL(A))  220,240,240
```

```
  220 CIN= (-1)**N*CI*CNB*(1.D0 + CN1 + CN2 + CN3)
      RETURN
  240 CIN= CNA*(1.D0 - CN1 + CN2 - CN3)
      RETURN
      END
C
      COMPLEX*16 FUNCTION  CKN (A,N)
      IMPLICIT COMPLEX*16(A-H), REAL*8(O-Z)
      DOUBLE PRECISION  CDABS,DREAL,DIMAG
      COMMON/CONST/PI,RGAMA,IOP1,IOP2
      IF (CDABS(A).GE.15.D0)  GO TO 200
      AA= 0.5D0*A
      B= (0.D0,0.D0)
      IF (N.EQ.0)  GO TO 150
      K= 0
  100 BNEW= (-1)**K*RFAC(N-K-1)/(RFAC(K)*AA**(N-2*K))
      B= B + BNEW
      IF (N-1-K)  140,140,120
  120 K= K + 1
      GO TO 100
  140 B= 0.5D0*B
  150 K= 0
      CKN= (0.D0,0.D0)
  160 CNEW= (AA**(2*K)/RFAC(K)/RFAC(N + K))*(0.5D0*(RFI(K) + RFI(N + K))
     1                                       - (CDLOG(AA) + RGAMA))
      CKN= CKN +CNEW
      IF (CDABS(CNEW).LT.1.D-10)  GO TO 180
      K= K + 1
      GO TO 160
  180 CKN= CKN*(-AA)**N + B
      RETURN
  200 CN1= (4.D0*N**2 - 1.D0)/(8.D0*A)
      CN2= CN1*(4.D0*N**2 - 9.D0)/(16.D0*A)
      CN3= CN2*(4.D0*N**2 - 25.D0)/(24.D0*A)
      CNA= CDEXP(-A)*CDSQRT(0.5D0*PI/A)
      CKN= CNA*(1.D0 + CN1 + CN2 +CN3)
      IF (DREAL(A))  220,240,240
  220 IF (DIMAG(A))  240,260,240
  240 RETURN
  260 B= -A
      CNA= CDEXP(-B)*CDSQRT(0.5D0*PI/B)
      CKN= CKN + (-1)**N*CNA*(1.D0 - CN1 + CN2 - CN3)
      RETURN
      END
C
      SUBROUTINE  CLEAR (CF,N)
      IMPLICIT COMPLEX*16(A-H)
      DIMENSION  CF(1)
      DO 20  I=1,N
   20 CF(I)= (0.D0,0.D0)
      RETURN
      END
C
      SUBROUTINE  CLFREE (CXM,CXK,NT,NS)
      IMPLICIT COMPLEX*16(A-H), REAL*8(O-Z)
      COMMON/TAPES/JIN,JOUT,JS1,JS2,JS3,JS4,JS5
      COMMON/COAX/RLA(10),RHO(10),OMR,RINT,NINT,N
      COMMON/ISHELL/DHI,DVI,QI,REI,SKI,PSI
      COMMON/OSHELL/DHO,DVO,QO,REO,SKO,PSO
      DIMENSION  CXM(NS,1),CXK(NS,1),AK(3,3)
      REWIND (JS2)
      DO 200  M=1,NT
      DO 200  K=1,NT
      CALL CLEAR (AK,9)
      U2= RE1(K,M,2)
      U3= RE1(K,M,3)
      W1= N
      W2= W1**2
C ... CALCULATE ELEMENTS OF THE MATRIX  J1B
      AK(2,1)=  0.5D0*W1*(1.D0 - PSI)*REI**2*U3
      AK(3,1)= -0.5D0*W2*SKI*(1.D0 - PSI)*REI**2*U3
      AK(1,2)= -PSI*W1*REI**2*U2
      AK(2,2)= -0.5D0*(1.D0 + 3.D0*SKI)*(1.D0 - PSI)*REI**2*U3
      AK(3,2)=  W1*SKI*REI**2*(PSI*U2 - 0.5D0*(3.D0 - PSI)*U3)
      AK(1,3)= -PSI*REI**2*U2
      AK(2,3)= -1.5D0*W1*SKI*(1.D0 - PSI)*REI**2*U3
      AK(3,3)=  W2*SKI*REI**2*(PSI*U2 - (2.D0 - PSI)*U3)
      DO 100  J=1,3
      JJ= M + NT*(J - 1)
      DO 100  I=1,3
      II= K + NT*(I - 1)
  100 CXK(II,JJ)= CXK(II,JJ) + AK(I,J)
  200 CONTINUE
      DO 300  J=1,NS
      DO 300  I=1,NS
  300 WRITE (JS2)  CXM(I,J),CXK(I,J)
      RETURN
      END
C
      COMPLEX*16 FUNCTION  CN (RA,M)
      IMPLICIT COMPLEX*16(A-H), REAL*8(O-Z)
      DOUBLE PRECISION  DABS,DMOD
      COMMON/CONST/PI,RGAMA,IOP1,IOP2
      COMMON/COAX/RLA(10),RHO(10),OMR,RINT,NINT,N
      COMMON/CLFR/RL,MODEL
```

```
      CN= (0.D0,0.D0)
      IF (MODEL)  20,20,40
   20 RETURN
   40 RB= RLA(M)*RHO(M)
      RD= RL - 1.D0
      RS= (-1)**(M + 1)
      R1= RA*RL
      R2= 2.D0*PI
      CI= (0.D0,1.D0)
      CJ= CI*DMOD(R1,R2)
      CA= CI*RA
      CB= CA*RL
      CD= CDEXP(CA)
      CE= CDEXP(CJ)
      GO TO (120,220,420,420), MODEL
C ... MODEL=1 :  STRAIGHT COLLECTOR PIPE MODEL
  120 IF (DABS(RA).LT.1.D-16)  GO TO 140
      FF1= (CE - (1.D0 + CA*RD)*CD)/RA**2
      GO TO 200
  140 FF1= -0.5D0*RD**2
  200 CN= -2.D0*RS*FF1/RD
      RETURN
C ... MODEL=2 :  CURVED PIPE MODEL
  220 IF (DABS(RA).LT.1.D-16)  GO TO 240
      FF0= (CE - CD)/CA
      FF1= ((1.D0 - CA*RD)*CE - CD)/RA**2
      FF2= ((2.D0*(CI+RA*RD)-CA*RA*RD**2)*CE-2.D0*CI*CD)/RA**3
      GO TO 300
  240 FF0= RD
      FF1= RD**2/2.D0
      FF2= RD**3/3.D0
  300 CN= 2.D0*RS*(FF0 + RB*FF1 - (1.D0/RD**2 + RB/RD)*FF2)
      RETURN
C ... MODEL=3  AND  MODEL=4
  420 IF (DABS(RA).LT.1.D-16)  GO TO 460
      FF0= (CE - CD)/CA
      FF1= ( CE*(1.D0 - CB) - CD*(1.D0 - CA) )/RA**2
      FF2= ( CE*(2.D0*(CI + RA*RL) - CB**2/CI)
     1          - CD*(2.D0*(CI + RA) - CA*RA) )/RA**3
      FF3= ( CE*((RA*RL)**2*(3.D0 - CB) + 6.D0*(CB - 1.D0))
     1          - CD*(RA**2*(3.D0 - CA) + 6.D0*(CA - 1.D0)) )/RA**4
      GO TO 500
  460 FF0= RD
      FF1= (RL**2 - 1.D0)/2.D0
      FF2= (RL**3 - 1.D0)/3.D0
      FF3= (RL**4 - 1.D0)/4.D0
C ... MODEL=3 :  CURVED PIPE MODEL WITH ZERO SLOPE AT  ZI=RL
  500 A= 2.D0*FF3-3.D0*(RL+1.D0)*FF2+6.D0*RL*FF1+RL**2*(RL-3.D0)*FF0
      B= FF3 - (2.D0*RL + 1.D0)*FF2 + RL*(RL + 2.D0)*FF1 - RL**2*FF0
      CN= 2.D0*RS*(A/RD + RB*B)/RD**2
      RETURN
      END
C
      BLOCK  DATA
C ... DATA FOR CLAMPED-FREE BEAMS
      IMPLICIT REAL*8(O-Z)
      COMMON/CONST/PI,RGAMA,IOP1,IOP2
      COMMON/TAPES/JIN,JOUT,JS1,JS2,JS3,JS4,JS5
      COMMON/COAX/RLA(10),RHO(10),OMR,RINT,NINT,N
      COMMON/SVFOR/SAL(11),SBT(11),RDI,RDO,RGI,RGO,VISI,VISA,SL
      DATA  PI/3.141592653589793D0/, RGAMA/0.5772156649015328D0/
      DATA  JIN/5/, JOUT/10/, JS1/1/, JS2/2/, JS3/3/, JS4/4/, JS5/5/
      DATA  RLA/ 1.875104068711961D0, 4.694091132974175D0,
     1           7.854757438237613D0, 10.99554073487547D0,
     2           14.13716839104647D0, 17.27875953208824D0,
     3           20.42035225104125D0, 23.56194490180645D0,
     4           26.70353755551830D0, 29.84513020910282D0 /,
     5      RHO/ 0.7340955137589127D0, 1.018467318759219D0,
     6           0.9992244965174283D0, 1.000033553251713D0,
     7           0.9999985501086500D0, 1.000000062655628D0,
     8           0.9999999972924051D0, 1.000000000117006D0,
     9           0.9999999999949437D0, 1.000000000000218D0 /
      DATA  SAL/ 0.06411D0, 0.1D0, 0.2D0, 0.3D0, 0.4D0, 0.5D0, 0.6D0,
     1              0.7D0, 0.8D0, 0.9D0, 1.0D0/,   SBT/ 0.56388D0,
     2           0.63925D0, 0.72964D0, 0.78990D0, 0.83964D0, 0.88330D0,
     3           0.92316D0, 0.95143D0, 0.97183D0, 0.98919D0, 1.0D0 /
      END
C
      SUBROUTINE  FORCES (FR,CQ,NT,ID)
C ... CALCULATE UNSTEADY INVISCID FORCES
      IMPLICIT COMPLEX*16(A-H), REAL*8(O-Z)
      DOUBLE PRECISION  DABS,DREAL
      COMMON/IFLUID/RHOI,UI,UIR
      COMMON/AFLUID/RHOA,UA,UAR
      COMMON/ISHELL/DHI,DVI,QI,REI,SKI,PSI
      COMMON/OSHELL/DHO,DVO,QO,REO,SKO,PSO
      COMMON/CONST/PI,RGAMA,IOP1,IOP2
      COMMON/TAPES/JIN,JOUT,JS1,JS2,JS3,JS4,JS5
      COMMON/COAX/RLA(10),RHO(10),OMR,RINT,NINT,N
      COMMON/SVFOR/SAL(11),SBT(11),RDI,RDO,RGI,RGO,VISI,VISA,SL
      DIMENSION  FR(NT,NT,1),CQ(NT,NT,1),XG(2),WGT(2),W[illegible](2)
      DATA  XG/-0.5773502691896260D0,0.5773502691896260D0/, WGT/1.D0,1.D0/
      FN= N
      GO TO (20,360,420), ID
   20 DO 100  J=1,2
```

```
  100 WG(J)= 0.5D0*RINT*WGT(J)
      RLIM= 0.5D0*RINT*NINT
      MT= 6*NT*NT
      CALL  CLEAR (FR,MT)
      DO 300  I=1,NINT
      RLOW= RINT*(I - 1) - RLIM
      RHI= RLOW + RINT
      DO 300  J=1,2
      WT= WG(J)
      RA= 0.5D0*(RLOW + RHI + RINT*XG(J))
      AEI= RA*REI
      RALFA= RA*REO
      AEO= RALFA
      B1= CIN(AEI,N)
      B2= CIN(AEI,N+1)
      CON1= B1/(B1*FN/AEI + B2)
      C1= CKN(AEI,N)
      C2= CKN(AEI,N+1)
      IF (DABS(RALFA).GT.72.D0)  GO TO 120
      B3= CIN(AEO,N)
      B4= CIN(AEO,N+1)
      C3= CKN(AEO,N)
      C4= CKN(AEO,N+1)
      CON= (B3*FN/AEO+B4)*(C1*FN/AEI-C2)-(B1*FN/AEI+B2)*(C3*FN/AEO-C4)
      CON2= ( (B3*FN/AEO + B4)*C1 - B1*(C3*FN/AEO - C4) )/DREAL(CON)
      GO TO 140
  120 CON= (C1*FN/AEI - C2)
      CON2= C1/DREAL(CON)
  140 DO 200  IT=1,3
      RB= RA**(IT - 2)
      DO 200  M=1,NT
      DO 200  K=1,NT
      HN= GH(RA,K,M,2)
      FR(K,M,IT)= FR(K,M,IT) + WT*RB*HN*DREAL(CON1)
  200 FR(K,M,3+IT)= FR(K,M,3+IT) + WT*RB*HN*DREAL(CON2)
  300 CONTINUE
      DO 320  IT=1,6
      DO 320  M=1,NT
      DO 320  K=1,NT
  320 WRITE (JS1)  FR(K,M,IT)
      RETURN
C ... READ IN VALUES OF INTEGRALS IN EXPRESSIONS OF FLUID FORCES
  360 DO 380  IT=1,6
      DO 380  M=1,NT
      DO 380  K=1,NT
  380 READ (JS1)  FR(K,M,IT)
      RETURN
C ... READ DATA FOR THE INTERNAL AND ANNULAR FLUIDS
  420 READ (JIN,1000)  VISI,RHOI,UIR
      READ (JIN,1000)  VISA,RHOA,UAR
      DO 600  IT=1,3
      IF (IT - 2)  440,460,480
  440 R1=  RHOI*UI**2/(2.D0*PI*QI*REI**2)
      R2= -RHOA*UA**2/(2.D0*PI*QI*(REO*OMR)**2)
      GO TO 500
  460 R1= -RHOI*UI**2*UIR/(PI*QI*REI)
      R2=  RHOA*UA**2*UAR/(PI*QI*REO*OMR)
      GO TO 500
  480 R1=  RHOI*UI**2*UIR**2/(2.D0*PI*QI)
      R2= -RHOA*UA**2*UAR**2/(2.D0*PI*QI)
  500 DO 600  M=1,NT
      DO 600  K=1,NT
  600 CQ(K,M,IT)= R1*FR(K,M,IT) + R2*FR(K,M,3+IT)
      RETURN
 1000 FORMAT (3D15.6)
      END
C
      COMPLEX*16 FUNCTION  GH (RA,K,M,ID)
C ... FUNCTIONS  GKM AND HKM FOR CLAMPED-FREE BEAMS
      IMPLICIT COMPLEX*16(A-H), REAL*8(O-Z)
      CI= (0.D0,1.D0)
      CA= CI*RA
C ... ID=1 FOR GKM, ID=2 FOR HKM
      GO TO (100,200), ID
  100 GK= 2.D0*(-1)**(K+1)*CDEXP(-CA) + CA*HH(RA,K,-1)
      GH= GK*(HH(RA,M,1) + CN(RA,M))
      RETURN
  200 GH= HH(RA,K,-1)*(HH(RA,M,1) + CN(RA,M))
      RETURN
      END
C
      COMPLEX*16 FUNCTION  HH (RA,M,I)
C ... FUNCTIONS  HK AND HM FOR CLAMPED-FREE BEAMS
      IMPLICIT COMPLEX*16(A-H), REAL*8(O-Z)
      DOUBLE PRECISION  DABS
      COMMON/COAX/RLA(10),RHO(10),OMR,RINT,NINT,N
C ... I=-1 FOR HK, I=+1 FOR HM
      CI= (0.D0,1.D0)
      CA= CI*RA*I
      RB= RLA(M)*RHO(M)
      RDIF= DABS(RA) - RLA(M)
      IF (DABS(RDIF).LT.1.D-16)  GO TO 50
      HH= (2.D0/(RLA(M)**4-RA**4))*( (-1)**(M+1)*RA**2*CDEXP(CA)*(CA-RB)
     1                             + RLA(M)**2*(CA + RB) )
      RETURN
```

```
   50 A= 0.5D0/RA**3
      B= RA**3 + (RB - 3.D0)*CA*RA + 2.D0*RB*RA
      HH= A*( (-1)**(M+1)*CDEXP(CA)*B - (CA/RA)*RLA(M)**2 )
      RETURN
      END
C
      SUBROUTINE  INPUT (NTERMS)
      IMPLICIT COMPLEX*16(A-H), REAL*8(O-Z)
      COMMON/IFLUID/RHOI,UI,UIR
      COMMON/AFLUID/RHOA,UA,UAR
      COMMON/ISHELL/DHI,DVI,QI,REI,SKI,PSI
      COMMON/OSHELL/DHO,DVO,QO,REO,SKO,PSO
      COMMON/COAX/RLA(10),RHO(10),OMR,RINT,NINT,MODE
      COMMON/CLFR/RL,MODEL
      COMMON/CONST/PI,RGAMA,IOP1,IOP2
      COMMON/TAPES/JIN,JOUT,JS1,JS2,JS3,JS4,JS5
      COMMON/SVFOR/SAL(11),SBT(11),RDI,RDO,RGI,RGO,VISI,VISA,SL
C ... READ DATA FOR THE INNER AND OUTER SHELLS
      READ (JIN,1000)  YNI,PSI,SDENI,THIKI,RDI,RGI,SHI,SVI
      READ (JIN,1000)  YNO,PSO,SDENO,THIKO,RDO,RGO,SHO,SVO
      WRITE (JOUT,1000)  YNI,PSI,SDENI,THIKI,RDI,RGI,SHI,SVI
      WRITE (JOUT,1000)  YNO,PSO,SDENO,THIKO,RDO,RGO,SHO,SVO
C ... READ VARIOUS PARAMETERS FOR THE COMPUTATION
      READ (JIN,1100)  SL,RL,RINT,NINT,MODEL,MODE,NTERMS,IOP1,IOP2
      WRITE (JOUT,1100)  SL,RL,RINT,NINT,MODEL,MODE,NTERMS,IOP1,IOP2
C ... GENERATE SPECIFIC DATA FOR LATER USE
      SKI= (THIKI/RDI)**2/12.D0
      SKO= (THIKO/RDO)**2/12.D0
      REI= RDI/SL
      REO= RDO/SL
      QI= YNI*THIKI*SL/(RDI**2*(1.D0 - PSI**2))
      QO= YNO*THIKO*SL/(RDO**2*(1.D0 - PSO**2))
      UI= DSQRT(YNI/(SDENI*(1.D0 - PSI**2)))
      UA= DSQRT(YNO/(SDENO*(1.D0 - PSO**2)))
      OMR= RDI*UA/(RDO*UI)
      CI= (0.D0,1.D0)
      DHI= 1.D0 + SHI*CI
      DHO= 1.D0 + SHO*CI
      DVI= SVI*UI*CI/RDI
      DVO= SVO*UA*CI/RDO
      RETURN
 1000 FORMAT (3D20.12/3D20.12/3D20.12)
 1100 FORMAT (3D15.6,5I5,I2)
      END
C
      SUBROUTINE  INVSE (A,N)
      IMPLICIT COMPLEX*16(A-H), REAL*8(O-Z)
      DOUBLE PRECISION  CDABS
      COMMON/TAPES/JIN,JOUT,JS1,JS2,JS3,JS4,JS5
      DIMENSION  A(N,1)
      NN= N*N
      NX= N + 1
      NY= 2*N
      CALL CLEAR (A(1,NX),NN)
      DO 20  I=1,N
   20 A(I,N+I)= (1.D0,0.D0)
      L= 1
   40 K= L + 1
C ... USE A PIVOT STRATEGY TO AVOID AN ACCIDENTAL ZERO PIVOT
      RBIG= CDABS(A(L,L))
      IBIG= L
      DO 60  I=L,N
      SMALL= CDABS(A(I,L))
      IF (RBIG.GT.SMALL)  GO TO 60
      RBIG= SMALL
      IBIG= I
   60 CONTINUE
      IF (IBIG - L)  120,120,80
   80 DO 100  J=L,NY
      CON= A(L,J)
      A(L,J)= A(IBIG,J)
  100 A(IBIG,J) = CON
  120 IF (RBIG - 1.D-08)  300,300,140
  140 COF= A(L,L)
      DO 160  J=L,NY
  160 A(L,J)= A(L,J)/COF
      IF (L.EQ.N)  GO TO 200
      DO 180  I=K,N
      COF= A(I,L)
      DO 180  J=L,NY
  180 A(I,J)= A(I,J) - A(L,J)*COF
      L= L + 1
      IF (L - N)  40,40,200
  200 L= N
  220 LZ= L - 1
      DO 240  K=1,LZ
      I= L - K
      COF= A(I,L)
      DO 240  J=L,NY
  240 A(I,J)= A(I,J) - A(L,J)*COF
      L= L - 1
      IF (L - 1)  260,260,220
  260 RETURN
  300 WRITE (JOUT,2000)
      STOP
```

```
 2000 FORMAT (51H *  *  *  PROGRAM STOPPED...  DUE TO ENCOUNTERING A,
     1        54H SINGULAR MATRIX.  ITS INVERSE MATRIX DOES NOT EXIST !)
      END
C
      SUBROUTINE  MCK (CXM,CXK,NT,NS)
      IMPLICIT COMPLEX*16(A-H), REAL*8(O-Z)
      COMMON/COAX/RLA(10),RHO(10),OMR,RINT,NINT,N
      COMMON/ISHELL/DHI,DVI,QI,REI,SKI,PSI
      COMMON/OSHELL/DHO,DVO,QO,REO,SKO,PSO
      DIMENSION  CXM(NS,1),CXK(NS,1),AM(3,3),AK(3,3)
      DO 200  M=1,NT
      DO 200  K=1,NT
      CALL CLEAR (AM,9)
      CALL CLEAR (AK,9)
      U1= RE1(K,M,1)
      V2= RE2(K,M,2)
      V3= RE2(K,M,3)
      V4= RE2(K,M,4)
      W1= N
      W2= W1**2
C ... CALCULATE ELEMENTS OF THE MASS MATRIX  M
      AM(1,1)= REI**2*V2
      AM(2,2)= U1
      AM(3,3)= U1
C ... CALCULATE ELEMENTS OF THE STIFFNESS MATRIX  K
      AK(1,1)= -0.5D0*W2*(1.D0 + SKI)*(1.D0 - PSI)*REI**2*V2 + REI**4*V4
      AK(2,1)= -0.5D0*W1*(1.D0 + PSI)*REI**2*V3
      AK(3,1)= ( 0.5D0*W2*SKI*(1.D0 - PSI) - PSI )*REI**2*V3
     1         + SKI*(REI*RLA(M))**4*U1
      AK(1,2)= 0.5D0*W1*(1.D0 + PSI)*REI**2*V2
      AK(2,2)= -W2*U1 + 0.5D0*(1.D0 + 3.D0*SKI)*(1.D0 - PSI)*REI**2*V3
      AK(3,2)= W1*( -U1 + 0.5D0*SKI*(3.D0 - PSI)*REI**2*V3 )
      AK(1,3)= (PSI-0.5D0*W2*SKI*(1.D0-PSI))*REI**2*V2 - SKI*REI**4*V4
      AK(2,3)= W1*( 0.5D0*SKI*(3.D0 - PSI)*REI**2*V3 - U1 )
      AK(3,3)= -(SKI*((W2 - 1.D0)**2 + (REI*RLA(M))**4) + 1.D0)*U1
     1         + 2.D0*SKI*(W1*REI)**2*V3
      DO 100  J=1,3
      JJ= M + NT*(J - 1)
      DO 100  I=1,3
      II= K + NT*(I - 1)
      CXM(II,JJ)= AM(I,J)
  100 CXK(II,JJ)= AK(I,J)
  200 CONTINUE
      RETURN
      END
C
      SUBROUTINE  OUTPUT (EIG,APX,IER,NX)
      IMPLICIT COMPLEX*16(A-H), REAL*8(O-Z)
      COMMON/CONST/PI,RGAMA,IOP1,IOP2
      COMMON/TAPES/JIN,JOUT,JS1,JS2,JS3,JS4,JS5
      COMMON/SVFOR/SAL(11),SBT(11),RDI,RDO,RGI,RGO,VISI,VISA,SL
      COMMON/IFLUID/RHOI,UI,UIR
      COMMON/AFLUID/RHOA,UA,UAR
      DIMENSION  EIG(1)
      WRITE (JOUT,2000)  UIR,UAR
      WRITE (JOUT,2020)  IER,APX
C ... PROPORTIONALITY CONSTANT TO GIVE FREQUENCIES IN CYCLES/SECOND
      CONST= UI/(2.D0*PI*RDI)
C ... PROPORTIONALITY CONSTANT TO GIVE FREQUENCIES IN RAD/SECOND
C     CONST= UI/RDI
      DO 100  I=1,NX
  100 EIG(I)= -CONST*EIG(I)
      CALL SORT (EIG,NX)
      DO 200  I=1,NX
  200 WRITE (JOUT,2040)  I,EIG(I)
      RETURN
 2000 FORMAT (/53H * * *  VALUES OF NON-DIMENSIONALIZED FLOW VELOCITIES,
     1        //20X,5HUIR =,D15.6,10X,5HUAR =,D15.6/)
 2020 FORMAT (41H * * *  RESULTS FROM THE ITERATIVE METHOD,
     1        //20X,5HIER =,I5//
     2          20X,22HPERFORMANCE INDEX =  (,2D12.4,2H )//
     3          40H * * *  RESULTS FOR THE FREQUENCIES (HZ)/)
 2040 FORMAT (4H I =,I5,5X,8HOM  =  (,2D24.16,2H ))
      END
C
      SUBROUTINE  REDUCE (CQ,AP,AQ,NT,NS,NX)
      IMPLICIT COMPLEX*16(A-H), REAL*8(O-Z)
      COMMON/TAPES/JIN,JOUT,JS1,JS2,JS3,JS4,JS5
      COMMON/ISHELL/DHI,DVI,QI,REI,SKI,PSI
      COMMON/CONST/PI,RGAMA,IOP1,IOP2
      DIMENSION  CQ(NT,NT,1),AP(NX,1),AQ(NX,1)
      REWIND (JS2)
      MX= NX*NX
      CV= (0.D0,0.D0)
      CALL CLEAR (AP,MX)
      CALL CLEAR (AQ,MX)
      DO 20  I=1,NS
      AP(I,NS+I)= (1.D0,0.D0)
   20 AQ(I,I)= (-1.D0,0.D0)
      IF (IOP1)  140,40,140
   40 IF (IOP2)  100,60,100
C ... WITHOUT STRUCTURAL AND VISCOUS DAMPING INCLUDED
C ... NO STEADY VISCOUS EFFECTS INCLUDED
   60 DO 80  J=1,NS
      DO 80  I=1,NS
```

```
      READ (JS2)  CM,CK
      AP(NS+I,J)= CK
   80 AQ(NS+I,NS+J)= CM
      GO TO 240
C ... WITH STRUCTURAL AND VISCOUS DAMPING INCLUDED
C ... NO STEADY VISCOUS EFFECTS INCLUDED
  100 DO 120  J=1,NS
      DO 120  I=1,NS
      READ (JS2)  CM,CK
      AP(NS+I,J)= DHI*CK
      AP(NS+I,NS+J)= DVI*CK
  120 AQ(NS+I,NS+J)= CM
      GO TO 240
  140 REWIND (JS3)
      IF (IOP2)  200,160,200
C ... WITHOUT STRUCTURAL AND VISCOUS DAMPING INCLUDED
C ... WITH STEADY VISCOUS EFFECTS INCLUDED
  160 DO 180  J=1,NS
      DO 180  I=1,NS
      READ (JS2)  CM,CK
      READ (JS3)  CV
      AP(NS+I,J)= CK + CV
  180 AQ(NS+I,NS+J)= CM
      GO TO 240
C ... WITH STRUCTURAL AND VISCOUS DAMPING INCLUDED
C ... WITH STEADY VISCOUS EFFECTS INCLUDED
  200 DO 220  J=1,NS
      DO 220  I=1,NS
      READ (JS2)  CM,CK
      READ (JS3)  CV
      AP(NS+I,J)= DHI*CK + CV
      AP(NS+I,NS+J)= DVI*CK
  220 AQ(NS+I,NS+J)= CM
C ... ADD TO AP AND AQ THE UNSTEADY INVISCID FORCES
  240 DO 260  M=1,NT
      J= M + 2*NT
      DO 260  K=1,NT
      I= K + 2*NT
      AP(NS+I,J)= AP(NS+I,J) + CQ(K,M,3)
      AP(NS+I,NS+J)= AP(NS+I,NS+J) + CQ(K,M,2)
  260 AQ(NS+I,NS+J)= AQ(NS+I,NS+J) + CQ(K,M,1)
C ... STORE AP ON TAPE JS3 TO SAVE STORAGE TO FIND INVERSE OF AQ
      REWIND (JS3)
      DO 280  J=1,NX
      DO 280  I=1,NX
      WRITE (JS3)  AP(I,J)
  280 AP(I,J)= AQ(I,J)
C ... FIND THE INVERSE OF MATRIX AQ (VALUES STORED IN AP)
      CALL INVSE (AP,NX)
C ... RETRIEVE AP FROM JS3
      REWIND (JS3)
      DO 300  J=1,NX
      DO 300  I=1,NX
  300 READ (JS3)  AP(I,J)
C ... PRE-MULTIPLY AP BY THE INVERSE OF AQ AND STORE THE PRODUCT ON JS3
      REWIND (JS3)
      DO 340  J=1,NX
      DO 340  I=1,NX
      ASUM= (0.D0,0.D0)
      DO 320  K=1,NX
  320 ASUM= ASUM + AP(I,NX+K)*AP(K,J)
  340 WRITE (JS3)  ASUM
C ... RETRIEVE THE PRODUCT FROM JS3 AND STORE IN ON AP
      REWIND (JS3)
      DO 360  J=1,NX
      DO 360  I=1,NX
  360 READ (JS3)  AP(I,J)
      RETURN
      END
C
      DOUBLE PRECISION FUNCTION  RE1 (K,M,ID)
C ... INTEGRALS INVOLVING FUNCTIONS OF CL-FR AND CL-CL BEAMS
      IMPLICIT REAL*8(O-Z)
      COMMON/COAX/RLA(10),RHO(10),OMR,RINT,NINT,N
      GO TO (100,200,300), ID
  100 IF (K.EQ.M)  GO TO 120
      RE1= 0.D0
      RETURN
  120 RE1= 1.D0
      RETURN
C ... FOR CLAMPED-FREE BEAMS ONLY.
  200 RE1= 4.D0*RLA(K)*RHO(K)*(-1)**(K+M)
      RETURN
  300 RE1= 4.D0*RLA(M)*RHO(M)*(-1)**(K+M)
      RETURN
      END
C
      DOUBLE PRECISION FUNCTION  RE2 (K,M,ID)
C ... INTEGRALS INVOLVING CHARAC. FUNCTIONS OF CLAMPED-FREE BEAMS
      IMPLICIT REAL*8(O-Z)
      COMMON/COAX/RLA(10),RHO(10),OMR,RINT,NINT,N
      RK= RLA(K)
      RM= RLA(M)
      SK= RHO(K)
      SM= RHO(M)
```

```
      IF (K.EQ.M)  GO TO 100
      GO TO (20,40,60,80), ID
   20 RE2= 4.D0/((-1)**(K+M) + (RM/RK)**2)
      RETURN
   40 TM= (-1)**(K+M)*(SM*RK**3 - SK*RM**3) + SM*RK*RM**2 - SK*RM*RK**2
      RE2= 4.D0*RK*RM*TM/(RK**4 - RM**4)
      RETURN
   60 RE2= 4.D0*(RK*SK - RM*SM)/((RK/RM)**2 - (-1)**(K+M))
      RETURN
   80 RE2= 0.D0
      RETURN
  100 GO TO (120,140,160,180), ID
  120 RE2= 2.D0
      RETURN
  140 RE2= RM*SM*(2.D0 + RM*SM)
      RETURN
  160 RE2= RM*SM*(2.D0 - RM*SM)
      RETURN
  180 RE2= -RM**4
      RETURN
      END
C
      DOUBLE PRECISION FUNCTION  RE3 (K,M,ID)
C ... INTEGRALS INVOLVING CHARAC. FUNCTIONS OF CLAMPED-FREE BEAMS
      IMPLICIT REAL*8(O-Z)
      COMMON/COAX/RLA(10),RHO(10),OMR,RINT,NINT,N
      RK= RLA(K)
      RM= RLA(M)
      SK= RHO(K)
      SM= RHO(M)
      IF (K.EQ.M) GO TO 100
      GO TO (20,40,60,80), ID
   20 TM1= RK*RM*SK*SM/(RK**4 - RM**4)
      TM2= 16.D0*TM1*RM**2*((-1)**(K+M)*RM**2 - RK**2)/(RK**4 - RM**4)
      RE3= 8.D0*TM1*(-1)**(K+M) + TM2
      RETURN
   40 TM1= 4.D0*RK*RM/(RK**4 - RM**4)
      TM2= (RM*TM1)**2*((-1)**(K+M)*RK**2 - RM**2)
      RE3= TM1*((-1)**(K+M)*(SM*RK**3 - SK*RM**3) - 2.D0*RK*RM) + TM2
      RETURN
   60 TM1= 4.D0*RM**2/(RK**4 - RM**4)
      TM2= (RM*TM1)**2*(RK**2 - RM**2*(-1)**(K+M))
      RE3= TM1*(RK**2 + RM**2*(-1)**(K+M)*(RK*SK - RM*SM - 3.[illegible] + TM2
      RETURN
   80 TM1= 4.D0*RK*RM**3*SK*SM/(RK**4 - RM**4)
      TM2= 4.D0*TM1*RM**4*(RK**2 - RM**2*(-1)**(K+M))/(RK**4 - RM**4)
      RE3= TM1*(RK**2 - 3.D0*RM**2*(-1)**(K+M)) + TM2
      RETURN
  100 GO TO (120,140,160,180), ID
  120 RE3= 0.5D0 + 2.D0*(SM/RM)**2
      RETURN
  140 RE3= 0.5D0*(RM*SM*(6.D0 + RM*SM) - 4.D0)
      RETURN
  160 RE3= 0.5D0*RM*SM*(2.D0 - RM*SM)
      RETURN
  180 RE3= -0.5D0*RM**4
      RETURN
      END
C
      DOUBLE PRECISION FUNCTION  RFAC (N)
      IMPLICIT REAL*8(O-Z)
      RFAC= 1.D0
      IF (N.LE.1)  RETURN
      X= 2.D0
      DO 20  I=2,N
      RFAC= RFAC*X
   20 X= X + 1.D0
      RETURN
      END
C
      DOUBLE PRECISION FUNCTION  RFI (N)
      IMPLICIT REAL*8(O-Z)
      RFI= 0.D0
      IF (N.EQ.0)  RETURN
      X= 1.D0
      DO 20  I=1,N
      RFI= RFI + 1.D0/X
   20 X= X + 1.D0
      RETURN
      END
C
      SUBROUTINE  SORT (DT,NX)
      IMPLICIT COMPLEX*16(A-H)
      DOUBLE PRECISION  DREAL
      DIMENSION  DT(1)
      NMIN= NX - 1
  100 IFLAG= 0
      DO 200  I=1,NMIN
      C1= DT(I)
      C2= DT(I+1)
      IF (DREAL(C1).GE.DREAL(C2))  GO TO 200
      DT(I)= C2
      DT(I+1)= C1
      IFLAG= 1
  200 CONTINUE
```

```
      IF (IFLAG.EQ.1)  GO TO 100
      RETURN
      END
C
      SUBROUTINE  VISFOR (CXV,NT,NS)
C ... CALCULATE STEADY VISCOUS FORCES FOR CLAMPED-FREE SHELLS
      IMPLICIT COMPLEX*16(A-H), REAL*8(O-Z)
      DOUBLE PRECISION  DLOG10,DSQRT
      COMMON/IFLUID/RHOI,UI,UIR
      COMMON/AFLUID/RHOA,UA,UAR
      COMMON/ISHELL/DHI,DVI,QI,REI,SKI,PSI
      COMMON/OSHELL/DHO,DVO,QO,REO,SKO,PSO
      COMMON/TAPES/JIN,JOUT,JS1,JS2,JS3,JS4,JS5
      COMMON/COAX/RLA(10),RHO(10),OMR,RINT,NINT,N
      COMMON/SVFOR/SAL(11),SBT(11),RDI,RDO,RGI,RGO,VISI,VISA,SL
      DIMENSION  CXV(NS,1),CV(3,3)
      R13= 0.33333333333333D0
C ... DETERMINE THE LOCATION OF THE MAXIMUM VELOCITY USING A MULTILINEAR
C     REPRESENTATION OF THE CURVE BY BRIGHTON & JONES (1965)
      RAB= RDI/RDO
      DO 5  I=1,11
      IF (RAB - SAL(I))  10,5,5
    5 CONTINUE
   10 SBETA= SBT(I-1)+(RAB-SAL(I-1))*(SBT(I)-SBT(I-1))/(SAL(I)-SAL(I-1))
      RM= RDO*(RAB + 0.5D0*SBETA*(1.D0 - RAB))
      IF (UIR)  40,40,20
   20 RNI= 2.D0*(UIR*UI)*RDI/VISI
      WFAI= 0.0055D0*(1.D0 + (2.D+04*RGI + 1.D+06/RNI)**R13)
      WFI= -0.5D0/DLOG10(RGI/3.7D0 + 2.51D0/(RNI*DSQRT(WFAI)))
      UTI= UI*UIR*WFI/DSQRT(8.D0)
      GO TO 60
   40 UTI= 0.D0
   60 IF (UAR)  100,100,80
   80 RNA= 2.D0*(UAR*UA)*(RDO - RDI)/VISA
      WFAOI= 0.0055D0*(1.D0 + (2.D+04*RGI + 1.D+06/RNA)**R13)
      WFAOO= 0.0055D0*(1.D0 + (2.D+04*RGO + 1.D+06/RNA)**R13)
      WFOI= -0.5D0/DLOG10(RGI/3.7D0 + 2.51D0/(RNA*DSQRT(WFAOI)))
      WFOO= -0.5D0/DLOG10(RGO/3.7D0 + 2.51D0/(RNA*DSQRT(WFAOO)))
      UTOI= UA*UAR*WFOI*DSQRT((RM**2 - RDI**2)/(8.D0*RDI*(RDO - RDI)))
      UTOO= UA*UAR*WFOO*DSQRT((RDO**2 - RM**2)/(8.D0*RDO*(RDO - RDI)))
      GO TO 120
  100 UTOI= 0.D0
      UTOO= 0.D0
  120 WBI= RHOI*UTI**2 + RHOA*UTOI**2
      WCI= 2.D0*(RHOI*UTI**2/RDI - RDO*RHOA*UTOO**2/(RDO**2 - RM**2))
      WDI= -SL*WCI
      RCONI= 1.D0/(QI*REI**2)
      A1I= -RCONI*WBI
      B1I= -A1I
      B2I=  RCONI*WBI*REI
      A3I= -RCONI*WCI*RDI
      B3I= -RCONI*WDI*REI
      EN= N
      DO 300  K=1,NT
      DO 300  M=1,NT
      CALL CLEAR (CV,9)
      CV(1,1)= REI**4*( A1I*RE3(K,M,4) + B1I*RE2(K,M,4) )
     1       - (EN*REI)**2*( A3I*RE3(K,M,2) + B3I*RE2(K,M,2) )
      CV(3,1)= REI**2*( A3I*RE3(K,M,3) + B3I*RE2(K,M,3) )
      CV(1,2)= B2I*EN*REI*RE2(K,M,1)
      CV(2,2)= REI**2*( A1I*RE3(K,M,3) + B1I*RE2(K,M,3) )
     1       - EN**2*( A3I*RE3(K,M,1) + B3I*RE1(K,M,1) )
      CV(3,2)= -EN*( A3I*RE3(K,M,1) + B3I*RE1(K,M,1) )
      CV(1,3)= REI*(B2I*RE2(K,M,1)-REI*(A3I*RE3(K,M,2)+B3I*RE2(K,M,2)))
      CV(2,3)= CV(3,2)
      CV(3,3)= CV(2,2)
      DO 200  J=1,3
      JJ= M + NT*(J - 1)
      DO 200  I=1,3
      II= K + NT*(I - 1)
  200 CXV(II,JJ)= CV(I,J)
  300 CONTINUE
      REWIND (JS3)
      DO 400  J=1,NS
      DO 400  I=1,NS
  400 WRITE (JS3)  CXV(I,J)
      RETURN
      END
```

```
 1
        2.8246D+06              0.47D+00           1.15880D+03
        1.3700D-03     0.0248400000D+00             0.000D+00
        0.0000D+00            5.79500D-05
        2.8246D+06              0.47D+00           1.15880D+03
        1.3700D-03     0.0326300000D+00             0.000D+00
        0.0000D+00            5.79500D-05
 203.200-03          3.000+00          2.0000+00   200     3     2     6     1 1
 1
 15.1782D-06    1.204908D+00    0.000000D+00            1TH
 15.1782D-06    1.204908D+00    0.500000D+00

 .282460000000D+07    .470000000000D+00    .115880000000D+04
 .137000000000D-02    .248400000000D-01    .000000000000D+00
```

```
  .000000000000D+00    .579500000000D-04
  .282460000000D+07    .470000000000D+00    .115880000000D+04
  .137000000000D-02    .326300000000D-01    .000000000000D+00
  .000000000000D+00    .579500000000D-04
   .203200D+00    .300000D+01    .200000D+01  200    3    2    6    1 1
* * *  VALUES OF NON-DIMENSIONALIZED FLOW VELOCITIES

                 UIR =    .000000D+00            UAR =    .500000D+00

* * *  RESULTS FROM THE ITERATIVE METHOD

                 IER =    0

                 PERFORMANCE INDEX =  (  -.5803D+00  -.5803D+00 )

* * *  RESULTS FOR THE FREQUENCIES (HZ)

I =    1     OM  =  (    .1048295907986013D+04    .2079812669793047D+03 )
I =    2     OM  =  (    .9687370979333850D+03    .1765845006798884D+03 )
I =    3     OM  =  (    .8983542221440896D+03    .1511760631110237D+03 )
I =    4     OM  =  (    .8504934584966479D+03    .1351954933088171D+03 )
I =    5     OM  =  (    .8142396837487305D+03    .1237338325031828D+03 )
I =    6     OM  =  (    .7971733367436865D+03    .1183860270744251D+03 )
I =    7     OM  =  (    .6550976307876988D+03    .7935024558909701D+02 )
I =    8     OM  =  (    .5304643841159377D+03    .5176234811343834D+02 )
I =    9     OM  =  (    .4796419564329192D+03    .4226071138682401D+02 )
I =   10     OM  =  (    .4306212277274291D+03    .3404057736096248D+02 )
I =   11     OM  =  (    .3927118227343979D+03    .2834658104876489D+02 )
I =   12     OM  =  (    .3700060774017385D+03    .2524060365152139D+02 )
I =   13     OM  =  (    .1559312520816564D+03    .5033849994597042D+01 )
I =   14     OM  =  (    .1197443137949527D+03    .3037408153925237D+01 )
I =   15     OM  =  (    .8461074233206870D+02    .1745735612743282D+01 )
I =   16     OM  =  (    .4999507802161132D+02    .9272538520444010D+00 )
I =   17     OM  =  (    .2268561789667530D+02    .6446207864839725D+00 )
I =   18     OM  =  (    .1408067546989129D+02    .6488697245787243D+00 )
I =   19     OM  =  (   -.1408067793137441D+02    .6488726324761072D+00 )
I =   20     OM  =  (   -.2268561936480004D+02    .6446162173731894D+00 )
I =   21     OM  =  (   -.4999508414492599D+02    .9272772279776373D+00 )
I =   22     OM  =  (   -.8461074596484617D+02    .1745729387742928D+01 )
I =   23     OM  =  (   -.1197443218464753D+03    .3037434017154329D+01 )
I =   24     OM  =  (   -.1559312667126923D+03    .5033856007432387D+01 )
I =   25     OM  =  (   -.3700060800556562D+03    .2524060437223972D+02 )
I =   26     OM  =  (   -.3927118242770698D+03    .2834658196644472D+02 )
I =   27     OM  =  (   -.4306212287544204D+03    .3404057759772115D+02 )
I =   28     OM  =  (   -.4796419568405938D+03    .4226071178283312D+02 )
I =   29     OM  =  (   -.5304643843734056D+03    .5176234831167818D+02 )
I =   30     OM  =  (   -.6550976305204057D+03    .7935024559172361D+02 )
I =   31     OM  =  (   -.7971733372212724D+03    .1183860271658074D+03 )
I =   32     OM  =  (   -.8142396852495957D+03    .1237338327181487D+03 )
I =   33     OM  =  (   -.8504934601772466D+03    .1351954939355281D+03 )
I =   34     OM  =  (   -.8983542233619941D+03    .1511760633806954D+03 )
I =   35     OM  =  (   -.9687370986895733D+03    .1765845011790282D+03 )
I =   36     OM  =  (   -.1048295908256465D+04    .2079812670273656D+03 )
```